

Advanced Ion Trap Development and Ultrafast Laser-Ion Interactions

by

Martin John Madsen

A dissertation submitted in partial fulfillment
of the requirements for the degree of
Doctor of Philosophy
(Physics)
in The University of Michigan
2006

Doctoral Committee:

Professor Christopher R. Monroe, Chair
Professor Roberto D. Merlin
Professor Georg A. Raithel
Professor Duncan G. Steel
Assistant Professor Luming Duan

ABSTRACT

Advanced Ion Trap Development and Ultrafast Laser-Ion Interactions

by

Martin John Madsen

Chair: Christopher R. Monroe

All of the essential elements for a trapped ion quantum computer have been demonstrated in previous experiments. There are, however, many technical challenges to scaling the number of quantum bits from the current state-of-the-art (about 8) to the number of qubits needed for practical quantum computing. Although there is experimental evidence supporting one possible method (using cw laser pulses and common motional modes as the ion interaction) for deterministic ion entanglement, it is not known if that will ultimately be the most practical method for building a large-scale quantum computer. One model for scalable quantum computing with trapped ions calls for large interconnected arrays of small traps. Several advancements reported in this work include the development of three layer alumina traps as well as MEMS fabricated microtraps. Other models for scalable trapped ion quantum computing do not call for local entanglement or call for relaxed constraints on the motional control of the ions. These proposals require the use of ultrafast laser

pulses interacting with the ions. This work reviews several experiments that explore the interaction between the ultrafast laser and single trapped ions including early indication of ultrafast control and entanglement between a single ion and a single photon frequency qubit.

“This is my bag of cake.”

© Martin John Madsen
All Rights Reserved
2006

To my wife.

ACKNOWLEDGEMENTS

I have had five excellent years here at the University of Michigan and I have a lot of people that I want to thank for their contributions and help over that time. About the time I arrived in Ann Arbor to start graduate school, I got a call from Chris Monroe inviting me to come tour his lab to see if it was something I wanted to do. I was eager to get started right away doing research, so I jumped at the chance. That first day I visited the temporary lab on the fourth floor of Old Randall (before we moved down to the sub-basement lab), Patty Lee, Louis Deslauriers, Boris Blinov and Russ Miller were working and had an ion loaded in the trap. I had vague recollections of elementary school teachers talking about the “hypothetical” atom, but here was one, “live” for me to watch. I became very excited about trapped ion research at that moment and the excitement has not worn off since.

The first year of research was very funny. I mean that the people were funny- Boris and Louis kept us in stitches the entire year. I remember long, exciting conversations with Louis about the physics involved. We all worked together in building the lab and the research project. By the end of that year, we had moved the lab down to the basement and the group began to grow. I started working on advanced trap development in the form of designing and fabricating the first gold-coated alumina linear trap. By the end of the next year, we were full-blown working on both the alumina trap, but also developing the technology for the semiconductor microtraps

with Dan Stick and Winnie Hensinger. We worked closely over the next 18 months, designing and building the new trap and vacuum system to house it. It was exciting to work together on what we saw was the future for trapped ion quantum computing. I spent the summer of 2003 working on the write-up of the computer model paper for the microtrap and I need to thank Chris, Dan, Winnie, and Jim Rabchuk (from Western Illinois University) for their patience with me during that process. It was my first crack at a scientific paper and it took about four times longer than it should have, due to my inexperience. But it got finished and was a good place for me to stop and change gears.

In January 2004, I talked with Chris about switching sub-groups and starting to work more intensely with actual ions doing physics research. At that point my options were to work with the team doing ground-state cooling or to work with the team doing quantum optics and ion-photon entanglement. The latter sounded interesting, so I joined with Boris and David Moehring on that experiment. I had gone to Purdue University with Dave and it was fun to work together on the research. We extended some of the work they had done previously and measured a violation of Bell's Inequality with the ion-photon system. We then pushed forward in trying to build a remote entanglement experiment between two atoms. Between attempts at that, we ran a precise measurement of the cadmium excited state lifetime. I want to thank David Gidley, Richard Vallery and Tracy Sanderson for their help in processing that data. It was my first experience with a precision measurement and not one I think I want to repeat- they are very difficult and without the expertise of David and his group, I don't think we would have made it.

About this time, Rudy Kohn joined our little group as an undergraduate researcher. He has continued faithfully and was instrumental in making the last ex-

periment described in this work possible. Without his help over the winter break in 2005-2006, we would not have finished the experiment in such a timely manner (three weeks before the laser died). We did squeeze one other successful experiment in between the failed attempts at remote ion entanglement and I want to thank Boris for pushing the broadband cooling experiment through. He made that one happen and it was a good result. In addition to Boris, I want to thank Peter Maunz, a post-doc who joined with us last summer, for his help in getting the experiment to happen. I appreciate the knowledge and wisdom that post-docs bring to the research table and value the contribution that they make.

Finally, there have been a number of people with whom I have not published directly that I want to thank for their help and contributions over the years. I could not have asked for better office mates than Mark Acton and Kathy-Ann Brickman. Our conversations have been rewarding many times over throughout these years. Paul Haljan was an incredibly dynamic post-doc for our group and I think we all leaned on his experience heavily. I also want to thank the newer grad students Steve Olmschenk, John Sterk and Kelly Younge for carrying the baton as the first group members have left. A research group is only as good as its newest members make it. I also want to thank David Hucul, Liz Otto, and Mark Yeo for their help and input as undergraduates. They were especially helpful as I was preparing for job interviews over the winter of 2006.

Most of all, though, I thank Chris for his understanding and support during this time. I was not a typical graduate student and he was always supportive of my family obligations throughout the entire time I was here. It is not often that the grad student and adviser have new babies in their families at the same time, but we made it through that. I also want to thank Jane for her support of me and my family.

It has been so nice to get together with Chris and his family and the group on our many social occasions. It has made the graduate school experience something very special.

And, of course, I want to thank my wife Jessica. Without her support from the home front, I would not have been able to do any of this. She has persevered through five years of intense work at home, two pregnancies, three children, too many conferences and business trips, and enough stress to last a lifetime. She is my strength and support and I thank her with my entire heart.

TABLE OF CONTENTS

DEDICATION	ii
ACKNOWLEDGEMENTS	iii
LIST OF TABLES	ix
LIST OF FIGURES	x
LIST OF APPENDICES	xiv
ABSTRACT	xv
CHAPTER	
I. Introduction	1
II. Ion Trapping Fundamentals and Equipment	4
2.1 Ponderomotive Potential	4
2.2 Doppler Cooling	7
2.3 Micromotion Detection	9
2.4 Vacuum Chamber	17
2.5 Ion Trap Mounting Requirements	37
2.6 Baking the Chamber	37
2.7 rf Generation and Delivery	44
III. Ion Trap Design	50
3.1 Linear Trapping Potentials	50
3.2 Transverse Electric Potential Simulation	50
3.3 3D Electric Potential Simulation	56
3.4 Errors in Finite Element Analysis Field Solvers	59
IV. Planar Microtrap Model	65
4.1 Background	65
4.2 Model Description	67
4.3 RF Ponderomotive Potentials	73
4.4 Static Potentials	86
4.5 Net Potential	91
4.6 Microtrap Principal Axes	93

4.7	Future Research	96
V.	Trap Fabrication	98
5.1	Gold-plated Alumina Linear Trap	98
5.2	GaAs Microtrap Assembly.	116
VI.	Precision Lifetime Measurement	126
6.1	Background	126
6.2	Experiment Setup	128
6.3	Data Fit and Systematic Shift	131
6.4	Error Analysis	134
VII.	Broadband Laser Cooling	140
7.1	Motivation	140
7.2	Cooling Experiment Setup	142
7.3	Theoretical Cooling Limit	146
VIII.	Ultrafast S to P Rabi Oscillations	151
8.1	Motivation	151
8.2	Pulsed Excitation Experiments	152
8.3	Ramsey Experiments	155
8.4	Excited State Hyperfine Splitting Measurement	159
IX.	Conclusion	162
	APPENDICES	164
	BIBLIOGRAPHY	194

LIST OF TABLES

Table

2.1	Vacuum Hardware	21
2.2	Parts needed for assembly of vacuum chamber	22
4.1	Sample calculations for trap performance	92
6.1	Lifetime measurement results (ns)	138

LIST OF FIGURES

Figure

2.1	The principal axes of the linear trap	11
2.2	Micromotion broadened lineshape for small amplitude	12
2.3	Micromotion broadened lineshape for large amplitude	12
2.4	The cross-correlated florescence signal for small β	14
2.5	The cross-correlated florescence signal for larger β	14
2.6	Screen shot of the micromotion detection program	15
2.7	Four-rod linear trap electric fields	17
2.8	A schematic overview of the entire vacuum system.	18
2.9	Knife edge illustration	20
2.10	CF Tightening pattern	25
2.11	Trap loading process illustration	26
2.12	Home-made electron gun illustration	28
2.13	Spot-welding instructional illustration	30
2.14	Electron gun wiring schematic	31
2.15	An illustration of the atomic source ovens	34
2.16	Oven crimping illustration	35
2.17	Oven mounting block illustration	36
2.18	Bake-out time data	40
2.19	An illustration of the oven with pumps and valves shown	43
2.20	Helical resonator diagram	46

2.21	RF filters and wiring diagram	48
2.22	RF generation diagram	49
3.1	The GUI for Setting up the model in the PDE Toolbox	52
3.2	The GUI for Solving the model in the PDE Toolbox	53
3.3	The GUI for Setting up the Project in Maxwell 3D	58
3.4	The GUI for Defining Materials in Maxwell	60
3.5	The GUI for Defining the Mesh in Maxwell	61
3.6	The GUI for Solving the Problem in Maxwell	62
4.1	A three-dimensional drawing of the linear microtrap	68
4.2	Two layer schematic of the potentials	69
4.3	Hyperbolic electrode geometry	75
4.4	Transverse Equipotential Lines	78
4.5	Transverse Geometric efficiency factor	80
4.6	Higher-order expansion coefficients	81
4.7	Scaled trap depth	82
4.8	Higher-order coefficients as a function of trap radius	83
4.9	Largest higher-order coefficients as a function of α	84
4.10	Residual axial ponderomotive potential	86
4.11	Residual ponderomotive potential for different center electrode lengths	87
4.12	Three-dimensional hyperbolic electrodes are shown here	88
4.13	Static potential numerical results in the linear microtrap	90
4.14	Charge model for principal axis rotation	95
4.15	Microtrap principal axis rotation	97
5.1	Four rod linear trap illustration	99
5.2	Ceramic linear trap design	100
5.3	Assembled ceramic trap photo	101
5.4	Transverse illustration of ceramic trap	101

5.5	Ceramic trap three electrical layers	103
5.6	A SEM photo of the tip of the chamfered edge of the static electrode substrate . .	104
5.7	Design for physical masks for the rf and static electrodes	106
5.8	Electrode layout for the static electrode layers in the alumina trap	107
5.9	Low-pass filter schematic	108
5.10	Capacitor wire-bonding diagram	109
5.11	Completed alumina trap in the vacuum chamber	111
5.12	Alumina trap rotated principal axes potentials	112
5.13	Alumina principal axes rotation	114
5.14	Alumina trap axial frequency	115
5.15	Fabrication process for a semiconductor ion trap	118
5.16	Scanning electron microscope image of a monolithic GaAs semiconductor linear ion trap	119
5.17	A close-up view of the completed microtrap in vacuum	120
5.18	Microtrap chip carrier socket design	121
5.19	Microtrap vacuum chamber mount	122
5.20	The LCC mounted in the socket via an early clamp system	123
5.21	The LCC mounted in the socket using the final squeeze plate	123
5.22	Microtrap ion image	124
6.1	The experimental apparatus for the lifetime measurement	128
6.2	Lifetime data with response function and residuals	130
6.3	Lifetime fit crossing point	134
6.4	Lifetime Error Estimation Data	136
6.5	Previous published results for the lifetime	139
7.1	The broadband laser cooling apparatus	142
7.2	Ion images with the pulsed laser	144
7.3	A summary of the cooling measurements	147
8.1	Rabi oscillation experiment setup	153

8.2	The ion bright state population as a function of pulse energy	156
8.3	Ramsey fringe contrast	158
8.4	Excited state hyperfine splitting measurement	160
A.1	Electromagnetic fields in a coaxial resonator	166
B.1	A linear microtrap model in the complex plane	169
C.1	Functional form of sech pulses	175
C.2	Autocorrelation data and functional form of sech versus Gaussian pulses	177
C.3	Excitation Probability as a function of laser power	180
E.1	The energy levels for the OBE model.	189

LIST OF APPENDICES

Appendix

A.	Coaxial Resonator Fields	165
B.	Analytic Solution of the Transverse Potential	169
C.	Picosecond Pulse Generation and Characterization	174
	C.1 Picosecond Generation	174
	C.2 Atomic Transitions.	178
D.	Two-Level Ultrafast Rabi Oscillation	181
	D.1 Introduction	181
	D.2 Simple Introductory Two Level Problem	181
	D.3 Two Pulse Approximation	185
E.	Ultrafast Optical Bloch Equations	187
	E.1 Density Matrix Setup	187
	E.2 Microwave Rotations	191
	E.3 Ultrafast Laser Rotations	192

ABSTRACT

All of the essential elements for a trapped ion quantum computer have been demonstrated in previous experiments. There are, however, many technical challenges to scaling the number of quantum bits from the current state-of-the-art (about 8) to the number of qubits needed for practical quantum computing. Although there is experimental evidence supporting one possible method (using cw laser pulses and common motional modes as the ion interaction) for deterministic ion entanglement, it is not known if that will ultimately be the most practical method for building a large-scale quantum computer. One model for scalable quantum computing with trapped ions calls for large interconnected arrays of small traps. Several advancements reported in this work include the development of three layer alumina traps as well as MEMS fabricated microtraps. Other models for scalable trapped ion quantum computing do not call for local entanglement or call for relaxed constraints on the motional control of the ions. Both of these proposals require the use of ultrafast laser pulses interacting with the ions. This work reviews several experiments that explore the interaction between the ultrafast laser and single trapped ions including early indication of ultrafast control and entanglement between a single ion and a single photon frequency qubit.

CHAPTER I

Introduction

The field of quantum computing was, to a large degree, initiated by Richard Feynman who first proposed that quantum bits (or qubits) could be used to perform computations [1]. In addition, early work by David Deutsch showed that there are certain algorithms for which a quantum computer can be faster than a classical computer [2, 3]. However, the level of interest in quantum information and quantum computing remained low until the work by Peter Shor and others in the mid-1990s that showed an exponential speed-up on a key algorithm for factoring large numbers using a quantum computer [4, 5, 6, 7, 8]. Combined with a proposal for using trapped ions as the qubits for such a quantum computer, the field of trapped ion quantum information was initiated [9, 10].

Over the last ten years many key aspects and components of scalable quantum computation have been demonstrated in various trapped ion systems [9, 11, 12, 13, 14, 15, 16, 17, 18, 19, 20, 21, 22]. These components have relied on several schemes for using quantum control of local entanglement gates that rely on the coupled motion of ions in a strong trap. Because these schemes require a pure state of motion, or at least that the ion is in the Lamb-Dicke limit, there are strong technical limitations to the number of ions that can be utilized in a given local

trap. There are two directions that could work around these technical limitations. One is to use an array of interconnected ion traps, shuttling small numbers of ions through an “interaction zone” for the quantum gates and then storing the ions in auxiliary traps until needed [23]. Chapter III describes the use of computer modeling software to aid in the design of more complicated trap geometries. Chapters IV and V cover two separate advances in advanced ion trap development that constitute progress in making these trap arrays. The other direction is to use ultrafast laser pulses interacting with trapped ions instead of the typical switched cw lasers [24, 25, 26]. By using ultrafast laser pulses, the interaction with the ion takes place on a time scale much faster than the ion motion. In addition, the use of ultrafast laser pulses to excite the ions could lead to networks of remotely entangled ions through a photonic coupling [27, 28, 29, 30], another possible architecture for scalable trapped ion quantum computing.

The first area of development for scalable trapped ion quantum computing is advanced ion trap development. Although the original proposal for trapped ion quantum computers called for all the qubits in one long linear trap [9], the technological difficulties in implementing that protocol have steered the research community away from that proposal. Rather, it has been shown that small numbers of ions in larger, segmented traps have been shown to be a successful, and possible scalable solution [31, 32, 18, 33]. In a sense, this transfers some of the technical difficulty in making a trapped ion quantum computer from the laser to the trap, making it necessary to have much more complicated trap structures.

Building toward more complicated structures, Chapter IV will describe a model for this type of trap as well as two possible implementations and the successful operation of one of those types [32]. Chapter V describes two new ion trap designs: a three-

layer gold-on-alumina linear trap and a MEMS-fabricated GaAs/ AlGaAs monolithic linear microtrap [33]. The three-layer design was a first step in building a trap that has solved the topological problem of making junctions in rf traps. By placing the rf electrode on the center layer, it is possible to make a wide variety of junctions without compromising the trapping capability. The microtrap design is a new way of fabricating a linear trap that is an order of magnitude smaller than current trap structures, yet is scalable using existing semiconductor fabrication techniques.

The current model of entanglement via slow-pulsed cw lasers interacting with ions in a strong linear trap has been very successful in working with a few qubits. But there are other proposals that have yet to be tested experimentally. These proposals for trapped ion quantum computing include an ultrafast gate using a series of ultrafast laser pulses to kick the ion in phase space on a time scale faster than the trap frequency and the excited state lifetime. In addition, there are proposals to use probabilistic ion-photon entanglement to build a cluster-state type network for scalable quantum computing. Both of these proposals require control of the ion motion and quantum state using ultrafast laser pulses, a new area of research.

Chapter VI describes experiments using a mode-locked pulsed laser to make a precise measurement of the excited state lifetimes, to perform a new type of broadband laser cooling (Chapter VII), and to measure coherence in the ion excited state as well as indirect evidence for ion-photon entanglement involving the ground state hyperfine qubit and a resolved frequency photonic qubit (Chapter VIII). All three of these results are key components in building both the deterministic ultrafast entanglement as well as in building the remote ion cluster state networks.

CHAPTER II

Ion Trapping Fundamentals and Equipment

2.1 Ponderomotive Potential

2.1.1 Pseudopotential Approximation. The rf ion trap is the time average behavior of inhomogeneous oscillating electric fields [34]. Consider a charged particle moving in one dimension in an oscillating electric field of the form

$$E(z) = E_0(z) \cos \Omega_T t \quad (2.1)$$

where $E_0(z)$ is the spatial dependence of the electric field. Consider the case in which the electric field is non-uniform so the $\partial E_0(z)/\partial z \neq 0$. The equation of motion for an ion of charge e and mass m is

$$m\ddot{z} = F_z(t) = eE(z). \quad (2.2)$$

A solution for small oscillations about some average position of the ion \bar{z} is desired such that the position is $z(t) = \bar{z} + \zeta(t)$. The small perturbation as a function of time is thus

$$\zeta(t) = -\zeta_0 \cos \Omega_T t \quad (2.3)$$

with amplitude $\zeta_0 = eE_0(z)/(m\Omega_T^2)$. The electric field is expanded about the average ion position \bar{z} , looking at the time average motion of the ion. Keeping only the first

order, the electric field is

$$E_0(z) \approx E_0(\bar{z}) + \left[\frac{\partial E_0(\bar{z})}{\partial \bar{z}} \right] \zeta \quad (2.4)$$

where it was assumed that the amplitude of the motion is small compared to the characteristic size of the electric field inhomogeneity, neglecting higher order terms ($|\zeta| \ll [\partial E_0(\bar{z})/\partial \bar{z}]$). Averaging the force on the ion over one period, one finds

$$\begin{aligned} \bar{F}(\bar{z}) &= e \left\langle E_0(\bar{z}) \cos \Omega_T t + \left[\frac{\partial E_0(\bar{z})}{\partial \bar{z}} \right] \zeta' \cos \Omega_T t \right\rangle \\ &= e \left[\frac{\partial E_0(\bar{z})}{\partial \bar{z}} \right] \langle \zeta' \cos \Omega_T t \rangle \end{aligned} \quad (2.5)$$

This can now be substituted into the equation of motion for the small perturbation (Eq. 2.3) and one finds

$$\langle \zeta' \cos \Omega_T t \rangle = -\frac{1}{2} \zeta_0 = -\frac{E_0(\bar{z})}{2m\Omega_T^2}. \quad (2.6)$$

The average force on the ion (in the limit of small perturbations) is thus

$$\bar{F}(\bar{z}) = -\frac{e [\partial E_0(\bar{z})/\partial \bar{z}] E_0(\bar{z})}{2m\Omega_T^2}. \quad (2.7)$$

This can also be written as a function of a pseudopotential $\psi(z) \equiv eE_0^2(z)/(4m\Omega_T^2)$ which represents the time-average potential such that the average force is

$$\bar{F}(\bar{z}) = -e \frac{\partial \psi(\bar{z})}{\partial \bar{z}}. \quad (2.8)$$

Because the time average behavior of the ion is only dependent on the spatial characteristics of the electric field amplitude, the trap can be modeled using electrostatic simulations and the electric field $E_0(\bar{z})$ can be used to describe the general ion behavior (see Chapters III and IV). The ion motion is characterized by an oscillation frequency

$$\omega_z = \frac{e}{2m\Omega_T} \left[\frac{\partial^2 E_0(\bar{z})}{\partial \bar{z}^2} \right]^{1/2} \quad (2.9)$$

This result can be generalized to three dimensions so that the average force on an ion near equilibrium $(\bar{x}, \bar{y}, \bar{z})$ is

$$\bar{F}(\bar{x}, \bar{y}, \bar{z}) = -e\nabla\psi(\bar{x}, \bar{y}, \bar{z}), \quad \psi(\bar{x}, \bar{y}, \bar{z}) \equiv [e/(4m\Omega_T^2)] E_0^2(\bar{x}, \bar{y}, \bar{z}). \quad (2.10)$$

2.1.2 Mathieu Equations. If one considers the type of quadrupole fields commonly used in ion trap experiments, the ion motion can be described in more detail. The ion is confined in the transverse (x, y) plane by the oscillating rf electric field described near the center of the trap by the potential [35]

$$\Phi = \frac{V_0 \cos \Omega_T t + U_r}{2} \left(1 + \frac{x^2 - y^2}{R^2} \right) \quad (2.11)$$

where the potential V_0 is the oscillating potential amplitude, U_r is a static offset potential, and R is the characteristic dimension of the trap. The ions are confined along the trap axis (z) by some static potential (of characteristic length z_0) which is quadratic near the center of the trap.

$$\Phi_s = \frac{U_0}{z_0^2} \left[z^2 - \frac{1}{2} (x^2 + y^2) \right] = \frac{m}{2e} \omega_z^2 \left[z^2 - \frac{1}{2} (x^2 + y^2) \right] \quad (2.12)$$

The frequency of oscillation along the z -axis is not dependent on the rf frequency Ω_T and is $\omega_z = \sqrt{2eU_0/(mz_0^2)}$, for simple harmonic oscillation. In the xy plane, however, the ion motion is more complicated. Combining both Eq. 2.11 and 2.12, the equations of motion can be written in the form of the Mathieu equations:

$$\frac{d^2x}{d\xi} + [a_x + 2q_x \cos(2\xi)] = 0 \quad (2.13)$$

$$\frac{d^2y}{d\xi} + [a_y + 2q_y \cos(2\xi)] = 0$$

where $\xi \equiv \Omega t/2$, and the coefficients are $a_x = (4e/m\Omega_T^2)(U_r/R^2 - U_0/z_0^2)$ and $q_x = 2eV_0/(\Omega_T^2 m R^2)$, $a_y = -(4e/m\Omega_T^2)(U_r/R^2 + U_0/z_0^2)$, and $q_y = -q_x$.

The solutions to the Mathieu equations are well known [36]. In the pseudopotential approximation (where $|a_x|, q_x^2 \ll 1$) the equations of motion in both the x and y directions are, to first order in a_i and to second order in q_i ,

$$u_i(t) = u_{0i} \left(\cos(\omega_i t + \varphi_i) \left[1 + \frac{q_i}{2} \cos(\Omega_T t) + \frac{q_i^2}{32} \cos(2\Omega_T t) \right] + \beta_i \frac{q_i}{2} \sin(\omega_i t + \varphi_i) \sin(\Omega_T t) \right) \quad (2.14)$$

where $u_i = x, y$, u_{0i} depends on initial conditions and

$$\omega_i = \beta_i \frac{\Omega_T}{2}, \quad \beta_i \simeq \sqrt{a_i + q_i^2/2}. \quad (2.15)$$

There are several parts to the motion of the ion. The large, slow oscillations at frequencies ω_i are the same as the oscillation frequency in the pseudopotential approximation from above (Eq. 2.9) for the electric field given by Eq. 2.11.

2.2 Doppler Cooling

Laser-ion interactions are currently the only method for executing quantum information experiments in trapped ion systems. In order to carry out many of these interactions over long periods of time, the ions must be well localized. It is necessary, therefore, to cool the ions from the thermal temperatures when they are first loaded in the rf trap to cold, localized ion crystals. This is done using Doppler cooling techniques that are now ubiquitous in atomic physics experiments. Included here is a brief overview of the theoretical background of the Doppler cooling technique.

2.2.1 Atomic Scattering Rate. Atom-laser interactions can be described using the Optical Bloch Equations and the density matrix formalism including spontaneous emission [37, 38, 39, 40]. For a simple two level atom, the rate at which the atom absorbs and then re-emits a photon can be written as a scattering rate

$$\gamma_p = \frac{s_0 \gamma / 2}{1 + s_0 + (2\delta/\gamma)^2} \quad (2.16)$$

for an atom with excited state natural linewidth γ and saturation parameter

$$s_0 \equiv I/I_s. \quad (2.17)$$

The laser intensity on the atom is I and the atom has a saturation intensity characteristic of the particular transition (at wavelength λ and with lifetime $\tau = 1/\gamma$) of

$$I_s \equiv \frac{\pi \hbar c}{3\lambda^3 \tau}. \quad (2.18)$$

The scatter rate (Eq. 2.16) for an atom that is moving with velocity \vec{v} is shifted due to the Doppler effect $\omega_D = -\vec{k} \cdot \vec{v}$ (note that a velocity opposite to the laser wavevector \vec{k} produces a positive Doppler shift). The scatter rate is therefore dependent on the ion velocity and is

$$\gamma_p = \frac{s_0 \gamma / 2}{1 + s_0 + (2(\delta - \omega_D)/\gamma)^2}. \quad (2.19)$$

2.2.2 Doppler Cooling. The Doppler shifted scatter rate (Eq. 2.19) gives rise to a velocity dependent force that behaves like a classical damping force. The atom experiences an average force due to the scatter of photons that is the momentum of the photon times the scatter rate $F_{sp} = \hbar k \gamma_p$. Substituting the Doppler-shifted scatter rate gives

$$F_{sp} = \pm \frac{\hbar k s_0 \gamma / 2}{1 + s_0 + (2(\delta - \omega_D)/\gamma)^2}. \quad (2.20)$$

The force acts along the direction of the laser wavevector such that an atom moving toward the laser feels an opposing force. However, when the atom moves away from the laser, the Doppler shift is such that the photon scattering stops and the atom does not feel the force. Three pairs of counter-propagating laser beams are thus required to cool a free atom in all directions. However, for a trapped ion only one beam is required as long as the laser wavevector is not parallel to any of the trap

principal axes [40]. The Doppler force results in a tiny displacement of the ion from the trap center.

2.3 Micromotion Detection

Although the motion described in Section 2.1 is approximately harmonic, the ion motion also has the small oscillations at the trap frequency. These oscillations are commonly referred to as “micromotion”. There are two types of micromotion: some micromotion is unavoidable and comes from the equations of motion of an ion in a rf trap. The other type of micromotion, called “excess” micromotion, comes from either a static bias field that pushes the ion off of the rf node, or from a phase difference in the rf fields applied via different electrodes. It is much more difficult to control that phase, although if proper precautions are taken (such as matching the path length to the rf electrodes and using large filter capacitors to match the rf potentials) this problem can be safely ignored.

There are several techniques that can be used to measure and then null the excess micromotion of an ion in the trap [41]. The first is to use the Doppler broadening of the absorption lineshape from the velocity of the excess micromotion. The second is to use a cross-correlation technique that measures preferential ion absorption at the trap frequency. Another technique that can be used is an amplitude-modulation of the rf while observing the physical position of the ion in the trap. After nulling micromotion using a combination of these techniques, the ion should be at the rf node.

The motion of the ion can be written (after solving the Mathieu equations, Eq. 2.13) in the following manner (see Eq. 2.14):

$$u_i(t) = (u_{0i} + u_{1i} \cos(\omega_i t + \varphi_{si})) \left[1 + \frac{q_i}{2} \cos \Omega_T t \right]$$

where $i = x, y, z$ are the three principal axes in the trap, u_{1i} is the equilibrium position of the ion in the center of the trap, u_{0i} is the offset position of the ion due to extra static electric fields pushing it off the center,

$$q_x = -q_y = 2eV_0/mR^2\Omega_T^2 \approx 0.45, \quad q_z = 0$$

for typical trap spacings and voltages in the lab, and $\Omega_T \approx 50$ MHz. The phase factor φ_{si} is determined by the initial conditions of the trap and is not important to the analysis of excess micromotion.

The interaction between the Doppler cooling laser and the micromotion of the ion can be characterized by a parameter

$$\beta = \frac{k_{laser}}{2} [u_{0x}q_x \cos \theta_x + u_{0y}q_y \cos \theta_y],$$

where k_{laser} is the laser wavevector and θ_i is the angle between the laser wavevector and the x and y principal axes of the trap (typically about 45 degrees). This parameter can be approximated as $\beta \approx 5.1(u_{0x} + u_{0y})$ where the offset positions are in micrometers.

For the alumina linear trap (Section 5.1), the laser has a component along both x and y , however displacements along a rotated axes illustrate the proper technique to use for minimizing micromotion. Figure 2.1 shows the electric field quadrupole lines for the alumina traps, indicating that the first-order Doppler shift is sensitive to displacements in the x' direction, as the ion micromotion in that direction has a velocity component along the laser wavevector [41]. Displacements in the y' direction do not lead to velocity dependent scattering and the amplitude modulation technique must be used.

For an ion displacement in the x' direction of Fig. 2.1, the lineshape of the excited state can be written in terms of a Bessell function expansion (normalized to one).

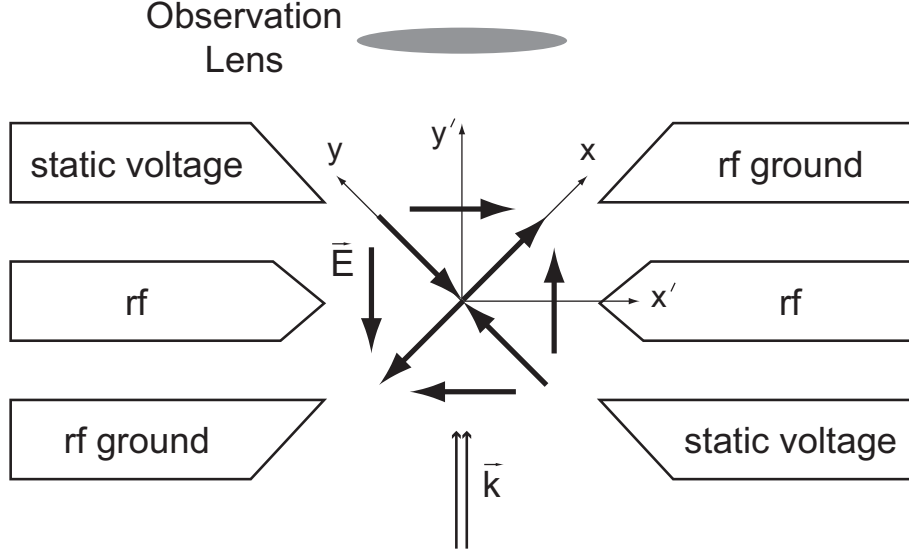


Figure 2.1: The principal axes of the linear trap. The electric field vectors for the trap point along the principal x, y axes. The laser wavevector \vec{k} also has a component along both axes, a requirement for 3D Doppler cooling. However, small displacements from the trap center along the rotated axes x', y' show the sensitivity to different micromotion minimization techniques.

The expansion is

$$P_e = \sum_{n=-\infty}^{\infty} \frac{J_n^2(\beta)}{(\omega_{atom} - \omega_{laser} + n\Omega_T)^2 + \left(\frac{\gamma}{2}\right)^2},$$

where γ is the linewidth of the excited state. The normalized lineshape $P'_e = 4P_e/\gamma^2$ is shown as a function of the laser-atom detuning over the linewidth $(\omega_{atom} - \omega_{laser})/\gamma$. The change in lineshape is a first order Doppler effect due to the micromotion velocity. Since the linewidth of cadmium ($\gamma \approx 60$ MHz) is approximately the same as the trap frequency, the absorption lineshapes are different from those in reference [41]. Figure 2.2 shows the lineshape for small β , or small displacements from the rf node. Note that there is an obvious broadening even for very small displacements of the ion from the rf node. For much larger values of β , shown in Fig. 2.3, the lineshape almost disappears.

The resonant scattering lineshape can thus provide information and a feedback mechanism for large displacements from the rf node. The ion position can be adjusted using compensation electrodes until the lineshape begins to look like a Lorentzian.

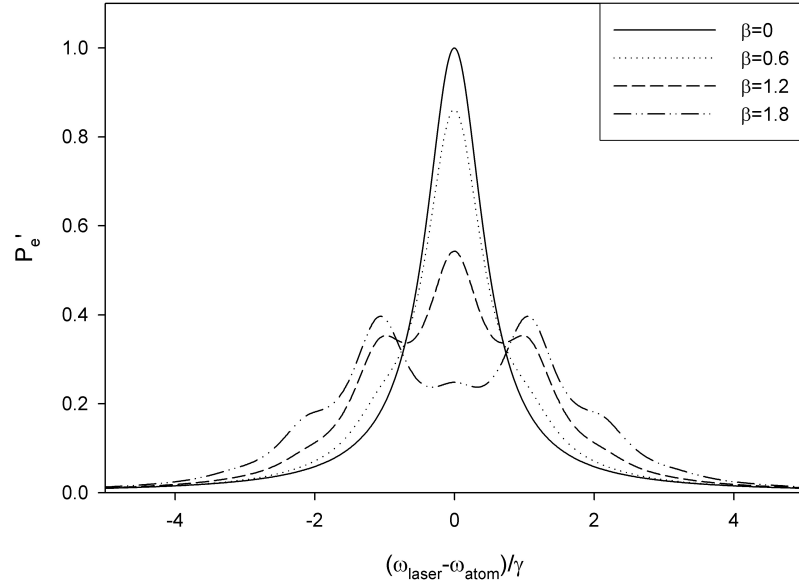


Figure 2.2: Micromotion broadened lineshape for small amplitude. Effect of micromotion on the excited state lineshape shown for a variety of parameters of β .

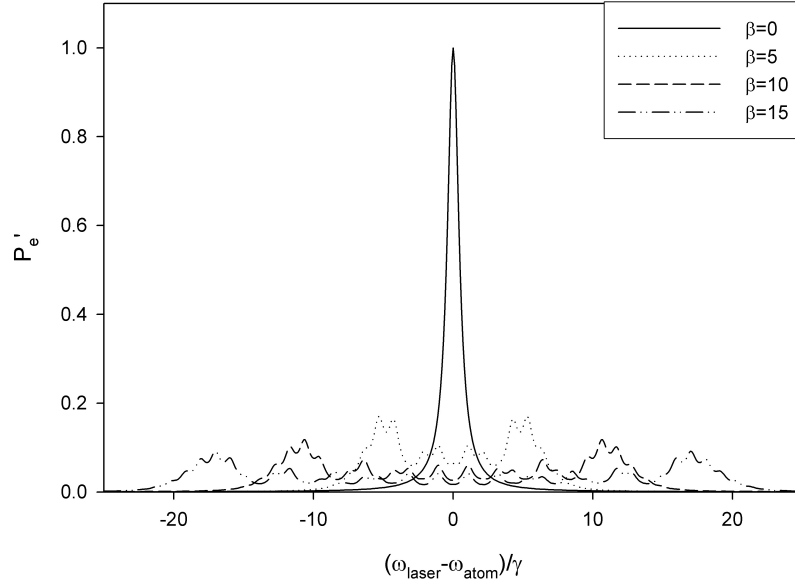


Figure 2.3: Micromotion broadened lineshape for large amplitude. Effect of micromotion on the excited state lineshape shown for a variety of parameters of β , for much larger β .

At that point, the cross-correlation technique, a more sensitive measure of the excess micromotion, can be used.

The second method for detecting micromotion is to use the “cross-correlation” technique where the fluorescence of the ion is modulated by the trap frequency in a first-order Doppler shift [41]. The fluorescence is correlated with the applied trap frequency and collected using a time-to-digital converter. The modulated fluorescence signal can be written

$$\frac{R_d}{R_{max}} = \frac{1}{1 + \left(1 - \frac{2\beta\Omega_T}{\gamma} \sin(\Omega_T t + \delta)\right)^2}$$

where the laser detuning from the atom is set at $\gamma/2$ where the modulation signal is strongest. The phase δ is also dependent on the micromotion, but not important given our method of detecting the modulation. The modulation of the fluorescence is shown in two figures, Fig. 2.4 and Fig. 2.5 for two different ranges of the parameter β . As seen in Fig. 2.5, for larger values of β , the cross-correlation signal becomes difficult to interpret. Thus this technique is only useful for small ion displacements.

This technique is implemented in Labview using the ACAM TDC in the program “TDC monitor.vi”. The TDC has a time resolution of 125 ps but the data is put into 20, 1 ns bins. The histogrammed data is refreshed and averaged over a period of about 10 seconds, with a form of analog persist to smoothly average the data. A screen shot of the program is shown in Fig. 2.6.

To set up the TDC micromotion detection, the reference signal from the back of the HP 8640D signal generator that powers the trap needs to be connected to the STOP signal on the TDC connector box. The signal is typically too small for the TDC to read, so it is put through an amplifier and then attenuated. Check on a scope before connecting that the signal is approximately 3 V amplitude. The signal

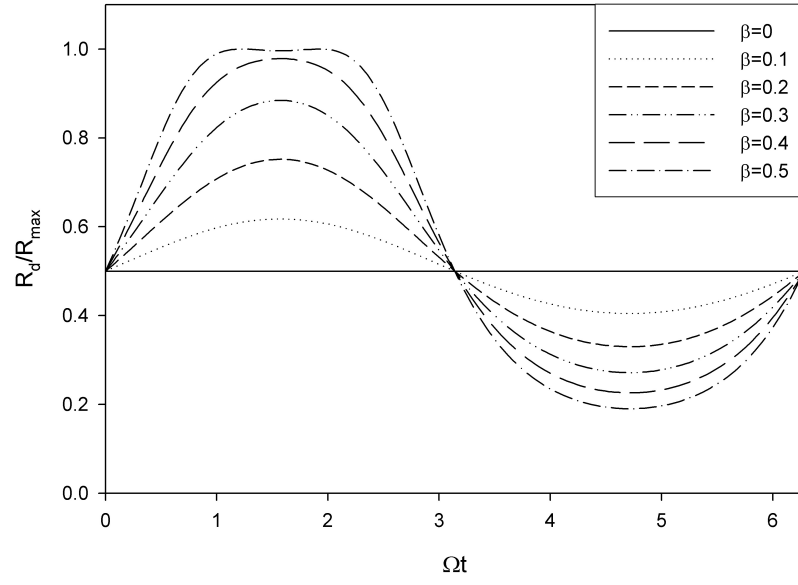


Figure 2.4: The cross-correlated fluorescence signal for small β .

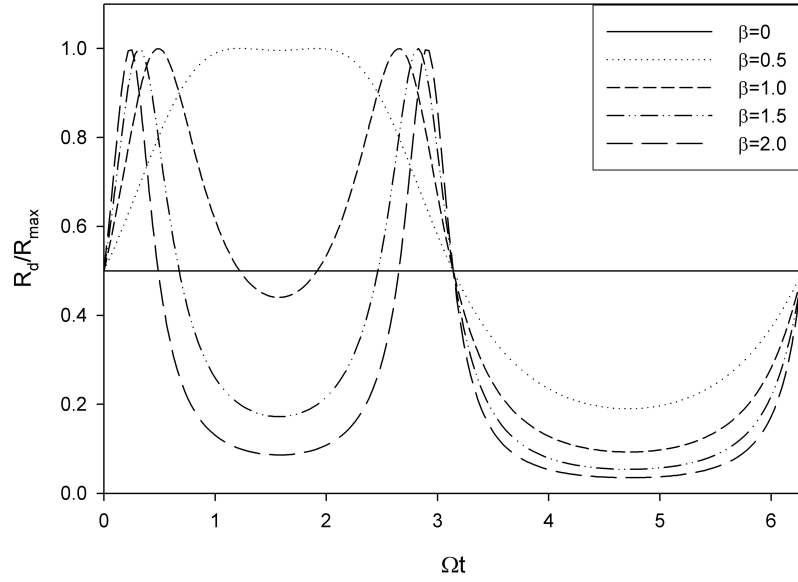


Figure 2.5: The cross-correlated fluorescence signal for larger β .

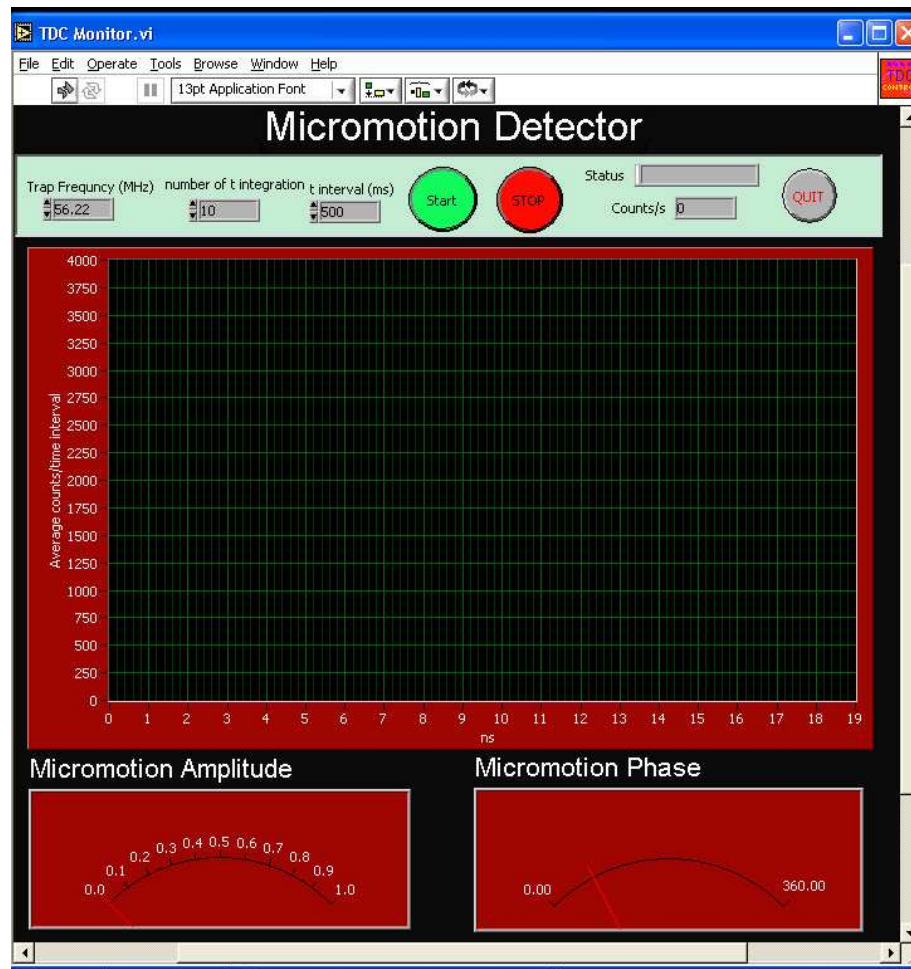


Figure 2.6: Screen shot of the micromotion detection program in LabView "TDC Monitor.vi".

from the PMT or the Quantar is connected to the START input. The TDC starts its timing when a photon is received and then stops when the rising edge of the trap rf crosses zero. The program collects these timing data and puts them into a histogram, binned by 1 ns, that is as wide as the period of the rf. A sinusoidal lineshape is evidence of excess micromotion.

Again, the micromotion can be minimized by adjusting the compensation electrodes until the sinusoid signal disappears. There is a phase change of the cross-correlation signal as the ion moves across the rf node. This can be used as a gauge if the compensation electrodes have pushed the ion too far in one direction.

The final technique to minimize excess micromotion is the amplitude modulation of the rf drive voltage. Displacements in the ion position from the rf node that do not lead to a micromotion velocity component along the laser wavevector can not be measured using either of the previous techniques. However, if it is possible to observe the ion along a specific direction, displacements can be visually identified by modulating the amplitude of the rf voltage sent to the trap. For example, displacements in the x' direction in the four-rod linear trap shown in Fig. 2.7 lead to a micromotion velocity orthogonal to the laser wavevector. However, a displacement in that direction is visible to the observer from the y' direction.

The micromotion is minimized by applying a few Hz amplitude modulation signal to the HP8640D signal generator. When the rf trap is weakened, by lowering the voltage, the static offset electric field pushes the ion further from position of the rf node. This appears as a “wobble” in the ion motion at the amplitude modulation frequency. The ion motion is minimized by adjusting the compensation electrode voltages until the motion stops. The sensitivity of the measurement can be increased by increasing the modulation amplitude of the rf voltage. It is often necessary to

then repeat the measurement of the excess micromotion in the other direction using the resonant fluorescence techniques. Several iterations of these techniques can be used to minimize the excess micromotion.

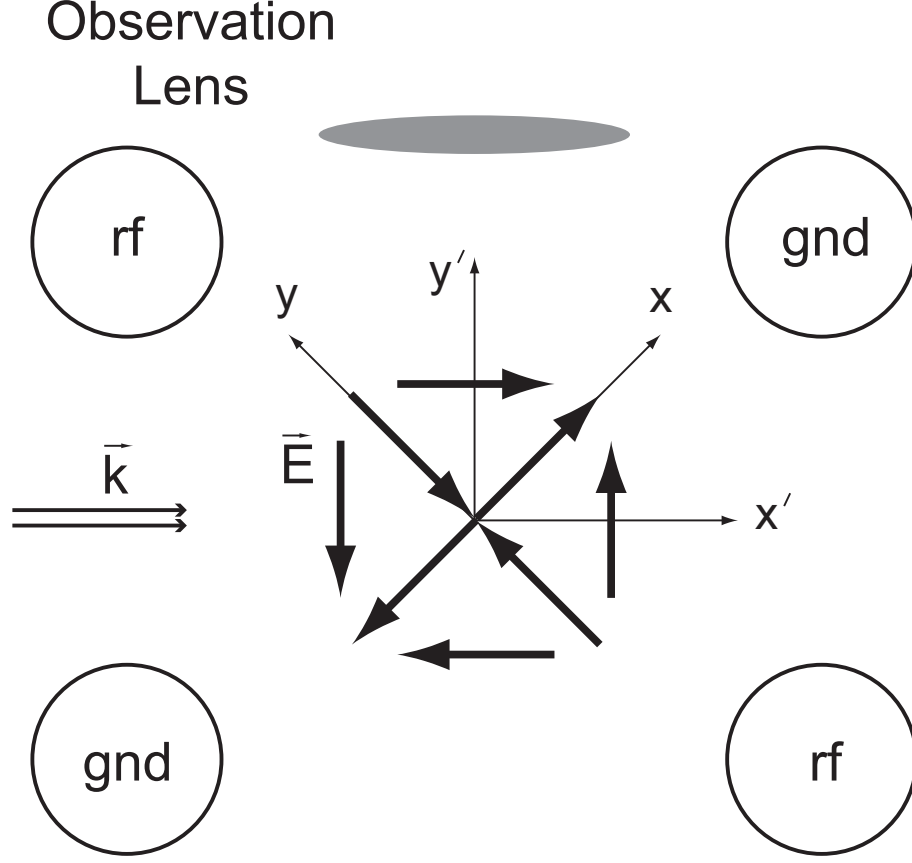


Figure 2.7: Four-rod linear trap electric fields. Ion displacements from the rf node in the y' direction can be detected using the resonance fluorescence techniques. However, displacements in the x' direction must be measured using the amplitude modulation technique.

2.4 Vacuum Chamber

Trapped ion quantum computing experiments require very high vacuum in order to ensure that background collisions do not affect the ions used in the experiment. Practically, this means that pressures on the order of 1×10^{-11} Torr are needed in the vacuum systems. At this pressure, the collision rate with background atoms is low enough (less than one per minute) that experiments at several kHz are not affected

by background collisions. Ion lifetimes in the trap at these pressures range from a few hours to a few days.

Thus, the vacuum system used must be capable of reaching and maintaining this ultra-high vacuum (UHV) environment. The basic procedure that will enable the system to reach this regime involves 1) pre-baking all steel vacuum parts used the the chamber, 2) ultrasonic cleaning of all parts that will be used to make the chamber, as well as all components put inside the chamber, 3) maintaining a clean environment while assembling the chamber, 4) using only bakable parts in the chamber (200 degrees Celsius), and 5) baking the chamber at a hot enough temperature for a long enough period of time. The final bake primarily removes the water stored in the stainless steel lattice. Each of these points will be addressed in turn. A schematic diagram of a typical vacuum chamber is shown in Fig. 2.8.

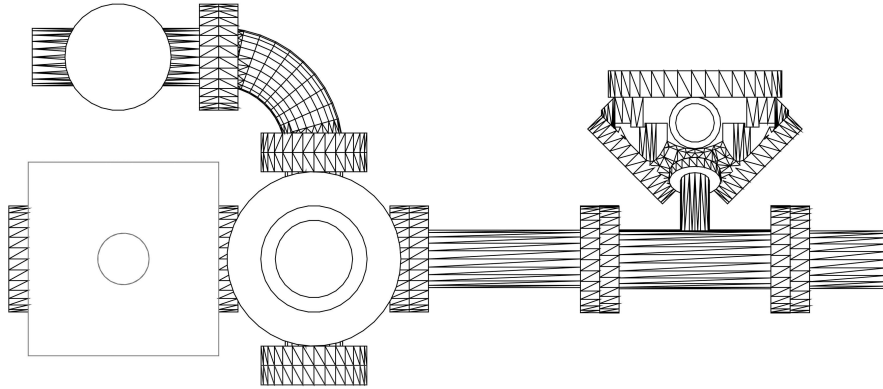


Figure 2.8: A schematic overview of the entire vacuum system.

2.4.1 Pumps and Gauges. The first step is to assemble the necessary parts for the vacuum chamber, ensuring that all parts can be baked in an oven at the required 200 degrees C. The primary vacuum pump for chambers used in the lab is a 20 L StarCell ion pump (Varian part number 9191145, \$1500, negative polarity with ferrous magnet). A bakable cable (Varian part number 9290705 \$355) is used to

connect the vacuum pump to the controller during the final bake and a MidiVac ion pump controller (Varian part number 9295000, \$1800 with three voltage settings) is used to provide the high voltage to the ion pump. This pump does a good job of removing background helium and hydrogen once the system has been pumped out and can maintain an environment of below 5×10^{-12} Torr. A nude Bayard-Alpert ionization gauge with tungsten filament is used to measure the pressure in the vacuum system (Varian part number 9715014, \$450). The UHV-24p gauge is sensitive down to 5×10^{-12} Torr. Again, a bakable cable is used to connect the gauge to the controller (Varian part number L64403025, \$325) and the SenTorr gauge controller is used with degas option (Varian part number L91103010100, \$1195).

In addition to the StarCell ion pump, a titanium sublimation pump is included in the vacuum system. This pump works by heating a titanium coated filament to the point where the titanium is ejected and coats the surrounding vacuum chamber walls. The titanium on the walls then reacts chemically with the background gas in the vacuum chamber, removing it from the vacuum and bonding it to the walls. A three filament pump (Duniway part number TSP-275-003, \$625) is installed in the chamber with cable (Duniway part number TSP-CABLE, \$290) and controller (Duniway surplus part number 922-0032, \$725). Note that the cable for the titanium sublimation pump is not bakable because the sublimation pump is not used during the final bake. The titanium sublimation pump will be run only occasionally, as the vacuum system pressure requires, to return to lower pressures if the lifetimes in the trap appear to be getting shorter.

Another option for the vacuum system is to add a residual gas analyzer (RGA)- a mass spectrometer. This enables measurement of the background neutral atoms that are used in the system. It is not necessary to do this, but it provides an additional

check that the ovens are providing enough neutral atoms. One option for the RGA is a Stanford Research Systems RGA (\$5000).

2.4.2 Hardware. Table 2.1 contains a listing of the necessary vacuum hardware for our system. The Conflat system of assembly for vacuum chambers contains a sharp knife edge on each flange. These knife edges are compressed into soft copper gaskets forming a UHV compatible, bakable seal. It is therefore necessary that the knife edges on all parts be inspected carefully to ensure that there are no defects (see Fig. 2.9). These defects will lead to leaks in the vacuum chamber. With the exception of the pumps, all of the steel vacuum hardware must be pre-baked. This will turn the steel from a silver color to more of a gold-bronze color, an indication of a chromium-oxide layer that reduces the water diffusion from the stainless steel parts [42]. The vacuum viewports, gauges, pumps, and feedthroughs are not typically pre-baked.

The parts are pre-cleaned with acetone and then wrapped with aluminum foil (shiny side toward the parts). They are then baked in an oven at 250 degrees Celcius for about a week or until they turn the nice bronze color. Care must be taken when baking to not damage the knife edges on the parts.

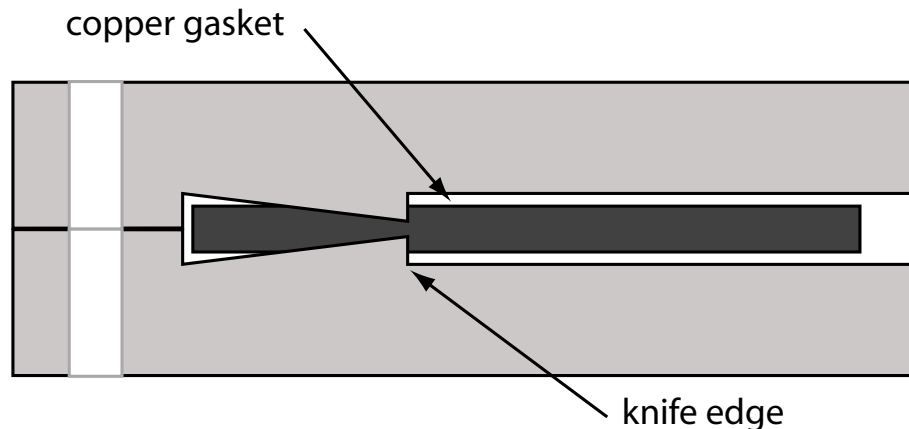


Figure 2.9: Knife edge illustration. An illustration of how the knife edge forms a seal on the copper gasket

Not included in Table 2.1 are the electrical feedthroughs or the viewports since

Item (Size indicates CF flange)	Part Number	Vendor	Quantity	Cost
2.75 in. 90 degree elbow	EL-275	Duniway	1	\$55
2.75 in. tee	TE-275	Duniway	1	\$100
2.75 in. 5-way cross	406002	MDC	1	\$200
2.75 in. cap	F275-000N	Duniway	3	\$12
2.75 in. nipple	NP-275	Duniway	1	\$50
2.75 in. to 1.33 in. reducer tee	404044	MDC	2	\$75
4.5 in. to 2.75 in. zero-length reducer	A450X275T	Duniway	1	\$77
4.5 in. nipple	NP-450	Duniway	1	\$175
4.5 in. to 2.75 in. reducer nipple	FA04500275	Varian	1	\$120
Magdeberg Hemisphere	MCF450-MH10204/8-A	Kimball Physics	1	\$935
2.75 in. bakable valve	9515027	Varian	1	\$655

Table 2.1: Vacuum Hardware.

those do not get the same pre-bake as the other vacuum parts. In addition, the parts listed in Table 2.2 are necessary for assembling the vacuum system.

Item (Size indicates CF flange)	Part Number	Quantity	Cost
2.75 in. bolts, 1.25 in. long thread with hex nuts	SBN-28-212	3	\$25
2.75 in. (tapped flange) bolts, 0.875 in. long	SBX-28-087	1	\$15
1.33 in. (tapped flange) bolts, 0.5 in. long	SBX-32-050	1	\$11
4.5 in. bolts, 1.5 in. long	SBN-24-200	1	\$32
4.5 in. (tapped flange) bolts, 1.25 in. long	SBX-24-125	1	\$25
1.33 in. copper gasket	G-133	1	\$12
2.75 in. copper gasket	G-275	2	\$14
4.5 in. copper gasket	G-450	1	\$22

Table 2.2: Parts needed for assembly of vacuum chamber. All parts numbers and prices are for Duniway. All prices for bolts are 25/pkg and for gaskets are 10/pkg.

2.4.3 Vacuum Chamber Cleaning. As was mentioned above, the first step in assembling the vacuum chamber is to pre-clean and then pre-bake all vacuum parts. After baking, it is important to re-clean all parts intended for the chamber. This can be done in a variety of ways, but it is important to use acetone and an ultrasonic cleaner to ensure that no organic residue remains on the inside of the vacuum parts. A small ultrasonic cleaner is used that fits most of the vacuum parts for cleaning. It is important to use a high grade acetone as well, or there is a risk of contaminating the chamber with residual organic chemicals in the acetone. Typically HPLC grade acetone is good enough (available from Fisher Scientific part number A949-4, \$86.30 for 4L bottle) and close to 16L is usually needed for cleaning an entire chamber.

Thought must be taken in assembling the vacuum system so that the parts are assembled in a logical order. Usually this means putting together small pieces first and working toward larger pieces. In addition, care must be taken to ensure that the rotatable and non-rotatable ConFlat flanges are matched in such a way as to allow assembly of the system as desired. Usually each piece comes with one end rotatable and one not.

In addition to cleaning, precautions must be taken to ensure that no foreign

organic particles enter the vacuum system such as hair, skin flakes, etc. It is good practice to dress in a long sleeve lab coat, use a hair net to gather hair up and use a face mask to keep particulates out of the chamber. Gloves must be worn at all times to keep body oils out of the chamber. Note that latex gloves are soluble in acetone and if they are used in conjunction with acetone, latex residue can be left on the vacuum parts.

The copper gaskets may be cleaned in acetone if their cleanliness is suspect. Typically if precautions are taken to not touch them out of their packaging, they can be used without pre-cleaning.

ConFlat flange assembly.

Because the seal in a ConFlat flange is made in the soft copper gasket around the knife edge (Fig. 2.9), the seal must be evenly tightened. This corresponds to tightening each flange using a star pattern as illustrated in Fig. 2.10. Also, make sure that the leak-detector grooves on each flange line up. This will facilitate leak testing the system. The 2.75 inch diameter flanges are designed to have 12 ft-lbs of torque on each bolt (7 ft-lbs for the 1.33 inch flanges and 15 ft-lbs for the 4.5 inch flanges), but it has been found that if the flanges are tightened to the point where the copper gasket is no longer visible between the flanges, or near that point, the joint is sealed.

If there are plans to remove the flange in the future, a small amount of molybdisulfide grease can be placed on the bolts. But, since most greases are not UHV compatible, extreme care must be taken to ensure that none of the grease gets into the chamber.

It is helpful, when assembling the 1 1/3 inch ConFlat flanges, to use a shortened Allen key. By reducing the length of the key that is inserted into the bolt, it is easier

to get the necessary torque to tighten the gasket.

2.4.4 Viewports. The choice of materials for the viewports depends on the particular ion used in the system. Some ions (such as barium, strontium and calcium) have cycling transitions in the blue or visible spectrum. With these, it is convenient to use less expensive materials. However, the ion used in this research (cadmium) along with beryllium, mercury and zinc, have cycling transitions in the ultraviolet. Because normal glass strongly absorbs in the UV, suprasil windows are used. Suprasil is an amorphous quartz-like material with low absorption in the range of 200 nm wavelength light. There are several companies that make suprasil windows such as Insulator Seal, Inc. The 4.5 inch flange window (ISI part number 9722207 \$1125) has a viewing area of 2.69 inches and has a clearance of 0.41 inches from the knife edge surface to the inside of the window. This clearance space means that the actual trap sits outside the hemisphere and close to the window. It is advantageous to put the trap as close to this window as possible to facilitate diffraction-limited imaging of the ions using low $f/\#$ microscope objectives. The other 2.75 inch flange windows are also from ISI as well (part number 722205 \$350) and have a viewing diameter of 1.4 inches.

2.4.5 Electron Guns. There are several options for the electron guns, which are one way to ionize the atomic beams while the atoms are in the trap. Loading an ion in the trap involves ionizing an atom while it is located in the capture area of the trap. The pseudopotential has a capture cross section that depends on a specific geometry, but is essentially the spacing between the electrodes. An ion approaching the trap from the outside is repelled from the trapping zone and will not be captured. In effect, the only way to capture an ion is to bring in a neutral atom that can pass through the barrier and then ionize it in the trap, illustrated in Fig. 2.11.

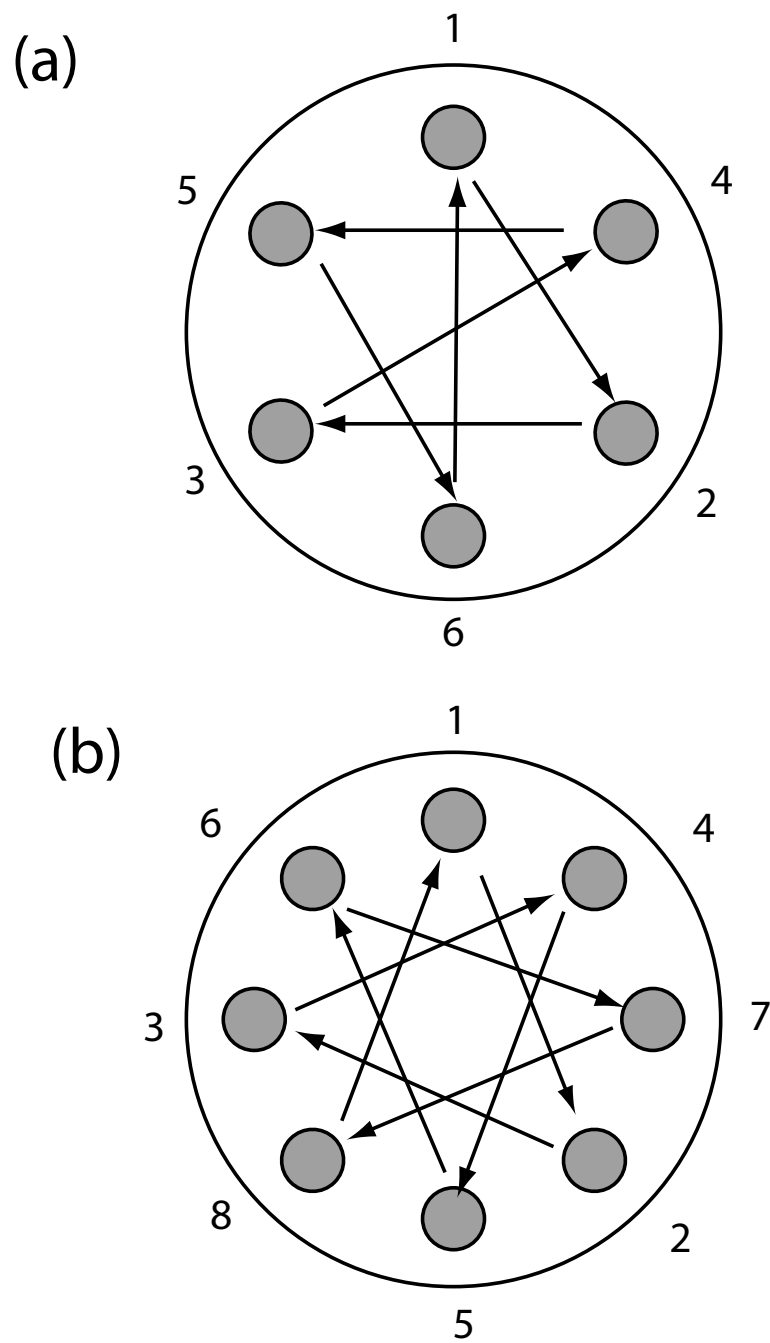


Figure 2.10: CF Tightening pattern. An illustration of how to tighten ConFlat flanges for (a) six bolt flanges and (b) eight bolt flanges.

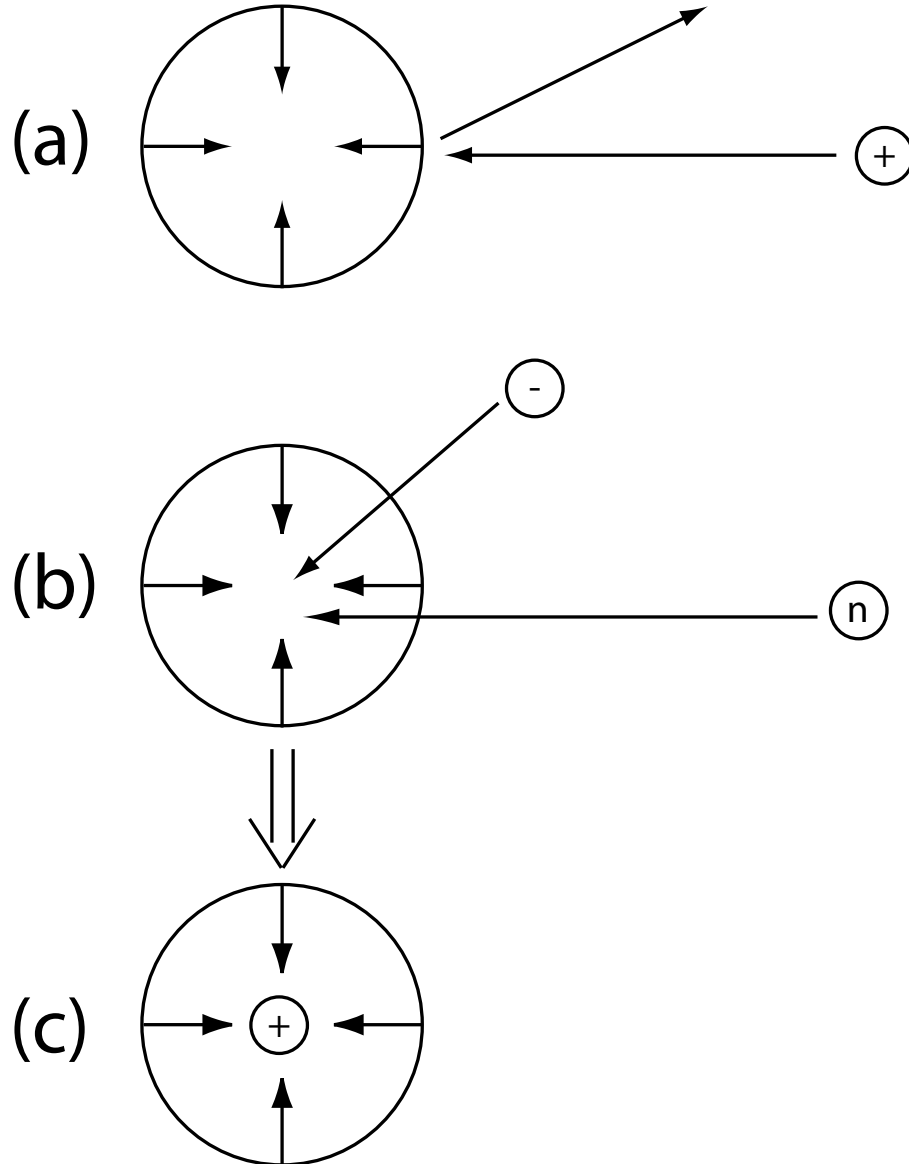


Figure 2.11: Trap loading process illustration (a) An ion is not loaded into an rf Paul trap from outside the trapping zone, but rather a neutral particle must be inside the trap zone where it is ionized (b) by a collision with an electron leaving the positively charged particle, or the electron is removed through photoionization processes (c) trapped.

An electron gun can be made from inexpensive parts for much less the then cost of a commercial electron gun. An electron gun is a small resistive filament that, when a current is passed through it, emits electrons. Figure 2.12 shows a drawing of a simple electron gun made from parts available from Scientific Instrument Services. The two hole ceramic tube (white in figure) has an outer diameter of 0.109 inches and inner diameter of 0.031 inches (SIS part number R27, \$8.40/6 in. rod). The length of the rod depends on the available room in the vacuum chamber, but typically ranges from 0.25 inches to 0.5 inches. Two tungsten rods, 0.025 inch diameter (SIS part number W334, \$6.50/foot), are inserted into the two holes and bent outward at the top of the insulator rod. The reason they are bent is to increase the length of the thoriated tungsten wire (0.0024 inch diameter, SIS part number W126, \$5.00/foot). The wire has a resistance of 0.22987 ohms/cm and a longer wire will need less current for the same amount of electron emission. Unbent tungsten rods (a filament length of about .03 inches) require a current of about 3A is required to get approximately 100 microamps of total electron emission, at which point the filament glows white. If the tungsten rods are bent out to the point where the filament length is about .1 inches or the outer diameter of the ceramic tube, the current required to give the same electron emission is reduced to about 1.5 amps.

The electron gun is assembled by first cutting the ceramic tubes and the tungsten rods to the appropriate length. Enough length must be left on the tungsten rods to allow for gluing the rods to the ceramic tube, attaching the filament to the front, and attaching electrical leads to the back. Next, attach the tungsten rods to the ceramic tube. One option to attach the rods is to use Sauereisen Ceramic Cement (SIS part number SCC8, \$8.00 for a 4 ounce bottle). The cement is an inorganic ceramic powder that becomes adhesive when mixed with water. The instructions

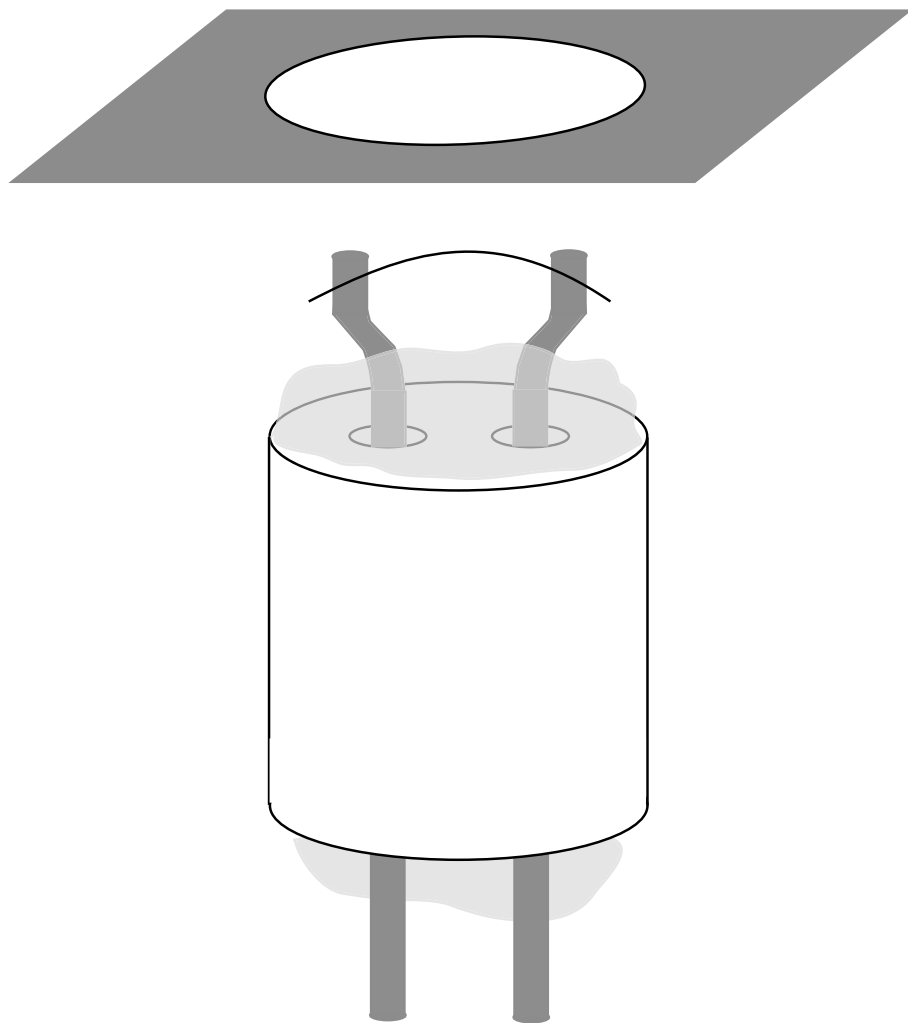


Figure 2.12: Home-made electron gun illustration. An illustration of an electron gun assembly made from a two hole ceramic tube (white), tungsten rods (dark gray, bent outwards at the top), a thoriated tungsten filament (black curved wire) and ceramic cement (light gray covering both ends).

specific a 100:13 ratio of powder to water by weight; a mixture is typically made with a consistency of a thick paste, adding powder or water as necessary. De-ionized, filtered water is used to reduce residual particulate or charged material in the glue. The glue requires at least overnight drying to set hard, the piece must be set up so that the glue can dry without the rods moving overnight. If wires are going to be attached to the end of the electron gun, doing that before gluing can save having to re-glue the rods. The glue on the back side would then cover over the spot welds where the Kapton insulated wire was attached. The wire leads from the electron guns to the vacuum feedthroughs are 0.024 inch diameter conductive wire covered with a 0.0055 inch thick Kapton film (total diameter 0.035 inches, MDC part number 680501, \$60 for a 30 foot roll). The ends of the Kapton insulator are stripped and a small sleeve out of 0.005 inch thick Constantan foil is placed over the conductor to attach the wire to the tungsten rod. Constantan is a nickel alloy that is easily spot welded to a variety of materials, available from a number of sources, including Goodfellow (part number 180-883-19 for a roll 150 mm wide, 0.1 mm thick and 0.5 m long \$226). The sleeve is illustrated in Fig. 2.13 and is useful whenever two metal wire are not readily attached by spot welding directly. The spot weld power can be determined by testing on similar scrap systems prior to doing the final spot welds.

Next, the thoriated tungsten wire is attached to the front end of the tungsten rods using low power spot welds. Since these connections can burn out, the electron guns must be tested prior to installation in the final vacuum chamber. In addition, any kinks or crimps in the filament can also readily burn out when current is applied through the filament: ensure that the the filament wire is a smooth arc.

When heated, the filament ejects electrons at energies of a few eV. These electrons are accelerated toward the trapping zone using an accelerator plate or grid with a

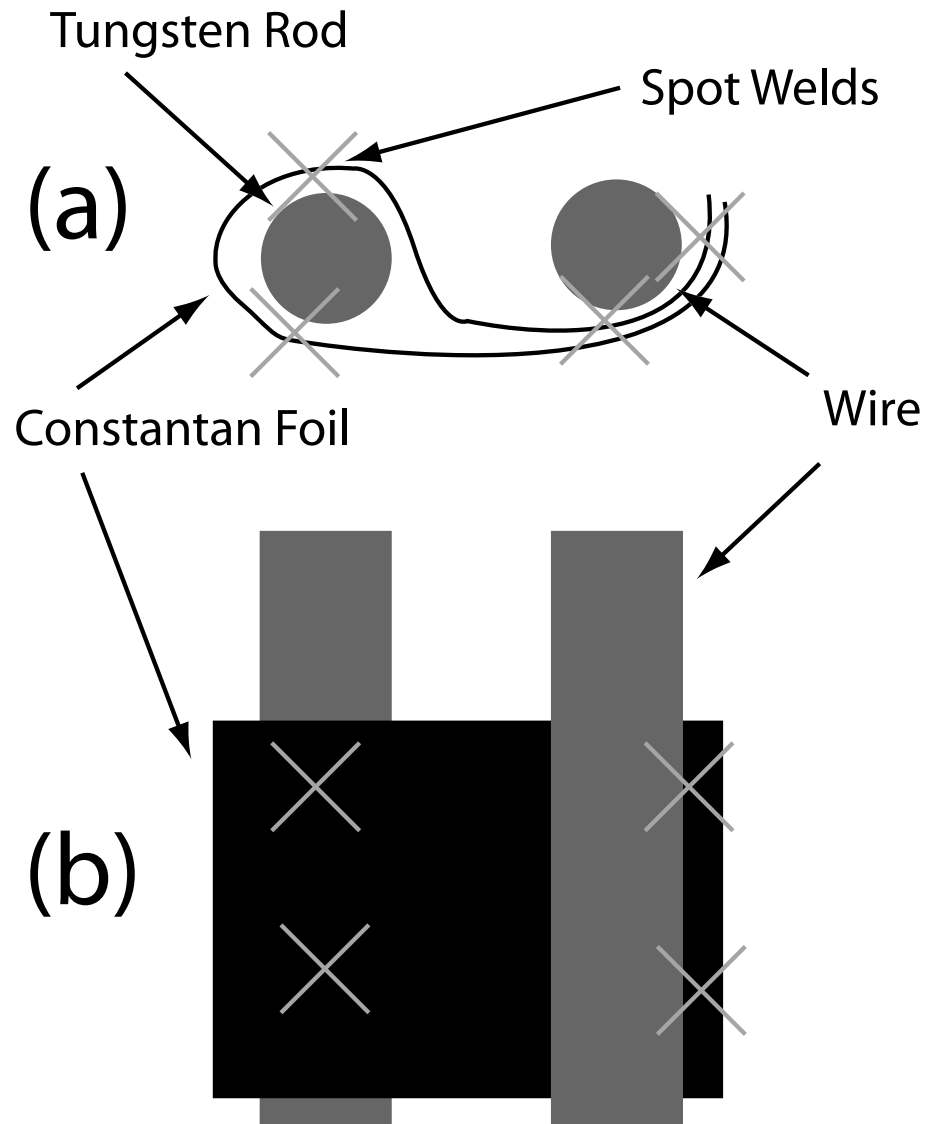


Figure 2.13: Spot-welding instructional illustration. When two wires are not readily welded together, a Constantan foil wrap can be used to attach the wires. First, make a loop in the foil and attach the first wire with several spot welds as shown in a side view (a). Then, attach the foil to itself on the flag. Then, attach the flag to the second wire, wrapping around the wire. The top view is shown in (b).

voltage drop of about 100 V. The accelerator plate is put together with the electron gun assembly, shown as a plate with a hole in it in Fig. 2.12. The diameter of the hole in the accelerator plate needs to be about the same as the distance from the plate to the filament, the best configuration for maximizing electron flow and directionality. The wiring diagram for the electron gun and accelerator grid is shown in Fig. 2.14. The filament is biased at -100V from the grounded accelerator plate and the current drawn from the bias voltage source is measured. This measures the electron flow off of the filament through the plate and provides a gauge as to the operating current of the electron gun.

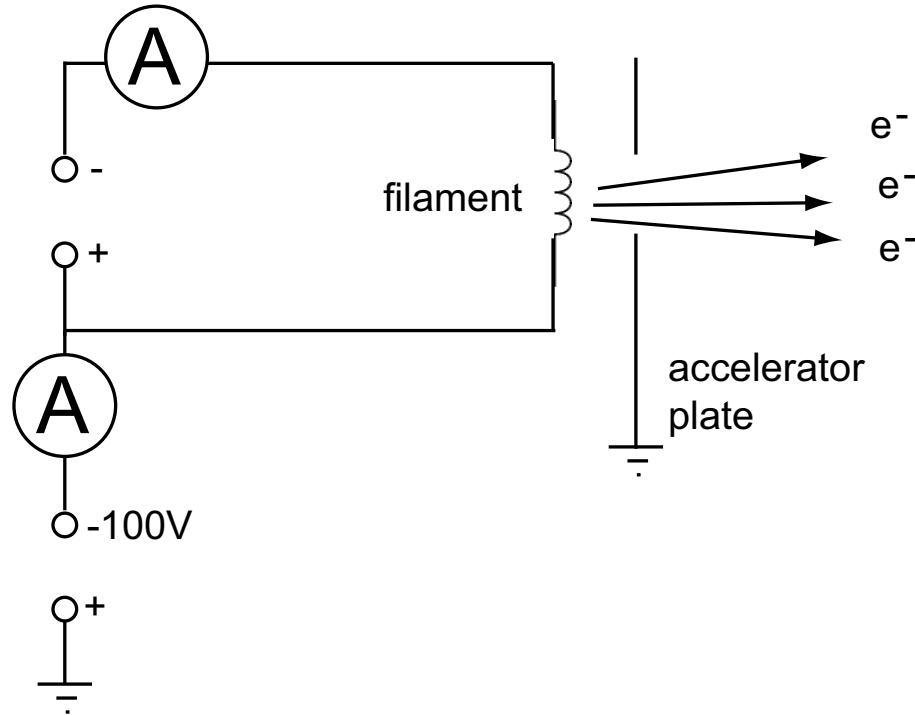


Figure 2.14: Electron gun wiring schematic. The schematic diagram showing the wiring for the electron guns. The top ammeter records the driving current through the filament. The current drawn through the bottom ammeter is the total emission current. It is safer to run the filament from a current-limited voltage supply, as opposed to a current supply, because the resistance of the filament increases with temperature, so the total power drawn decreases as the filament heats up. The -100 V bias voltage is applied to the filament which must be electrically isolated from the vacuum chamber. The accelerator grid is typically a metal plate with a hole cut in it.

The electron guns can be tested in a small bell jar attached to an auxiliary pump

at pressures below 10^{-5} Torr. A small piece of foil can be placed in front of the accelerator plate to collect the electrons from filament to give a gauge of the efficiency of the accelerator plate. About 1% of the total electron current is typically collected on the foil. When testing the electron gun on the trap electrodes, around 0.1% of the total electron current is collected, as the surface area of the electrodes is typically much smaller than the test foil.

2.4.6 Atomic source ovens. The basic idea behind the atomic source ovens is to create a vapor of neutral atoms in the vicinity of the trap which can then be ionized by the electrons. One method involves making a neutral atomic “gun” of sorts that emits a low density atomic beam that is aimed at the center of the trap. The gun is a small metal tube that has a small piece of solid material (cadmium wire) inside. When the tube is heated, the material melts to some extent and the vapor is ejected out the end of the tube. Figure 2.15 illustrates this point. Stainless steel hypodermic needle tubing with 0.042 inch outer diameter and 0.035 inch inner diameter (available from Small Parts, part number HTX-19XTW-12, \$4.70 for 10, 6 inch long tubes) is used as the metal tube. The walls are heated by running a current through the tube from the bottom to the top. The hypodermic needle tubes must be pinched off on the bottom so the source material does not leak out. The end of the tube is crimped with a pair of pliers, but since the tube walls are so thin, care must be taken that the walls are not torn at the crimp point. In addition, the back crimp end is spot welded closed to keep any vapor from exiting. Then, as a final precaution, the back end is wrapped with Constantan foil and spot welded to the crimped tube. The back of the tube must be inspected to make sure that the spot welds have not burned holes through the tubing walls, opening up a potential leak. This also leaves us a small Constantan flag to which the wire lead can be attached. Figure 2.16 illustrates the

details of the crimp and foil wrap. The current is then run from the back of the oven to the front. If a heat sink is attached to the front of the oven, the resulting atomic beam is well collimated. The heat sink is also used as the other lead to run the current through the oven. The result is that the back of the oven gets the hottest and that the cold front acts as a collimator. Although this may lead to clogging of the oven for other atomic sources, it was not found to do so for cadmium metal sources loaded in the oven. The wiring diagram is shown in Fig. 2.17.

The ovens are tested in a bell jar with the front of the oven near one of the glass walls. A current is run through the oven until a small spot begins to appear on the glass in front of the oven. For the 0.042 inch outer diameter, 0.034 inner diameter walls, currents are typically in the range of 2 to 3 amps, run for about 5 minutes before spots appear. Since this varies with oven length and heat sink size, each oven must be tested to determine the proper current range. When the oven is used in the final vacuum chamber, the operating current is typically much lower to reduce the atomic plating on the trap electrodes. But, by doing the spot test, the output from the oven is checked for collimation and that there are no leaks in the crimp.

Another oven design is the ceramic tube design, where the atomic source is packed in a ceramic tube and then the tube is wrapped in a resistive tungsten filament. The filament is heated, which then heats the tube and vaporizes the atomic source. This design is good if the atoms used in the trap do not have a suitable solid at room temperature. Because the ceramic tube can be heated much hotter, even chemical compounds of the substance (such as oxides) can be vaporized and dissociated, yielding an atomic beam.

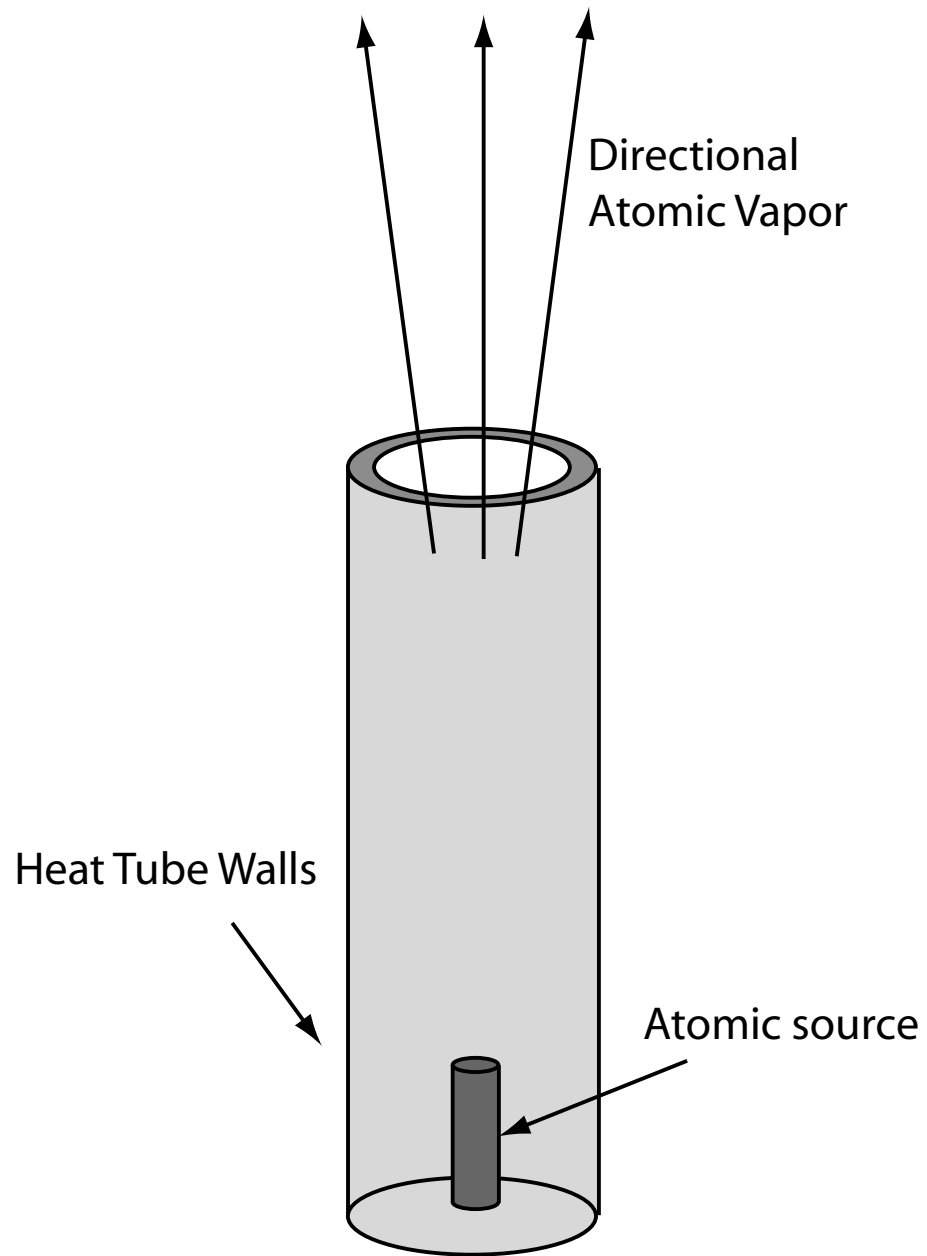


Figure 2.15: An illustration of the atomic source ovens. Solid source material is placed inside the oven tube. When heated, the source melts and vapors are ejected from the front of the tube.

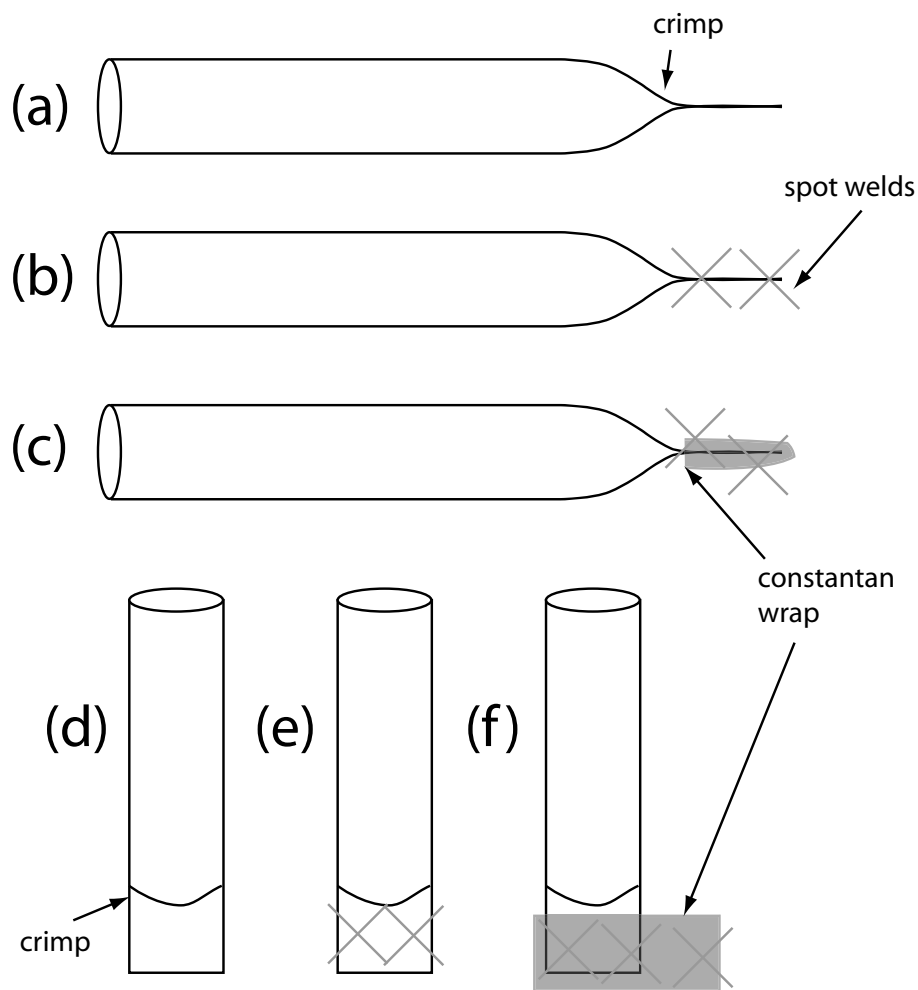


Figure 2.16: Oven crimping illustration. Crimping the ovens shut on the back side keeps the atomic source from leaking out. (a) (side view) and (d) (top view) illustrate where to crimp the oven tube flat. The, by spot welding the crimped area, (b) and (e), the tube becomes sealed. Then adding a Constantan flag, (c) and (f), allows us to attach a lead to the flag without having to spot weld the oven tube again.

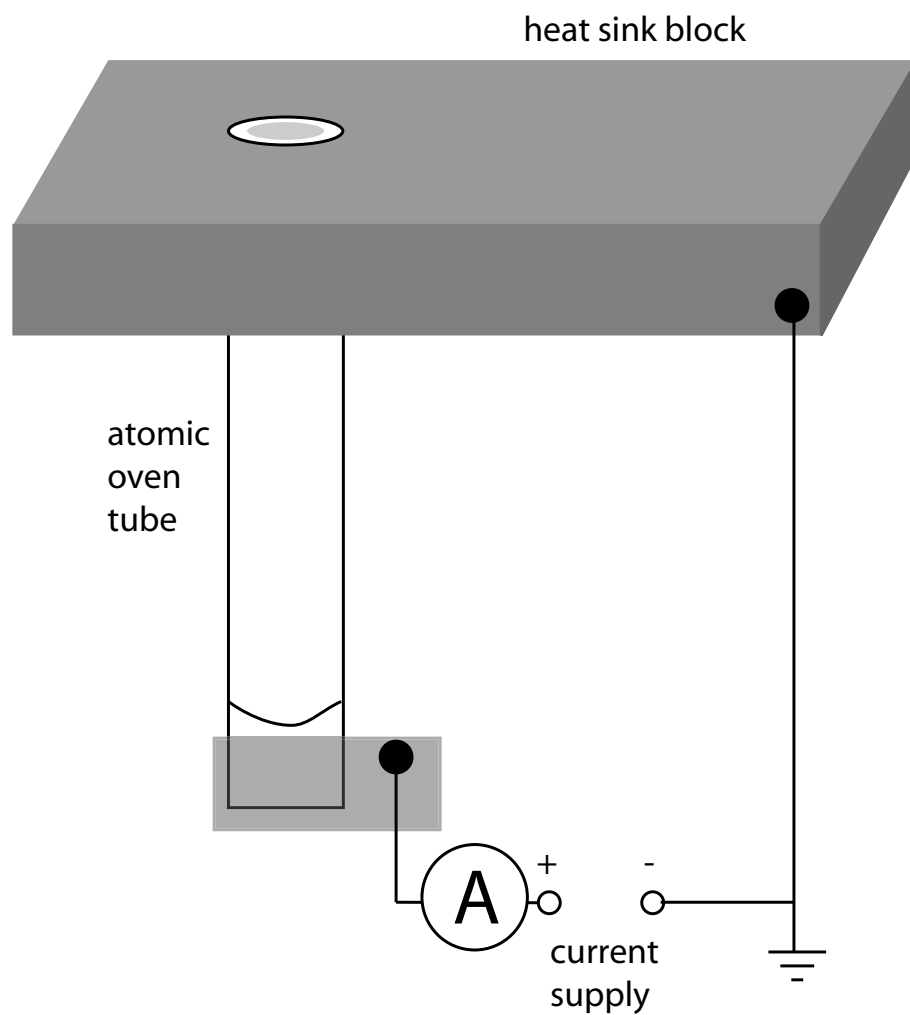


Figure 2.17: Oven mounting block illustration. A heat sink block attached to the front of the oven keeps the oven tip cooler than the back and provides a good, directional atomic beam. A current supply attached to the end of the oven provides a constant current to heat the oven walls.

2.5 Ion Trap Mounting Requirements

The trap structure must be mounted in an ultra-high vacuum (UHV) system. This places strict bounds on the types of materials that can be used in trap construction and in trap mounting schemes. There are established lists of materials known to be compatible [43] with UHV environments. Typically inorganic metals and ceramics are UHV compatible and, with the exception of a few inert polymers such as Teflon and Kapton, organic compounds are not UHV compatible.

In order to construct a linear trap, there must be both rf and static electrodes. These electrodes must be good conductors and electrically isolated from each other. The rf loss tangent of the conductor and insulator set must be small. The rf potential is transmitted via the electrodes and appropriate care must be made to design an rf transmission line that will efficiently transmit the rf potentials to the trapping region.

Trapping individual ions also requires laser access to the trapping region for photo-ionization and for Doppler cooling. The trap structure should be sufficiently open to allow for the lasers to be focused through the trap without clipping the Gaussian beams on the electrodes. For a $5\text{ }\mu\text{m}$ waist at 214.5 nm , this implies that there is a clear cone of height $\sim 2.5\text{ mm}$ and base diameter of $100\text{ }\mu\text{m}$. Imaging the ions can be difficult if the beams clip the trap. The laser access must be such that there is some component of the laser wavevector along all three principal axis of the trap [40].

2.6 Baking the Chamber

Once all components of the vacuum chamber have been cleaned, tested, and assembled, the chamber is baked to remove all water vapor from the stainless steel lattice and to reach the ultra-high vacuum environment. Vacuum bake-out is typi-

cally done with heater tape and fiberglass insulation, however, a large free-standing oven simplifies the bake-out procedure.

2.6.1 Pre-Bake Testing. Before actually baking out the chamber, but after finishing assembling the chamber, including the trap, it is important to take care of some degassing steps and some pre-bake tests in the chamber. There is a particular ordering of the following steps for a given chamber and each pre-bake checklist must be customized. The first step is to pump the chamber down to 10^{-6} Torr or so using the roughing pump and turbo pump. At these pressures, ion gauges, electron guns, RGA filaments, and titanium sublimation pumps can be safely degassed.

- Degas ion gauge. Many controllers have this function available on the front panel. The ion gauge filament will be run at higher currents to expel any trapped residue. Degassing times vary from 5 minutes to an hour or more.
- Degas RGA filament. If a residual gas analyzer is attached to the system, run the degas function to clean the filament.
- Test electron guns. This is a more involved step since it requires actually turning on the electron guns along with the accelerator grid. One useful test at this point is to collect electron current from available feed-through connections. For example, the electron gun could be run and electron current collected off of the static electrodes of the trap. This will give some diagnostics as to whether metal pieces have moved during the bake-out.
- Fire cadmium ovens. This is to primarily degas the filaments or oven tubes used to heat the cadmium. As with anything that gets hot in the vacuum chamber, it must be degassed. Typically firing the ovens for five to ten minutes at low current will degas them.

- Fire the titanium sublimation pump. Each filament must be degassed at a current of 37 amps for about an hour. This will help lower the peak pressure that the sublimation pump reaches when fired after bake-out. If the filaments can be fired for longer, it will reduce that pressure even more.
- Check continuity on electrodes and check for shorts. Check capacitances and resistances between any electrodes using in-vacuum filter electronics. If a short develops during bake-out this will help to diagnose it.
- If the trap has never had rf voltages on it before, it is helpful to do that now. Helical resonator design is described in Subsection 2.7.1, but this is a good point to test out the rf on the trap. After the bake-out, the same resonator will be used to get the high voltage rf on the trap.

Record all measurements, since the numbers will be good diagnostic tools in the event of problems after the bake. Note that most metals, as they bake, will shift and move. The information gathered here will help to check if anything changes.

2.6.2 Bake Times. A surplus DeLorian Motor Company oven is used to bake out the vacuum chamber. The internal oven space is approximately 1.5 meters wide, 0.5 meters deep and about 1 meter tall. The oven has temperature control circuits so that it maintains a set temperature fairly well (within five degrees over several days). The maximum temperature of the oven is well over the 200 degrees C that is used to bake our chamber. The maximum temperature to bake at is determined by the suprasil windows. The seals between the window and the CF flange is rated up to 200 degrees C, do not go above that when baking. The ramp times vary from bake to bake, but a conservative timing is to not ramp up the oven more the 30 degrees Fahrenheit per hour. In practice, the ramp up time is limited by the pressure. For a

new vacuum chamber that has not been previously baked, there can be a lot of water stored in the stainless steel. The initial ramp of temperature can spike the pressure in the vacuum chamber above 10^{-5} Torr. To keep the gauge from automatically shutting off, reduce the ramp speed so the pressure does not peak quite that high. Figure 2.18 shows the complete record for four different bake-outs. Each of these bakes ended with the base pressure below 10^{-10} Torr, but experience has shown that if the chamber pressure is in the low 10^{-10} s when cooled after the bake, the titanium sublimation pump can reduce the pressure that last order of magnitude (provided there are no leaks).

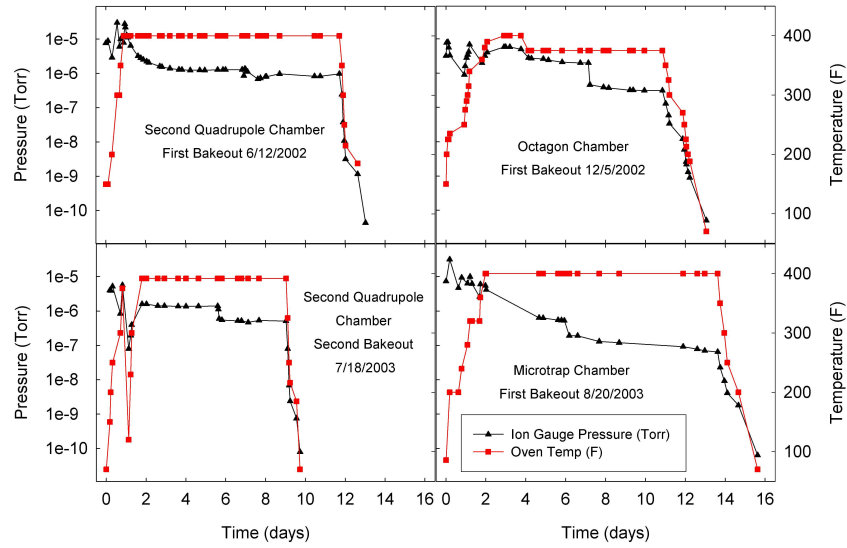


Figure 2.18: Bake-out time data. Four separate chamber bakes using the DMC oven. Shown are the pressures on the internal ion gauge and the oven temperature in Fahrenheit.

Typically a bake will last between 10 and 14 days. The drop in pressure on the graphs in Fig. 2.18 at about day 6 is from the switch between the external ion pump and the internal ion pump. The bakeout procedure is as follows (see Fig. 2.19 for an illustration of where to connect the chamber and which valves are being discussed).

1. Connect vacuum chamber to the flexible 36 inch long vacuum tube in oven using a 2.75 inch copper gasket.
2. Connect 20L StarCell ion pump to controller using bakeable cable through the oven exhaust port.
3. Connect the ion gauge to controller using bakeable cable through the oven exhaust port.
4. Cover all exposed feed-throughs and viewports with aluminum foil (shiny side toward the chamber).
5. Connect the turbopump to the vacuum system on the external valve (a Viton O-ring may be used) with a second 36 inch long flexible vacuum tube.
6. If the vacuum chamber is already at low pressure (below 10^{-4} Torr, first open the valve to the turbo pump, leaving the chamber valve closed. Start the turbo pump and pump down to 10^{-4} before opening the chamber valve. If the chamber is at atmospheric pressure, open the chamber valve before starting the turbo pump.
7. When the turbo pump reaches low 10^{-6} Torr, slowly open the 500L ion pump valve making sure that the pressure on the ion pump does not exceed 10^{-7} . When the ion pump is completely on, close the turbo pump valve.
8. Turn on the ion gauge and note the pressure. When the pressure stabilizes in the low 10^{-6} range, the oven can be turned on.
9. Slowly ramp up the oven temperature, keeping the ramp speed slow enough so the pressure does not go above the low 10^{-5} range. A log is kept of the bakeout including the following information: Date, time, oven temperature actual, oven

temperature set, ion gauge pressure, ion pump pressure (both the 500L pump and the 20L StarCell current) and any notes on the bakeout.

10. Once the temperature has reached 200 degrees Celcius (392 degrees Fahrenheit), keep track of the pressure. When the pressure reaches a stable equilibrium (does not change over the course of a day) it is time to close the chamber valve and start the internal pump.
11. Start the internal 20L StarCell pump with the voltage set to 3kV and with the chamber valve open. Since the pump has high voltages, it might initially spike in pressure. If the automatic shutoff activates, turn the pump off and on again to get past that point.
12. When the 20L pump is running at 3kV, close the chamber valve hand tight. Since the chamber valve is hot, do not close it to full torque, as that ruins the valve
13. Increase the voltage on the 20L StarCell to 7 kV.
14. Again, monitor the pressure until it reaches equilibrium over the span of a day or two.
15. Slowly ramp down the temperature (30 degrees Fahrenheit per hour is good).
16. Let the chamber and oven cool with the oven doors closed for a half day or so and then open the doors to let the chamber come down to room temperature.
17. Close the 500L ion pump valve and torque the chamber valve to the appropriate torque (see the manual, but it is usually 25 ft-lbs to start and more each time the valve is used).

18. If the pressure is not in the low 10^{-11} range, fire the titanium sublimation pump on a regular basis (once every few hours) until the pressure comes down to the desired point. (See below for more information on the firing the titanium sublimation pump).
19. Install pinch-off valve on top of the chamber valve to protect against any possible leaks in the valve. Typically the pinch-off valve is pumped using the turbopump to the low 10^{-6} range and then sealed.

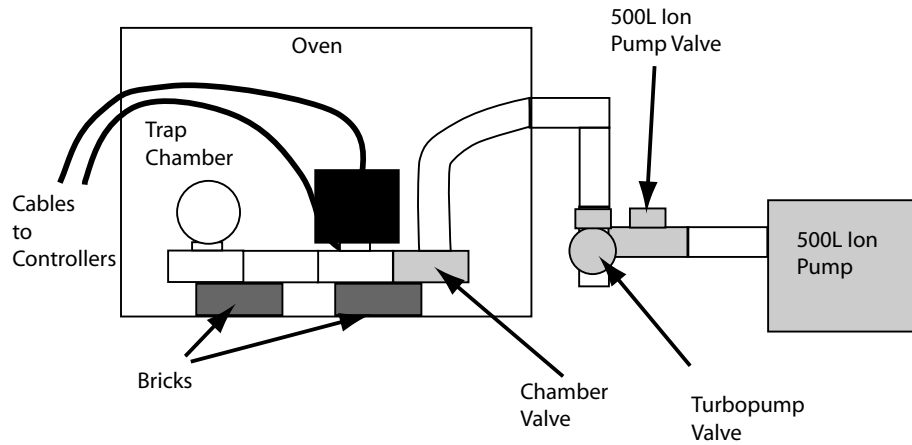


Figure 2.19: An illustration of the oven with pumps and valves shown.

2.6.3 Titanium Sublimation Pump. As noted above, to reach the low pressures needed for ion trapping experiments, it is helpful to fire the titanium sublimation pump several times to lower the background pressure. The ti-sub pump works by plating the walls of a tube with a titanium layer which then absorbs surrounding molecules and atoms. For the pumps and parts listed in the vacuum chamber assembly section, operation is as follows:

- Record the base pressure before firing the pump.
- Turn up the current on the pump controller to 43 amps for normal operation.
- The pressure on the gauge should spike at around 10^{-7} Torr under normal

conditions. If the pump has not been sufficiently degassed, this pressure may be higher. Be careful that the pressure is not so high that it overwhelms the ion pump- if the pressure goes above 10^{-6} , the pump may need to be shut off.

- After the spike, the pressure should slowly decrease. Leave the pump running for a minute or two. The limiting factor in leaving the pump running is the temperature of the outer tube walls. As the temperature rises, the walls start to degas. If they degas at a rate faster than the pumping speed, the pressure will start to rise again. If this happens, shut the pump down or cool the walls (wet paper towels work well).
- Shut the pump off and let the vacuum system return to equilibrium. This can take anywhere from a couple of hours to overnight. The final pressure should be a factor of 2 or so lower than the starting pressure.

If all goes well, it is possible to reduce the pressure from the 10^{-10} range down to below 5×10^{-12} with a week of regular firing.

2.7 rf Generation and Delivery

With the vacuum chamber set in a UHV environment, it is now ready to apply rf voltage to the trap and image the ions. The rf delivery and static voltage leads are connected to the trap through the electrical feedthroughs in the vacuum system.

2.7.1 RF Helical Resonators. In general, the higher the rf voltages applied to the trap, the higher the secular frequencies will be (see Section 2.1.2). There are limitations, however, to the secular frequency based on the trap dimensions, the mass of the ion and the rf frequency such that the ponderomotive approximation is still valid. One way to get high voltages on the trap electrodes is to place them in a resonant circuit with a helical quarter wave resonator. The design and construction

of the resonator is discussed in a series of papers written in the 1960s [44, 45, 46]. Given a desired frequency, outer conductor diameter and desired Q, it is possible to calculate the number of windings, the winding pitch, the coil length and the inner conductor diameter. Solid copper elements are used for the outer conductor, the inner coil and the end caps on the resonator. One thing to note about designing the resonator is that, depending on the load on the resonator, the actual loaded frequency of the resonator is typically one half the frequency the resonator is designed for. Thus, to have a 50 MHz resonator (with the trap attached), design the resonator for 100 MHz. Also note that since copper wire comes in set gauges, it might not be possible to use the initial design parameters. Use a series of iterations in the design to accommodate the available copper wire diameters. One example of a resonator constructed in the lab has the following characteristics:

Outer Conductor diameter: 2 inches

Resonant Frequency: 158 MHz

Coil wire diameter: 0.1285 inches (8 gauge)

Number of turns: 6

Unloaded Q (designed): 1260

Winding pitch: 0.26 inches

Coil Length: 1.54 inches

Inner coil diameter: 1.0 inches

Outer conductor length: 2.54 inches

The actual resonant frequency with a 30pF capacitor on the end is about 35 MHz. Without a capacitive load, this resonator works at around 70 MHz with a Q of

about 500. Again, see the references for details on how to design the resonators. In addition, it helps to clean the resonator before using it- the copper has fewer losses when it is clean, leading to a higher Q . Copper can be cleaned to a shiny luster using phosphoric acid. The end result is shown in both a CAD drawing and actual photos in Fig. 2.20.

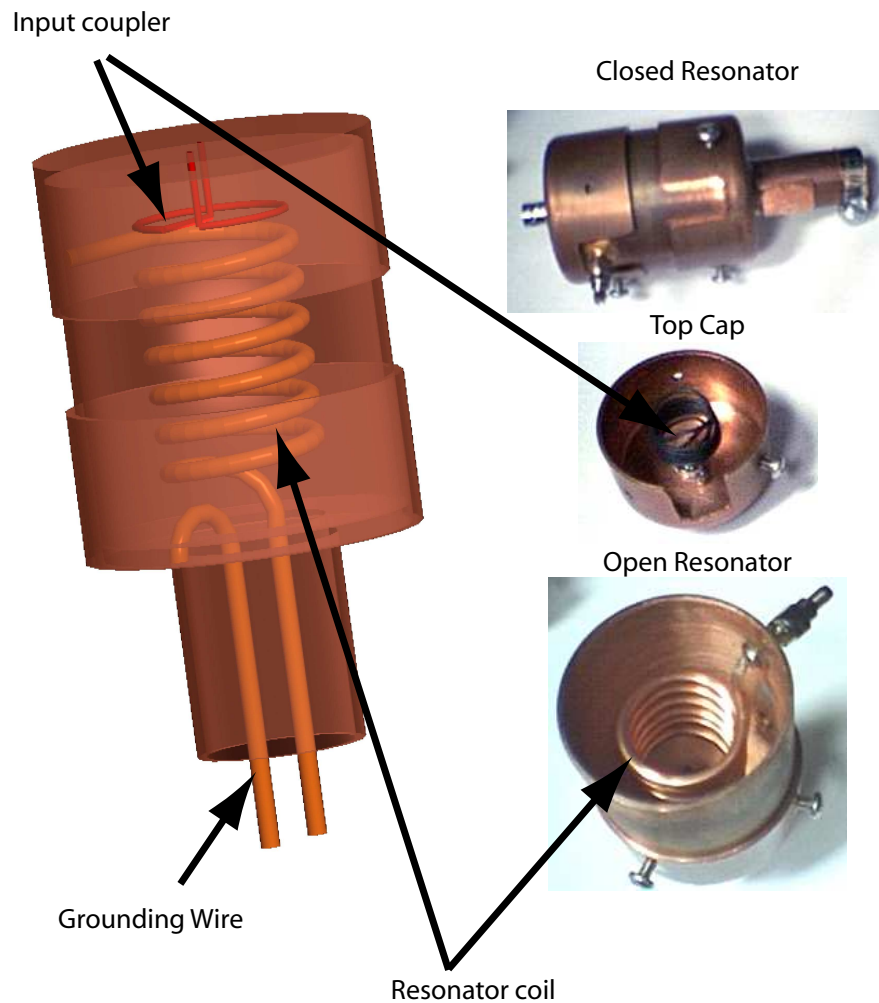


Figure 2.20: Helical resonator diagram. The helical quarter wave resonator consists of an inner helical conductor inside a conductive cylinder. Shown on the left is a schematic drawing of the completed resonator. On the right are photographs of an actual resonator with specifications given in the text.

RF power can be coupled into the resonator in two ways. A small closed loop of bare wire (shorted from the center of the coaxial connector to ground) with a diameter of about one inch can be placed on the inside of the cap closing the top

end of the resonator. The normal to this loop should point down the center axis of the resonator. This loop couples the rf into the magnetic field of the resonator and can be tuned so that all the power is transferred into the resonator by adjusting both the number of turns in the loop, the loop diameter, and the proximity of the loop to the end of the inner helical conductor. If the other parameters are close, fine-tuning of the coupling is accomplished by moving the cap and loop together through the resonance and then fixing the cap when the back reflection from the resonator is zero.

The other method is to couple the electric field to the resonator near the bottom using a small variable capacitor. The center coaxial lead is sent to the variable capacitor (usually a 2-30 pF parallel-plate variable capacitor) and from there connected directly to the center helical conductor close to the end of the resonator. The capacitor is adjusted such that the back reflected power from the resonator is again zero.

2.7.2 Static Electrodes. Any electrodes that are used to apply static voltages to the trap, either as endcap static voltages or as compensation electrodes, must be filtered so that they all act as rf grounds. In particular, the static electrodes on the ceramic linear trap (Section 5.1) must all be filtered so that the trap is linear along the axis. The schematic drawing shown in Fig. 2.21 illustrates the relevant capacitances, resistances, and inductances for the rf circuit from the resonator to the trap. The vacuum chamber itself is held at rf ground through a connection to the resonator. The trap has a capacitance $C_1 \sim 1$ pF to the nominal rf ground electrode. This might be augmented by filters in the vacuum chamber (Section 5.1.4). The capacitance $C_2 \sim 1$ pF is also primarily geometric, although it also might have the in-vacuum filters. The resistances R_1 and R_2 are the residual resistances of the conductors used

to carry the rf in the chamber and are less than $1\ \Omega$. The vacuum feedthroughs have a capacitance between leads and to the housing of $C_3 \approx C_4 \approx 10\ \text{pF}$. And the rf electrode has a capacitance to the vacuum chamber itself of $C_5 \sim 1\ \text{pF}$. Outside the vacuum system, the resonator is connected to the vacuum chamber such that the resonator can and vacuum chamber form the rf grounding surface. Static voltages 1, 2, and 3 can be applied through the filter networks with $C_0 = 1\ \mu\text{F}$ and inductor $L_0 = 1\ \text{mH}$.

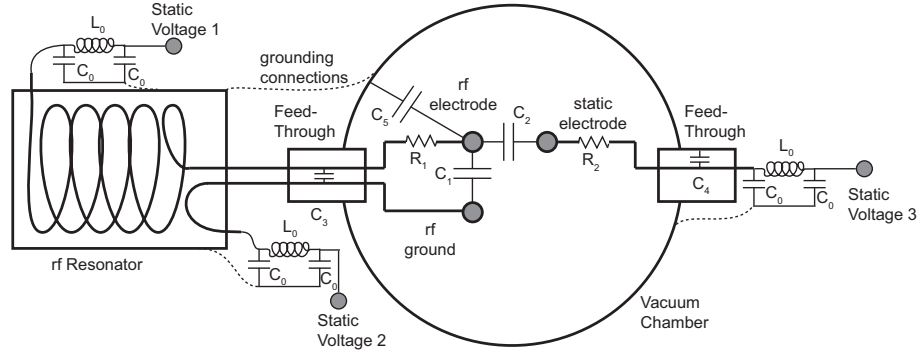


Figure 2.21: RF filters and wiring diagram. This schematic diagram shows the relevant capacitances and resistances for the trap in the vacuum chamber. The “ π ” filter networks allow the application of static voltages to various electrodes in the chamber. The internal capacitances and resistances are geometric in nature and are distributed across the entire physical element.

2.7.3 RF Generation The helical resonators transform radiofrequency power into high voltage, but very little current. It is necessary to couple a significant amount of power into the resonator in order to obtain the level of rf voltages desired on the trap. The voltage on the trap, V_0 is related to the input power in the resonator P by the quality factor of the resonator Q :

$$V_0 = \zeta \sqrt{PQ} \quad (2.21)$$

where ζ is on the order of about 10 [Appendix A]. To get 500 V rf on the trap, the resonator must have a $Q \approx 500$ and around 10 W of rf power must be applied to the resonator. The rf delivery system is shown in Fig. 2.22. A directional coupler is

included to be able to optimize the input coupling to the resonator. On resonance, the entire trap-resonator circuit should appear to the rf amplifier to be a $50\ \Omega$ circuit. Fine tuning the input coupling allows for perfect coupling to the resonator. The directional coupler also permits a measurement of the loaded Q of the resonator.

The Q of the resonator is measured by first tuning the frequency of the oscillator to the resonant frequency ν_0 . If the off-resonant amplitude of the back-reflected signal is V_{max} , then the frequency at which the amplitude is $V_{max}/\sqrt{2}$ above the resonance is ν_+ . The frequency with amplitude $V_{max}/\sqrt{2}$ below the resonance is ν_- with frequency difference $\delta\nu = \nu_+ - \nu_-$. The loaded Q of the resonator is

$$Q = \frac{\delta\nu}{\nu_0}. \quad (2.22)$$

A good resonator has a loaded Q of greater than 300.

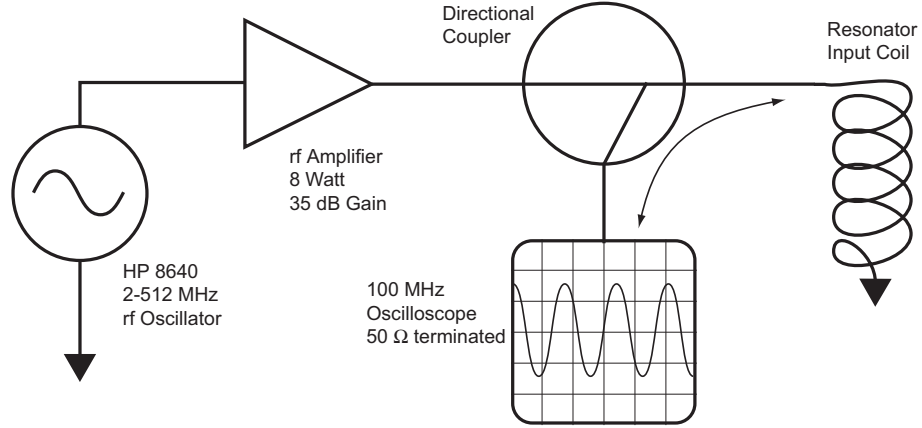


Figure 2.22: RF generation diagram. This schematic diagram illustrates the rf generation and delivery to the helical resonator. The directional coupler is used to monitor the back-reflected power to tune the input coupling on the resonator. The input coupling is perfect when the back-reflected signal disappears.

CHAPTER III

Ion Trap Design

3.1 Linear Trapping Potentials

The first step in advanced trap development is to model the electrodes and resulting potentials using numerical Finite Element Analysis (FEA) software packages. The three-dimensional trap potential can be described by splitting the potential into the two-dimensional rf and three-dimensional static components. The rf potential is described using the ponderomotive approximation (see Section 2.1) such that the pseudopotential is described by static electric field amplitudes. The potentials are then modeled using static FEA solvers and fit to quadratic functions with some geometric scale factor. The rf and static portions of the potential can then be combined to calculate the overall trapping frequencies and trap depth.

3.2 Transverse Electric Potential Simulation

The transverse trapping potentials in a linear trap can be approximated by a two-dimensional problem. In the limit of an infinitely long linear trap with no axial confinement, this describes the entire potential. But the approximation is reasonable for the kinds of trapping structures described here and can be an efficient tool in modeling the potentials.

3.2.1 Finite Element Analysis. Recent versions of the Matlab software suite come packaged with a simple finite element analysis (FEA) solver package called the “Partial Differential Equation (PDE) Toolbox (pdetool)”. Pdetool contains a graphical user interface [shown in Figs. 3.1,3.2] with user-defined boundary values, a grid construction algorithm, the FEA solver, and a graphical display of the field solutions. The PDE Toolbox [47] can solve a general class of problems that can be described by the elliptical equation

$$-\nabla \cdot (c \nabla u) + au = f \text{ in } \Omega \quad (3.1)$$

where Ω describes the bounded area in a complex plane, and c , a , and f are functions defined in the area Ω and u is the field solution. The boundary conditions can be of both the Dirichlet and Generalized Neumann types. In modeling the electrostatic potentials that give rise to the effective rf trap, a much simpler problem can be solved because of the constraints of the Poisson equation $\nabla^2 \psi = 0$, again defined in the bounded area Ω and for no free charges in the area of interest (as is the case for our ion trap potentials). This corresponds to the elliptical equation solved by the PDE toolbox with $c = 1$, $a = 1$ and $f = 1$. The approximate solution to Eq. 3.1 with these constraints is found in three steps. First, the geometry Ω is described along with the Dirichlet boundary conditions on the bounding curve C [Fig. 3.1]. Second, a triangular mesh is constructed in the domain Ω . Last, the PDE and the boundary conditions are discretized to obtain a system of linear equations $Ku = F$ that can be solved using well known algebraic algorithms [Fig. 3.2] [48].

3.2.2 PDE Toolbox. The graphical user interface, shown in Figs. 3.1,3.2 is useful for an initial design or for relatively few design iterations. However, for large numbers of design iterations, the Matlab PDE Toolbox provides access to the solver functions necessary for building the model, creating the mesh, and solving for the potential.

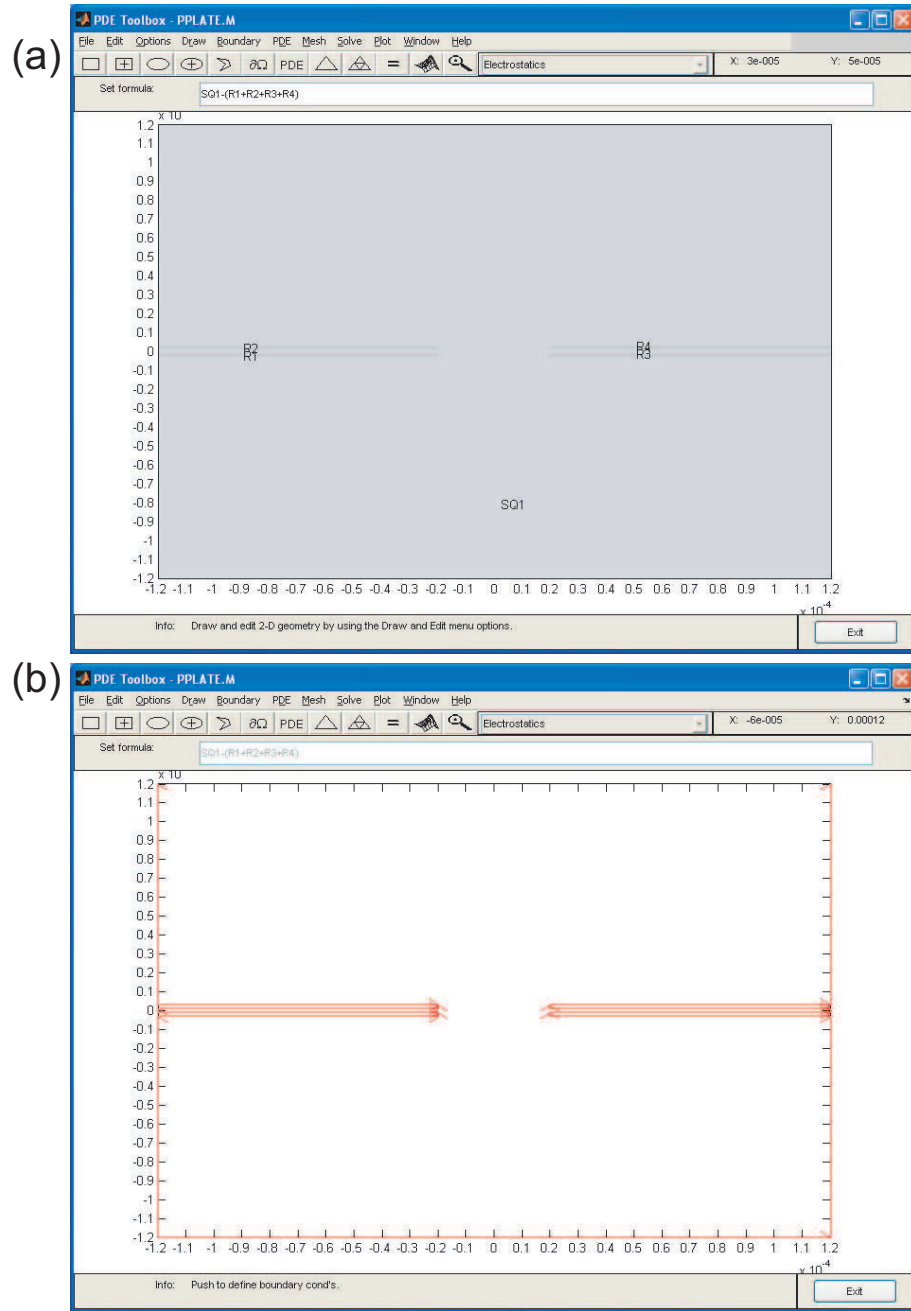
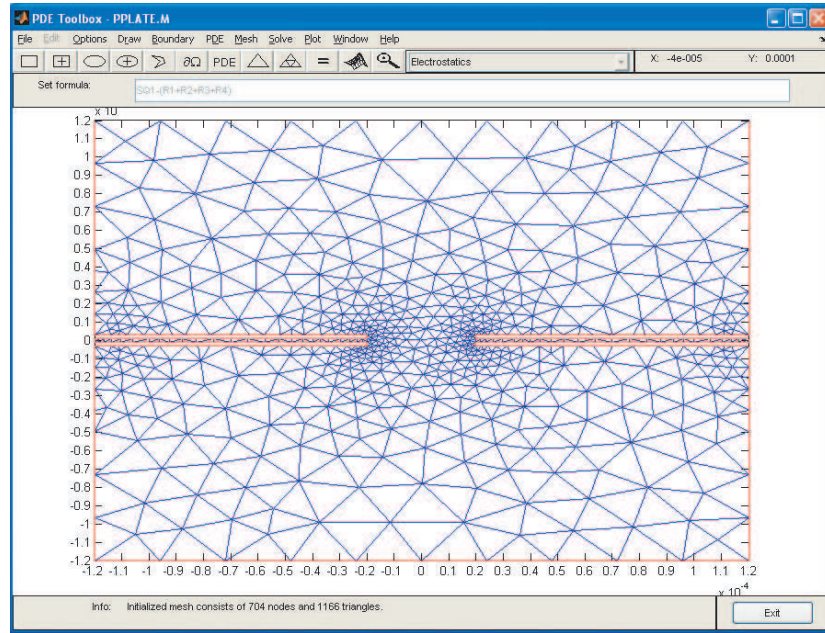


Figure 3.1: The GUI for Setting up the model in the PDE Toolbox. This screenshot of the graphical user interface for the PDE Toolbox shows a simple layout and boundary conditions. (a) The basic drawing interface for defining object areas. (b) The boundary tool for setting the Dirichlet boundary conditions for the trap.

(a)



(b)

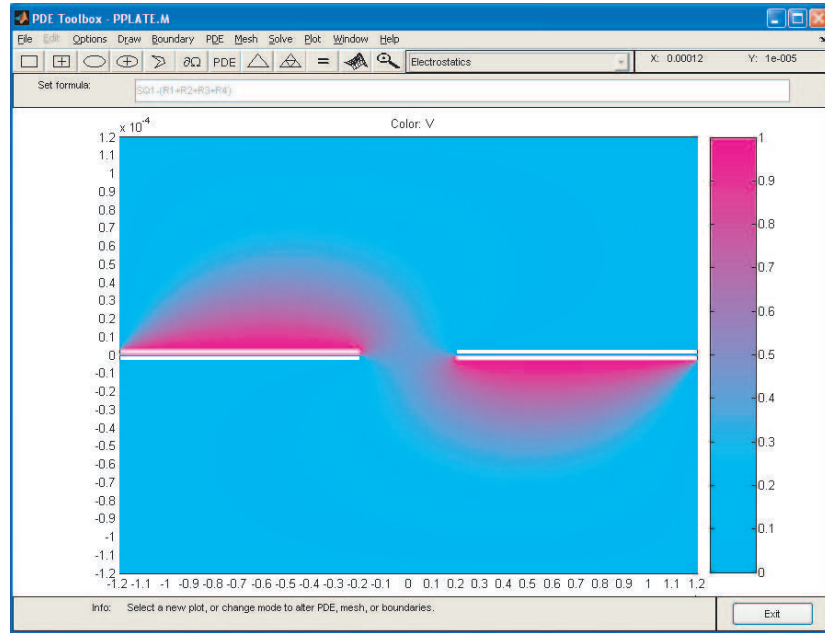


Figure 3.2: The GUI for Solving the model in the PDE Toolbox. This screenshot of the graphical user interface for the PDE Toolbox shows a simple mesh and solution for one microtrap design. (a) The mesh tool constructs and refines the triangular mesh. (b) The solution is shown as a 2-D color plot.

The tip-to-tip separation is defined as a , the distance between cantilevers is d , the cantilever thickness is dt , and the bounding box is given by $c1$.

```
%coefficient matrix

          %R1          %R2          %R3          %R4          %SQ1
geometry=[3.0000      3.0000      3.0000      3.0000      3.0000
          4.0000      4.0000      4.0000      4.0000      4.0000
          -(a/2+c1) -(a/2+c1) a/2          a/2          -(a/2+c1)
          -a/2          -a/2          (a/2+c1) (a/2+c1) (a/2+c1)
          -a/2          -a/2          (a/2+c1) (a/2+c1) (a/2+c1)
          -(a/2+c1) -(a/2+c1) a/2          a/2          -(a/2+c1)
          -(d/2+dt) d/2          -(d/2+dt) d/2          -(a/2+c1)
          -(d/2+dt) d/2          -(d/2+dt) d/2          -(a/2+c1)
          -(d/2)      d/2+dt      -(d/2)      d/2+dt      (a/2+c1)
          -(d/2)      d/2+dt      -(d/2)      d/2+dt      (a/2+c1)];
```

The first two lines of the geometry matrix are variables that describe the particular geometry (a rectangle in this case) and the remaining eight lines are used to define each geometrical shape.

A namespace matrix is defines to set forth the text labels for each column in the geometry matrix. In addition, the formula string defines how the different geometry elements are to be combined to make the region Ω .

```
%namespace matrix

ns=[82      82      82      82      83
    49      50      51      52      81
    0       0       0       0      49];
```

```
%formula string
sf='SQ1-(R1+R2+R3+R4)';
```

The PDE toolbox then requires that the geometry, namespace and formula string matrices be processed to define a reduced geometry matrix containing all the individual segments of the boundary curve C . The boundary values can then be set for all the individual segments using a boundary value matrix. Only the first two columns (out of 20) are shown. The first six rows define the type of boundary condition to use and the last three are ASCII code for a particular value (i.e. -0.5).

```
%calculate reduced geometry matrix (20 line segments)
[reducedgeom booleanline]=decsq(geometry, sf, ns);

%boundary value matrix
boundary=[1      1  ...
          1      1  ...
          1      1  ...
          1      1  ...
          1      1  ...
          1      1  ...
          48     48  ...
          48     48  ...
          49     49  ...
          48     48  ... ];
```

The mesh can then be created and refined using an interactive process and the `mesh` commands.

```
%create initial mesh
```

```
[points edges triangles]=initmesh(reducedgeom);
%refine mesh a bit to get a better solution
[points edges triangles]=refinemesh(reducedgeom,points,edges,triangles);
points=jigglemesh(points,edges,triangles);
```

The actual FEA solver command, `assemblpde` is called using the refined mesh and the coefficients for the elliptical equation, Eq. 3.1.

```
%coefficients for assemblpde
coef1=1.0;
coef2=1.0;
coef3=1.0;
%get solution now
potential=assemblpde(boundary,points,edges,triangles,coef1,coef2,coef3);
```

To extract the potential in a rectangular coordinate system (useful for taking the gradient and for plotting the potential along a given line), the PDE toolbox provides the command `tri2grid`, which is called using the solution found from the FEA solver.

```
potential_xz=tri2grid(points,triangles,potential,x,z);
```

The potential can then be evaluated, or in the case of finding the absolute potential depth, the gradient can be found using Matlab's standard matrix evaluation tools.

3.3 3D Electric Potential Simulation

The FEA solver that is bundled with the MATLAB software package is good for two-dimensional problems, but it is unable to solve three-dimensional problems. In a

linear ion trap, the rf field typically has enough symmetry to be considered as a two-dimensional problem. The static confinement fields that provide the transverse trap are, however, three-dimensional in nature. A more powerful FEA solver is needed to model the static fields and provide a complete picture of the ion trap characteristics.

Three-dimensional FEA problems are significantly more complicated due to the increased number of elements needed to fill a volume as opposed to an area. There are different ways of filling the volume space using different geometric shapes including tetrahedra, hexagonal blocks, cubes, and other more complicated shape schemes. The various commercially available software packages use different techniques and different shapes to fill the FEA volume. One such solver is called “Maxwell 3D” by a company called Ansoft. This solver was used to model the potentials and electric fields in both the three-layer alumina traps as well as the microtraps.

Like the MATLAB FEA solver, Maxwell uses multiple windows to define the problem, set the initial boundary conditions, solve for the fields, and analyze the solution. The project window is general tool for calling each of these steps when defining the problem [Fig. 3.3(a)]. The first step is to draw the shapes associated with the trap electrodes as well as the bounding box that defines the overall solution area [Fig. 3.3(b)]. Maxwell has the capability to do both electrical, magnetic and other thermal and mechanical solutions. The software uses a materials library to define the relevant material properties for all the elements of the model. The second step is to assign the material properties to the various components of the model. Using a good conductor is typically sufficient and the “gold” material is often used for most electrodes [Fig. 3.4(a)].

Once the surfaces have been defined and material properties set, the boundary conditions are set using the boundary window. For a typical Dirichlet boundary

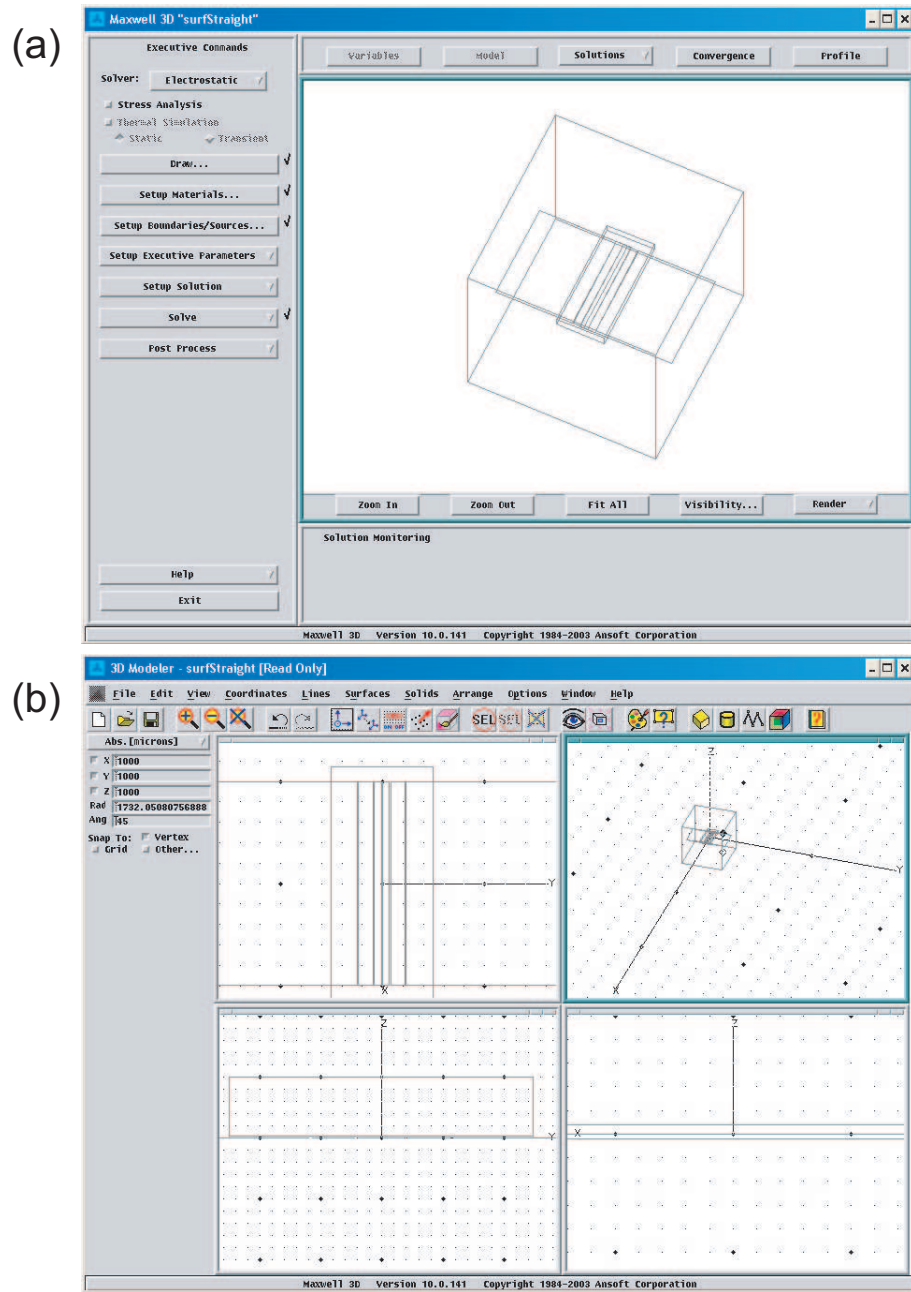


Figure 3.3: The GUI for Setting up the Project in Maxwell 3D. (a) The Maxwell 3D Project window. From this window, all aspects of the model are managed including the model type and the steps to a solution. (b) The model is drawn in this window using three-dimensional shapes. The draw mode also defines the bounding box for the region of interest.

condition, the surface is set to be a voltage “source” with a given electric potential. The bounding box can also be set as a potential source and is typically set to ground (0 V) [Fig. 3.4(b)].

Maxwell uses an iterative algorithm to solve for the fields in the defined area. There is an initial 3-D mesh of tetrahedra defined in the volume. This initial mesh can be customized by defining vacuum elements in critical areas [Fig. 3.5(a)]. Then, inside these elements, the number of tetrahedra can be increased to have a finer grid spacing for calculating trap potentials and trap frequencies. The solver then calculates the field at every mesh element. Then, the software analyzes the points where the potential is greatest and increases the number of mesh elements at those points and re-solves for the field in the volume using the greater number of tetrahedra [Figs. 3.5(b), 3.6(a)]. The solution converges on an answer using an error estimate of the fields based on the deviation from expected values.

After the solver has reached an acceptable error level (which can be set for more accurate solutions and larger meshes), the solution can be viewed using the visualization tools provided. Visualizing a three-dimensional field is difficult, but two-dimensional cuts through the volume of the trap can provide a good picture of the field characteristics. Maxwell also provides elementary tools for calculating the electric field ($\vec{E} = \vec{\nabla} \cdot \phi$) magnitude from the potential and can plot the magnitude along a line. These tools can be accessed from the “calculator” function in the project solution window. From this data, the static trap potentials can be extracted [Fig. 3.6(b)].

3.4 Errors in Finite Element Analysis Field Solvers

There are several common errors that can occur when using FEA solvers to model new trap geometries. The degree to which each of these affects the final potential

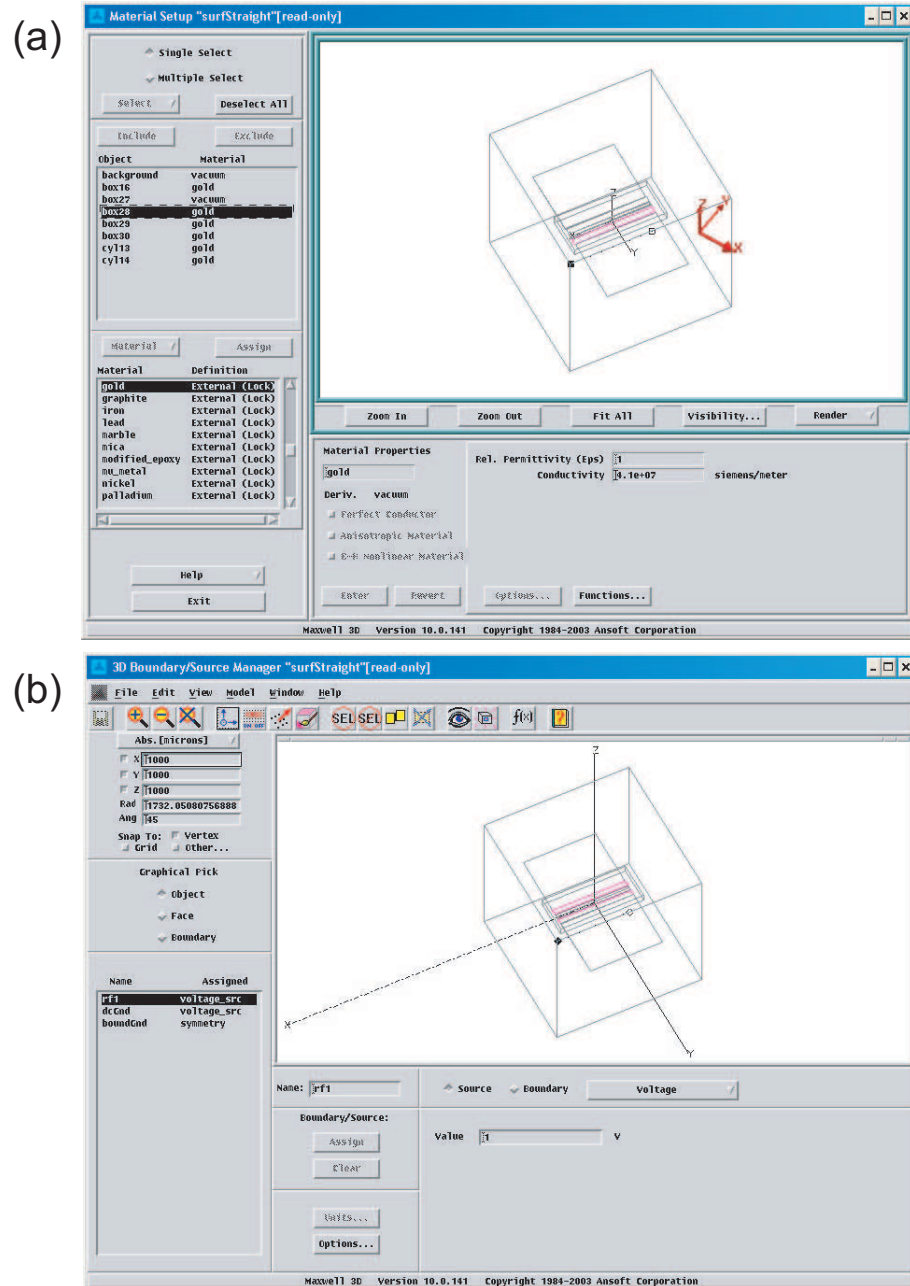


Figure 3.4: The GUI for Defining Materials in Maxwell. (a) The materials library is used to define the material properties for all elements of the model. Typically the conductivity is the only critical parameter. (b) The boundary conditions are set including the bounding box surfaces.

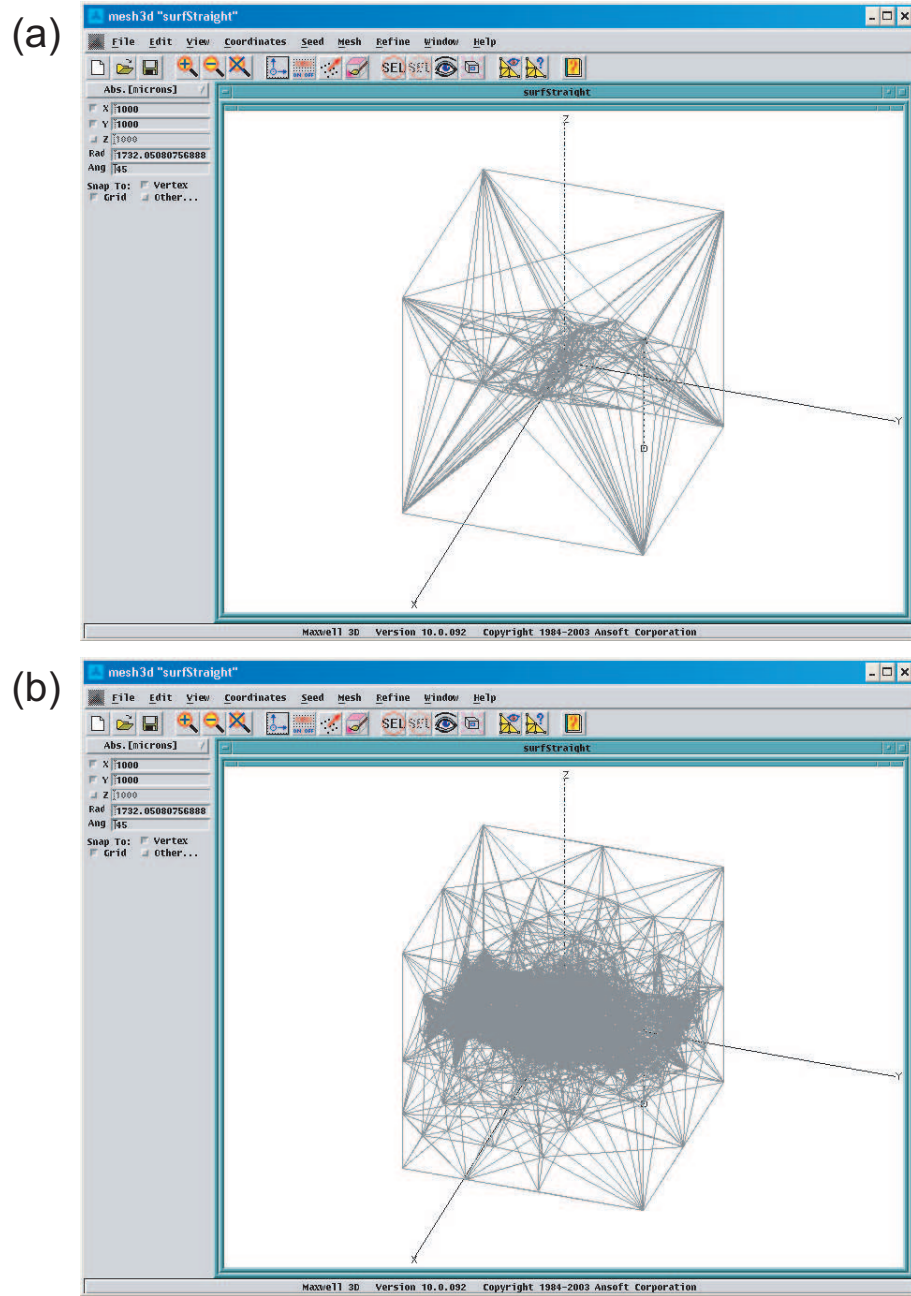


Figure 3.5: The GUI for Defining the Mesh in Maxwell. (a) The initial mesh is set to a low number of tetrahedra. The density of tetrahedra can be increased in regions of interest by creating vacuum elements and manually increasing the mesh density. (b) After an interactive solution, the mesh density is higher at points where the field is more concentrated.

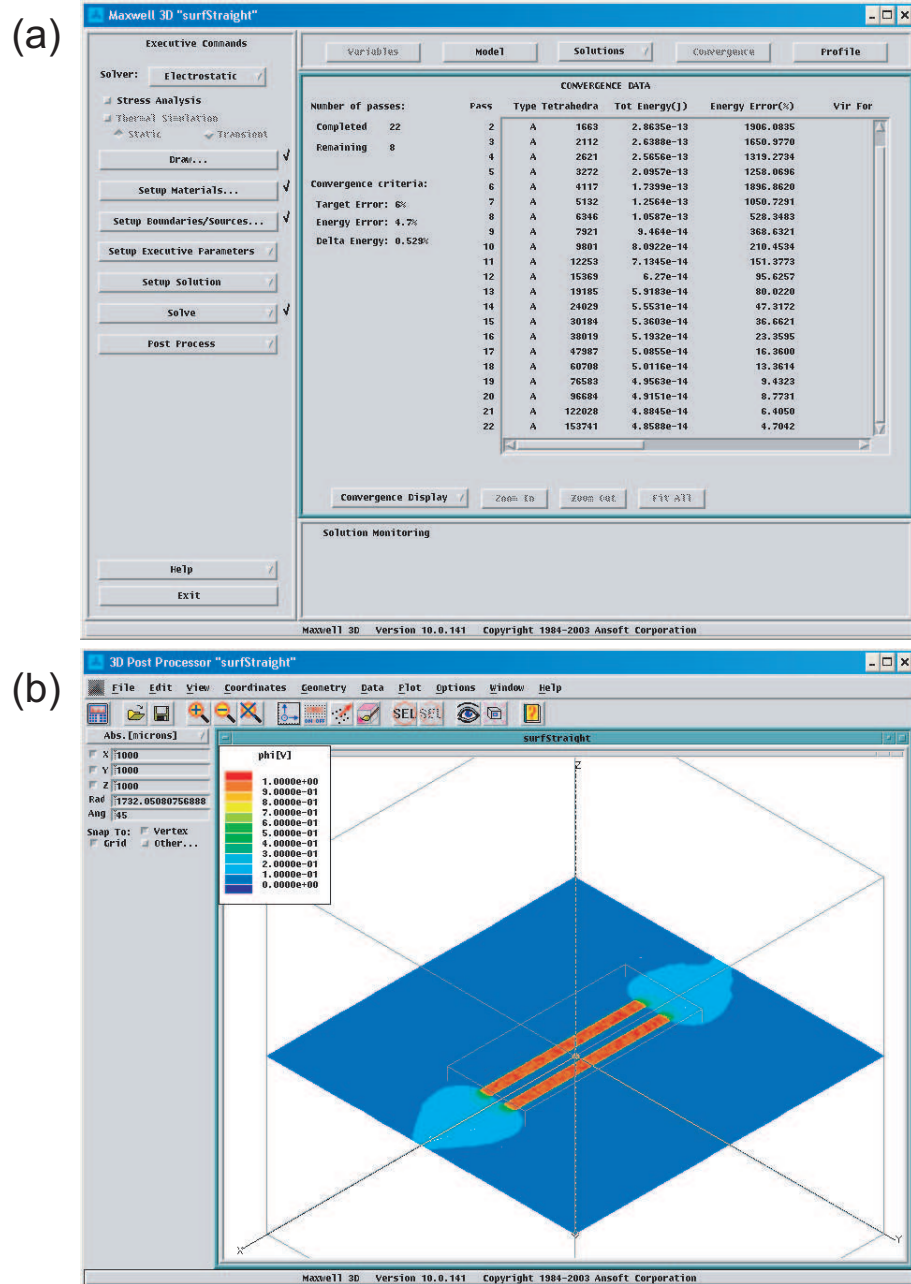


Figure 3.6: The GUI for Solving the Problem in Maxwell. (a) The solving window tracks the progress of the adaptive solution algorithm and the proximity to the final error tolerance. (b) The project solution interface can be used to visualize and extract the potentials.

solution can be evaluated and bounds can be set on the error magnitude.

3.4.1 Bounding Box Size Error. The FEA solution requires a finite space Ω , also called the bounding box, in which the potential is evaluated. This requires a boundary condition set on the bounding box, which is typically set to ground. If the bounding box is too small, this grounded surface can change the solution to the potential. This error can be measured by increasing the size of the bounding box, leaving all other physical dimensions unchanged, and re-evaluating the potential. If the new potential is equal to the original within a specified tolerance level, then the bounding box size was sufficiently large.

3.4.2 Mesh Size Error. The solution of the potential is dependent on the size of the mesh compared to the feature size of the trap model structure. If the mesh elements are larger than the feature sizes, there will be errors in the potential, especially near the features. Sharp corners in the physical trap features lead to high potential gradients and need additional mesh elements surrounding them to properly calculate the value of the potential. At the center of the trap, there needs to be a sufficient number of elements to ensure a proper, smooth calculation of the field so that trap frequencies can be extracted from the potential. The mesh size error can be calculated by increasing the mesh size by a substantial amount and then re-calculating the potential. Again, if the new potential is equal to the original within specified tolerance levels, the mesh is sufficiently fine.

3.4.3 Interpolation Error. After the potential is calculated in the mesh, to extract out trap frequencies and the trap depth, it is necessary to make an interpolation along either a line or a grid of the irregular mesh elements. If the mesh elements are much larger than the characteristic size of the region of interest for the interpolation, then the potential will be jagged after the interpolation is made. This can be resolved

by increasing the mesh size in the area of interest.

CHAPTER IV

Planar Microtrap Model

4.1 Background

The ion trap has become an essential tool in several areas of physical science, including mass spectroscopy [49], atomic frequency standards [50], precision atomic and molecular measurements [51], studies of fundamental quantum dynamics [36] and quantum information science [52, 35]. Many of these applications would benefit from miniaturized and multiplexed ion trap electrode structures well below the typical millimeter to centimeter scale. Furthermore, smaller electrode dimensions offer the potential for stronger confining forces.

In this Chapter, the electrical characteristics of a new type of micrometer-scale radiofrequency (RF) Paul ion trap fabricated using semiconductor micromachining and lithographic techniques such as micro-electro-mechanical-systems (MEMS) and molecular beam epitaxy (MBE) is modeled using the FEA techniques described in Ch. III [32]. Such a device may enable new applications of ion trap technology such as “quantum CCD” scalable quantum computers [23], optical cavity-QED with a localized single atom [53, 54, 55, 56], and multiplexed quadrupole mass spectrometers that could be orders of magnitude smaller than previous devices [57].

There has been much recent progress in the miniaturization of neutral atom elec-

tromagnetic trapping structures, involving, for example, micrometer-scale current-carrying wires on a substrate resulting in Bose-Einstein condensates on a microchip [58]. Microscopic ion trap electrodes present their own challenges, as the confining forces are orders of magnitude stronger than those for neutral atom traps. Consequently, such ion traps will require greater control of unwanted or noisy electrode potentials, including the presence of thermal electric fields [59, 60], residual charge on exposed insulating barriers, and “patch” potentials from inhomogeneities on the electrode surfaces [35, 61]. None of these potential pitfalls appears fundamental, and such problems will only be overcome by testing various materials and approaches. The focus of this Chapter is on novel features of a proposed high aspect-ratio ion trap geometry and the resulting confining potentials.

The physical parameters of a model of the linear microtrap are discussed in Sec. 4.2 along with a discussion of design considerations and issues with heating and power dissipation in semiconductor materials. Section 4.3 contains a discussion of the RF ponderomotive potential of the linear microtrap model with results from numerical simulations of the potential. A geometrical efficiency factor is calculated, showing the performance of the linear microtrap as compared to an ideal quadrupole potential. The static potential used for axial confinement in a linear trap is discussed in Sec. 4.4 along with results from numerical simulations and comparison to an ideal hyperbolic trap. The total potential along with examples of how to use the various geometric efficiency factors to calculate the trap frequencies of a given geometry are given in Sec. 4.5. The principal axes of the linear microtrap, which determine the efficiency of laser cooling ions in the linear microtrap, are evaluated in Sec. 4.6. A method for rotating the axes for more efficient cooling is given.

4.2 Model Description

4.2.1 Basic Model. The design of this new type of micrometer-scale RF trap is constrained by conventional semiconductor fabrication techniques, the need for clear laser optical access, and the characteristics of electrodes needed for linear traps. The design, illustrated in Fig. 4.1, is a two-layer planar geometry where both layers are divided into separate electrodes. The division of each layer into six electrodes accommodates both the RF potentials and the static potentials needed to create a linear Paul trap [62]. This planar design is compatible with conventional photolithography techniques to define the electrode pattern. Each electrode is a cantilever anchored to an electrically isolated, conductive substrate and suspended from both sides of the planar structure. This ensures that there are no insulators near the center of the trap that could accumulate uncontrolled charge. Ions will be trapped in the space between the tips of each cantilever, along the z -axis in Fig. 4.1, near the center of the middle electrode.

The cross-section of this linear microtrap (LMT) model at the center of the trap ($z = 0$) is shown in Fig. 4.2(a). The thickness of each layer is labeled w ; the layer separation is d ; the tip-to-tip separation of the cantilevers is a . Two ratios are useful for characterizing the behavior of the electric potentials: the trap aspect ratio, or the ratio of the tip-to-tip cantilever separation to the layer separation $\alpha = a/d$, and the ratio of the layer separation to the layer thickness $\delta = d/w$. An RF voltage is applied between each set of diagonally opposing electrodes as shown in Fig. 4.2(a).

A top view of the linear microtrap model is shown in Fig. 4.2(b). The width of the center cantilevers along the z -axis of the trap is labeled b ; the width of the end-cap cantilevers is c ; and the length of the cantilevers in the model is h . In

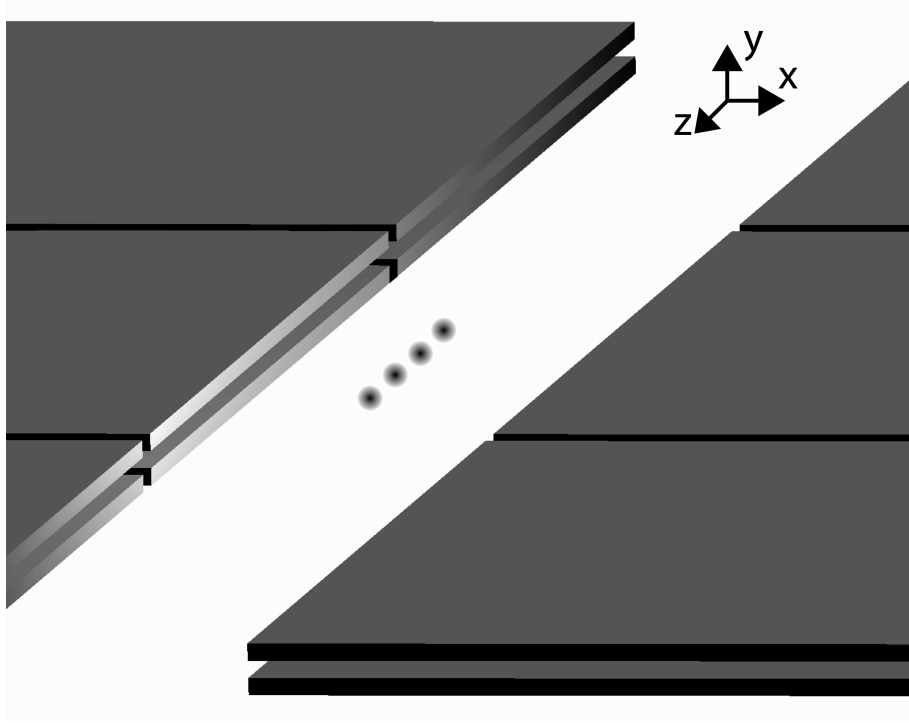


Figure 4.1: A three-dimensional drawing of the linear microtrap. A string of ions would lie along the z -axis as drawn.

order to electrically insulate the center from the end-cap cantilevers, a small gap is introduced of width g . This allows for separate potentials to be applied to all twelve cantilevers, or electrodes. Static voltages are applied to both layers on the four end-cap electrodes on either side of the center cantilevers to provide axial confinement, as shown in Fig. 4.2(b).

The potentials of the LMT can be separated into two parts for analysis, following the guide from Ch. III. The first part is the ponderomotive potential generated by the RF voltages. In the limit where gap width g is much smaller than a , b and c (Fig 4.2(b)), the RF potential is approximately independent of z near the center of the trap. In the cross-sectional plane at $z = 0$, this RF potential generates a two-dimensional trapping pseudopotential and is discussed in Section 4.3. The second part is the potential generated by applying static voltages to the end-cap electrodes.

This potential provides axial confinement for ions in the center of the trap and is described in Section 4.4. Note that the end-cap electrodes have both the RF voltages applied to reduce the z dependence of the RF field near the center of the trap and static voltages to create the end-caps. The center electrodes are all assumed to be held at static ground.

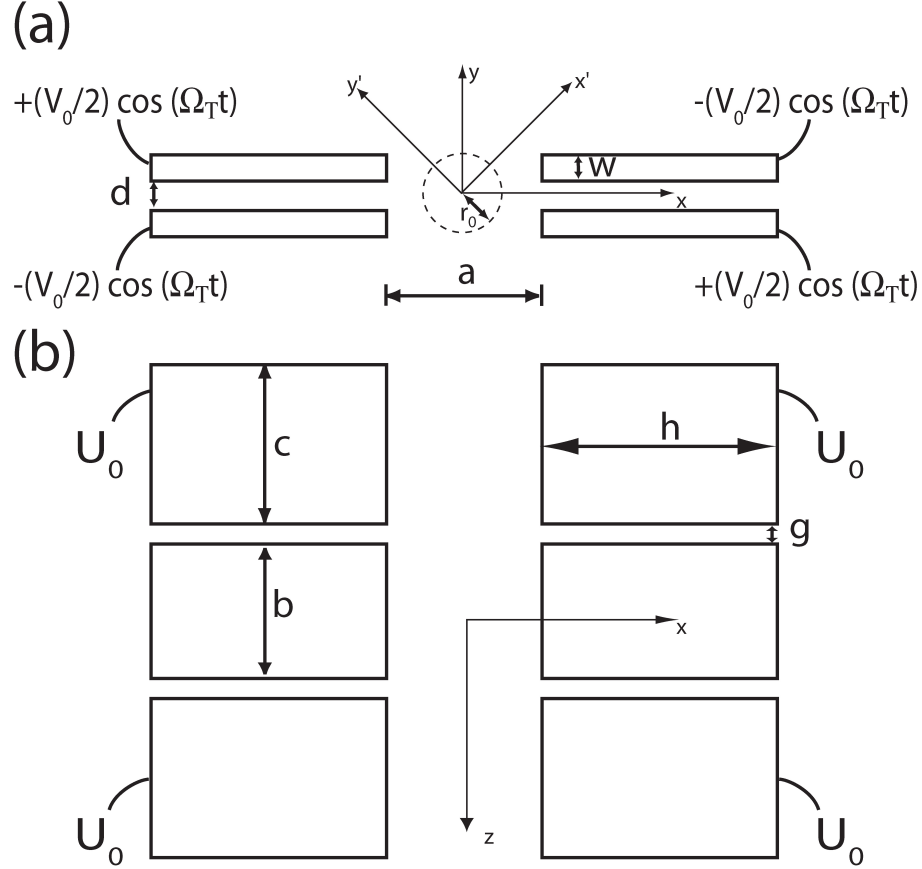


Figure 4.2: Two layer schematic of the potentials. (a) A schematic diagram of the linear microtrap design showing the side view. The dimensions are labeled as are the RF voltages applied to the electrodes. (b) The top view of the linear microtrap with dimensions and static voltages as shown.

4.2.2 Fabrication Considerations. The linear microtrap model is designed to simulate a trap design that can be fabricated using conventional micro-processing techniques. The sizes of the electrode features that will be analyzed in this model are typical of current fabrication processes. There are several different processes that could be used to fabricate these microtraps: a) Silicon-based microelectromechani-

cal machining (MEMS) techniques; b) Gallium-Arsenide (or other suitable material) based molecular-beam epitaxy (MBE) grown wafers and associated etching processes; or c) other relevant techniques such as anodic wafer bonding or flip-chip technologies. The length of the cantilevers is limited by allowable mechanical vibrations in the cantilevers themselves, as well as limits to the mechanical stability of the cantilevers under electromechanical forces due to the applied RF and static voltages. The mechanical forces exerted on the cantilevers can be approximated using structural cantilever analysis [63]. Following this analysis, the spring constant of the center rectangular cantilever can, for example, be expressed as

$$k = E \left(\frac{w^3 b}{4h^3} \right) \quad (4.1)$$

where E is the Young's Modulus of the relevant material. The force on one cantilever due to an applied potential difference V_0 between layers can be approximated as the gradient of the potential in a parallel plate capacitor of area $A = hb$ and plate separation d .

$$\begin{aligned} F &= - \frac{\partial U_{Capacitor}}{\partial d} \\ &= - \frac{\epsilon_0}{2} \frac{\partial}{\partial d} \left(\frac{hbV_0^2}{d} \right) \\ &= \frac{\epsilon_0}{2} \left(\frac{hbV_0^2}{d^2} \right) \end{aligned} \quad (4.2)$$

Although the actual force is distributed across the length of the capacitor, by approximating the force as being concentrated at the tip, one can find an upper bound on the cantilever tip deflection. Treating the cantilever as a classical spring with the force applied at the tip, and using the spring constant from Eq. 4.1, the maximum tip deflection $x_d^{(0)}$ can be approximated as

$$x_d^{(0)} \sim \frac{2\epsilon_0 h^4 V_0^2}{E d^2 w^3}. \quad (4.3)$$

A typical deflection for a GaAs cantilever with $E = 85.5\text{GPa}$ and dimensions $h = 100\mu\text{m}$, $d = 2\mu\text{m}$, $w = 2\mu\text{m}$, with an applied voltage difference of $V_0 = 20\text{V}$, is $x_d^{(0)} = 260\text{nm}$. The resonant frequency of the cantilever can also be calculated [63] as a function of the material density ρ , the Young's Modulus, the cantilever width w and the length h :

$$\omega_{vib}/2\pi = 0.162\sqrt{E/\rho}\frac{w}{h^2} \quad (4.4)$$

which for GaAs ($\rho = 5.31\text{gm/cm}^3$) is $\omega_{vib}/2\pi \approx 130\text{kHz}$ for the same dimensions as previously discussed.

For an RF potential $V_0 \cos(\Omega_T t)$ applied to the cantilever electrodes, the amplitude of the tip deflection in Eq. 4.3 is expected to be further reduced by a Lorentzian factor of $\omega_{vib}^2/\Omega_T^2 \ll 1$. Here, it is assumed that the RF frequency is far from resonance, or $\Omega_T \gg \omega_{vib}/Q$, where $Q \gg 1$ is the quality factor of the mechanical resonance [64]. While the above electromechanical forces do not appear troublesome, the actual forces may be considerably higher due to free charges on the electrode layers that are driven by the applied potentials. In any case, it may be necessary to isolate the cantilevered electrodes from noisy electrical signals near the mechanical resonance.

The trap strength may be limited by the maximum voltage that can be applied to the electrodes before the occurrence of electric field break-down. The theoretical limit to the breakdown voltage is dependent on the bandgap of the semiconductor material and, for Si and GaAs, is on the order of $40\text{-}50\text{ V}/\mu\text{m}$ [65] and for silicon nitride, on the order of $300\text{ V}/\mu\text{m}$ [66]. For a layer separation of $2\mu\text{m}$, the maximum applied voltage is expected to be of order $V_0 = 100\text{V}$.

4.2.3 RF Dissipation and Thermal Fields. The fabrication considerations for the implementation of this new type of linear microtrap suggest that highly doped semiconductors could be used as electrodes. Because doped semiconductors have a resis-

tivity several orders of magnitude greater than the metal conductors typically used in ion traps, it is necessary to estimate the power dissipation of the microtrap due to RF losses in the cantilevers. Additionally, the finite conductivity of semiconductor materials will lead to thermal electric fields that will generate heating of the quantized motion of ions in the center of the trap.

The RF dissipation can be estimated with a simple model of lumped circuit elements, since the trap structure is much smaller than the RF wavelength. Each RF electrode is modeled as a small series resistance R shunted by a capacitance C at the trap; inductance of the electrodes is assumed negligible compared to $1/(C\Omega_T^2)$. In addition, RF loss in the insulator separating the electrodes contributes to a parallel resistance characterized by the loss tangent $\tan \delta$. Assuming $RC\Omega_T, \tan \delta \ll 1$, the power loss is

$$P_d = \frac{V_0^2 C \Omega_T}{2} (RC\Omega_T + \tan \delta). \quad (4.5)$$

For values envisioned here, $V_0 \sim 20\text{V}$ at $\Omega_T/2\pi \sim 50\text{MHz}$, $C \sim 10\text{pF}$, $\tan \delta \sim 0.0002$ and $R \sim 10\Omega$, resulting in a power dissipation of $P_d \sim 40\text{mW}$ per electrode.

Additionally, Johnson noise in the electrodes will generate thermal electric fields that will cause heating of the quantized ion motion. A simple model can be used to calculate the heating due to the resistivity of the trap electrodes [35, 60]. For an ion held at a distance z from a conductive plane, the heating rate is given by

$$\begin{aligned} \frac{\partial E}{\partial t} &= \hbar \omega \dot{\bar{n}} \\ &= \frac{e^2 k_B T R(\omega_s)}{m z^2} \end{aligned} \quad (4.6)$$

where ω is the secular frequency and \bar{n} is the average vibrational quantum number of an ion in the trap. In the limit where the conductor thickness w is much smaller than the distance to the ion z , and both dimensions are smaller than the skin depth δ

of the conductor ($w \ll z \ll \delta$), the resistance R in Eq. 4.6 is frequency independent: $R \approx \rho z/(zw)$, where ρ is the material resistivity. Here, the effective volume of the conductor contributing to the thermal fields is of order z^2w . Again, using typical values for doped semiconductors, the skin depth δ is a few hundred micrometers, the thickness of the conductor is $2\mu\text{m}$ and the ion is $20\mu\text{m}$ from the conductor. In this limit, using a secular frequency of $\omega_s/2\pi = 10\text{MHz}$, and $^{111}\text{Cd}^+$ ions, Eq. 4.6 predicts a thermal heating rate of about 10 quanta/sec. Since this model pertains to fluctuating uniform thermal electric fields from a single conducting plane, the actual thermal electric fields are expected to be much smaller because the trap structure surrounds the ion with a high degree of symmetry, resulting in some degree of cancellation of thermal fields from opposite electrodes. In any case, the heating rate will likely be limited in practice by fluctuating patch fields on the electrode surfaces [60].

4.3 RF Ponderomotive Potentials

4.3.1 Time-dependent RF potentials. As described above, the analysis of the potentials in a linear RF Paul trap can be divided into the transverse RF trap generated by RF voltages applied to the appropriate electrodes, and the axial trap and transverse anti-trap generated by static voltages applied to the end-cap electrodes. Focusing first on the time-varying potential generated by the RF voltages, the analysis can be simplified by using a pseudopotential approximation. The motion of an ion in an RF potential of the form

$$\Phi(x, y, z, t) = V(x, y, z) \cos(\Omega_T t) \quad (4.7)$$

can be approximated using a ponderomotive pseudopotential [34]:

$$\psi = \frac{e^2}{4m\Omega_T^2} |\nabla V(x, y, z)|^2 \quad (4.8)$$

Ion motion in the pseudopotential can be approximated as secular harmonic motion [35] with frequency

$$\omega_p^2 = \frac{e^2}{4m^2\Omega_T^2} \frac{\partial^2}{\partial x^2} (|\nabla V(x, y, z)|^2). \quad (4.9)$$

The micromotion due to the time dependence of the RF potential is small in the limit where $q \equiv 2\sqrt{2}\omega_p/\Omega_T \ll 1$ [34].

Since the secular ion motion is dependent only on the gradient of $V(x, y, z)$, it is possible to calculate the effective (or ponderomotive) potential of the linear microtrap using an electrostatic analysis. Moreover, since the RF potential is approximately uniform along the z -axis near the center of the trap, it can be described in the $z = 0$ plane as a function only of x and y , reducing the calculation of the RF potential to two dimensions.

4.3.2 Hyperbolic Electrode Model. One common configuration of a linear Paul trap consists of four infinitely long hyperbolic electrodes. This hyperbolic electrode model will be used as a standard of comparison for the linear microtrap. The cross-section of hyperbolic electrodes with a characteristic radius R_0 is shown in Fig. 4.3. For the potentials applied according to Fig. 4.3, the exact potential amplitude is

$$\begin{aligned} V_{\text{hyp}}(x', y') &= \frac{V_0}{2R_0^2} (x'^2 - y'^2) \\ &= \frac{V_0}{2} \frac{r^2}{R_0^2} \cos 2\theta'. \end{aligned} \quad (4.10)$$

where the coordinate system (x', y') is indicated in Fig. 4.3.

The pseudopotential that corresponds to this hyperbolic potential is calculated using Eq. 4.8.

$$\psi_{\text{hyp}} = \frac{e^2 V_0^2}{4m\Omega_t^2 R_0^4} (x'^2 + y'^2) \quad (4.11)$$

The secular frequency of a ion moving in this ponderomotive pseudopotential is

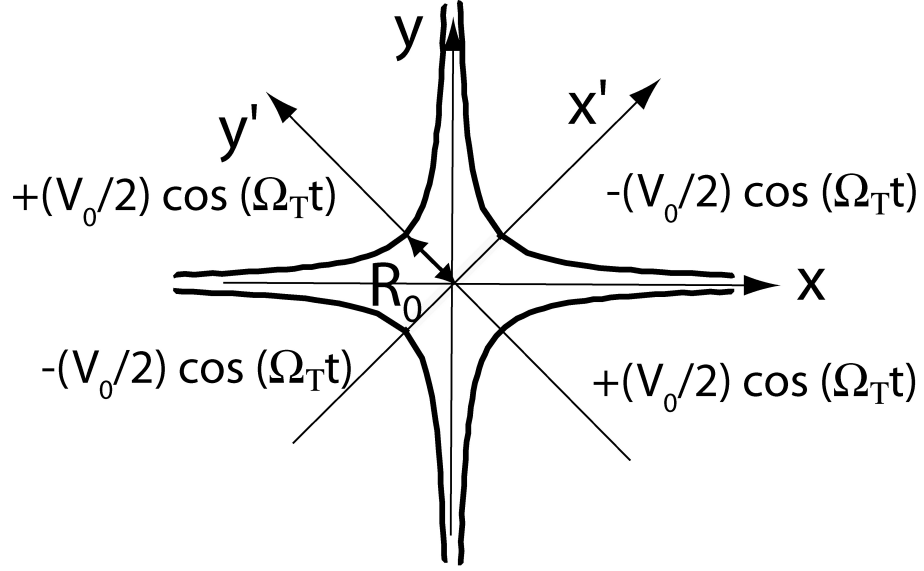


Figure 4.3: Hyperbolic electrode geometry. The hyperbolic electrode geometry is used as a basis for comparing the linear microtrap. The characteristic dimension of the hyperbolic electrode geometry is the radius R_0 as shown.

therefore

$$\begin{aligned}
 \omega_{p,\text{hyp}} &= \frac{eV_0}{\sqrt{2}m\Omega_t R_0^2} \\
 &= \sqrt{\frac{eV_0 q}{4mR_0^2}}.
 \end{aligned} \tag{4.12}$$

4.3.3 Linear Microtrap Transverse Potential Analysis. The microtrap potential amplitude V_{LMT} is computed near the center of the trap. This potential is then decomposed as an infinite set of cylindrical harmonics [67]:

$$\begin{aligned}
 V_{\text{LMT}}(r, \theta') &= V_0 \left[\sum_{m=1}^{\infty} C_m (r/r_0)^m \cos(m\theta') \right. \\
 &\quad \left. + \sum_{n=1}^{\infty} S_n (r/r_0)^n \sin(n\theta') \right]
 \end{aligned} \tag{4.13}$$

where C_m and S_n are expansion coefficients and θ' is taken as the angle from the x' axis. The characteristic radius over which the potential is approximated by this expansion is r_0 .

The C_2 coefficient provides a comparison between the potential of the linear microtrap and the quadrupole potential of the hyperbolic electrode geometry of radius r_0 . Other nonzero coefficients in the expansion of Eq. 4.13 describe the anharmonic character of the microtrap potential. Symmetry considerations reduce the number of terms allowed in the expansion. Given the potential amplitude of $\pm V_0/2$ applied to opposite electrodes as shown in Fig. 4.2(a), the potential is antisymmetric along the lines $x = 0$ and $y = 0$ and symmetric in reflection about the origin leading to the only non-zero terms in Eq. 4.13 as $m = 2, 6, 10, \dots$ and $n = 4, 8, 12, \dots$

The expansion coefficients are calculated by numerically evaluating the LMT potential using finite element analysis or other appropriate numerical field simulators and calculating the overlap integrals within a circle of radius r_0 of the potential V_{LMT} with the cylindrical harmonics $(r/r_0)^m \cos(m\theta')$ and $(r/r_0)^n \sin(n\theta')$ [67].

A geometric efficiency factor η can be used to compare the microtrap potential with the quadrupole potential of the hyperbolic electrodes of comparable size. The size of the linear microtrap is given by the distance from the center of the trap to the nearest point on the tip of the electrodes $\ell_{\text{eff}} \equiv \sqrt{(a/2)^2 + (d/2)^2}$. Then, η is defined as the ratio of the quadrupole part of the potential generated by the LMT $V_{\text{LMT}}^{(2)}$ and a hyperbolic trap with $R_0 = \ell_{\text{eff}}$.

$$\eta = \frac{V_{\text{LMT}}^{(2)}}{V_{\text{hyp}}} = \frac{2C_2\ell_{\text{eff}}^2}{r_0^2}. \quad (4.14)$$

The quadrupole portion of the linear microtrap can therefore be written in a form differing from the hyperbolic electrode potential (Eq. 4.11) by only the geometric factor η .

$$V_{\text{LMT}}^{(2)}(x', y') = \frac{V_0\eta}{2\ell_{\text{eff}}^2} (x'^2 - y'^2) \quad (4.15)$$

The ponderomotive potential for the microtrap can then be evaluated using Eq. 4.8:

$$\psi_{\text{LMT}} = \frac{e^2 V_0^2 \eta^2}{4m\Omega_T^2 \ell_{\text{eff}}^4} (x^2 + y^2). \quad (4.16)$$

Finally, the effective secular frequency of an ion in the linear microtrap is only modified by the factor η from the form of the secular frequency in the trap due to the hyperbolic electrodes (Eq. 4.12). With this form of the secular frequency, one can compare the trap strength and performance of the linear microtrap.

$$\omega_{p,\text{LMT}} = \frac{eV_0\eta}{\sqrt{2}m\Omega_T\ell_{\text{eff}}^2} \quad (4.17)$$

The equipotential lines of the calculated ponderomotive potential are shown in Fig. 4.4 along with the potential magnitude indicated by a gray-scale. Note that, although the cantilever geometry does not have cylindrical symmetry, the pseudopotential is approximately circular within a distance on the order of one-eighth the tip-to-tip separation a as will be shown from the numerical results in Sec. 4.3.4 where C_2 is found to be the dominant term in the expansion at this distance from the center.

4.3.4 Finite Element Analysis Method. The class of finite element analysis solvers that is used here divides a two-dimensional space into a series of triangles to calculate the linear microtrap potential. The two-dimensional finite element analysis package in Matlab version 6.5 was used to calculate the RF potentials. The results were compared with the two-dimensional projection of potentials calculated using two different three-dimensional finite element analysis packages, Maxwell 3D from Ansoft, and Opera 3D from VectorFields, and found consistent. The field is approximated at each vertex on the triangles, then an interpolation is made within each element to calculate the field on an rectangular grid. Different trap configurations are analyzed using the method described above and the ratio η of the microtrap potential to

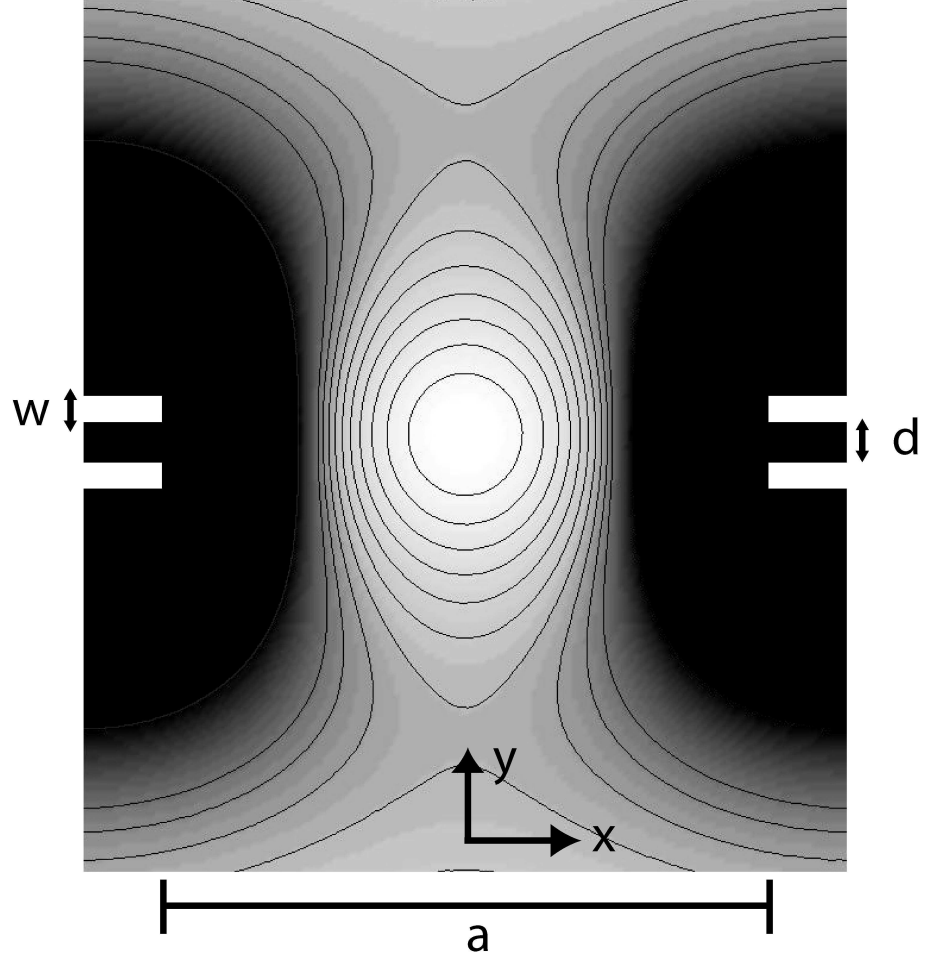


Figure 4.4: Transverse Equipotential Lines. Equipotential lines of the pseudopotential ψ_{LMT} in the $z = 0$ plane for aspect ratio $\alpha = 10$ and ratio of layer separation to layer thickness of $\delta = 1$. The ponderomotive potential reaches a maximum along the y axis near ℓ_{eff} . The contour lines are spaced on a linear scale and are shown to illustrate the circular nature of the ponderomotive potential at the center of the trap. The gray-scale shading is also on a linear scale.

the quadrupole hyperbolic potential is shown in Fig. 4.5 evaluated at a radius of $r_0 = a/8$. The uncertainty of the simulation data is less than 5% and is due primarily to a finite grid spacing and the finite bounding box size. The solid line in the figure is an analytic solution for cantilevers of infinitesimal thickness.

One can see that as the trap aspect ratio $\alpha = a/d$ increases, the geometric factor η approaches a constant, non-zero value. The asymptotic value can be evaluated using complex analysis techniques and is described in Appendix B. The result from Eq. B.10 for large α is $\eta = 1/\pi$. Additionally, as the aspect ratio approaches one, the trap becomes more like the hyperbolic electrode geometry. The other degree of freedom of the linear microtrap is the ratio of the layer separation to the layer thickness, $\delta = d/w$. Note that the strength of the microtrap decreases as the layer thickness decreases with respect to the layer separation.

The higher-order coefficients of the expansion shown in Eq. 4.13 for the potential V_{LMT} are shown in Fig. 4.6. The dominant higher-order term is S_4 , which, at a fixed radius of $r_0 = a/8$, is only a few percent of C_2 . The two next largest terms are also shown although the magnitude is small enough to be negligible when considering ion motion. The relationship between the C_2 and the next three largest terms of the expansion as a function of the aspect ratio α and δ is shown in Fig 4.6. Coefficients S_4 , C_6 appear to approach an asymptotic value as the trap aspect ratio increases. The ratios of all higher-order terms to the coefficient C_2 (C_m/C_2 and S_n/C_2) for $m, n > 6$ are less than 10^{-3} .

The absolute depth of the ponderomotive RF trap is also of interest when considering ion loading and collisions with background gas. The trap depth is defined as the maximum height of the ponderomotive potential barrier along the weak axis of the trap and is plotted in Fig. 4.7. A trap frequency of $\Omega_T/2\pi = 50\text{MHz}$ and the mass of

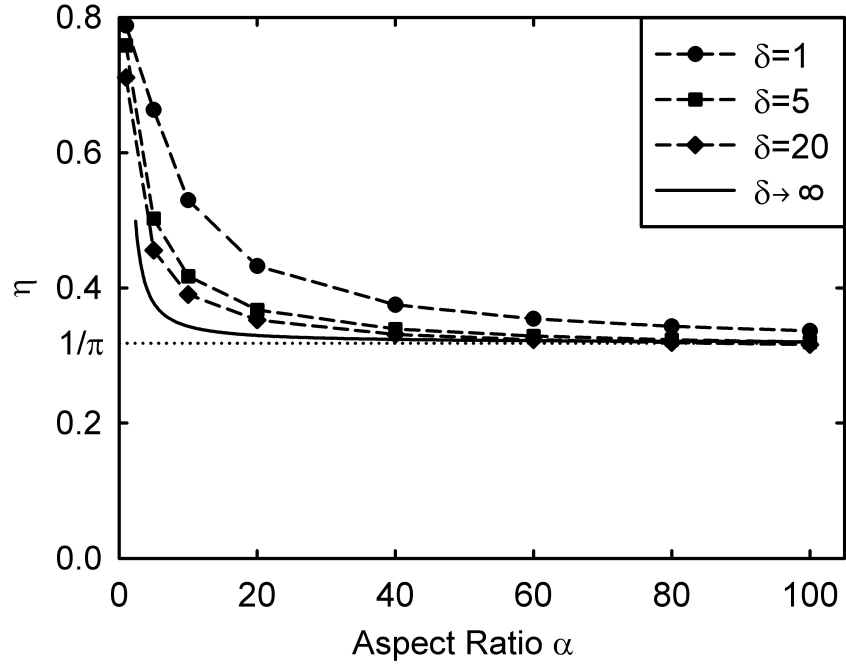


Figure 4.5: Transverse Geometric efficiency factor. The ponderomotive potential geometric efficiency factor η as a function of the ratio of the tip-to-tip separation to the layer separation: the aspect ratio α . The other degree of freedom is the ratio of the electrode separation to the layer thickness, $\delta = d/w$. The solid line is an analytic solution for η found using complex analysis techniques with $\delta \rightarrow \infty$ and is valid for $\alpha \gg 1$

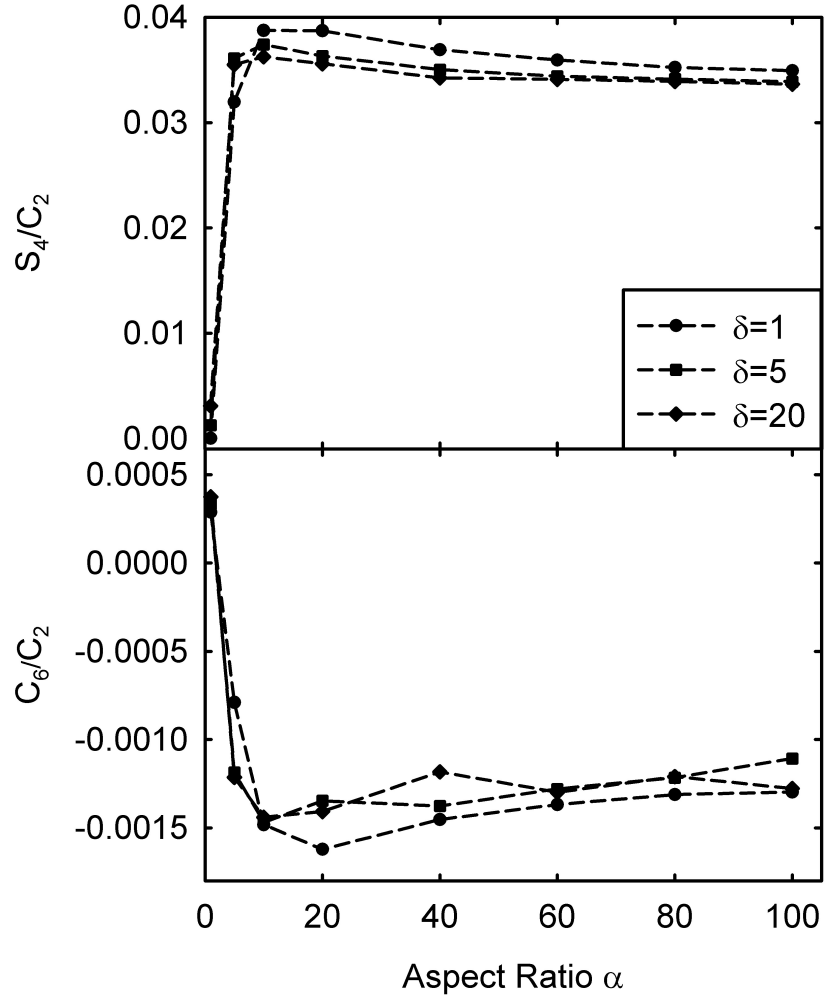


Figure 4.6: Higher-order expansion coefficients. The two largest higher-order terms of the expansion in Eq. 4.13 shown as a ratio over C_2 for various trap aspect ratios $\alpha = a/d$ and given as a function of the layer separation over the layer thickness $\delta = d/w$ evaluated at $r_0 = a/8$

$^{111}\text{Cd}^+$ were used to calculate the depth, given in scaled units of $[\text{K}\cdot\mu\text{m}^2/\text{V}^2]$. To find the depth of a specific trap, the data must be multiplied by the applied voltage V_0^2 in $[\text{V}^2]$ and divided by the square of the absolute tip-to-tip separation a^2 in $[\mu\text{m}^2]$. The depth asymptotically approaches a constant value of approximately $2400\text{K}\cdot\mu\text{m}^2/\text{V}^2$ for large cross-sectional aspect ratio as can be found from the analytic solution (Eq. B.13). The size of the ponderomotive trap r_{max} is characterized by either the distance of the maximum in the ponderomotive potential from the center of the trap or $a/2$, whichever is smaller. As the trap aspect ratio increases r_{max} is determined by the maximum in the RF pseudopotential along the y -axis and is approximately half the tip-to-tip electrode separation $0.5a$.

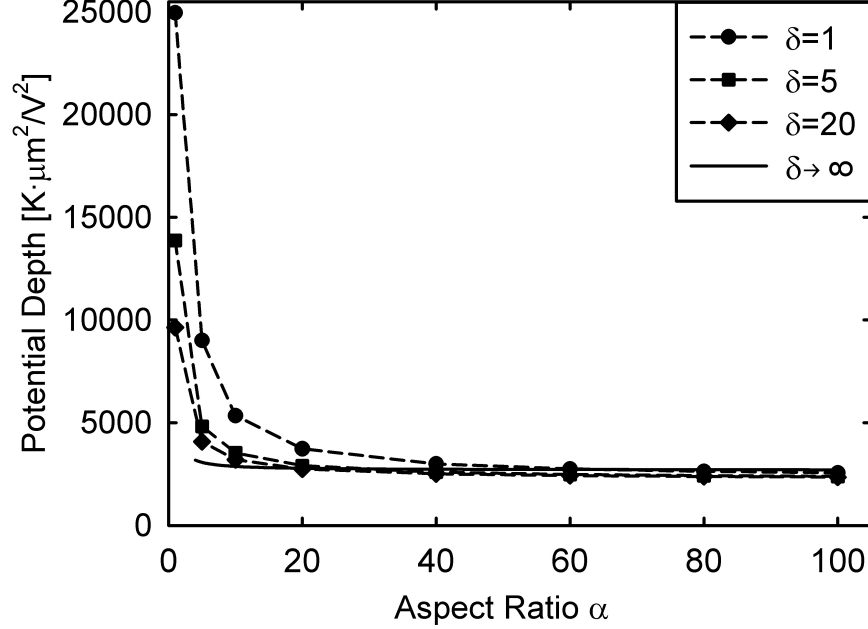


Figure 4.7: Scaled trap depth. The scaled trap depth as a function of the trap aspect ratio $\alpha = a/d$ and the ratio of layer separation to layer thickness $\delta = d/w$. The trap depth is scaled to the tip-to-tip separation a , in micrometers and to the applied voltage V_0 . The analytic result is shown as a solid line with $\delta \rightarrow \infty$ and is valid for $\alpha \gg 1$.

Since the ponderomotive potential within the region $r < r_{\text{max}}$ will trap ions, the

expansion of the potential from Eq. 4.13 within that entire area is also of interest. The expansion of the potential within a circle of radius $r_0 = r_{\max}$ contains a larger contribution from the higher-order coefficients than an expansion fixed at $r_0 = a/8$ as illustrated in Fig. 4.8. The higher-order coefficients for the expansion of the linear microtrap potential are shown in Fig. 4.9, evaluated at $r_0 = r_{\max}$.

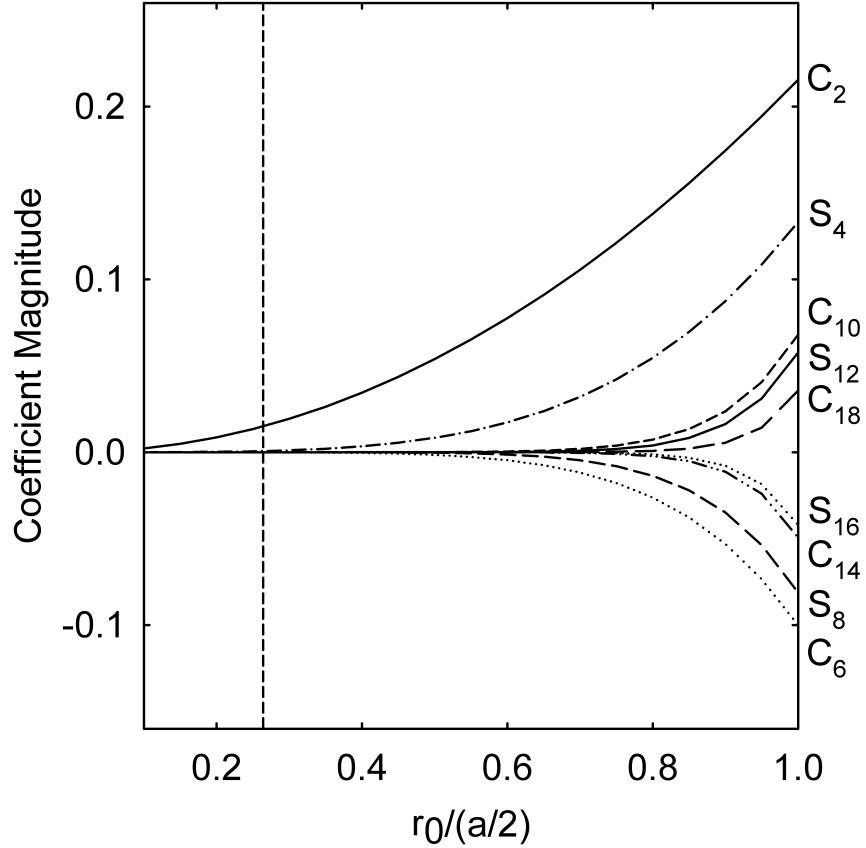


Figure 4.8: Higher-order coefficients as a function of trap radius. The dependence on the expansion coefficients C_m and S_n as a function of $r_0/(a/2)$. The higher order terms become significant as the overlap integrals cover more of the area between the electrodes. The geometry used was $\alpha = 20$ and $\delta = 1$, a worst case scenario from Fig. 4.9. The dashed vertical bar indicates $r_0 = a/8$.

4.3.5 Residual Axial Ponderomotive Potential. The previous analysis is based on the assumption that the linear microtrap electrodes are infinitely long in the z -dimension. However, the actual trap has finite electrode lengths, labeled b and c in Fig. 4.2(b), which together with the small electrode gaps (labeled g in Fig. 4.2) lead

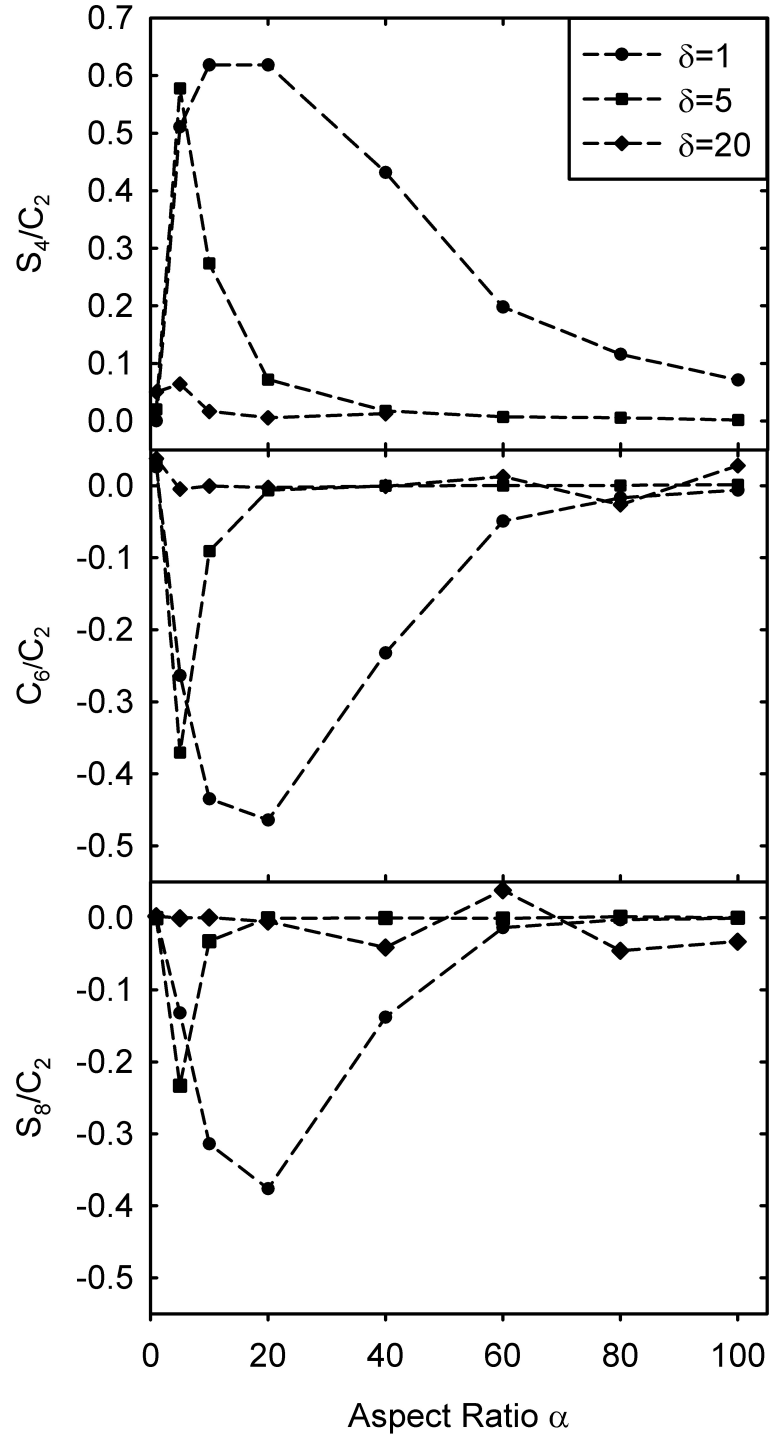


Figure 4.9: Largest higher-order coefficients as a function of α . The three largest higher-order terms of the expansion in Eq. 4.13 evaluated within a radius $r_0 = r_{\max}$, where r_{\max} is the maximum of the ponderomotive potential. The coefficients are shown as a percentage of the largest term C_2 for various trap aspect ratios $\alpha = a/d$ and given as a function of the layer separation over the layer thickness $\delta = d/w$ with an error of 5%.

to a small ponderomotive potential in the z direction. The magnitude of this axial ponderomotive potential can be compared to the transverse ponderomotive potential ψ_{LMT} of Eq. 4.16. To find the axial contribution, the entire three-dimensional RF potential $V_{\text{LMT}}(x, y, z)$ must be computed. Once found, one can use the ponderomotive potential approximation Eq. 4.8 to calculate the trap frequency along the z -axis.

The gradient of the three-dimensional potential is found, then the pseudopotential is evaluated. A Taylor expansion of the pseudopotential along the z axis (about $z = 0$) gives the coefficient for the harmonic z^2 term in the ponderomotive potential:

$$H_z = \frac{1}{2} \frac{\partial^2}{\partial z^2} (|\nabla V_{\text{LMT}}(x, y, z)|^2). \quad (4.18)$$

The details of the three-dimensional potential calculation are given below, but the method is similar to the two-dimensional finite difference analysis. Typically the data is extracted along the z axis and then fit to a quadratic polynomial to find the coefficient H_z . This coefficient allows one to make a comparison between the quadrupole trapping pseudopotential in the $z = 0$ cross-sectional plane, and the ponderomotive potential along the z -axis. This three-dimensional ponderomotive potential is similar to the transverse potential of Eq. 4.16 with the addition of the z^2 term.

$$\psi_{\text{LMT}}(x, y, z) = \frac{e^2 V_0^2 \eta^2}{4m\Omega_T^2 \ell_{\text{eff}}^4} (x^2 + y^2 + \sigma_z z^2), \quad (4.19)$$

where $\sigma_z = H_z \ell_{\text{eff}}^4 / \eta^2$ is the ratio of the residual axial to transverse ponderomotive potential. The resulting frequency along the z -axis is $\omega_z = \sqrt{\sigma_z} \omega_{p, \text{LMT}}$.

The results from the numerical simulation in Fig. 4.10 are given for a cross-sectional aspect ratio of $\alpha = 20$ and for $\delta = 1$ (ratio of the layer separation to the layer width). The ponderomotive potential along the z -axis is shown in Fig. 4.11 to illustrate the degree to which the notch gap g contributes to the residual potential at

the center of the trap. Since $\sigma_z \ll 1$, the ponderomotive contribution to the potential along the z -axis can be neglected.

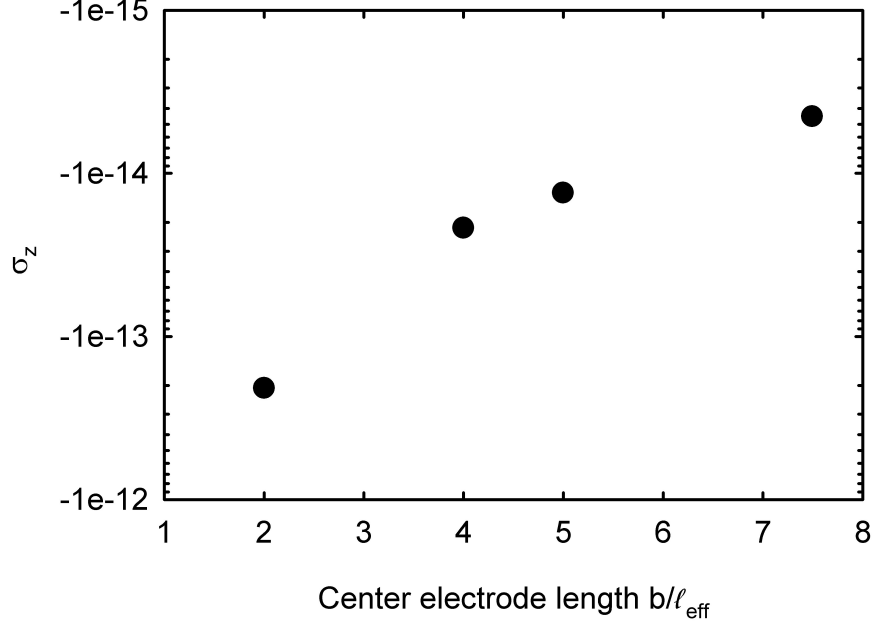


Figure 4.10: Residual axial ponderomotive potential. The ratio of the residual axial frequency to the transverse ponderomotive frequency σ_z as a function of the center electrode length. The end-cap electrodes were fixed at $5\ell_{\text{eff}}$ with a fixed gap spacing of $1/10\ell_{\text{eff}}$, $\alpha = 20$, and $\delta = 1$.

4.4 Static Potentials

4.4.1 Hyperbolic Geometry. Like the two-dimensional potential in Sec. 4.3.2, the static potential used to confine the ions along the z -axis in the linear microtrap can be compared to a three-dimensional idealized hyperbolic electrode potential. Figure 4.12 shows an elliptical hyperbolic electrode geometry where x_0 , y_0 , and z_0 are the distances along the principal axes of the ellipse from the center of the trap to the electrodes. The potential within the electrodes, up to a constant term, is

$$U_{\text{hyp}} = \frac{U_0}{s^2} (-\epsilon x^2 - (1 - \epsilon)y^2 + z^2) \quad (4.20)$$

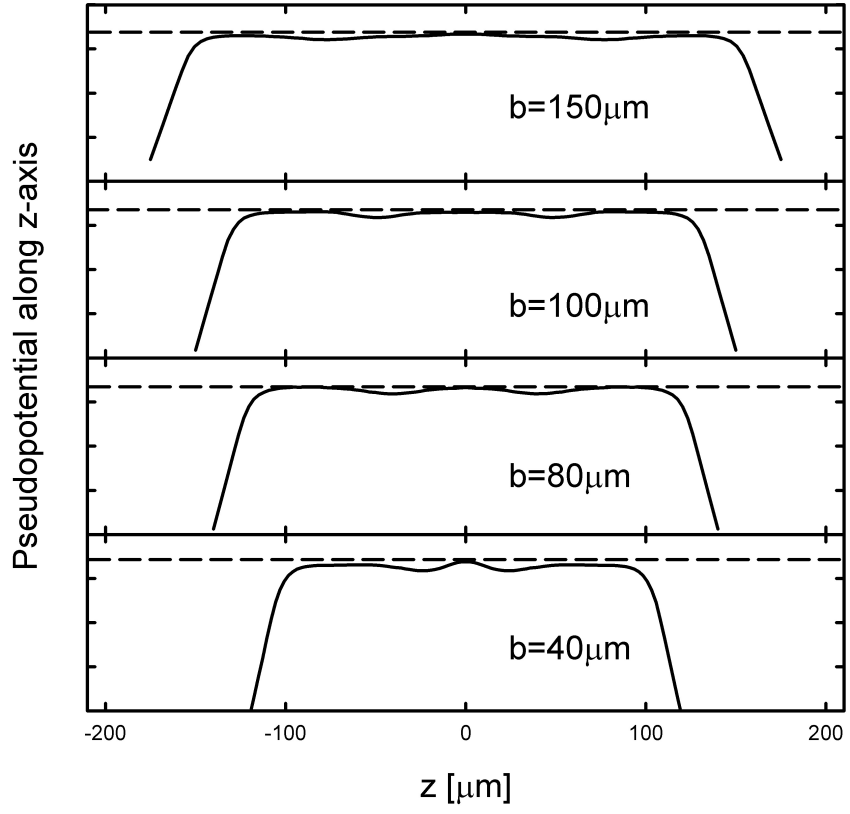


Figure 4.11: Residual ponderomotive potential for different center electrode lengths. Illustration of the change in the residual axial ponderomotive potential for various center electrode lengths (b). The potential along the z -axis is shown for various center electrode lengths where the end-cap electrodes have been fixed at $100 \mu\text{m}$.

where $s^2 = z_0^2 + \epsilon x_0^2$ and $\epsilon x_0^2 = (1 - \epsilon)y_0^2$. The geometric anisotropy factor ϵ is related to the eccentricity of various conic sections that can be superimposed on the three-dimensional hyperbolic electrode structure. The special case where $\epsilon = 1/2$ corresponds to circular symmetry in the xy plane. For values of $0 < \epsilon < 1$ and $U_0 > 0$, the potential is trapping in z and anti-trapping in the xy plane, as shown in the figure for $\epsilon = 0.86$. Outside of that range, the axes in the figure must be rotated to describe the potential of Eq. 4.20. When $\epsilon > 1$ and $U_0 > 0$, the potential is trapping in the zy plane and anti-trapping in x ; and for $\epsilon < 0$ and $U_0 > 0$, the potential is trapping in z and x , but anti-trapping in y . Whereas, at $\epsilon = 0$ and $\epsilon = 1$, the potential is independent of x and y respectively. The frequency along the z -axis is

$$\omega_{z,\text{hyp}} \equiv \sqrt{\frac{2eU_0}{ms^2}}. \quad (4.21)$$

The frequencies along the x and y axis are discussed in connection with the net linear microtrap potential below.

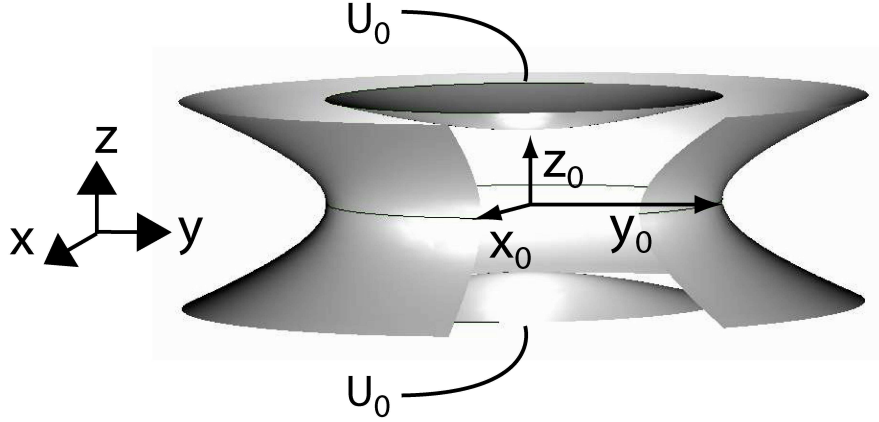


Figure 4.12: Three-dimensional hyperbolic electrodes are shown here. The electrodes along the z -axis are held at a voltage of U_0 , while the center electrode is grounded. The potential has an elliptical cross-section in the xy plane corresponding to $\epsilon = 0.86$ and, for $U_0 > 0$, is trapping along the z -axis, but anti-trapping along x and y , valid for $0 < \epsilon < 1$.

4.4.2 Linear Microtrap Static Potential Analysis. The static potential is computed using a three-dimensional finite element solver. The distance from the center of the

trap to the bounding box that was used in the simulation was more than twice the tip-to-tip cantilever separation. To reduce the error in the simulation results, several different grids were used and the results were averaged.

It is possible to approximate the three-dimensional static potential of the linear microtrap, $U_{\text{LMT}}(x, y, z)$ by doing a Taylor expansion about the center of the trap. Because equal voltages are applied to all capping electrodes as shown in Fig. 4.2(b), the cross-terms in the Taylor expansion are zero. The coefficients of the harmonic terms are:

$$D_x = \frac{1}{U_0} \frac{\partial^2 U_{\text{LMT}}}{\partial x^2}(0, 0, 0) \quad (4.22)$$

$$D_y = \frac{1}{U_0} \frac{\partial^2 U_{\text{LMT}}}{\partial y^2}(0, 0, 0) \quad (4.23)$$

$$D_z = \frac{1}{U_0} \frac{\partial^2 U_{\text{LMT}}}{\partial z^2}(0, 0, 0) \quad (4.24)$$

The derivatives are then evaluated numerically on the calculated potential along the axes. The potential is therefore

$$\begin{aligned} U_{\text{LMT}} &\approx \frac{U_0}{2} (D_x x^2 + D_y y^2 + D_z z^2) \\ &= \frac{U_0 D_z}{2} \left(\frac{D_x}{D_z} x^2 + \frac{D_y}{D_z} y^2 + z^2 \right) \end{aligned} \quad (4.25)$$

A static potential geometric efficiency factor κ compares the static potential of the linear microtrap with the hyperbolic electrode geometry of similar characteristic dimension. The characteristic dimension of the linear microtrap that corresponds to the distance s in the hyperbolic electrode geometry is the distance from the center of the trap to the nearest point on the end-cap electrodes: $d_{\text{eff}} = \sqrt{\ell_{\text{eff}}^2 + (b/2 + g)^2}$.

$$\kappa \equiv D_z d_{\text{eff}}^2 / 2 \quad (4.26)$$

The static potential in the linear microtrap can then be written in the same form

as the potential in the hyperbolic electrode geometry.

$$U_{\text{LMT}} = \frac{U_0 \kappa}{d_{\text{eff}}^2} (-\epsilon x^2 - (1 - \epsilon)y^2 + z^2) \quad (4.27)$$

where $\epsilon = -D_x/D_z = 1 + D_y/D_z$. Given this approximation of the electrostatic potential in the linear microtrap, the form of the trap frequency along the z -axis is similar to that of the hyperbolic electrodes (Eq. 4.21) with the difference being only the static potential geometric efficiency factor κ

$$\omega_{z,\text{LMT}} = \sqrt{\frac{2\kappa e U_0}{m d_{\text{eff}}^2}}. \quad (4.28)$$

The results characterizing the linear microtrap for κ and ϵ from the numerical simulations are shown in Fig. 4.13.

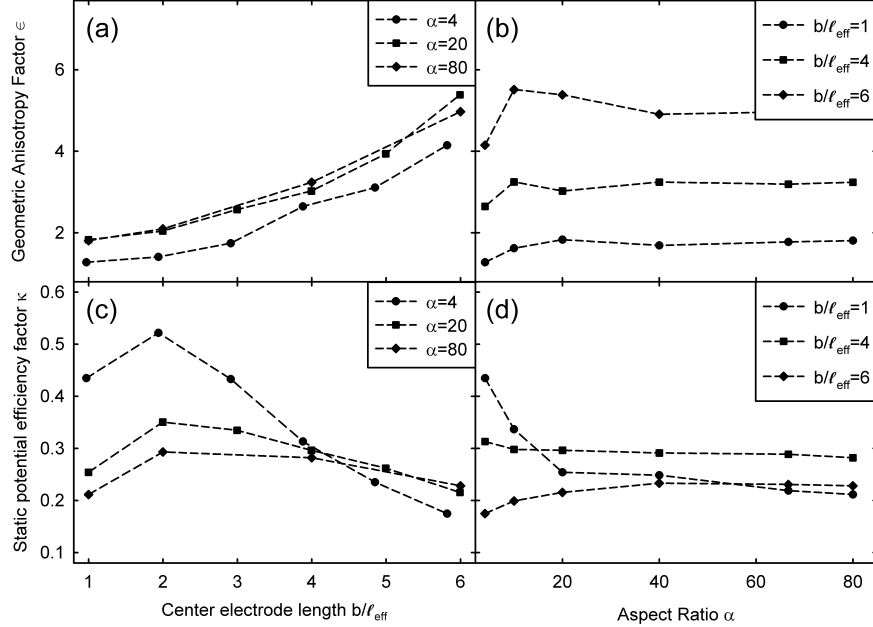


Figure 4.13: Static potential numerical results in the linear microtrap. The results for the three-dimensional numerical simulations of the static potential in the linear microtrap. Both the anisotropy factor ϵ and the static potential geometric efficiency factor κ are shown. The ratio of the layer separation over the layer width was fixed at one and the gap separation at two ($g=2$ from Fig. 4.2(b)).

4.5 Net Potential

The combined static and ponderomotive potentials that determine the motion of a ion in the linear microtrap are written as a three-dimensional uncoupled harmonic oscillator potential:

$$\begin{aligned}
\phi_{\text{LMT}} &= \psi_{\text{LMT}} + U_{\text{LMT}} \\
&= \frac{e^2 V_0^2 \eta^2}{4m^2 \Omega_T^2 \ell_{\text{eff}}^4} (x^2 + y^2) \\
&\quad + \frac{\kappa U_0}{d_{\text{eff}}^2} (-\epsilon x^2 - (1 - \epsilon)y^2 + z^2)
\end{aligned} \tag{4.29}$$

where the residual axial ponderomotive potential has been neglected. Considering this full potential, the effective trapping frequencies consist of the quadrature sum of the ponderomotive and the static frequencies.

$$\omega_{x,\text{LMT}} = \sqrt{\omega_{p,\text{LMT}}^2 - \epsilon \omega_{z,\text{LMT}}^2} \tag{4.30}$$

$$\begin{aligned}
&= \sqrt{\frac{e^2 V_0^2 \eta^2}{2m^2 \Omega_T^2 \ell_{\text{eff}}^4} - \frac{2\epsilon \kappa e U_0}{m d_{\text{eff}}^2}} \\
\omega_{y,\text{LMT}} &= \sqrt{\omega_{p,\text{LMT}}^2 - (1 - \epsilon) \omega_{z,\text{LMT}}^2}
\end{aligned} \tag{4.31}$$

$$\begin{aligned}
&= \sqrt{\frac{e^2 V_0^2 \eta^2}{2m^2 \Omega_T^2 \ell_{\text{eff}}^4} - \frac{2(1 - \epsilon) \kappa e U_0}{m d_{\text{eff}}^2}} \\
\omega_{z,\text{LMT}} &= \sqrt{\frac{2\kappa e U_0}{m d_{\text{eff}}^2}}
\end{aligned} \tag{4.32}$$

Table 4.1 provides a few examples of the calculation of the total trap frequencies given a specific geometry. The mass of the ion used in calculating the frequencies was ^{111}Cd with an RF frequency of $\Omega_T/2\pi = 50\text{MHz}$. The values for η , ϵ , and κ were taken from Figs. 4.5 and 4.13.

a=40 μm d=10 μm w=10 μm b=100 μm	$\alpha = 4$ $\delta = 1$ $\ell_{\text{eff}} = 21\mu\text{m}$ $d_{\text{eff}} = 59\mu\text{m}$	$\eta = 0.7$ $\epsilon = 3$ $\kappa = 0.3$	$V_0 = 40\text{V}$ $U_0 = 20\text{V}$ $\omega_{p,\text{LMT}}/2\pi = 20\text{MHz}$ $\omega_{z,\text{LMT}}/2\pi = 8.7\text{MHz}$	$\omega_{x,\text{LMT}}/2\pi = 13\text{MHz}$ $\omega_{y,\text{LMT}}/2\pi = 23\text{MHz}$ $\omega_{z,\text{LMT}}/2\pi = 8.7\text{MHz}$
a=40 μm d=2 μm w=2 μm b=100 μm	$\alpha = 20$ $\delta = 1$ $\ell_{\text{eff}} = 20\mu\text{m}$ $d_{\text{eff}} = 58\mu\text{m}$	$\eta = 0.43$ $\epsilon = 3.5$ $\kappa = 0.26$	$V_0 = 20\text{V}$ $U_0 = 1\text{V}$ $\omega_{p,\text{LMT}}/2\pi = 6.7\text{MHz}$ $\omega_{z,\text{LMT}}/2\pi = 1.8\text{MHz}$	$\omega_{x,\text{LMT}}/2\pi = 5.8\text{MHz}$ $\omega_{y,\text{LMT}}/2\pi = 7.3\text{MHz}$ $\omega_{z,\text{LMT}}/2\pi = 1.8\text{MHz}$
a=80 μm d=2 μm w=2 μm b=160 μm	$\alpha = 40$ $\delta = 1$ $\ell_{\text{eff}} = 40\mu\text{m}$ $d_{\text{eff}} = 89\mu\text{m}$	$\eta = 0.38$ $\epsilon = 3.2$ $\kappa = 0.28$	$V_0 = 35\text{V}$ $U_0 = 0.9\text{V}$ $\omega_{p,\text{LMT}}/2\pi = 2.6\text{MHz}$ $\omega_{z,\text{LMT}}/2\pi = 1.2\text{MHz}$	$\omega_{x,\text{LMT}}/2\pi = 1.5\text{MHz}$ $\omega_{y,\text{LMT}}/2\pi = 3.2\text{MHz}$ $\omega_{z,\text{LMT}}/2\pi = 1.2\text{MHz}$

Table 4.1: Sample calculations for trap performance. A trap frequency of $\Omega_T/2\pi = 50\text{MHz}$ was assumed for a ^{111}Cd ion.

4.6 Microtrap Principal Axes

Principal axes are the axes along which it is possible to describe the motion of an ion in the total potential as a three-dimensional uncoupled harmonic oscillator. This means that the motion of the ion along each axis is independent of the other two spatial coordinates. The equations of motion for an uncoupled harmonic oscillator are

$$\ddot{x} = -\omega_x^2 x, \text{ etc.} \quad (4.33)$$

An uncoupled harmonic oscillator corresponds to a potential with symmetries along the principal axes. Since the RF ponderomotive potential (Eq. 4.16) is radially symmetric, the principal axes of a linear ion trap are determined by the static potential. The principal axes of an ion trap are of concern when considering laser cooling an ion in the trap. Laser cooling along all three dimensions of motion is possible only if the laser wave vector \vec{k}_{laser} has a vector component along all three principal axes. The symmetry of the microtrap is such that the z -axis is a principal axis, therefore, the axes of concern are in the xy plane. It is possible to rotate the principal axes by applying different static voltages to the electrodes, which give rise to an xy cross-term in the static potential.

To find the new principal axes, one can rotate the coordinate system via Eq. 4.34.

$$\begin{aligned} x &= x' \cos \theta + y' \sin \theta \\ y &= -x' \sin \theta + y' \cos \theta \end{aligned} \quad (4.34)$$

This rotation can be applied to the potential with an xy cross-term of magnitude λ

$$U'_{\text{LMT}} = \frac{\kappa^2 U_0}{d_{\text{eff}}^2} (-\epsilon x^2 - (1 - \epsilon) y^2 + \lambda xy + z^2) \quad (4.35)$$

to find an angle at which the cross term in the rotated coordinate system ($\lambda' x' y'$)

vanishes. This new coordinate system, rotated about the z -axis by an angle θ , now determines the principal axes of the trap. The angle at which the cross-term vanishes is found as a function of the coefficient of the cross-term λ and the geometric factor ϵ .

$$\tan(2\theta) = \frac{\lambda}{2\epsilon - 1} \quad (4.36)$$

The static axial potential can then be written in an uncoupled form, showing explicitly the new principal axes x' and y' .

$$U'_{\text{LMT}} = \frac{\kappa^2 U_0}{d_{\text{eff}}^2} (-\epsilon' x'^2 - (1 - \epsilon') y'^2 + z^2) \quad (4.37)$$

where $\epsilon' = \epsilon \cos(2\theta) + \frac{\lambda}{2} \sin(2\theta) + \sin^2 \theta$.

A simple point charge potential model can be used to provide a qualitative idea of how the principal axes may be rotated. Twelve charges are fixed at the corners of three rectangles as shown in Fig. 4.14(a). The positions of eight charges of value $+q$ are at $(\pm a/2, \pm d/2, \pm b)$ and an additional four with charge $-q$ at $(\pm a/2, \pm d/2, 0)$. A Taylor expansion of the point charge potential where $b \gg a, d$ can be written as

$$U_{\text{point}} = \frac{U_0}{r_0^2} (-\epsilon x^2 - (1 - \epsilon) y^2 + z^2) \quad (4.38)$$

where $U_0 = 2q/(4\pi\epsilon_0 r_0)$, $r_0 = \sqrt{(a/2)^2 + (d/2)^2}$, and $\epsilon = (2a^2 - d^2)/(a^2 + d^2)$. If two charges are increased from q to q' on either end-cap as in Fig. 4.14(b), the principal axes are rotated. Alternatively, one could increase the negative charge on two of the four point charges in the $z = 0$ plane. This would correspond to applying a negative static potential to two of the center electrodes in the linear microtrap and is more effective at rotating the principal axes. The potential in the point charge model, with the addition of these modified charges, becomes

$$U_{\text{point}} = \frac{2(q + q')}{(4\pi\epsilon_0)r_0^3} (-\epsilon x^2 - (1 - \epsilon) y^2 + \lambda xy + z^2) \quad (4.39)$$

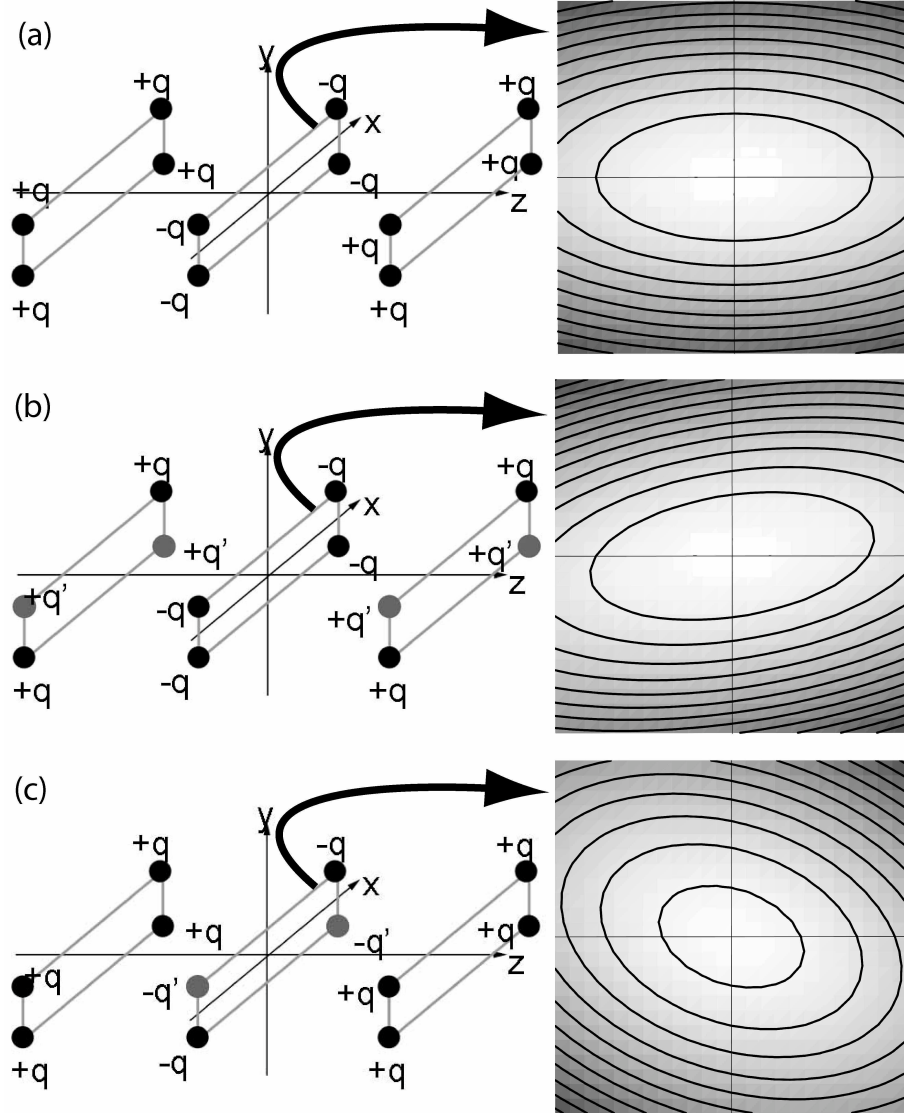


Figure 4.14: Charge model for principal axis rotation. (a) Unrotated static 12 point charge potential, shown as cross section in the $z = 0$ plane. (b) By changing the charge on four of the eight end-cap points, the principal axes rotate. (c) The same result can be achieved by applying additional negative charge to the center electrodes. The aspect ratio of $\alpha = 4/3$ was used to illustrate the rotation of the axes of symmetry of the potential.

where now, the xy cross term has a coefficient

$$\lambda = 6 \frac{q - q'}{q + q'} \frac{ad}{a^2 + d^2} \quad (4.40)$$

Substituting Eq. 4.40 into the condition for the rotation angle (Eq. 4.36), and using the explicit form for ϵ in the point charge model, the rotation angle can be expressed as a function of the applied charges and the trap aspect ratio ($\alpha = a/d$, the tip-to-tip cantilever separation over the layer spacing).

$$\tan 2\theta = \frac{1 - q'/q}{1 + q'/q} \frac{2\alpha}{\alpha^2 - 1} \quad (4.41)$$

There are several features of this model that give a qualitative understanding of the rotation of the principal axes. First, for a given trap aspect ratio α , by increasing the ratio of charges, one can rotate the principal axes a fixed amount. However, as the aspect ratio increases, the amount of rotation that can be given the principal axes by changing the charge ratio is decreased, eventually approaching zero.

The principal axes rotation in the xy plane for the linear microtrap as a function of the applied voltage on two diagonally opposing center electrodes is shown in Fig. 4.15. The aspect ratio was fixed at $\alpha = 20$ and $\delta = 1$. The other two center electrodes were held at static ground with all eight end-cap electrodes at $U_0 = 1V$. As discussed above, by applying small voltages to the appropriate center electrodes, it is possible to rotate the principal axes so that laser cooling is effective.

4.7 Future Research

A new design for a microfabricated linear ion trap has been discussed. Calculations of the RF ponderomotive potential have shown a surprising degree of isotropy near the center of the trap, even for very high aspect ratios. For high transverse electrode aspect ratios, the trap strength approaches $1/\pi$ times that of a comparable

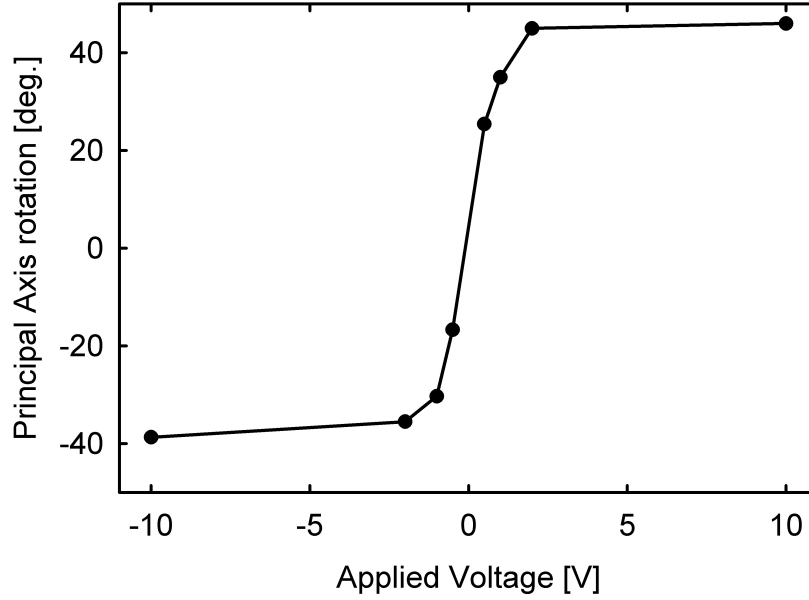


Figure 4.15: Microtrap principal axis rotation. The principal axis rotation from the xy axis shown in Fig. 4.2(a) as a function of the applied voltage on two diagonally opposing center electrodes. The other center electrodes were held at static ground with the end-cap voltages fixed at $U_0 = 1\text{V}$. The trap dimensions are $a = 40\mu\text{m}$, $d = 2\mu\text{m}$, $w=2\mu\text{m}$, with all electrodes having a width of $100\mu\text{m}$.

hyperbolic electrode structure. This may be of importance in the design of microtraps in applications such as Cavity QED [68] and miniature mass spectrometers where conventional ion trap designs can not be used. Geometric scaling factors for the linear microtrap provide an easy comparison between these new trap designs and conventional ion traps, facilitating implementation in future experiments.

Further investigations will require actual fabrication and experimentation with this new type of trap and include an investigation of the patch potentials on the surfaces of the doped semiconductors, the limiting electric field, and laser scatter from the small aperture. These factors are all technical in nature and should not prohibit the future implementation of this novel linear microtrap design. The actual fabrication and performance of the GaAs trap is discussed in Section 5.2.

CHAPTER V

Trap Fabrication

There are many different geometries and configurations that can be used to trap ions that range from a simple asymmetrical ring-and-fork trap to a complicated gold-plated laser machined alumina substrate. In this Chapter, the fabrication and assembly of the linear gold-plated alumina trap is detailed. The fabrication of the first monolithic semiconductor ion trap based on conventional GaAs MEMS technology is also discussed.

The gold-plated alumina linear trap described in this Chapter has been used extensively in quantum information experiments [69, 70, 21, 71, 72, 73]. In addition, the novel three-layer design and fabrication technology was extended to the first two-dimensional array of ion traps, including the first example of shuttling an ion around a corner [74]. The GaAs trap was also successfully loaded, with details reported in Ref. [33].

5.1 Gold-plated Alumina Linear Trap

The first of the two traps discussed in this Chapter is based on a two-layer design used at NIST in earlier experiments [13, 75]. This design, however, uses three layers of electrodes, allowing for three-dimensional compensation of stray electric fields for the minimization of excess micromotion (see Section 2.3). In addition, the use of

a single layer for the rf electrode allows the geometry to be extended into more complicated junctions [74].

5.1.1 Electrode Layout All linear traps can be modeled with the simple geometry of the basic linear rf trap [62]. Four parallel rods are placed on the corners of a rectangle such that, when the right rf voltages are applied, they provide trapping ponderomotive potentials in the transverse plane (transverse to the length of the rods). To trap the ions along the length of the rods (the axial direction), static voltages are applied to end-cap electrodes of one type or another. A simple schematic drawing of a linear trap is shown in Fig. 5.1.

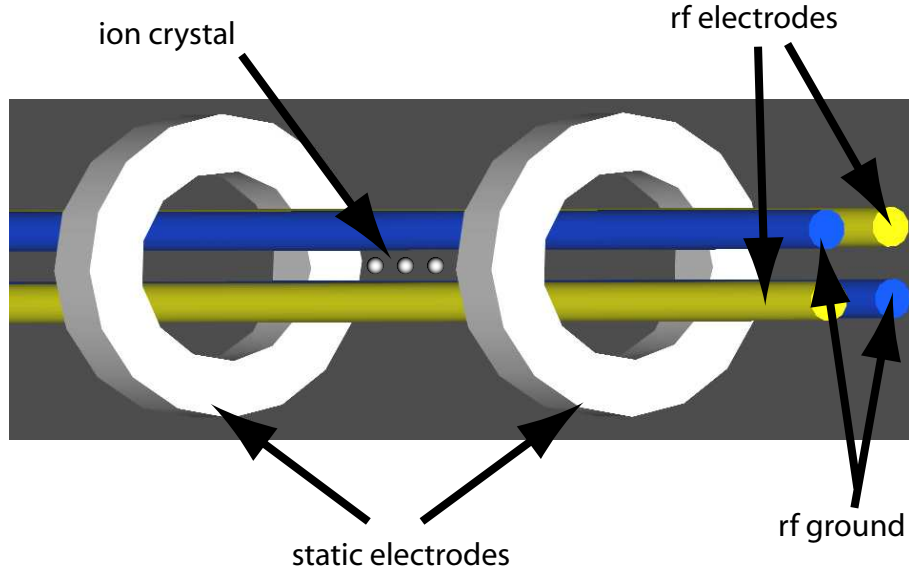


Figure 5.1: Four rod linear trap illustration. An illustration of a four rod linear trap. Shown are the rf electrodes and the static electrodes needed for three-dimensional confinement of ions.

The gold plated alumina trap is a variation of a linear trap where the rf ground electrodes have been split into two pieces and separated by the width of the trap. The result looks like six rods set in two planes. Two different substrate thicknesses were used as well as two spacer layers to electrically isolate the gold electrodes, creating a seven-layer stack of ceramic substrates. The top and bottom substrates were used for the static axial confinement electrodes and were 254 microns (10 mils) thick. They

were separated from the rf layer by alumina substrates where the rf layer and the spacer layers were both 125 microns (5 mils) thick. The stack thus was assembled with: a static electrode layer, a spacer layer, the rf layer, then a second spacer and finally a static electrode layer. Each substrate had 4 assembly holes drilled in it that were aligned in the final assembly with steel dowel pins, 1 mm diameter, 6 mm long. A fifth hole was originally cut to serve as an alignment pin, but it was discovered that alignment was easier if that pin was left out. The entire stack was held together with thick alumina mount bars. The mount bars had blind holes drilled in them to match the assembly holes of the substrates. The stack was placed on the dowel pins on top of one of the mount bars. The other bar was placed on top of the stack and the entire assembly was held together with four screws (4-40 thread) with spring lock washers to provide even compression. The complete assembly is drawn in Fig. 5.2 and shown in a photo in Fig. 5.3.

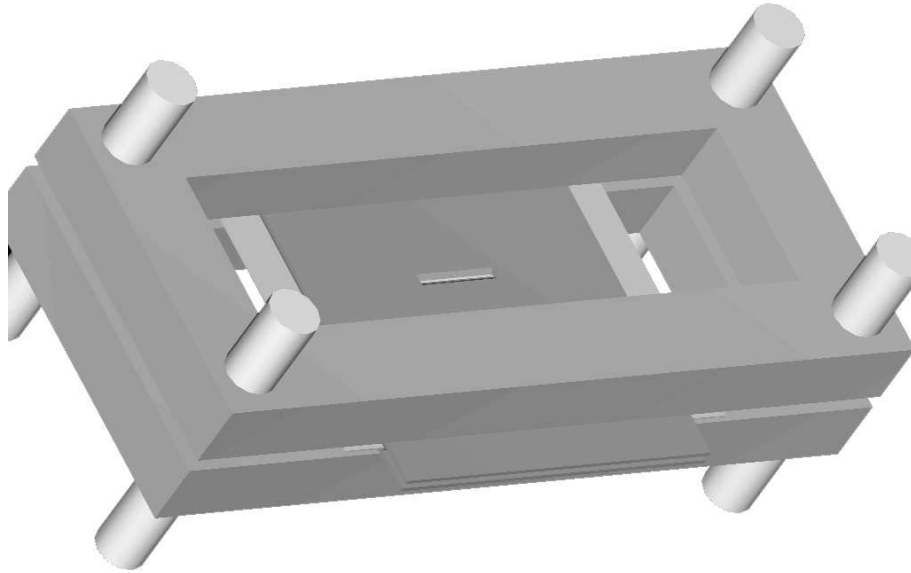


Figure 5.2: Ceramic linear trap design. The design for the assembly of the linear trap. Shown are the 7 layer substrate stack, the two mount bars and the four screws used to clamp the mount bars down onto the stack.

The transverse plane of the trap is illustrated in Fig. 5.4. The static electrode

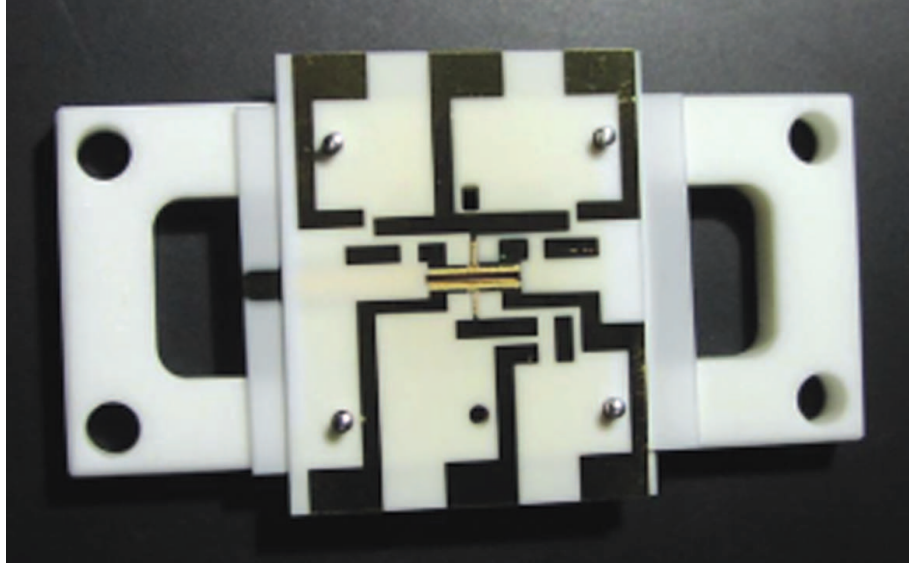


Figure 5.3: Assembled ceramic trap photo. A picture of the gold plated alumina linear trap assembly. The dark regions are the gold plated electrodes on the alumina substrates.

layers act as the rf grounding planes as well as providing the axial confinement potential and the static compensation voltages for minimizing micromotion. There is no potential applied to the spacer layer- it only separates and electrically isolates the rf layer from the static electrode layers.

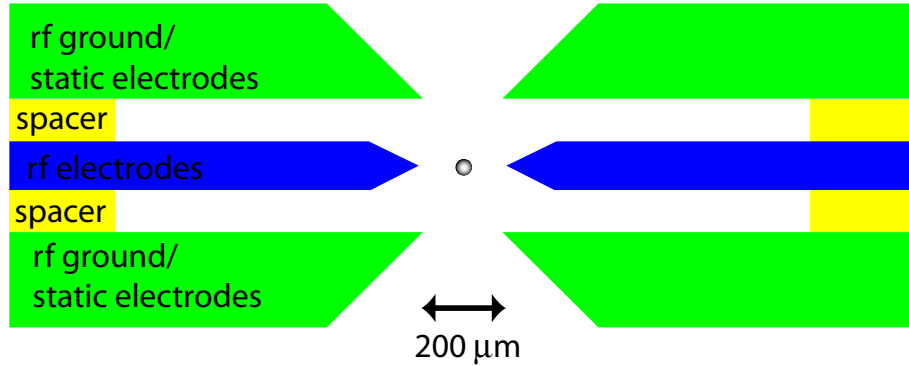


Figure 5.4: Transverse illustration of ceramic trap. The transverse diagram of the gold plated alumina trap. The gap distance shown is $200\ \mu\text{m}$. The thickness of the rf and spacer layers is $125\ \mu\text{m}$ and the thickness of the static electrode layers is $250\ \mu\text{m}$. The chamfer angles on all layers is 45 degrees.

5.1.2 Alumina Substrate Fabrication These alumina substrates were purchased from CoorsTek ceramics company polished on both sides and dimensioned as discussed

below. The laser machining was done by a company called Resonetics. The outer dimensions of the substrates are not critical; a large dimension of 25 mm and a smaller dimension of 20 mm was used to give enough room on the substrate for the gold patterning and the on-board filtering electronics. The static electrode substrate and the rf substrate were cut so that they overlap with their long dimensions not in the same direction. The spacer layer was cut 20 mm by 20 mm to fit between the static and rf layers without protruding.

A central gap, 5 mm long and nominal width $200\text{ }\mu\text{m}$ was cut in the static electrode for the trapping region. The static electrode layers, shown in Fig. 5.5(a,d), had four slits cut perpendicular to the trap gap, used to ensure electrical isolation between the center electrodes and the end electrodes. The slits were cut so that there is a $375\text{ }\mu\text{m}$ long center electrode. The slit width was $25\text{ }\mu\text{m}$ and the length was a total of 1.9 mm from the edge of the substrate to the back of the slit. The edges along the trap gap of the static electrode substrates were chamfered at 45 degrees from the outside of the trap structure, giving length of the chamfered part is $250\text{ }\mu\text{m}$. However, the laser machining of the substrates typically left a rough edge at the tip of the chamfer. To smooth this rough edge, the center edge was cut vertically, leaving a $20\text{ }\mu\text{m}$ high vertical drop at the tip. A SEM photo of the tip is shown in Fig. 5.6 that shows this edge.

The spacer layers (see Fig. 5.5(c)) had a rectangle 9 mm by 10 mm cut out of the center to isolate the trap from the insulating surfaces. The c-cut is 3 mm wide and was cut to prevent rf shorts going through the spacer substrate. This effectively isolated the gold patterning on the rf electrode from any direct path through material to the gold patterning on the static electrodes.

The rf layer (Fig. 5.5(b,e)) had a similar 5 mm long gap cut in the middle. The

chamfer on this substrate was cut from both sides to a length of only $62\text{ }\mu\text{m}$, leaving a nominal gap width from tip to tip of $200\text{ }\mu\text{m}$. This chamfer also has a vertical edge, about $20\text{ }\mu\text{m}$ thick cut at the end to clean up the edges from the laser machining. In order for the laser machining to be aligned properly, two $75\text{ }\mu\text{m}$ diameter holes were drilled in the ceramic substrates along the center of the gap, 1 mm from the edge of the gap length. These holes were used for aligning the machine for the chamfered cuts.

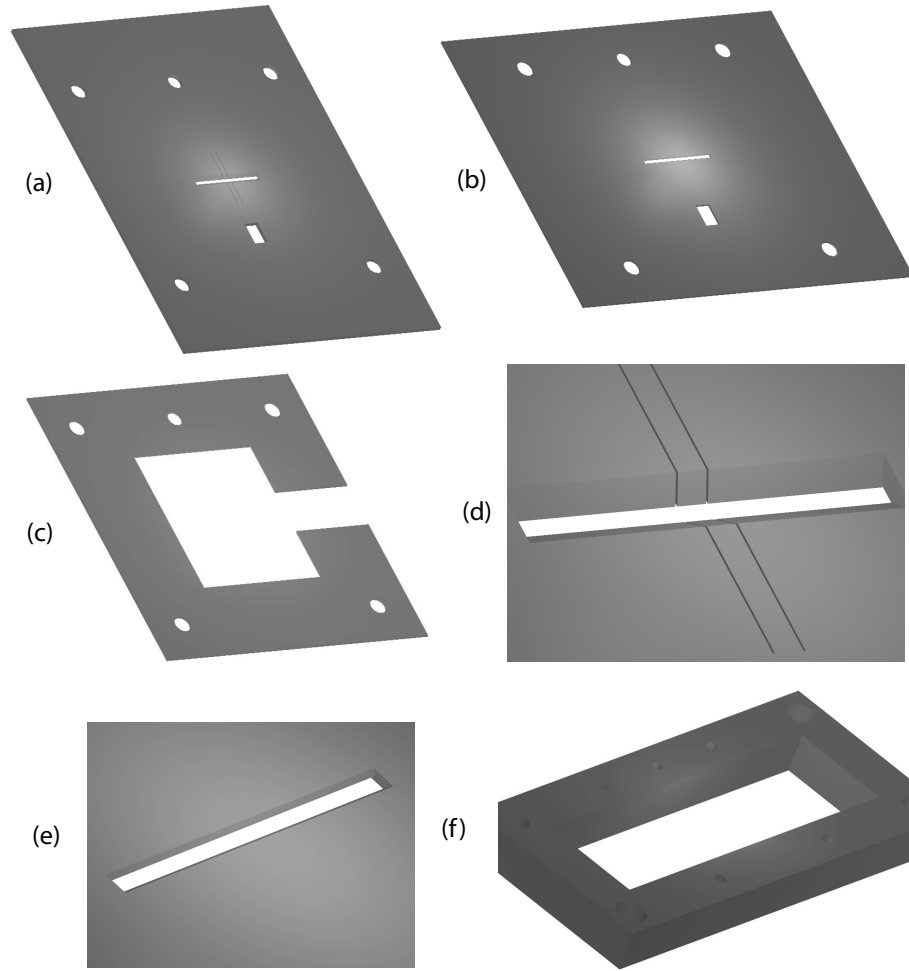


Figure 5.5: Ceramic trap three electrical layers. (a)The static electrode substrate. (b) The rf substrate. (c) The spacer substrate. (d) A close-up view of the static electrode substrate gap. (e) A close-up view of the rf substrate gap. (f)One of the mount bars.

The mount bars used to sandwich the entire structure together were 45 mm long

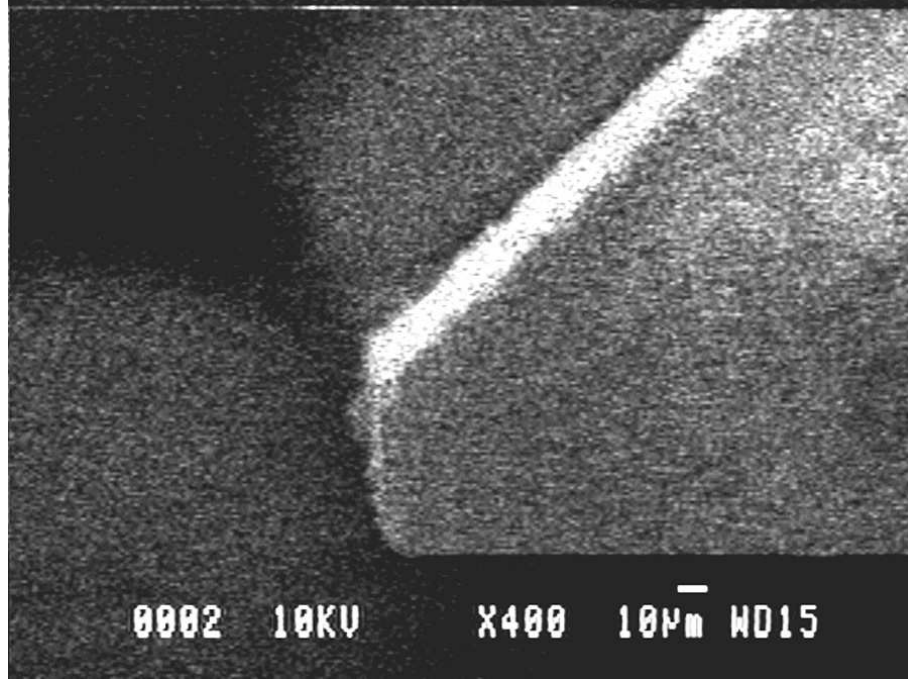


Figure 5.6: A SEM photo of the tip of the chamfered edge of the static electrode substrate. Note the vertical edge that is approximately $20\ \mu\text{m}$ thick.

by 20 mm wide and were 4 mm thick. The inner rectangle is 35 mm long and 10 mm wide. The 5 blind holes were machined with a 1 mm diameter and were sunk 3 mm deep. The four end through holes were 3 mm in diameter. The mount bars were machined conventionally by a company named Mindrum.

5.1.3 Gold Electrode Plating The laser-machining of the alumina substrates formed the physical structure of the trapping electrodes. The actual delivery of rf and static potentials to the trapping zone was accomplished by plating a gold layer on top of the alumina. The gold was patterned to allow for on-board rf filtering electronics to be mounted directly to the static electrode substrates.

The gold patterning on the alumina substrates was fixed using physical masks. Various iterations of the trap used both gold sputtering and e-beam evaporation techniques to deposit the gold through the physical masks, onto the substrate. The process, however, is similar. The physical mask was held in contact with the substrate

directly above the evaporation source. The source was either heated or ablated, coating the alumina with a thin layer of titanium (for adhesion, typically about 20 nm thick) and then gold (thickness ranging from $0.1\ \mu\text{m}$ to $2\ \mu\text{m}$, depending on the process). The sputter tool allowed for a thicker gold layer to be deposited on the substrate, but the gold was typically rougher in appearance and seemed to have more surface defects. Both sides of the static electrode and rf substrates were coated so the gold would completely cover the area of the alumina near the center of the trap. The rf was coated with the same physical mask on both sides, whereas the static electrodes had two separate masks- a top mask with patterning for the surface mount electronics, and a bottom mask to cover the center of the trap. The masks are shown in Fig. 5.7. The masks are designed to allow gold to coat the center electrodes, but not far enough back along the slits so that the center and end electrodes short.

The electrodes were designed with the capability to move the ions in all three dimensions, allowing the position of the ion to be shifted so that it corresponded with the rf node. This minimizes ion micromotion and provides the cleanest environment for doing quantum logic. In order to get compensation in all three directions, the static electrodes were configured to be able to apply static potentials to both the top and bottom layers and to all three segments of the static electrode. It is not necessary to have control of all 12 available static electrodes as that proves to have redundant control. The use of six electrodes is sufficient to control the ion in all three dimensions while minimizing the number of needed electrical feed-throughs and filtering electronics. The electrode positions are shown in Fig. 5.8. By adjusting potentials on electrodes a and e with respect to the potentials on b and f, the ion is shifted in the z direction. By changing the potential on the d, e, and f electrodes, the ion is moved in the x direction. Likewise, by changing the potential on a, b, and

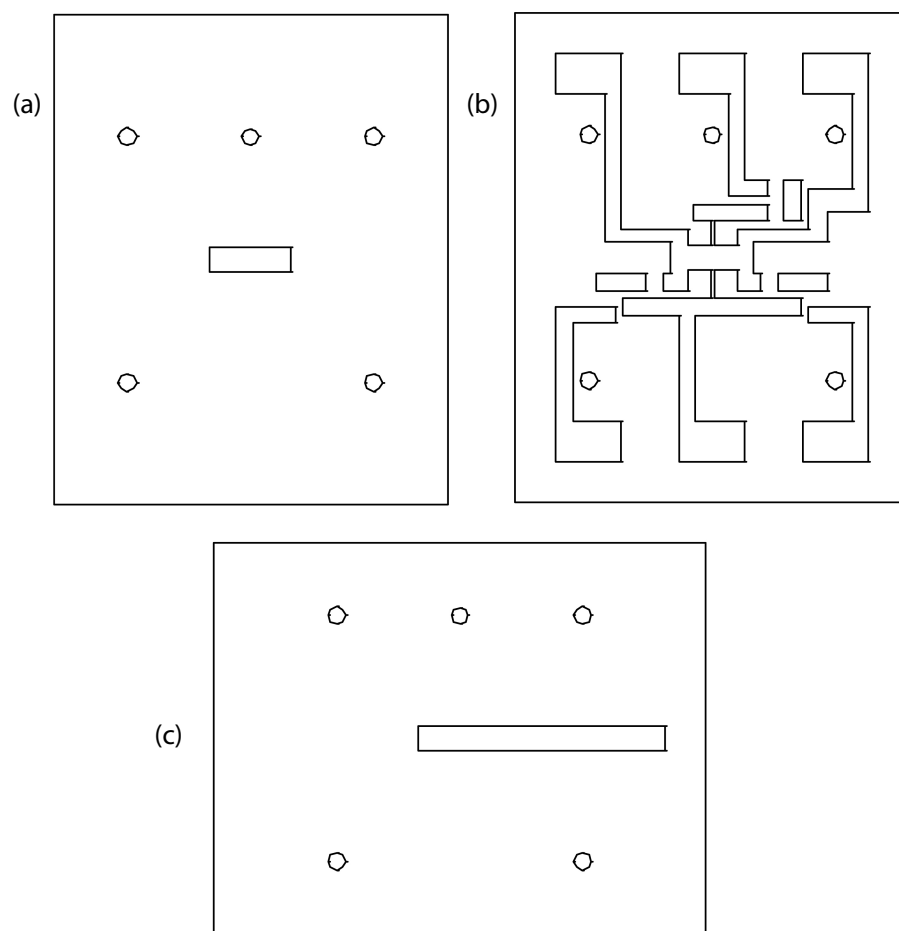


Figure 5.7: Design for physical masks for the rf and static electrodes. (a) The bottom mask for the static electrode. The rectangle shape in the middle is open, allowing gold to plate the center. (b) The top static electrode mask. The patterning is set to allow surface mount rf filters to be attached to the chip. The center of the pattern is open. (c) The rf physical mask lets gold plate the electrodes and then brings the gold lead off to the side of the substrate.

d, the ion is moved in the y direction.

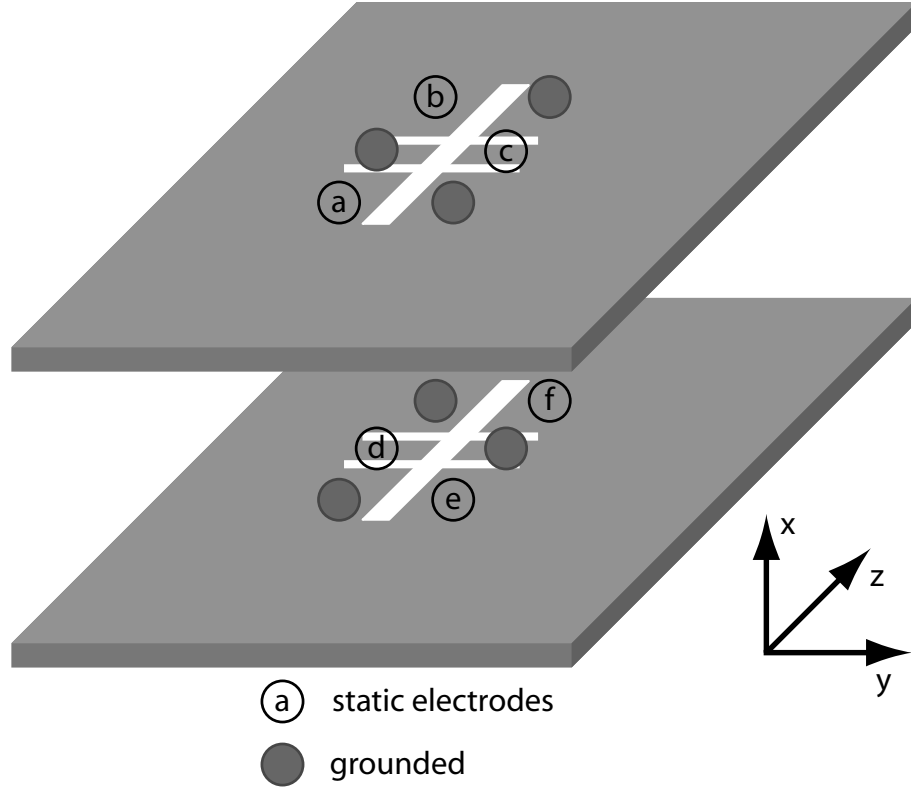


Figure 5.8: Electrode layout for the static electrode layers in the alumina trap. Shown are the top and bottom static electrode layers (the rf layer, in between, is not shown). Each electrode is labeled with a circle- those with letters indicate static electrodes that can have arbitrary potentials. The other six (solid filled circles) are held at ground.

5.1.4 Surface-mount Filters The static electrodes serve a dual purpose as both confinement electrodes and as rf grounding electrodes. This is accomplished by placing near the trap region, low-pass filters that shunt the rf back to the ground provided by the rf resonator (see Sec. 2.7.

After plating each substrate with gold, surface mount electronics were placed in the appropriate positions to create the pi-network low-pass filter for each of the six static electrodes. The schematic diagram for the pi-network is shown in Fig. 5.9. The right side of the filter is the actual electrode at the trap. The left side is fed off of the alumina substrate and out of the vacuum chamber through an 8 pin electrical feed through (ISI part number 9412009 \$140). The resistors used are 1 k Ω

surface mount resistors with gold bond pads from Amitron (part number R2A1508-1001J3G0, \$1/resistor). They are rated to 0.56 W and 120 V. The capacitors are from Novacap (part number 0402B102J251P, \$1/capacitor) and are nominally 1000pF with palladium-silver contacts, rated to 250V.

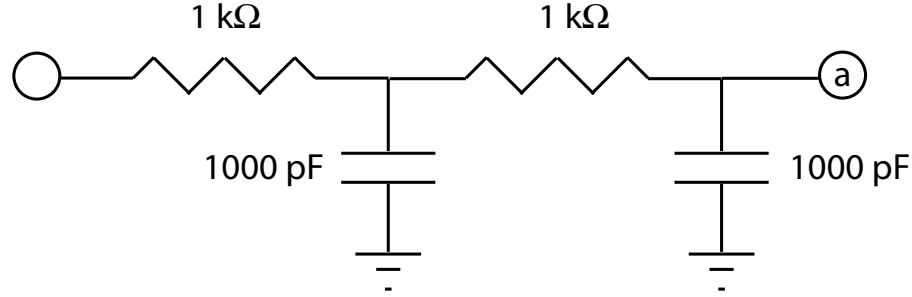


Figure 5.9: Low-pass filter schematic. A schematic diagram of the low-pass pi-network filters used on chip to make the static electrodes act as rf ground. The left side of the circuit represents the electrical feed through and the right side (circle with a letter) is the actual electrode.

Both the capacitors and the resistors were mounted on the alumina substrate using gold ribbon, attached with a wire bonding machine. The K&S 4129 deep access wire bonder was used with a titanium wedge (Small Precision Tools part number VR45-TI-1950-1/16-3/4-CGM, \$70/wedge). The gold ribbon (99.99% pure, Semiconductor Packaging Materials, \$10/ft) used to connect the electronics to the gold plating on the substrate was 0.015 inches wide and 0.0005 inches thick. The parameters used on the wire bonder depend on the actual capacitors and resistors and required some experimentation to make good electrical and physical connections to both the surface-mount electronics and the gold plating. Maximum power, force and time available on the machine, as well as a heated wedge and work holder, were used to attach the gold ribbon firmly to the components and the substrate. The resistors were attached in a two step process. First, gold ribbon was attached to both ends of component and left hanging off the ends as short streamers. Then, the component was placed and held by hand in the appropriate position on the gold

plated alumina substrate. An empty wire bonder wedge (no gold ribbon inserted) was used to bond the gold ribbon to the gold plated substrate on both sides of the component. This process is illustrated in Fig. 5.10.

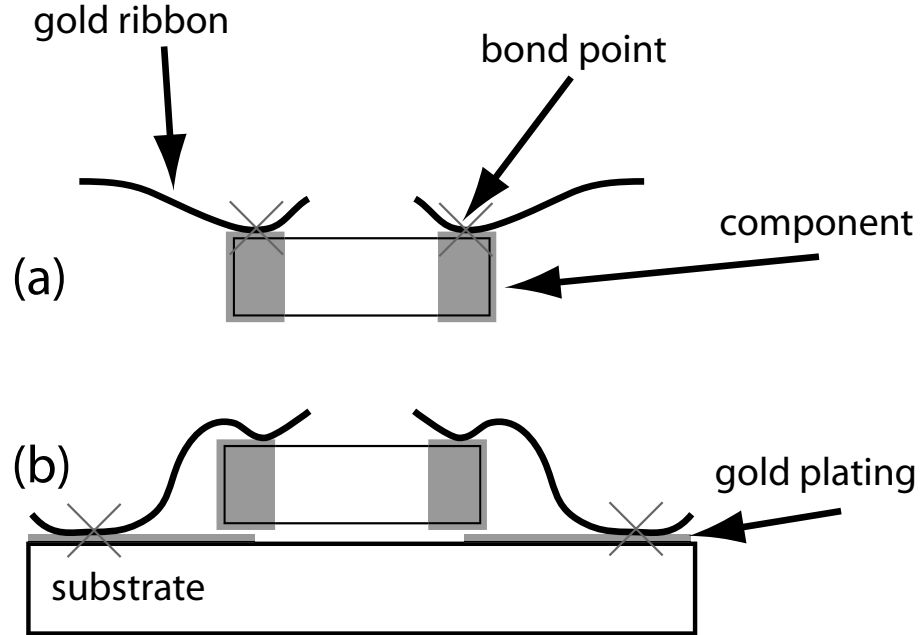


Figure 5.10: Capacitor wire-bonding diagram. To attach the on-chip pi-network low-pass filter components, first bond the gold ribbon to the component (a), leaving a tail of ribbon. Bend the ribbon down so that it holds the shape of the component and bond the tail to the gold bond pad (b) on the alumina substrate.

Finally, to ensure that the components did not become disconnected, ceramic cement was used to fix them in place on the substrate. Care was taken to ensure that all the components, along with the ceramic cement areas, fit inside the available space in between the mount bars. The electrodes on the alumina substrates were attached to the vacuum feed-throughs via several long gold ribbons that were wire-bonded to the substrate on each of the electrode bond pads. Each piece was then cleaned using standard vacuum cleaning procedure, as outlined in Section 2.4.3. These ribbons were connected to small Constantan foil flags using a spot welder (see Sec. 2.4.5) after the trap stack was assembled and installed in the vacuum chamber.

5.1.5 Alumina Trap Assembly The trap stack was assembled in the following procedure:

1. One mount bar was placed with blind holes up and the steel dowel pins inserted in the 4 blind holes.
2. The bottom static electrode layer was placed on the pins with the electronics side facing down. The electrodes were lined up to give the configuration shown in Fig. 5.8.
3. A spacer layer was placed on top of the static electrode layer with the c-gap facing to the left.
4. The rf layer was placed next, with the rf gold leads pointed off the left side, aligned with the c-gap in the spacer layer.
5. The next spacer layer was added with the same orientation as the previous.
6. The top static electrode layer was placed with the electronics side up, again with the proper orientation to give the correct electrode pattern.
7. The top mount bar was placed, aligning the blind holes with the dowel pins.
8. The bolts, lock washers and nuts used to clamp the mount bars were put through the corner through-holes, leaving the nuts loose enough to adjust the trap alignment. Looking through a microscope, the rf and two static electrode layers were aligned so that the trap gaps were parallel in all three layers.
9. The bolts and nuts were tightened to fix the trap assembly in the proper position.

The entire trap assembly was then mounted in the vacuum chamber on a custom-made jig, attached to groove grabbers (Kimball Physics part number MCF-GG-CT02-A, \$62) in the 4.5 inch diameter window in the hemisphere. The gold leads

from each of the electrodes were then either spot welded to an electrical feed through (via a Kapton coated wire with a Constantan foil flag) or to a grounding plane [Fig. 5.11].

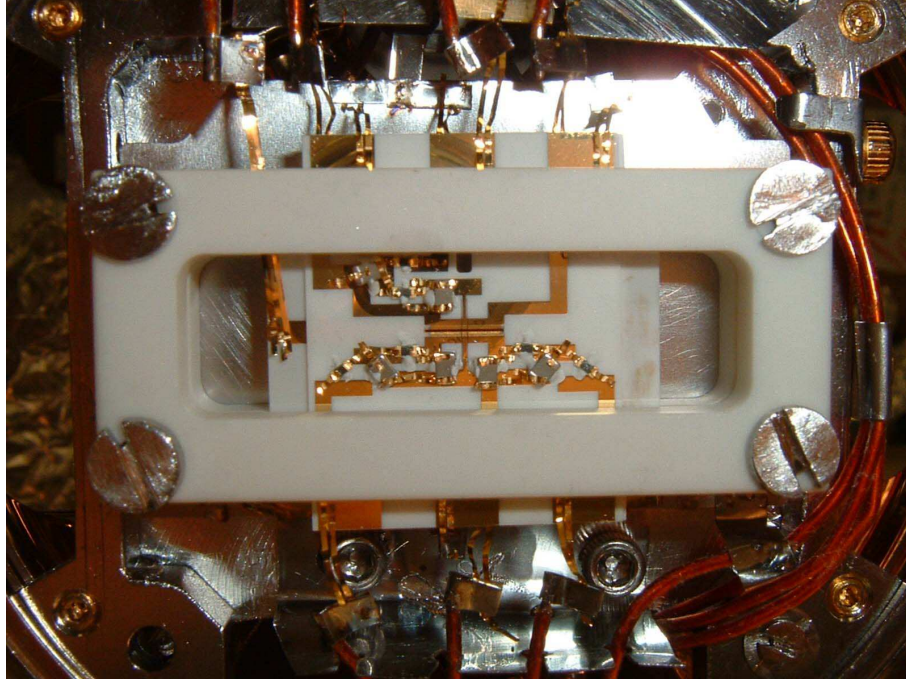


Figure 5.11: Completed alumina trap in the vacuum chamber. The surface mount electronics for filtering the rf from the static electrodes are visible between the large ceramic mount bars. Each electrode was attached to a wire that then was attached to a vacuum feed-through.

5.1.6 Alumina Trap Operation Several FEA models were made of the alumina trap before actual operation (Chapter III). An initial evaluation of the linear trap geometry (for example in Fig. 5.4) suggests that, by the symmetry of the electrodes, the principal axes are the geometric axes of the trap electrodes. If this were the case, the laser for Doppler cooling would not have a component along the y -axis (Fig. 5.8) and ions in the trap would not crystallize in that direction. Following the procedure from Section 4.6, the rotation of the alumina trap principal axes were modeled to learn how to rotate the axes in the xy plane, such that the Doppler-cooling laser had a component along each of the two axes.

The model was made using the Maxwell3D software package (Section 3.3) and

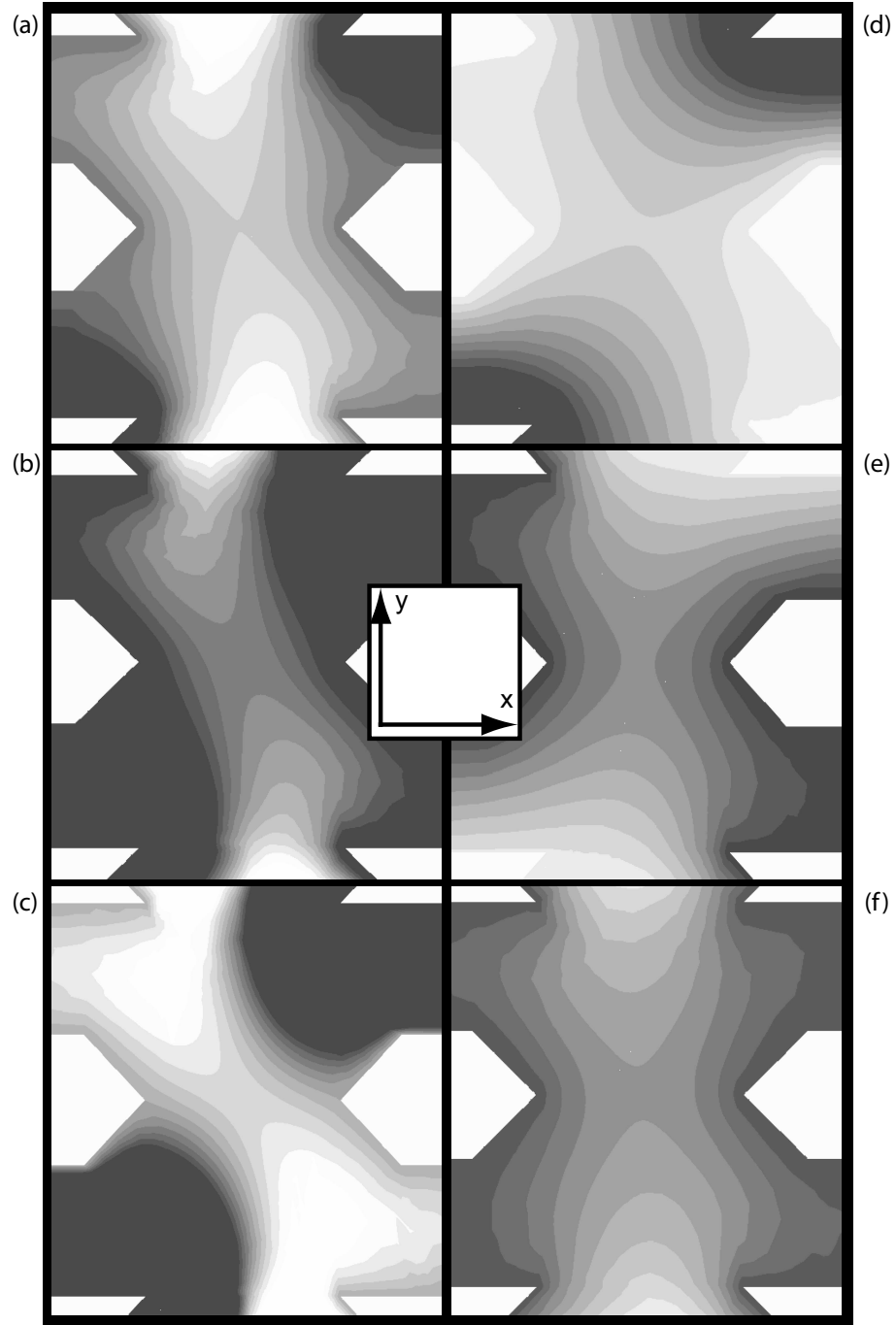


Figure 5.12: Alumina trap rotated principal axes potentials. The geometric xy axes are shown in the center of the figure. Each entry represents a cross-section of the static potential for a single set of endcap and center electrode voltages. The principal axes are extracted by fitting to the direction of greatest curvature in the potential and the orthogonal direction. (a) Endcap: 1 V, Center: -0.5 V (b) Endcap: 1 V, Center: -0.1 V (c) Endcap: 1 V, Center: -0.2 V (d) Endcap: 0 V, Center: -1 V (e) Endcap: 1 V, Center: 0.1 V (f) Endcap: 1 V, Center: 0 V

the electrodes were set such that all six endcap electrodes (Fig. 5.4(a,b,e,f)) were held at the same voltage, as were the center electrode (Fig. 5.4(c,d)) voltages. The model was run to a 1.75% error level with 87,655 tetrahedra in the final potential. The bounding box was fixed at 8 mm by 8 mm by 4 mm. The potential in the xy plane is shown in Fig. 5.12 for a number of endcap and center voltages. Note that the principal axes are rotated from the geometric axes for non-zero center electrode voltages. The center electrodes break the symmetry of the trap, as they are only applied to two of the four electrodes. Breaking the geometric symmetry allows for the rotation of the principal axes and, therefore, efficient Doppler cooling. Actual operation of the trap used endcap and center electrode voltages with similar ratios $V_{\text{endcap}}/V_{\text{center}}$, as the absolute scale is not important to the rotation of the principal axes. The model shows a rotation of up to 45° from the principal axes (Fig. 5.13(a)). In addition, the static potential geometric factor was also evaluated for the different voltages and is shown in Fig. 5.13(b).

The axial trap frequency ω_z was also extracted from the model as a function of different endcap and center voltages. Measurements of the actual trap frequency taken from various experiments are compared to the model trap frequencies in Fig. 5.14 as a function of the quadrature frequency sum $\sqrt{V_{\text{endcap}}^2 + V_{\text{center}}^2}$ of the endcap and center electrode voltages. This simple dependence does not fully model the trap behavior, as the actual operation of the trap did not use symmetric endcap voltages. The data in Fig. 5.14 used an average of the different endcap voltages in the quadrature sum. Both the model data and the experimental data were fit to $\omega_z = a\sqrt{V_{\text{endcap}}^2 + V_{\text{center}}^2}$, with the fits shown in the figure. The axial trap frequency, from Eq. 4.28, is expected to be dependent on the square root of the potential, as seen in Fig. 5.14.

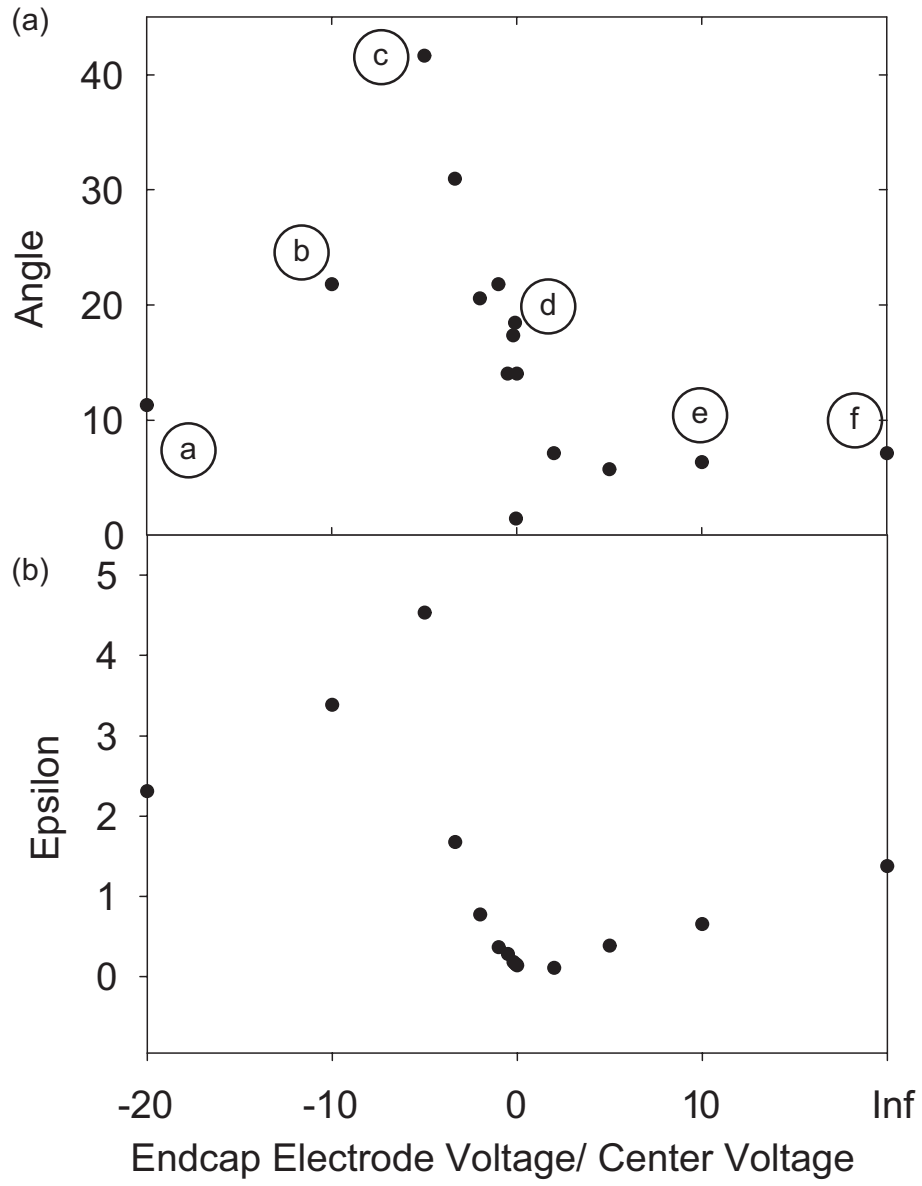


Figure 5.13: Alumina principal axes rotation. (a) The rotation angle of the principal axes as a function of the endcap-to-center voltage ratio. The points from Fig. 5.12 are highlighted. (b) The geometry of the static potential (Eq. 4.27) also changes for different voltage ratios.

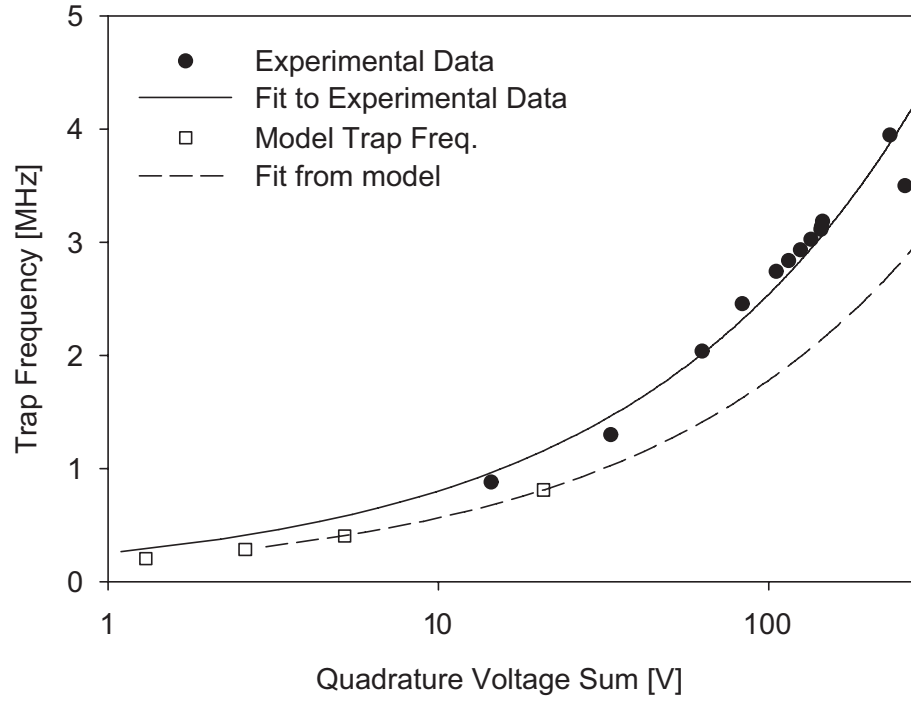


Figure 5.14: Alumina trap axial frequency. Measured axial trap frequencies in the alumina trap as a function of the quadrature sum of the endcap and center Voltages. The data are fit to $\omega_z = a\sqrt{V_{\text{endcap}}^2 + V_{\text{center}}^2}$. Also shown are trap frequencies from the three-dimensional model of the linear trap along with a similar fit to just those data.

5.2 GaAs Microtrap Assembly.

The fabrication of the GaAs microtrap constitutes the first ion trap made from a monolithic substrate using conventional semiconductor processing techniques [33]. This section describes the basic fabrication procedure as well as the equipment used to mount the microtrap into the vacuum chamber. Also included are some preliminary data about the performance of the microtrap. The microtrap design was based on models described in Chapter IV.

5.2.1 GaAs substrate fabrication The microtrap was fabricated from four alternating layers of aluminum gallium arsenide (AlGaAs) and gallium arsenide (GaAs) epitaxially grown on a GaAs substrate as illustrated in Figs. 5.15 and 5.16. The wafer (Fig. 5.15a) consists of a doped substrate on top of which are four layers grown by molecular beam epitaxy. Directly above the substrate is a $4\text{ }\mu\text{m}$ layer of $\text{Al}_{0.7}\text{Ga}_{0.3}\text{As}$, chosen for its insulating properties and selective etching versus GaAs. On top of it is a $2.3\text{ }\mu\text{m}$ layer of silicon-doped ($3 \times 10^{18}\text{ e/cm}^3$) GaAs, $4\text{ }\mu\text{m}$ of $\text{Al}_{0.7}\text{Ga}_{0.3}\text{As}$ and $2.3\text{ }\mu\text{m}$ of doped GaAs. As shown in Fig. 5.15, a series of dry and wet etch procedures define the cantilevered GaAs electrodes. The final step undercuts the $\text{Al}_{0.7}\text{Ga}_{0.3}\text{As}$ from the edges of the GaAs cantilever by about $15\text{ }\mu\text{m}$ to shield the trapped ion from the exposed insulator. Figure 5.16 shows a scanning electron micrograph of the final structure.

The GaAs layers were formed into cantilevered electrodes surrounding the free-space trap region. A through-hole was etched in the substrate allowing clear optical access. The electrodes were electrically isolated from each other and from the doped GaAs substrate by the interleaved AlGaAs layers (thickness $h = 4\text{ }\mu\text{m}$). These insulating layers were undercut $\sim 15\text{ }\mu\text{m}$ from the tips of the GaAs cantilevers to

shield the trapped ion from stray charge on the exposed insulator. The electrodes were segmented along the axis of the linear trap, as shown in Fig. 5.15. Each of the four segments had an axial width of $w = 130 \mu\text{m}$ and was separated from adjacent segments by a $25 \mu\text{m}$ gap. The tip-to-tip separation between opposing cantilevers in the plane of the chip was $s = 60 \mu\text{m}$. The rf potential was applied to all axial segments of the top GaAs cantilevers on one side of the trap and bottom cantilevers on the opposite side. Static potentials were applied to the other cantilevers, which were held near radiofrequency ground with on-board filters. Ions were trapped in one of two zones with appropriate static potentials applied to the four segments. Each of the local trap zones was primarily controlled by three adjacent segments: two endcap segments surrounding a center segment nearest to the ion. Mechanical resonances of the cantilevers were expected to occur in the 1-10 MHz range [32], with quality factors expected to be of order 10^3 .

5.2.2 Trap Assembly The GaAs ion-trap chip is attached to a ceramic chip carrier and attach $25\text{-}\mu\text{m}$ -diameter gold wires from the bond pads on the trap to the chip carrier, with a single wire connecting radiofrequency electrodes and individual wires going from the static-electrode bond pads to the chip carrier electrodes. The static electrodes are shunted to ground through 1,000 pF surface mount capacitors attached to the chip carrier using a similar process as described in Section 5.1.4, and our measurements show that the induced radiofrequency potential on the static electrodes is reduced to less than 1% of the applied radiofrequency potential [Fig. 5.17]. The chip carrier is then plugged into an ultra-high-vacuum-compatible socket [Fig. 5.18], that is permanently connected in the vacuum chamber [Figs. 5.19, 5.20]. This arrangement allows for fast turnaround time; replacing an ion trap does not involve changing any other components inside the vacuum chamber [Fig. 5.21].

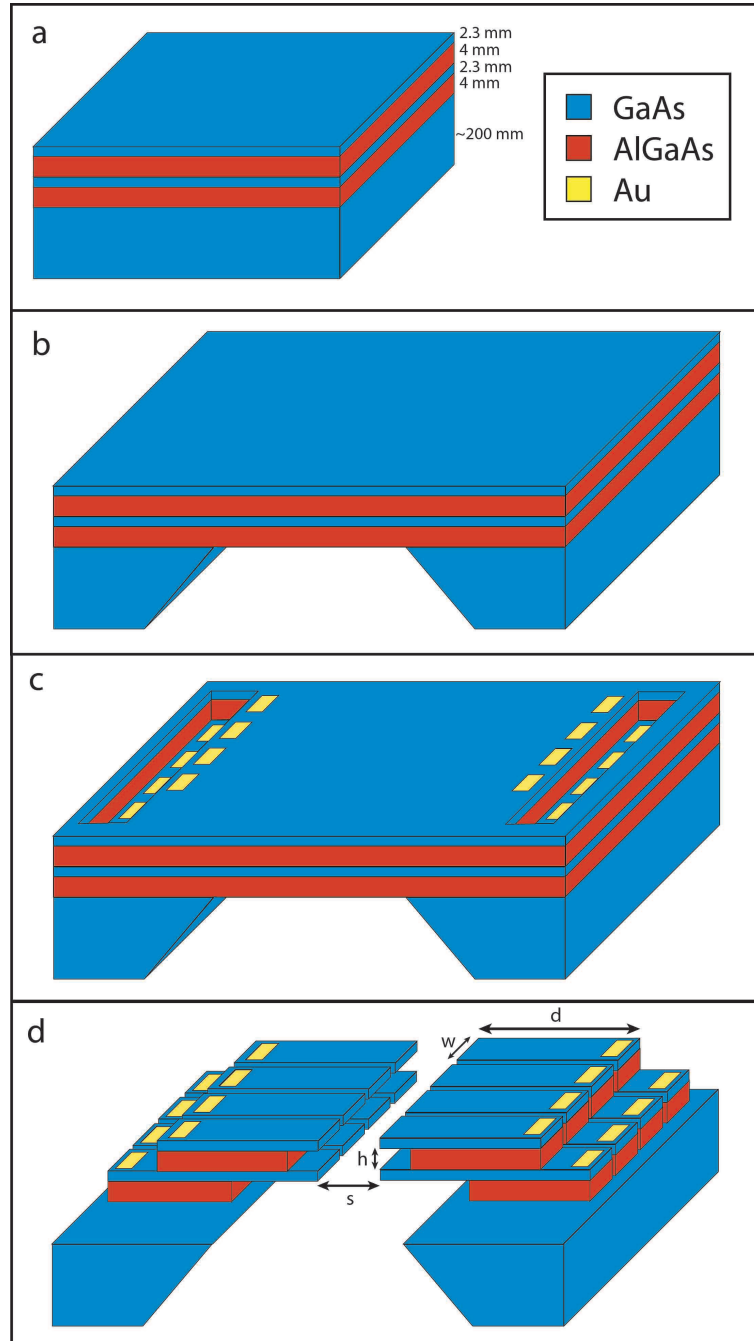


Figure 5.15: Fabrication process for a semiconductor ion trap. (a) The structure grown by molecular beam epitaxy consists of alternating GaAs/AlGaAs membrane layers on a GaAs substrate. (b) Backside etch removes substrate material for clear optical access through the chip. (c) Inductively-coupled plasma etch through membrane creates access to submerged GaAs layers, and gold/germanium bond pads are deposited for electrical contacts to the trap electrodes. (d) A further inductively-coupled plasma etch through the membrane defines and isolates the cantilevered electrodes, and a hydrofluoric acid etch undercuts the AlGaAs insulator material between the electrodes.

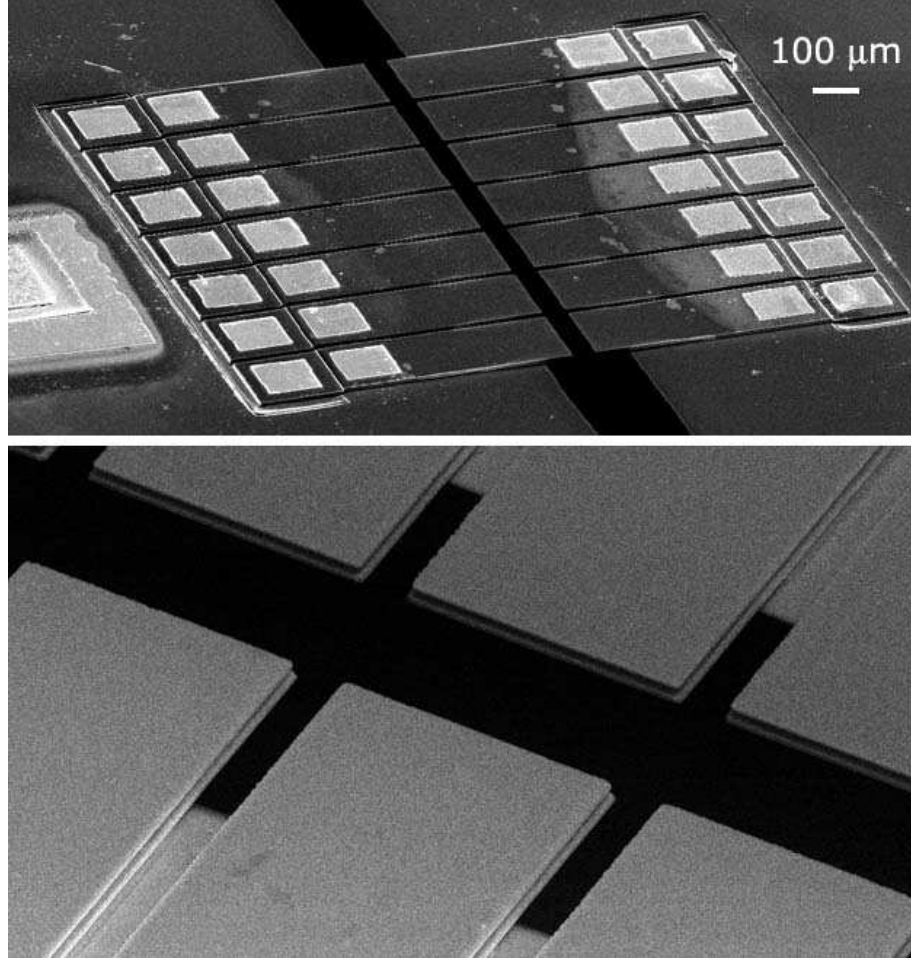


Figure 5.16: Scanning electron microscope image of a monolithic GaAs semiconductor linear ion trap. TOP: Ion trap chip with seven axial segments (28 electrodes) cantilevered over a rectangular through-hole (black). The 28 gold bonding pads are visible as bright squares, along with a single bond pad at the left connecting to the substrate beneath. In the experiment, ions are trapped in a similar structure with four segments instead of seven. The tip-to-tip separation of electrodes across the gap is $s = 60 \mu\text{m}$. BOTTOM: Closeup of a single ion trap segment, clearly showing the upper and lower GaAs layers separated by $h = 4 \mu\text{m}$. The microscope was a JEOL 6500.

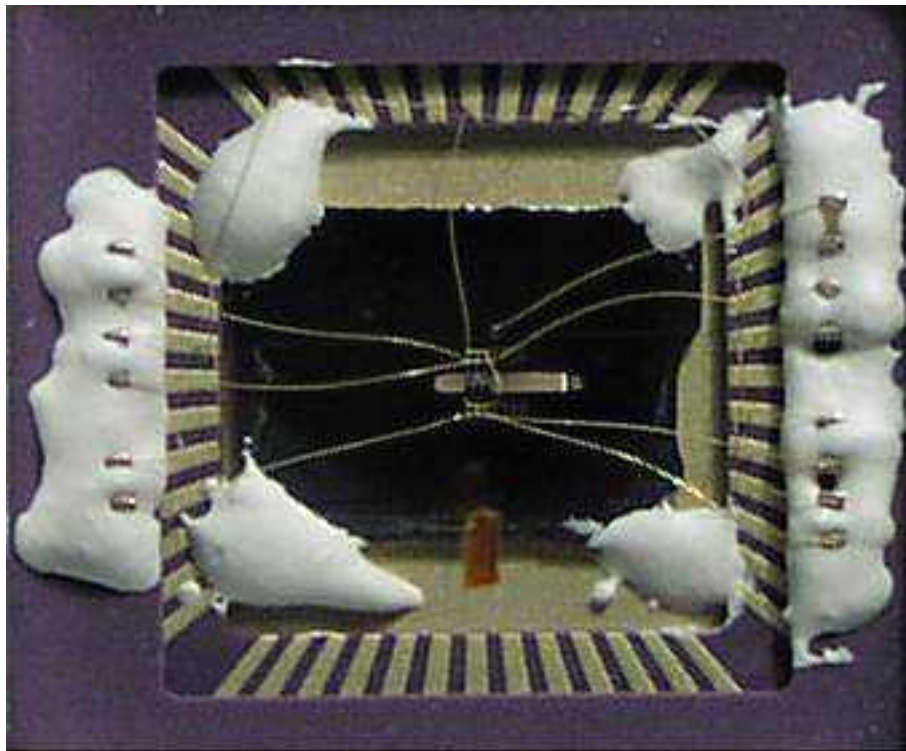


Figure 5.17: A close-up view of the completed microtrap in vacuum. The gold wires connected the die to the LCC are visible. The ceramic capacitors used to filter the rf from the static electrodes are glued around the perimeter of the LCC and also wire-bonded to the LCC.

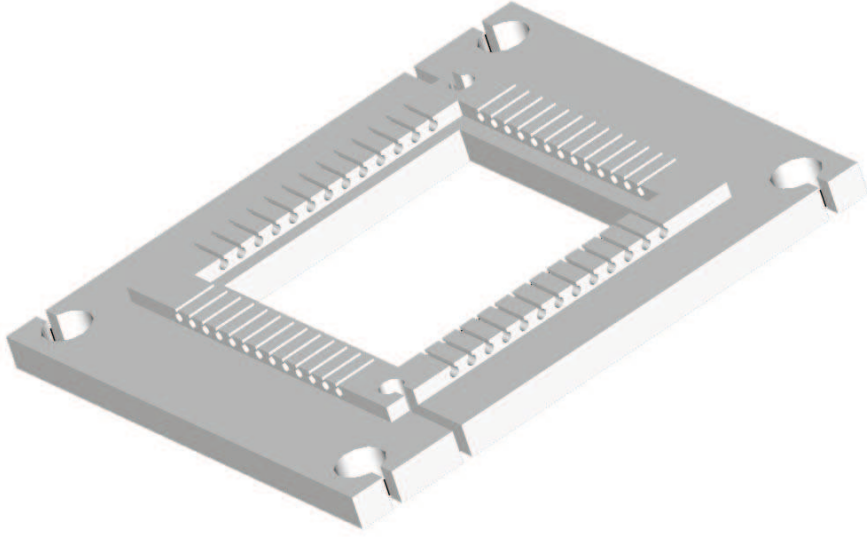


Figure 5.18: Microtrap chip carrier socket design. The leadless chip carrier (LCC) used to mount the GaAs die containing the microtrap was custom designed to fit the 52-lead LCC. To make the socket UHV compatible, it was machined from MACOR, a soft, brittle ceramic. Stainless steel pins were inserted in the channels and glued in place to make electrical contact to the LCC.

Rf potentials were applied to the trap using a helical resonator of unloaded quality factor $Q \approx 500$ and self-resonant frequency 54.9 MHz (see Sec. 2.7.1). When a capacitive coupler was impedance matched to the resonator-trap system, the resonant frequency fell to 15.9 MHz, and the unloaded quality factor of the system dropped to 50. Breakdown of the AlGaAs layer appears to limit the amount of rf voltage that can be applied to the trap. Static potentials as high as ~ 70 V were applied between top and bottom cantilevers on a separate trap sample without breakdown, and a radiofrequency potential amplitude as high as $V_0 = 11$ V at 14.75 MHz before breakdown. Nonlinear current-voltage behaviors were observed across the GaAs electrodes, where the measured current depended upon the polarity of the applied voltage and even the level of room lights at particular voltages. However, none of these effects were measurable at applied potentials below ~ 40 V and are thus not

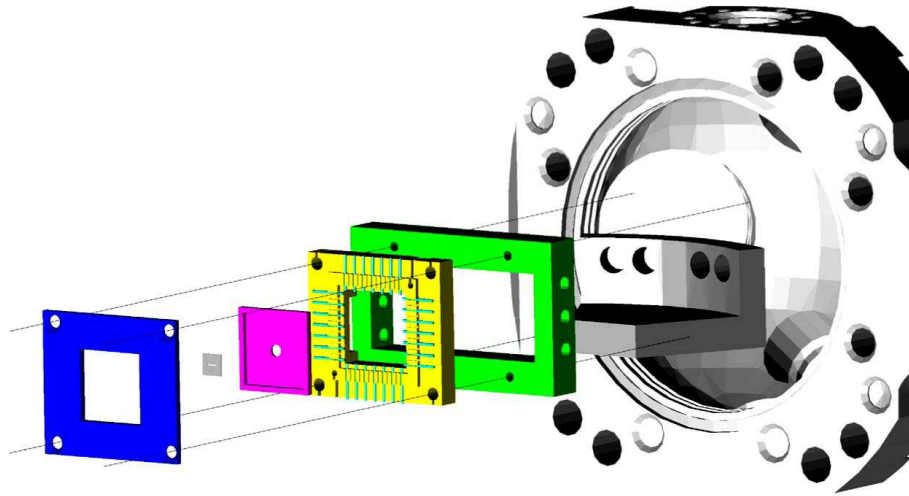


Figure 5.19: Microtrap vacuum chamber mount. The jig that held the microtrap in the hemisphere vacuum chamber was designed to hold both the trap and the oven/e-gun assembly in one block. This expanded view of the jig shows the plate used to fix the LCC to the socket (blue), the die (gray), the socket (magenta), the aluminum bar to hold the socket in the vacuum chamber (green) and the oven/e-gun “firing range” (shaded). The block was first assembled as a unit then attached to the hemisphere using groove-grabbers through the green block.

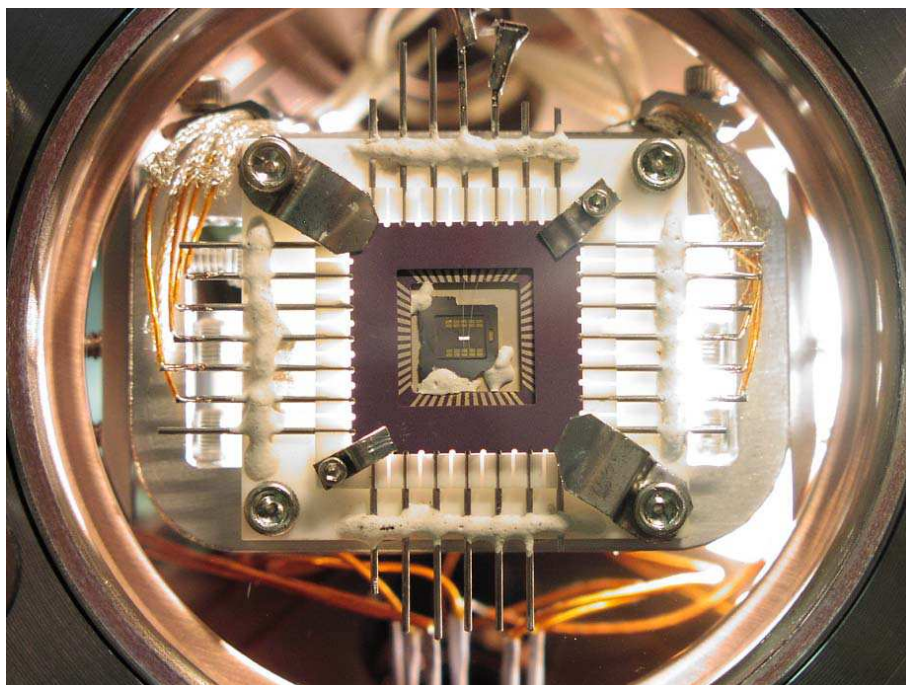


Figure 5.20: The LCC mounted in the socket via an early clamp system. This is a photograph of the LCC mounted in the MACOR socket. The stainless steel connector pins that terminate below the LCC are visible.

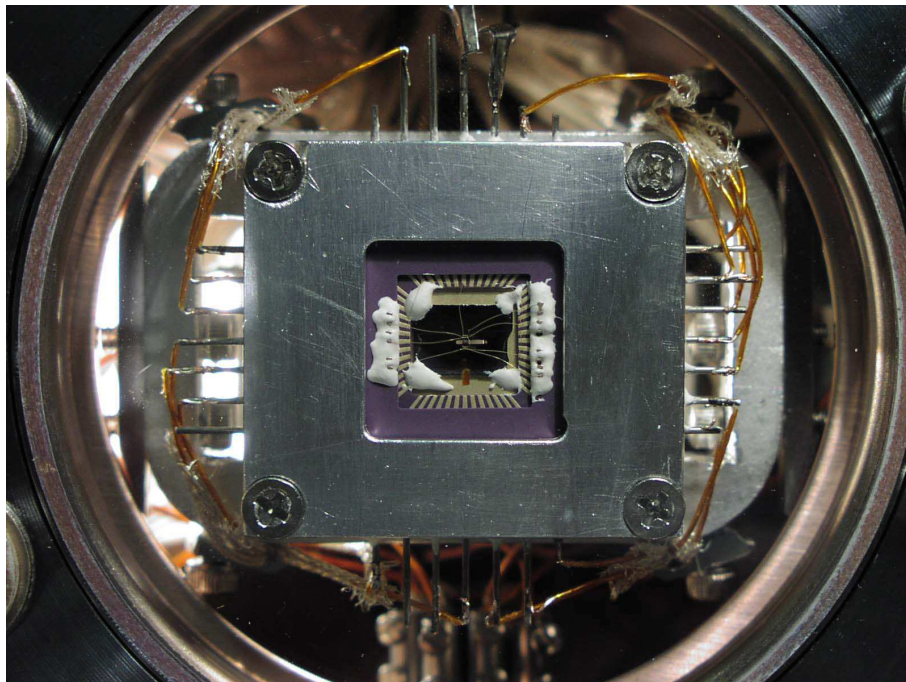


Figure 5.21: The LCC mounted in the socket using the final squeeze plate. It was found that the four clips did not hold the LCC to the stainless steel pins with enough force to maintain good electrical contact. The larger aluminum squeeze plate did a better job of maintaining good electrical contact.

expected to play a role in the operation of the trap.

5.2.3 Ion Image in Trap A single cadmium ion was loaded in the trap and imaged with a charge-coupled-device camera to a nearly diffraction-limited spot with $f/2.1$ optics, where f is the focal length, as displayed in Fig. 5.22. Storage lifetimes in excess of 1 h were observed, but a histogram of many loads shows an exponentially-distributed confinement time with a mean lifetime of 10 min when the ion is continuously Doppler-cooled.

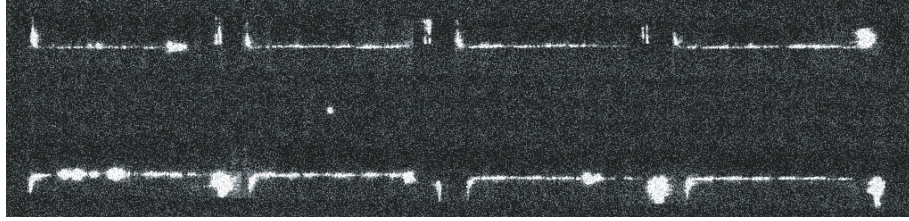


Figure 5.22: Microtrap ion image. An image of a single trapped Cd^+ ion along a view perpendicular to the chip plane after ~ 1 s of integration. The ion fluoresces from applied laser radiation directed through the chip at a 45° angle and nearly resonant with the $\text{Cd}^+ {}^2S_{1/2} \rightarrow {}^2P_{3/2}$ electronic transition at a wavelength of 214.5 nm. The fluorescence is imaged onto a charge-coupled-device camera with an $f/2.1$ objective lens, resulting in a near-diffraction-limited spot with $\sim 1 \mu\text{m}$ resolution at the ion. The profile of the electrodes is also clearly visible as scattered radiation from a deliberately misaligned laser that strikes the trap electrodes. The vertical gap between the top and bottom set of electrodes is $s = 60 \mu\text{m}$.

The secular frequency of the trapped ion were measured by applying a weak, variable frequency potential to one of the electrodes and observing changes in the ion fluorescence owing to the resonant force while it is continuously laser-cooled. For an applied rf potential amplitude of $V_0 = 8.0$ V at a drive frequency of $T/2 = 15.9$ MHz, and static potentials of 1.00 V on the endcap electrodes and 0.33 V on the center electrodes, the axial secular frequency was measured to be $z/2 = 1.0$ MHz. The measured transverse secular frequencies were $x/2 = 3.3$ MHz and $y/2 = 4.3$ MHz, indicating a radiofrequency trap stability factor of $q = 0.62$ [34]. These measurements were consistent with a 3-dimensional numerical simulation of the trapping potential, which further indicates that one of the transverse principal axes of the trap is rotated

$\sim 40^\circ$ out of the plane of the chip (Chapter IV).

CHAPTER VI

Precision Lifetime Measurement

The focus of this work now changes from advanced trap development to ultrafast pulsed laser interactions with a single ion, the first of such work to be done. As described in the Introduction, these experiments are the first steps toward the realization of new types of scalable quantum computation. The first experiment [76] describes a measurement of the $5p\ ^2P_{3/2}$ and $5p\ ^2P_{1/2}$ excited state lifetimes in a single Cd^+ ion and are the most accurate measurements of these excited state lifetimes to date. This experiment served as an initial pulsed laser-ion experiment and enabled us to learn the operation of the mode-locked ultrafast laser and learn how to control the laser-ion interactions.

6.1 Background

Precise measurements of atomic data are of great interest throughout many fields of science. Lifetime measurements are of particular importance to the interpretation of measurements of atomic parity non-conservation [77], tests of QED and atomic structure theory [78], and even astrophysical applications [79]. Because of this, new and more accurate ways of measuring excited state lifetimes are constantly being investigated. Previous methods include time-correlated single photon techniques [80, 81, 82, 83, 84, 85], beam-foil experiments [83], fast beam measurements [86, 87],

electron-photon delayed coincidence techniques [88, 89], luminescent decay [90, 91], linewidth measurements [92], photoassociative spectroscopy [93], and quantum jump methods [94].

This chapter describes excited state lifetime measurements using a time-correlated single photon counting technique. The experiment uniquely combines the isolation of single laser-cooled trapped ions with the precise timing of ultrafast lasers. This method, designed especially to eliminate common systematic errors, involves selective excitation of a single trapped ion to a particular excited state (lifetime of order nanoseconds) by an ultrafast laser pulse (duration of order picoseconds). Arrival of the spontaneously-emitted photon from the ion is correlated in time with the excitation pulse, and the excited state lifetime is extracted from the distribution of time delays from many such events.

By performing the experiment on a single trapped ion [81, 82, 94], we are able to eliminate prevalent systematic errors, such as: pulse pileup that causes multiple photons to be collected within the time resolution of the detector, radiation trapping or the absorption and re-emission of radiation by neighboring atoms, atoms disappearing from view before decaying, and superradiance or subradiance arising from coherent interactions with nearby atoms. By using ultrafast laser pulses [80], we can eliminate potential effects from applied light during the measurement interval including AC Stark shifts, background laser light, and multiple excitations which can also lead to pulse pileup.

With this setup, at most one photon can be emitted following an excitation pulse. While this feature is instrumental in eliminating the above systematic errors, it would appear that this signal would require large integration times for reasonable statistical uncertainties. However, with a lifetime of only a few nanoseconds, millions of such

excitations can be performed each second, thus potentially allowing sufficient data for a statistical error of under 0.1% to be collected in a matter of minutes [81].

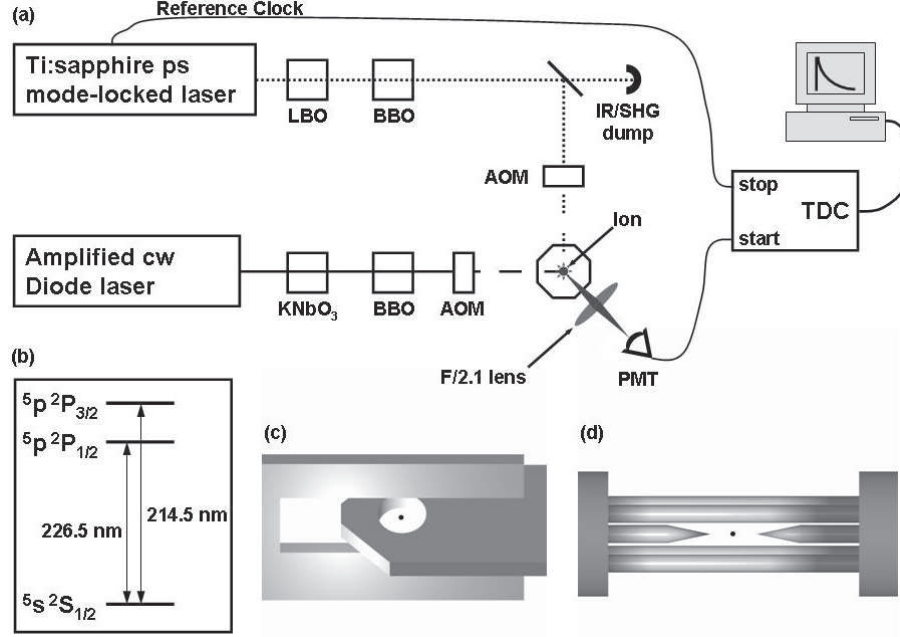


Figure 6.1: The experimental apparatus for the lifetime measurement. (a) A picosecond mode locked Ti:sapphire laser is tuned to four times the resonant wavelength for either the $5p\ ^2P_{1/2}$ or the $5p\ ^2P_{3/2}$ level of Cd^+ . Each pulse is then frequency-quadrupled through non-linear crystals, filtered from the fundamental and second harmonic, and directed to the ion. An amplified cw diode laser is also frequency quadrupled and tuned just red of the $^2P_{3/2}$ transition for Doppler cooling of the ion within the trap. Acousto-optic modulators (AOM) are used to switch on and off the lasers as described in the text. Photons emitted from the ion are collected by an $f/2.1$ imaging lens and directed toward a photon-counting photo multiplier tube (PMT). The output of the PMT provides the start pulse for the time to digital converter (TDC), whereas the stop pulse is provided by the reference clock of the mode-locked laser. (b) The relevant energy levels of Cd^+ . (c) An asymmetric quadrupole trap. (d) A linear trap.

6.2 Experiment Setup

A diagram of the experimental apparatus is shown in Fig. 6.1. Individual cadmium ions are trapped and isolated in one of two rf quadrupole traps. First, the experiment is conducted using an asymmetric quadrupole trap of characteristic size ~ 0.7 mm [95] [Fig. 6.1(c)]. The entire experiment is then repeated in a linear trap with rod spacings of 0.5 mm and an endcap spacing of 2.6 mm [Fig. 6.1(d)]. Both traps have secular trapping frequencies on the order of $\omega/2\pi \sim 0.1 - 1.0$ MHz.

Two types of laser radiation are incident on the ion: pulsed and continuous wave (cw) lasers. The pulsed light is from a picosecond mode-locked Ti:Sapphire laser (see Appendix C) whose center frequency is resonantly tuned to provide excitation to one of the 2P states [Fig. 6.1(b)]. For excitation to the $5p\ ^2P_{1/2}$ ($5p\ ^2P_{3/2}$) state, each pulse is frequency quadrupled from 906 nm to 226.5 nm (858 nm to 214.5 nm) through phase-matched LBO and BBO nonlinear crystals. The UV is filtered from the fundamental and second harmonic via dichroic mirrors and directed to the ion with a near transform-limited pulse width of $t_{\text{uv}} \approx 1$ ps. Since the pulsed laser bandwidth (~ 0.40 THz) is much smaller than the fine-structure splitting (~ 74 THz), selective excitation to the different 2P excited states is possible. Each pulse has $E \approx 10$ pJ of energy, which will excite the ion with a probability of approximately ten percent¹:

$$P_{\text{exc}} = \sin^2 \sqrt{(\gamma^2/4\pi I_s)(Et_{\text{uv}}/w_o^2)}, \quad (6.1)$$

where γ is the atomic linewidth, I_s is the saturation intensity, and $w_o \approx 6\ \mu\text{m}$ is the beam waist. This pulsed laser is also used to load ions in the trap via photoionization by tuning to the neutral cadmium 1S_0 - 1P_1 resonance at 228.8 nm. Once loaded, a single ion will typically remain in the trap for several days.

After the ion is loaded, it is crystallized within the trap via Doppler cooling on the D2 line at 214.5 nm using the cw laser. This laser is tuned approximately one linewidth to the red of resonance and localizes the ion to under $1\ \mu\text{m}$. Residual micromotion at the rf drive frequency (~ 40 MHz) is reduced via offset electric fields supplied from compensation electrodes [41]. We estimate the kinetic energy from this micromotion to be under 1 Kelvin.

Following excitation from the pulsed laser, the spontaneously emitted photons

¹It would be possible to increase the data rate by increasing this excitation probability, however, it was kept to near 10% since higher pulsed laser powers also tend to load extra ions into the trap.

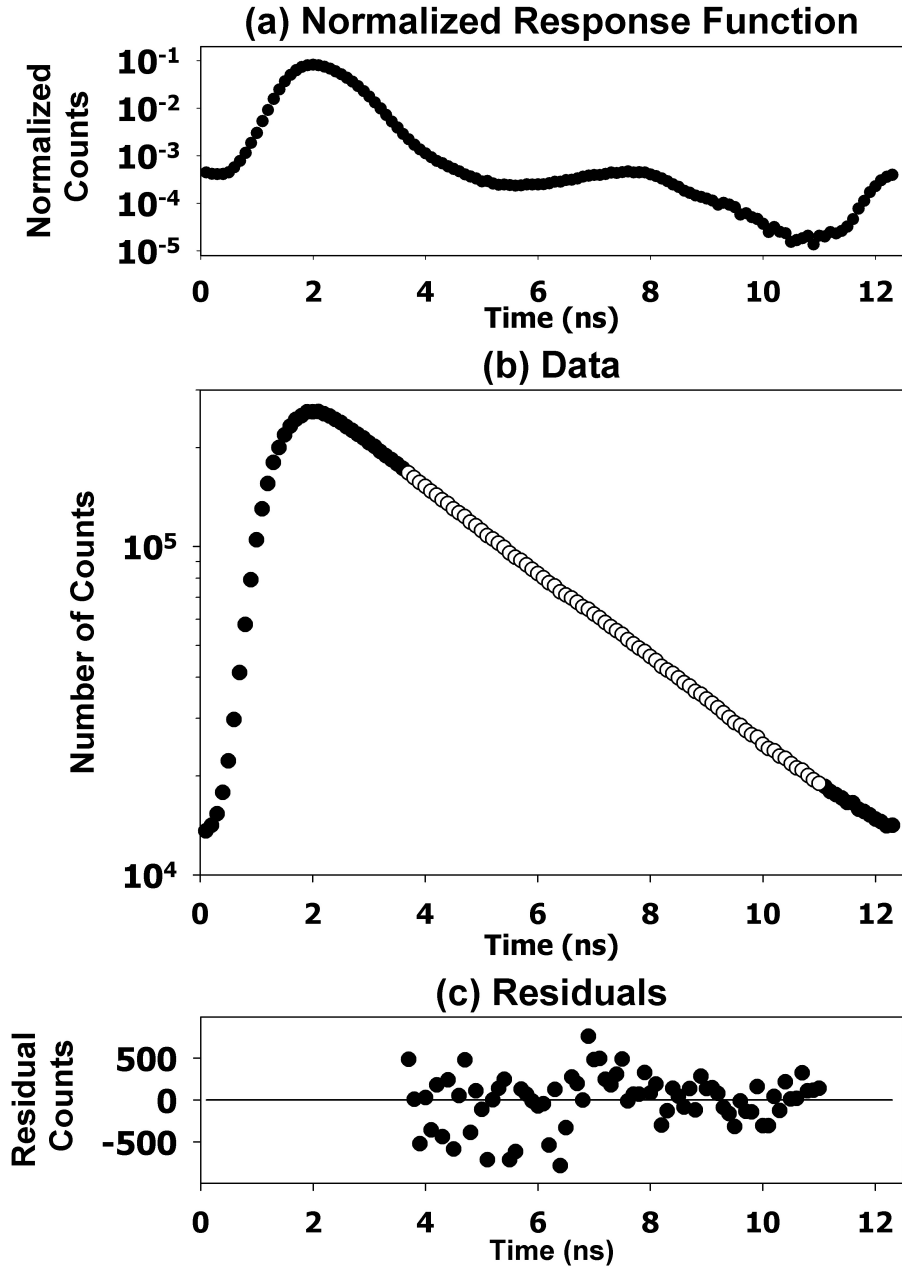


Figure 6.2: Lifetime data with response function and residuals. (a) The response function of the instrument when viewing light scattered off an electrode surface (no atomic physics). The main peak asymmetry is due to the response time of the PMT of ≈ 0.5 ns, whereas the secondary peaks are due to noise in the TDC triggering electronics ($\sim 0.6\%$ of the main peak amplitude). While laser light scattered off an electrode is not a single photon source, this curve was taken at a sufficiently low photon collection rate so that pulse pileup effects were negligible. (b) Data for the $5p\ ^2P_{1/2}$ state taken in the quadrupole trap. The open circles show the data used to extract the excited state lifetime (see text). (c) The deviations from the fit function (residuals). Due to the difficulty in accurately defining a prompt peak background, the fit is not performed around the time of the excitation pulse. This has a small effect on the residuals, but as discussed in the text, is virtually independent of the resulting extracted lifetime.

are collected by an $f/2.1$ imaging lens and directed toward a photon-counting photo multiplier tube (PMT)². The output signal of the PMT provides the start pulse for the time to digital converter (TDC), whereas the stop pulse is synchronized to the reference clock of the mode-locked laser. This time-reversed mode is used to eliminate dead time in the TDC. The PMT used is a Hamamatsu H6240 Series PMT of quantum efficiency $\approx 20\%$, and the TDC is an ORTEC model 9353 time digitizer that has 100 ps digital time resolution with no interpolator, accuracy within 20 ppm, less than 145 ps time jitter, and an integral non-linearity within 20 ps rms.

In the experiment, an acousto-optic modulator (AOM) is used to switch on the cw beam to Doppler cool the ion for 500 ns. Following the cooling pulse, a reference clock from the pulsed laser (synchronized with the laser pulse train) triggers an AOM in the pulsed laser beam and directs a number of pulses to the ion (≈ 15 pulses, with adjacent pulses separated by ≈ 12.4 ns). The repetition rate of this cycle is limited to 1 MHz due to the update time of the pulse generator, and during a given excitation pulse the success probability of detecting an emitted photon is $\sim 2 \times 10^{-4}$. This gives an average count rate of about 3000 counts per second and thus an expected statistical precision of

$$\Delta\tau_{rms}/\tau \approx 0.25\%/\sqrt{T}, \quad (6.2)$$

where τ is the excited state lifetime and T is data collection time in minutes.

6.3 Data Fit and Systematic Shift

Despite the absence of previously mentioned common systematic effects, possible effects that still must be considered in this system include Zeeman and hyperfine quantum beats [96]. Zeeman quantum beats have no significant effect (shifts of

²Due to the chromatic aberration of this imaging system, state-selective light collection between $^2P_{1/2}$ and $^2P_{3/2}$ is also achieved.

$< 0.05\%$) when working in sufficiently low magnetic fields (< 0.5 Gauss), whereas hyperfine beating is eliminated by using an even isotope of Cd that has no hyperfine structure (i.e. $^{110}\text{Cd}^+$). Potential effects from off-resonant laser light - AC stark shifts, background counts, etc. - are also greatly reduced or eliminated in this experiment by taking data only when the cw cooling beam is switched off via the AOM. Hence, immediately following the excitation pulse, the only light present is the single spontaneously emitted photon from the ion. Other possible effects such as relativistic shifts or isotopic dependencies are negligible. Because this technique is devoid of these typical systematic effects, the only significant errors are those arising from the particular equipment used, as discussed below.

To determine the excited state lifetime, the data in a 12.4 ns range for each laser pulse are summed and time-inverted. These spectra are corrected for uncorrelated background events and then fit to a single exponential lifetime τ . As the start time of the fit is stepped-out from the peak [97], the fitted lifetime for the experimental data has an expected systematic bias of 3 to 5 percent (a natural consequence of the convolution of the of the timing system response function [Fig. 6.2(a)] with the pure exponential decay of the excited state). This effect can be further exacerbated by the presence of “prompt” events from background laser light from the ultrafast excitation pulse that is scattered from the apparatus, described by an additional convolution of a delta function at $t = 0$. The relative intensity of the prompt peak varies between the four measurements, and depends upon the particular optical alignment in each experimental run. The time response function distorts the spectrum from a pure exponential and has the net effect of shifting events to longer times thereby increasing the fitted lifetime by 3 to 5 percent. To account for these time-dependent shifts and extract the true lifetime, a simulated spectrum is generated by convolving the

measured time-response function with an exponential decay and delta-function at $t = 0$. The relative intensity of the prompt δ -function is determined by convolving a pure exponential with the approximate true lifetime, intensity I_P , and then subtracting that from the real data for a difference intensity I_{diff} . The excess events are integrated and converted into the δ -function scale;

$$\delta_{\text{PP}} = \frac{I_{\text{diff}}}{I_P} \frac{\tau}{10}. \quad (6.3)$$

The simulated spectra and the real data are fit in precisely the same manner: the start channel of the fit is successively stepped out from $t_s = 1$ ns to $t_s = 6$ ns in 0.1 ns increments. The parameter τ in the simulated spectra is varied to best match the fitted data over the entire time range. The systematic error in the lifetime is determined by varying τ until the data over the time range is no longer in statistical agreement with the simulated spectra. While the resulting variation of the fits over the full fitting range for the simulations are sensitive to the choice of the prompt δ -function intensity (Eq. 6.3), the fitted lifetime over the range $t_s = 1.7 - 1.8$ ns is virtually independent of the prompt δ -function intensity and thus the results for the lifetimes and the statistical error bar quoted in Table 6.1 are taken from this range of t_s [Fig. 6.3]. Doing so greatly reduces the systematic uncertainty from the prompt delta function in all but one set of runs. The presence of an order-of-magnitude larger prompt peak for the $^2P_{1/2}$ transition measured in the linear trap, due to poor optical alignment, results in a significantly larger variation in the fit over the time range and hence the resulting systematic uncertainty for this data set is 3 times larger than for the other three measurements. Despite this problem, the agreement between the measured $^2P_{3/2}$ lifetimes in both trap apparatus is nominal, giving us great confidence in our technique to account for the much smaller effect of the prompt

scattered events in the other three data sets.

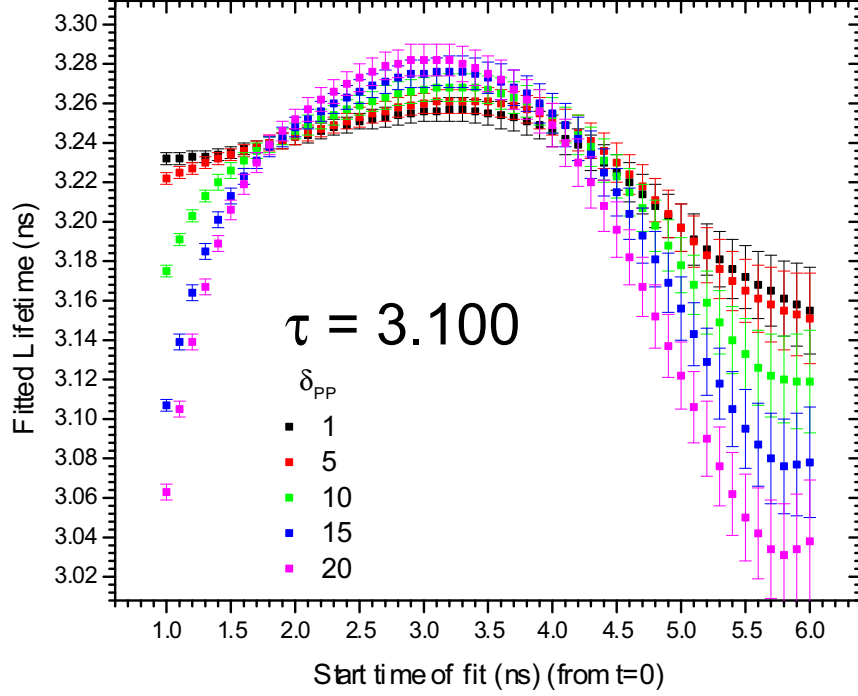


Figure 6.3: Lifetime fit crossing point. The lifetime fit of data showing that the fits all cross at $t_s = 1.8$ ns. The fit values were found using the procedure outlined in the text and were varied for different values of δ_{PP} , Eq. 6.3. The range from $t_s = 1.7 - 1.8$ ns is virtually independent of the value of δ_{PP} and thus was used to find the value of the lifetime.

6.4 Error Analysis

There are several factors to consider when determining the error bar that results from this analysis. The first is the statistical error that results from the fitting of the data which we take to be the error from the fit at $t_s \sim 1.8$ ns. Normally, this is simply the error bar quoted from the fitting program (POSFIT) for the start time of the fit. However, for this data, the background level has been fixed and therefore, the associated error must be determined. This depends strongly on the confidence of the selected background value and, as previously mentioned, depends on which of the individual experimental sets are handled. The statistical error from the background comes by varying it over an appropriate range and looking for the variation of the

fitted lifetime. The final statistical error quoted is the RMS average of the two error bars.

There are two major systematic errors in the analysis. The first is the choice of δ_{PP} used in the convolution. Since an attempt was made to use data with a small prompt peak and the choice of lifetime is somewhat insensitive to the choice of δ_{PP} , a very small systematic (probably negligible) of ~ 0.001 ns is assigned to this error. However, the fact that the resolution function requires a 5% systematic correction on the measured data to determine the actual lifetime, requires careful consideration. This depends strongly on the shape and intensity of the resolution function, the shape and intensity of the prompt peak, and several other factors. A systematic error due to the resolution function was assigned by exploring the range to actual τ that encompass the fitted experimental data as shown in Fig. 6.4. This particular fit for the linear trap for the $P_{1/2}$ excited state shown in Fig. 6.4(a), which is in fact the worst data set, requires that τ range from 3.06 ns to 3.14 ns to encompass all of the data. The fit for the ring trap on for the same excited state, Fig. 6.4(b), is much better. A systematic error due to the resolution function is therefore assigned to be ± 0.040 . Errors are quoted initially as $\tau \pm (\text{fitted stat}) \pm (\text{background stat})$.

6.4.1 Linear Trap 214: This data set consisted of 4 runs. Runs 1 and 4 had clearly large prompt peaks (and less data) and were not used. Since the prompt peaks in runs 2 and 3 appeared to be different the spectra were fitted independently. Run 2 has 5.6 M events while run 3 has 4.2 M events. Both spectra has a large amount of data in the wings with few prompt and decay events so the backgrounds are determined by simply inspecting the left and right regions. Results for linear 214 run 2: $2.648 \pm (0.003) \pm (0.002)$ ns $\rightarrow 2.651 \pm 0.004$ ns and linear 214 run 3: $2.651 \pm (0.003) \pm (0.0035)$ ns $\rightarrow 2.651 \pm 0.005$ ns. The final averaged result is

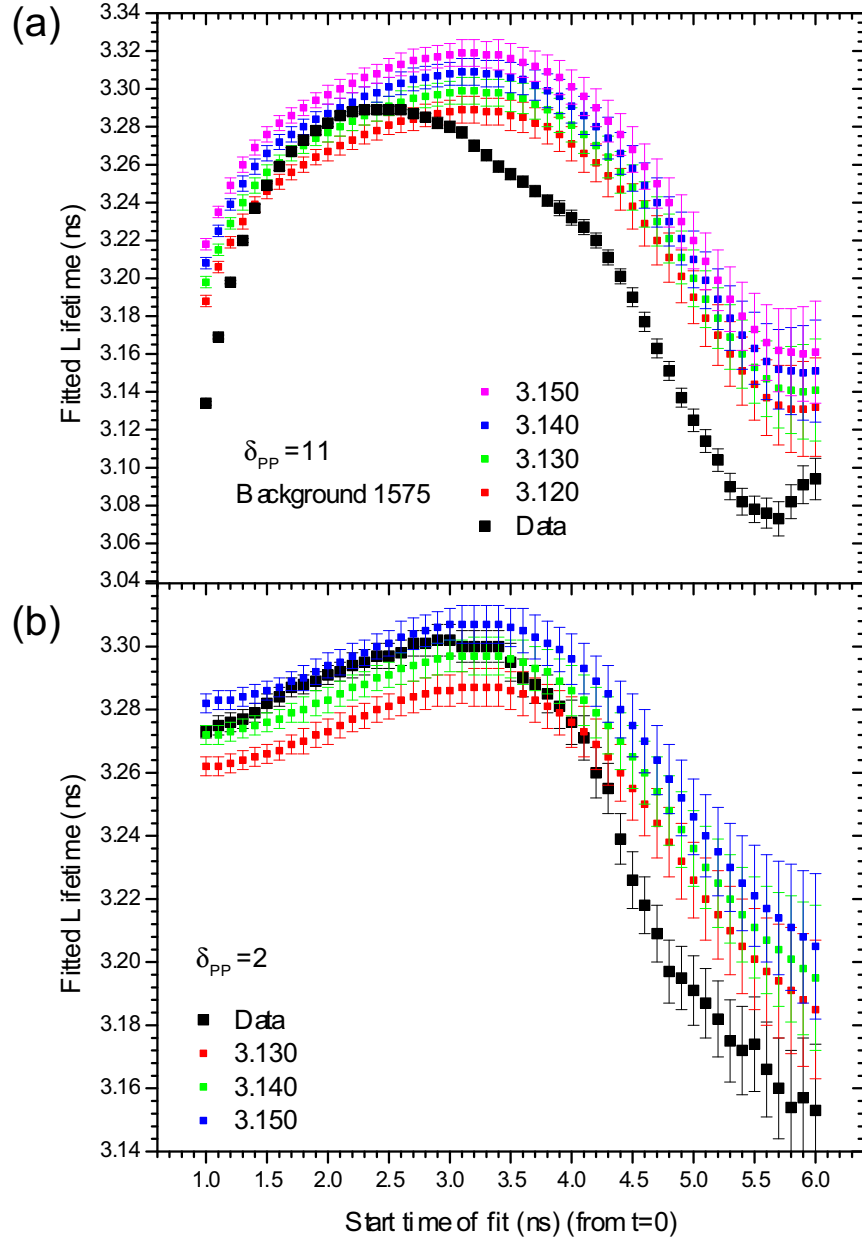


Figure 6.4: Lifetime Error Estimation Data. (a) The lifetime fits for the $P_{1/2}$ excited state measurement in the linear trap with several different values of τ from the simulated spectra. All the simulated spectra use a value of $\delta_{PP} = 11$ for the δ -function prompt peak. (b) The lifetime fits for the same $P_{1/2}$ excited state measurement in the ring trap, with $\delta_{PP} = 2$, a much smaller prompt peak.

$2.649 \pm (0.0032) \pm (0.010)$ ns.

6.4.2 Ring Trap 214: This data set consists of 2 runs both of which have a very small prompt peak. There is very little data in the wings of run 1 and it was not possible to determine the background; hence this data set was not fit. There are sufficient wings in set 2 to extract background information, however there is also a large prompt/decay intensity as well. This necessitated extracting and summing 3 peaks in the right wing and 2 peaks in the left wing to fit the background. The lifetime was held fixed and the background determined. There are 25 M events in ring set 2. The result for ring 214 run 2 is: $2.646 \pm (0.0013) \pm (0.0016)$ ns $\rightarrow 2.646 \pm 0.002$ ns. The final result is $2.646 \pm (0.002) \pm (0.010)$ ns.

6.4.3 Linear Trap 226: This data set consisted of one run. The spectrum has a large amount of data in the wings with few prompt and decay events so the background is determined by simply inspecting the left and right regions. There are 26M decay events. This data had the largest prompt by far ($\delta_{PP} \sim 12$) and hence was difficult to fit given the sensitivity of the fitting to the resolution function. The result for linear 226 is: $3.132 \pm (0.002) \pm (0.001) \rightarrow 3.132 \pm 0.002$ ns. While the statistical error is quite good, the larger prompt peak results in a large systematic of 0.003 ns. The final result is: $3.132 \pm (0.002) \pm (0.030)$ ns.

6.4.4 Ring Trap 226: This data set consisted of 6 runs. The prompt peak for all of the spectra was small and all spectra were summed for a total of 10 M events. Unfortunately, the background wings were very small, never reaching the “true” background seen in the other spectra. The small two peaks on the left and the smallest peak on the right were extracted and fit independently in a manner similar to ring 214. From this, it was possible to fit the background fairly well. The result for ring 226 is: $3.148 \pm (0.003) \pm (0.004)$ ns $\rightarrow 3.148 \pm 0.005$ ns. The final result is

Trap	Error	$5p\ ^2P_{1/2}$	$5p\ ^2P_{3/2}$
Quadrupole	...	3.148	2.646
	Statistical	0.005	0.002
	Systematic	0.010	0.010
Linear	...	3.132	2.649
	Statistical	0.002	0.003
	Systematic	0.030	0.010
Final Results		3.148 ± 0.011	2.647 ± 0.010

Table 6.1: Lifetime measurement results (ns). The asymmetric quadrupole and linear trap results are in good statistical agreement for the $^2P_{3/2}$ transition and the final result is a weighted average of the two values (the systematic error is common to both). For the $^2P_{1/2}$ transition, the contribution from the linear trap is omitted from the final result due to an order of magnitude larger prompt peak giving rise to an unusually large systematic error.

$$3.148 \pm (0.005) \pm (0.010) \text{ ns.}$$

The final values, summarized in Table 6.1 for each trap, are 3.148 ± 0.011 ns for the $^2P_{1/2}$ state and 2.647 ± 0.010 ns for the $^2P_{3/2}$ state. The final error is the average of the statistical error (less than 0.15% for all measurements) and the systematic error. The systematic error of approximately 0.4% is due to the uncertainty in comparison of the fitted values of the convolved spectrum and the experimental data. These new results are plotted in Figure 6.5 along with previously reported theoretical and experimental values for these levels. It is seen that the results reported in this paper are the most precise measurements of these particular excited states of Cd^+ .

In this chapter, a new technique for measuring excited state atomic lifetimes was described that is able to eliminate common systematic errors associated with such measurements. The results herein are not only the most precise to date for Cd^+ , but with absolute uncertainties of order 10 ps, are among the most precisely measured excited state lifetimes in any atomic system. Furthermore, this technique has the potential to achieve ~ 100 ppm precision by eliminating the remaining systematic effects due to prompt events and electronic noise. Other possible improvements include increasing the data collection rate by using a faster pulse generator and

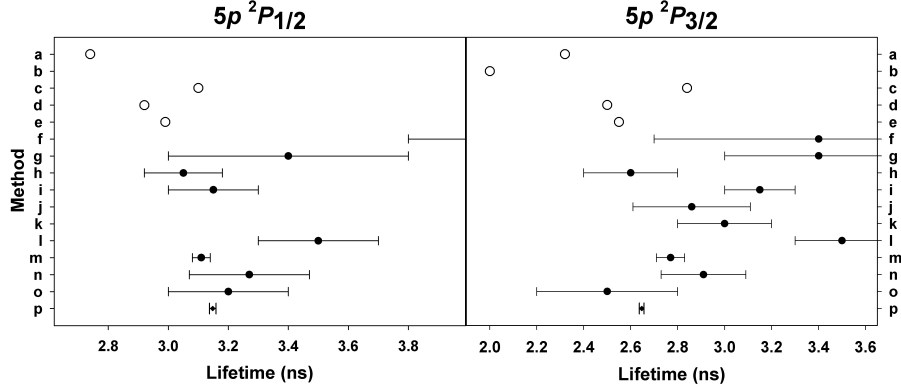


Figure 6.5: Previous published results for the lifetime. Published results of theoretical (open circles) and experimental (filled circles) lifetimes, including this work (filled diamonds), for the $5p\ ^2P_{1/2}$ and $5p\ ^2P_{3/2}$ states of Cd^+ . (a) Hanle Theory (1974) [98], (b) Theory (1975) [99], (c) Many Body Perturbation Theory (1997) [100], (d-e) Pseudorelativistic Hartree-Fock Theory (2004) [85], (f) Phaseshift (1970), $^2P_{1/2}$ value is 4.8 ns [101], (g) Beam-Foil (1973) [102], (h) Hanle (1974) [98], (i) Electron-Photon (1975) [89], (j) Hanle (1976) [103], (k) Hanle (1976) [104], (l) Delayed Coincidence (1980) [105], (m) Beam-Laser (1994) [83], (n) Beam-Foil (1994) [83], (o) Laser-Induced Fluorescence (2004) [85], (p) This Experiment.

TDC, and measuring a longer decay range by pulse-picking individual pulses.

CHAPTER VII

Broadband Laser Cooling

7.1 Motivation

Laser cooling of atoms [38, 106] has become a cornerstone of modern day atomic physics. Doppler cooling and its many extensions usually involve narrow-band, continuous-wave lasers that efficiently cool atoms within a narrow velocity range (~ 1 m/s) that corresponds to the radiative linewidth of a typical atomic transition. To increase the velocity capture range, several laser cooling methods were investigated that modulate or effectively broaden a narrow-band laser [107, 108, 109, 110, 111, 112]. Modelocked pulsed lasers have been used to narrow the velocity distribution of atomic beams within several velocity classes given by the bandwidth of each spectral component of the frequency comb [113, 114, 115]. This chapter describes an experiment that demonstrated Doppler laser cooling of trapped atoms with individual broadband light pulses from a modelocked laser [116].

To efficiently capture and cool high-velocity atoms, it is necessary to achieve a laser bandwidth large enough to cover the large range of atomic Doppler shifts. For example, Cd^+ ions used in this experiment are initially created with kinetic energy below 10 eV, which corresponds to an average velocity of about 4000 m/s and a Doppler shift of $\Delta_D/2\pi \sim 20$ GHz. Power broadening an atomic transition

(saturation intensity I_s and natural linewidth γ) would require a laser intensity of

$$I/I_s \sim (2\Delta_D/\gamma)^2, \quad (7.1)$$

which can be prohibitively high. For Cd^+ ($\gamma/2\pi \simeq 50\text{MHz}$, $I_s \simeq 5000\text{W/m}^2$) this requires $I \sim 10^{10}\text{W/m}^2$. Modulating a narrow-band laser to generate high bandwidths would allow for significantly less laser power, but it is technically difficult to generate a 100 GHz wide modulation spectrum [108]. On the other hand, an ultrafast laser whose pulse is a few picoseconds long will naturally have a bandwidth in the above range, as well as sufficient intensity to excite the transition.

The laser cooling rate depends critically on the photon scatter rate, which for a pulsed laser can be no larger than the laser repetition rate R (about 80 MHz for a typical modelocked laser), given that the atom is excited with unit probability by each pulse. Once excited, the atom decays back to the ground state faster than the time period of the modelocked pulse train $1/R$. In this case, the atom has little memory between pulses, or equivalently, the absorption spectrum is a single broad line of width $\Delta \sim 1/\tau$ (τ is the pulse duration) and the frequency comb of spacing R has very little contrast.

The equilibrium temperature for broadband pulsed laser cooling of trapped atoms is expected to scale approximately with the laser bandwidth Δ (Sec. 7.3), and is much higher than typical narrowband laser-cooled atom temperatures. Still, cooling of atoms in a strong trap to these higher temperatures can localize them to less than the diffraction limit ($\sim 1\mu\text{m}$) of typical imaging optics. This cooling may thus be sufficient for the implementation of quantum optics applications that interface atoms with photons [27, 28, 29]. In these applications, it is necessary to mode-match single photons emitted by individual atoms, so the atomic image quality is important, while cooling to near the ground state of motion or within the Lamb-Dicke limit is

not required [36].

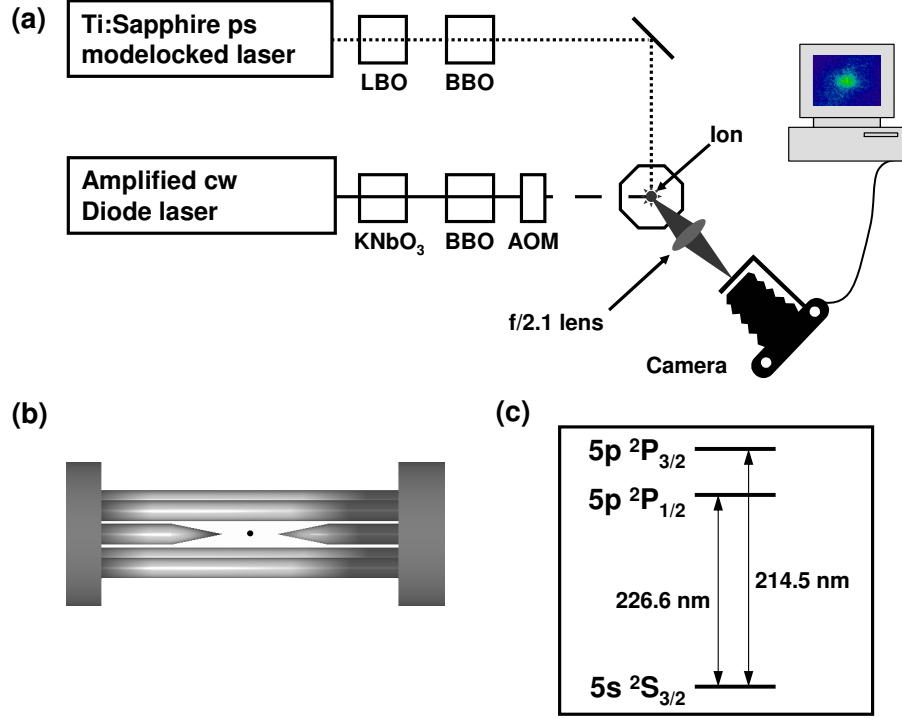


Figure 7.1: The broadband laser cooling apparatus. (a) Frequency-quadrupled pulses from a picosecond modelocked Ti:Sapphire laser (Spectra-Physics Tsunami) are tuned to the $5p\ ^2P_{1/2}$ transition in Cd^+ near 226.5 nm and directed onto the trapped ion. An amplified narrow-band diode laser is also frequency-quadrupled and tuned a few linewidths red of the $5P\ ^2P_{3/2}$ transition for initial Doppler cooling of the ion. An acousto-optic modulator (AOM) is used to switch on and off the narrow-band light. Photons emitted from the ion are collected by an f/2.1 imaging lens and directed toward a photon-counting intensified camera. (b) Schematic drawing of the linear rf trap used in the experiment, with the ion position indicated by the black dot in the middle. (c) The relevant energy levels of Cd^+ .

The experimental setup is shown schematically in Fig. 7.1. Atomic cadmium ions are trapped in a linear rf (Paul) trap [76], shown in Fig. 7.1(b). The spacing of four 0.5 mm diameter rods is about 1 mm, while the separation of the two end cap needles is about 2.6 mm. The strengths of the radial rf trap and the axial static trap are adjusted to be approximately (but not exactly) equal: $\omega_x \simeq \omega_y \simeq \omega_z \simeq 2\pi \times 0.85$ MHz, and the rf drive frequency is $\Omega_{\text{rf}} = 2\pi \times 35.8$ MHz. The trapped ions can be either Doppler-cooled with a narrow-band, cw laser tuned a few linewidths

red of the $^2S_{1/2} - ^2P_{3/2}$ transition at 214.5 nm, or by a modelocked pulsed laser tuned red of the $^2S_{1/2} - ^2P_{1/2}$ transition at 226.5 nm. Both laser beams are oriented to have significant k -vector components along each principal axis of the trap to efficiently cool all degrees of freedom of the trapped ion. The ion fluorescence is collected by an f/2.1 lens and directed to a photon-counting intensified camera. The inherent chromatic aberration of the imaging system allows us to selectively image the 226.5 nm or the 214.5 nm fluorescence by simply adjusting the focus on the f/2.1 lens.

To measure the cooling efficiency of the modelocked laser, a single Cd^+ ion is first Doppler-cooled using the narrow-band laser, with the pulsed laser also directed onto the ion¹. The narrow-band laser beam is then turned off, and an image of the trapped ion fluorescence is recorded using the camera, with an integration time of up to 10 minutes. A series of broadband laser-cooled ion images taken at various detunings $\delta = \omega_l - \omega_a$, where ω_l is the modelocked laser central frequency, and ω_a is the atomic resonance frequency, is shown in Fig. 7.2(a). The modelocked laser average power is held constant at 1 mW, which corresponds to individual pulse energies of about 12.5 pJ. The resulting image is analyzed to measure its rms width, x_{im} , by fitting its cross section to a Gaussian distribution [Fig.7.2(b)].

To determine the actual Gaussian rms radius x_{rms} of the time-averaged ion position, two effects must be considered. First is the finite resolution x_r of the imaging optics, which was measured by recording an image of a narrowband laser-cooled ion [Fig.7.2(c)], resulting in a near point-source with an estimated object size of ~ 30 nm. Fitting its cross section [Fig.7.2(d)] to a Gaussian distribution provides a good estimate of $x_r = 1.15 \pm 0.01 \mu\text{m}$. This is about a factor of two larger than the expected

¹The initial narrow-band laser cooling is only necessary for technical reasons and does not affect the results of the pulsed laser temperature measurement. Once the narrow-band laser is turned off, the ion quickly reaches thermal equilibrium that only depends on the pulsed laser properties.

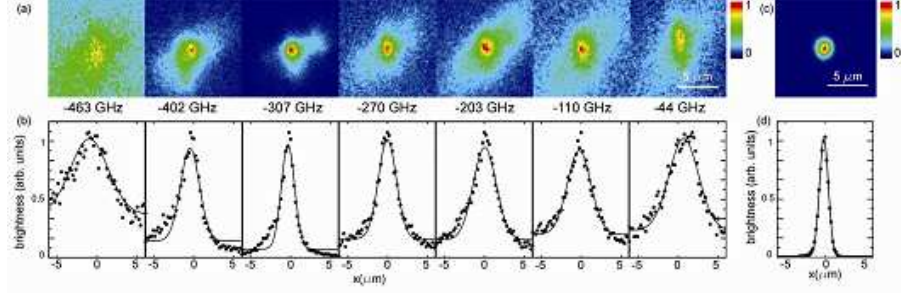


Figure 7.2: Ion images with the pulsed laser. (a) Images of a single trapped ion taken at various pulsed laser detunings $\delta/2\pi$ indicated at the bottom. The pulsed laser beam direction in each image is diagonal from lower-left corner to upper-right corner. (b) cross sections of the images in (a) along the vertical direction. The solid lines are Gaussian fits to the data. (c) An image of a narrow-band laser-cooled ion localized to ~ 30 nm, with its cross section and a Gaussian fit plotted in (d).

diffraction-limited image size of about $0.55 \mu\text{m}$, which can be attributed to an incomplete correction of the spherical aberration of the $f/2.1$ lens. Using properties of the convolution of Gaussian functions, the resolution-corrected image width is:

$$x_{\text{corr}} = \sqrt{x_{\text{im}}^2 - x_{\text{r}}^2}. \quad (7.2)$$

The second effect is the modulation of the ion brightness due to laser light intensity variation across the waist, whose measured rms width is $x_{\text{w}} = 3.35 \pm 0.15 \mu\text{m}$. The true rms ion motion size is

$$x_{\text{rms}} = \frac{x_{\text{w}} x_{\text{corr}}}{\sqrt{x_{\text{w}}^2 - x_{\text{corr}}^2 \sin^2(\phi)}}, \quad (7.3)$$

where ϕ is the angle between the laser beam direction and the direction of ion image cross section. The temperature is analyzed in the radial and the axial directions, where $\phi = \pm 45^\circ$.

The effect of the ion micromotion (fast oscillations near the rf drive frequency) on the image size is negligible in this experiment. With the proper compensation of the background electric fields, the micromotion amplitude is [41]

$$x_{\text{m}} = \frac{\sqrt{2}\omega}{\Omega_{\text{rf}}} x_{\text{rms}} \simeq 0.035 x_{\text{rms}}, \quad (7.4)$$

where ω is the ion's secular frequency along the particular principal axis. Broadening of the image due to excess micromotion, which arises from an incomplete compensation of the background electric fields, is taken to be much smaller than the resolution x_r of our optics.

The ion rms velocity in the trap v_{rms} along a principal axis is directly proportional to the rms displacement: $v_{\text{rms}} = \omega x_{\text{rms}}$. The temperature T of the ion (assuming a normal distribution of its velocity) is then given by $k_B T = m v_{\text{rms}}^2$, where k_B is the Boltzmann constant, and m is the ion mass.

A summary of the results is shown in Fig. 7.3. For the ion temperature data in Fig. 7.3(a), each point is measured using the procedure described above². The absorption lineshape in Fig. 7.3(b) is taken in a separate experiment by measuring the fluorescence rate of a single cold ion under a pulsed laser average power of 1 mW. For this, a 100 μs narrowband laser-cooling cycle is interlaced with a 200 μs period when only the pulsed laser light is incident on the ion and the ion fluorescence is collected. There is a wide range of pulsed laser detunings in Fig. 7.3(a) for which the ion temperature is well below 5 K, reaching as low as 1 K. These detunings correspond to the region of high slope in the absorption line curve, as expected in Doppler cooling [37]. The ion temperature increases sharply as δ approaches zero; it also grows significantly on the far-red side of the resonance, where the cooling rate is very slow due to low photon scatter rate, while additional background heating [117, 60] presumably increases the equilibrium temperature of the ion.

The bandwidth of the laser pulses used in the experiment is measured to be $\Delta \sim 2\pi \times 420$ GHz, as shown in Fig 7.3(b), which is almost four orders of magnitude larger than the linewidth $\gamma/2\pi \simeq 50.5$ MHz of the $5p^2P_{1/2}$ Cd^+ excited state [76].

²Here, we present the analyzed temperature data for radial direction in the trap only (vertical in Fig. 7.2(a)). In the axial direction (horizontal in Fig. 7.2(a)), the observed temperature is about 5 times lower. This suggests that our simple theoretical model does not fully describe the cooling mechanism.

Thus, the velocity-dependent (frictional) force that leads to cooling arises from the laser line shape rather than the atomic line shape.

7.3 Theoretical Cooling Limit

The cooling mechanism can still be understood in terms similar to conventional Doppler cooling [37]. The probability of absorbing a photon by the ion is velocity-dependent, due to Doppler shifts. With the laser central frequency tuned to the red of the atomic resonance ($\delta < 0$), the atom has higher probability of absorbing a photon when it is moving toward the laser beam, experiencing a blue Doppler shift. This absorption reduces the atom velocity in the direction of motion. The following spontaneous emission is random and equally likely in any direction; thus, the net effect of absorption and emission is to lower the kinetic energy of the atom. For a bound atom, as in the case of an ion in an rf trap, only one cooling laser beam is necessary, provided that its k -vector has components along all three trap principal axes [39, 40]. The expressions derived for cooling rate and the cooling limit remain the same for a free atom and three pairs of counter-propagating cooling laser beams.

The average force due to scattering of photons from the laser beam experienced by the atom along a principal axis in the trap in this configuration is:

$$F = \Delta p R P_{\text{exc}}, \quad (7.5)$$

where $\Delta p = \hbar k / \sqrt{3}$ is the average momentum kick along the principal axis from each photon absorption, with k being the photon's wavenumber, R the modelocked laser repetition rate, and we assume that \vec{k} has equal components along each trap axis [40]. The atomic excitation probability P_{exc} can be derived analytically for hyperbolic secant pulses [118]

$$E_0 \text{sech}(\pi t / \tau) \quad (7.6)$$

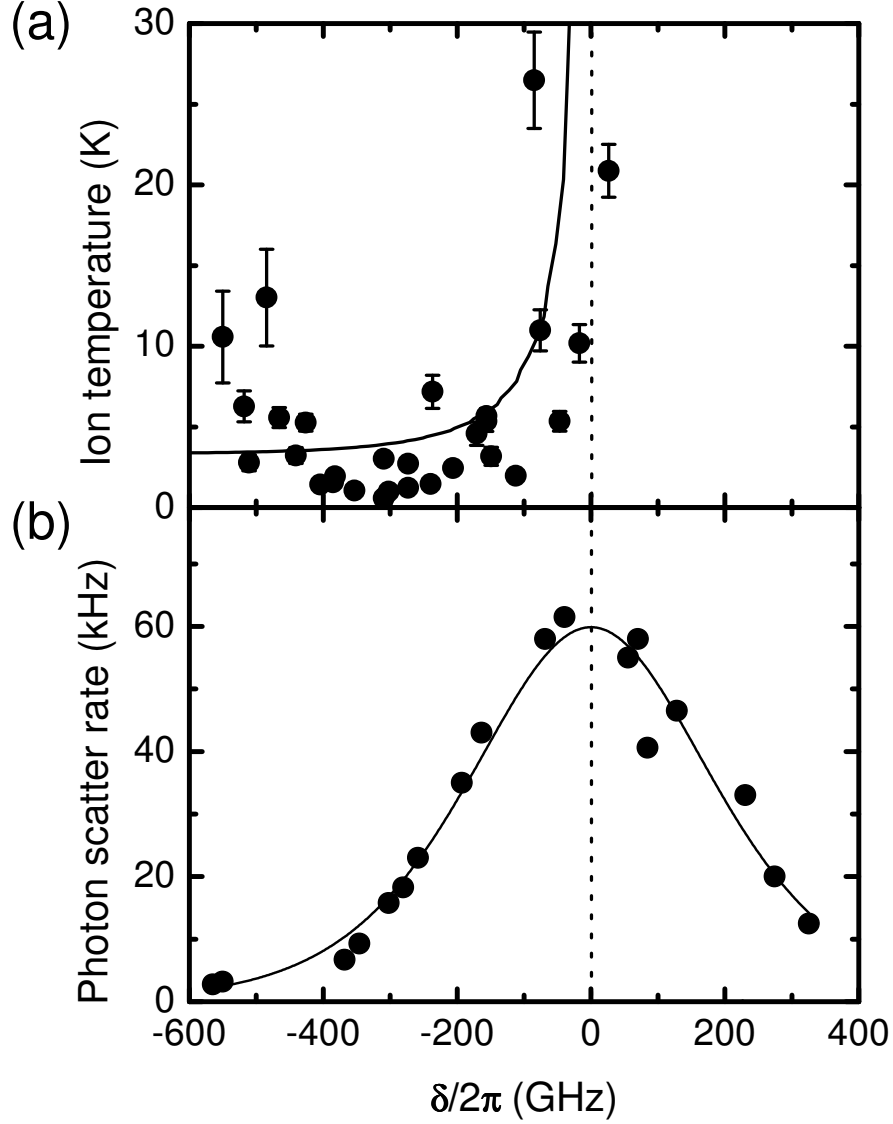


Figure 7.3: A summary of the cooling measurements. (a) The measured radial ion temperature is plotted against the pulsed laser detuning δ . The solid line represents the theoretically predicted temperature [Eq. 7.13]. (b) Photon scatter rate from a single, cold ion is plotted against the pulsed laser detuning. The vertical dashed line indicates the atomic resonance position, corresponding to the wavelength 226.57 nm. The solid line is a fit to the data using sech^2 spectrum [Eq. 7.7], indicating $\Delta/2\pi \sim 420$ GHz and $\tau \simeq 1.3$ ps

of electric field amplitude E_0 and duration τ , expected from the modelocked laser:

$$P_{\text{exc}} = \sin^2(\theta/2) \text{sech}^2(\tau(\delta + kv)/2), \quad (7.7)$$

where θ is the Rabi rotation angle from a resonant laser pulse, τ is the pulse duration, and v is the atom velocity component along the laser beam.

For small values of v , the force [Eq. 7.5] becomes

$$F \simeq F_0 + \beta v, \quad (7.8)$$

where the offset force

$$F_0 = \Delta p R \sin^2(\theta/2) \text{sech}^2(\tau\delta/2) \quad (7.9)$$

shifts the equilibrium position of the trapped atom by $F_0/(m\omega^2) \sim 1$ nm in our trap [40], and

$$\beta v = \Delta p k \tau R \sin^2(\theta/2) \text{sech}^2(\tau\delta/2) \tanh(\tau\delta/2) v \quad (7.10)$$

is a damping force for $\delta < 0$, corresponding to red detuning of the laser, with the cooling rate β/m . In our experiment, the maximum cooling rate $\beta/m \simeq 2 \text{ sec}^{-1}$.

This cooling is opposed by diffusion heating resulting from photons emitted by the atom in random directions:

$$D = \frac{1}{3} (2E_r) R P_{\text{exc}}, \quad (7.11)$$

where

$$E_r = \frac{(\hbar k)^2}{2m} \quad (7.12)$$

is the photon recoil energy, and the factor of 1/3 is due to the diffusion energy equally distributed between the three degrees of freedom [40]. Equating the cooling power βv^2 to the heating power D , one can find the equilibrium temperature of the atom:

$$T = \frac{\hbar}{\sqrt{3}\tau k_B} \frac{1}{\tanh(\tau\delta/2)}, \quad (7.13)$$

where substitutions for β and P_{exc} have been made. The lowest possible temperature is similar to narrow band Doppler cooling, but with a final temperature of

$$T = \frac{\hbar\gamma}{\sqrt{3}k_{\text{B}}}. \quad (7.14)$$

The predicted ion temperature T corresponding to Eq. 7.13 is plotted in Fig. 7.3(a) in a solid line. Note that this line is not a fit to the data; rather, it is a theoretical prediction based on the laser and trap parameters used in the experiment. The theory and experiment are in a good agreement for the radial measurements, while the measured axial temperatures (not shown in Fig. 7.3) were consistently lower than the theory ³.

It is important to point out that the lifetime of the $\text{Cd}^+ 5p \ ^2P_{1/2}$ excited state is only 3.15 ns [76], while the period of the laser pulses is 12.5 ns. Thus, by the time the next laser pulse arrives, the excited state population is only about 2%. This cooling process is then primarily due to absorbing single photons from individual pulses, and not due to an optical frequency comb effect [113, 114, 119]. For optimal cooling of a given atomic species, the pulsed laser repetition rate should be of the order of the atom's excited state linewidth, while the energy in each laser pulse should correspond to $P_{\text{exc}} \simeq 1$

The laser-cooling of a single, trapped atom by broadband, modelocked laser pulses has been observed and quantified. The cooling is efficient, while the lowest temperatures are in single digits Kelvin. Such cooling of ions in strong rf traps localizes them to under 1 μm , which allows diffraction-limited ion imaging. Lower temperatures should be possible if longer modelocked laser pulses are used, as predicted by Eq. 7.13, where the final atom temperature scales approximately as the inverse of

³Here, the analyzed temperature data are presented for radial direction in the trap only (vertical in Fig. 7.2(a)). In the axial direction (horizontal in Fig. 7.2(a)), the observed temperature is about 5 times lower. This suggests that our simple theoretical model does not fully describe the cooling mechanism.

the pulse duration τ and quantified. The cooling is efficient, while the lowest temperatures are in single digits Kelvin. Such cooling of ions in strong rf traps localizes them to under $1\ \mu\text{m}$, which allows diffraction-limited ion imaging. Lower temperatures should be possible if longer modelocked laser pulses are used, as predicted by Eq. 7.13, where the final atom temperature scales approximately as the inverse of the pulse duration τ .

CHAPTER VIII

Ultrafast S to P Rabi Oscillations

8.1 Motivation

Recent progress in trapped ion quantum computing has relied on the entanglement of internal electronic states through the Coulomb-coupled motion of multiple ions mediated by optical dipole forces [9, 10, 18, 20, 21, 22]. However, these entangling operations require that the ions be kept in a pure motional quantum state, or at least within the Lamb-Dicke regime, where the ions are localized to well below an optical wavelength. Alternative entanglement schemes significantly relax this stiff requirement at the expense of controlling a coupling between trapped ions and ultrafast laser pulses [27, 28, 29, 24, 25, 26, 30].

In this Chapter, experiments are described that implement key components of these alternative quantum logic gate schemes by using ultrafast optical pulses to drive picosecond optical Rabi oscillations between the $5s\ ^2S_{1/2}$ and $5p\ ^2P_{3/2}$ states in a single trapped cadmium ion [120]. Such an ultrafast excitation results in the spontaneous emission of at most one photon which is crucial for the probabilistic generation of entanglement between ions based on the quantum interference of photons [27, 28, 29]. By adding a second, counter-propagating ultrafast pulse, the atom is excited from $S_{1/2}$ to $P_{3/2}$ then de-excited back to the $S_{1/2}$ ground state. The

resulting $2\hbar k$ momentum kick from the pulse pair is a fundamental component of ultrafast quantum logic gates [24, 25, 26]. When the ultrafast excitation drives an initial superposition stored in $S_{1/2}$ hyperfine qubit states of the ion, the frequency of the spontaneously-emitted photon becomes entangled with the hyperfine qubit, evidenced by the loss and recovery of contrast in a Ramsey interferometer. The entanglement of trapped ion qubits with photonic frequency qubits is critical to the operation of quantum gates between remotely-located ions [30].

8.2 Pulsed Excitation Experiments

A diagram of the experimental apparatus is shown in Fig. 8.1(a). Individual cadmium ions are trapped in a linear rf Paul trap with drive frequency $\Omega_T/2\pi = 36$ MHz and secular trapping frequencies $(\omega_x, \omega_y, \omega_z)/2\pi \approx (0.9, 0.9, 0.2)$ MHz [76]. Figure 8.1(b) shows the energy levels of $^{111}\text{Cd}^+$ relevant for the picosecond (ps) pulse excitation. The bandwidth of the ps pulses (~ 420 GHz [116]) is much larger than both the ground state and excited state hyperfine splittings (14.5 GHz and 0.6 GHz respectively) but is much smaller than the excited state fine structure splitting ($\sim 74,000$ GHz), enabling simultaneous excitation of all hyperfine states without coupling to the $5p\ ^2P_{1/2}$ excited state. In addition, the pulse length is much shorter than both the 2.65 ns excited state lifetime and the oscillation period of the ion in the trap ($> 1\ \mu\text{s}$), allowing for fast excitations without spontaneous emission or ion motion during the excitation pulse [76].

The ion is prepared in the $F = 0, m_F = 0$ ground state ($|\uparrow\rangle$) through optical pumping [121]. The ion is then excited from $|\uparrow\rangle$ to the $P_{3/2}$ excited state $F' = 1, m'_F = 0$ ($|\uparrow'\rangle$) by a single linearly polarized ps laser pulse [Fig. 8.1(b)]. Selection rules prevent the population of the $F' = 2, m'_F = 0$ ($|\downarrow'\rangle$) excited state. After

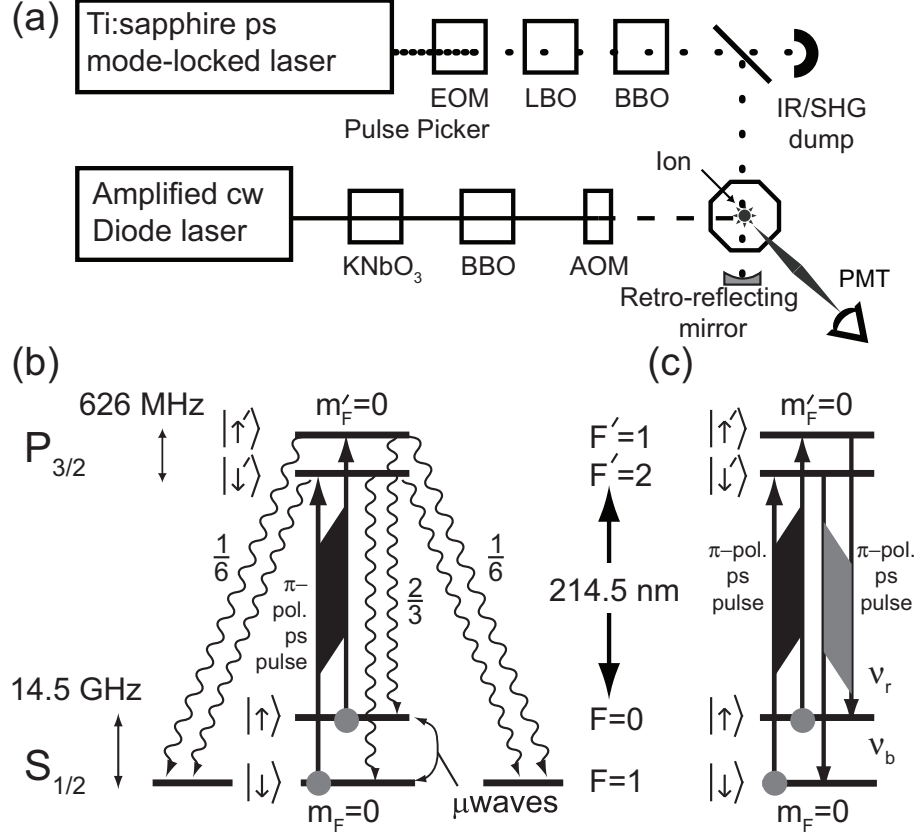


Figure 8.1: Rabi oscillation experiment setup. (a) A picosecond mode locked Ti:sapphire laser is tuned to four times the resonant wavelength of the ground state to $5p\ ^2P_{3/2}$ transition in $^{111}\text{Cd}^+$. The 80 MHz pulse train is sent through an electro-optic pulse picker, allowing the selection of single pulses while blocking all other pulses with an extinction ratio of better than 100:1 in the infrared. This single pulse is then frequency-quadrupled through non-linear crystals, filtered from the fundamental and second harmonic, and directed to the ion. The extinction ratio is expected to be on the order of 10^8 :1 in the UV. An amplified cw diode laser is also frequency quadrupled and tuned just red of the $S_{1/2}$ to $P_{3/2}$ transition for Doppler cooling of the ion within the trap, optical pumping to the dark state ($|\uparrow\rangle$) and ion state detection using the σ^+ cycling transition. Acousto-optic modulators (AOMs) are used to switch on and off the cw laser and to shift the optical pumping beam. Photons emitted from the ion are collected during state detection by an $f/2.1$ imaging lens and directed toward a photon counting photo-multiplier tube. (b) The relevant energy levels of $^{111}\text{Cd}^+$ where the π -polarized ultrafast laser pulse excites the ion from the ground state to the excited state. Selection rules prohibit both the $|\uparrow\rangle \rightarrow |\downarrow'\rangle$ and the $|\downarrow\rangle \rightarrow |\uparrow'\rangle$ transitions. The three possible decay channels for each excited state are shown with fluorescence branching ratios. (c) The first ultrafast laser pulse coherently excites and the second pulse coherently de-excites the ion.

waiting a time ($10\ \mu\text{s}$) much longer than the excited state lifetime, the resulting atomic ground state populations are measured through fluorescence detection [122]. All three $F = 1$ states are equally bright, while the $F = 0$ state is dark [71]. The results for 60,000 runs at each pulse energy are fit to known bright and dark state histograms [70] giving an average ion brightness shown in Fig. 8.2(a). The probability of measuring a bright state is $1/3$ the excitation probability of the $P_{3/2}$ excited state, as expected from the fluorescence branching ratios [Fig. 8.1(b)]. Therefore, the bright state probability as a function of pulse energy is fit to $P_{\text{bright}} = (1/3) \sin^2(\theta/2)$, where the Rabi oscillation rotation angle $\theta = a\sqrt{E}$ for a single pulse energy E (in pJ) and fit parameter a . The single fit parameter for the data shown in Fig. 8.2(a) is $a = 0.42\ \text{pJ}^{-1/2}$, which is on the same order as the estimated value ($0.28\ \text{pJ}^{-1/2}$) based on the beam waist, pulse length, and pulse shape (Appendix C). The maximum rotation angle was approximately $\theta = \pi$, limited by the available UV laser power.

In order to achieve rotations larger than π , the first ps pulse is retro-reflected via a curved mirror (radius 10 cm) and sent back to the ion as a second pulse. The time delay between the two pulses is approximately 680 ps corresponding to the position of the retro-reflecting mirror (an optical path delay of about 20 cm) giving a probability of spontaneous emission of $\sim 23\%$ between the pulses. The second pulse changes the state population of the ion [Fig. 8.2(b)] by adding coherently to the rotation of the first pulse. However, over many runs the relative optical phase between these rotations is scrambled, owing to the thermal motion of the ion. The rms extent of the Doppler-cooled motion is about twice the optical wavelength ($k\sqrt{\langle x_{\text{ion}}^2 \rangle} = \eta\sqrt{2\bar{n} + 1} \approx 1.9$ where $\eta \approx 0.22$ is the Lamb-Dicke parameter and $\bar{n} \sim 40$ from Doppler cooling). Therefore, even though each pair of counter-propagating pulses interacts with the ion on a time scale much faster than the motional period

of the ion, there is an incoherent averaging over many runs of the optical phase between the two pulses. For a two-level system without spontaneous emission and with the same rotation angle θ for both pulses, an average of many experiments gives an excited state population of $\sin^2(\theta) \langle \cos^2(kx_{ion}) \rangle$. This has twice the Rabi rotation angle but, after averaging over the motional extent of the ion, half the brightness of the single pulse experiment (Appendix D). Numerical solutions to the Optical Bloch Equations (OBE) for the relevant states including spontaneous emission are shown in Fig. 8.2(b) for various attenuation levels of the second pulse due to imperfect transmission of the vacuum windows, beam clipping on the optics, and imperfect focusing (Appendix E). The OBE solution for 60% attenuation is in qualitative agreement with the data compared to the ideal case, where the ion brightness is larger than the expected maximum of $1/6$ due to spontaneous emission and second pulse attenuation.

8.3 Ramsey Experiments

To show coherence in the ultrafast excitation of the ion, these optical pulses are inserted into a Ramsey interferometer consisting of two microwave $\pi/2$ -pulses (Ramsey zones). The ion is again initialized to the dark ($|\uparrow\rangle$) state and the first microwave $\pi/2$ -pulse prepares the ion in the superposition $|\uparrow\rangle + |\downarrow\rangle$ of the ground state “clock” qubit, where $|\downarrow\rangle$ is the $F = 1, m_F = 0$ ground state. A single ultrafast laser pulse of variable energy is sent to the ion and the resultant ion state is rotated with a second microwave $\pi/2$ -pulse, phase shifted with respect to the first after a time delay sufficiently long to allow for spontaneous emission. The ion brightness is measured as a function of the second microwave pulse phase, giving Ramsey fringes [inset of Fig. 8.3(a)]. The contrast of the Ramsey fringe is extracted from a sinusoidal

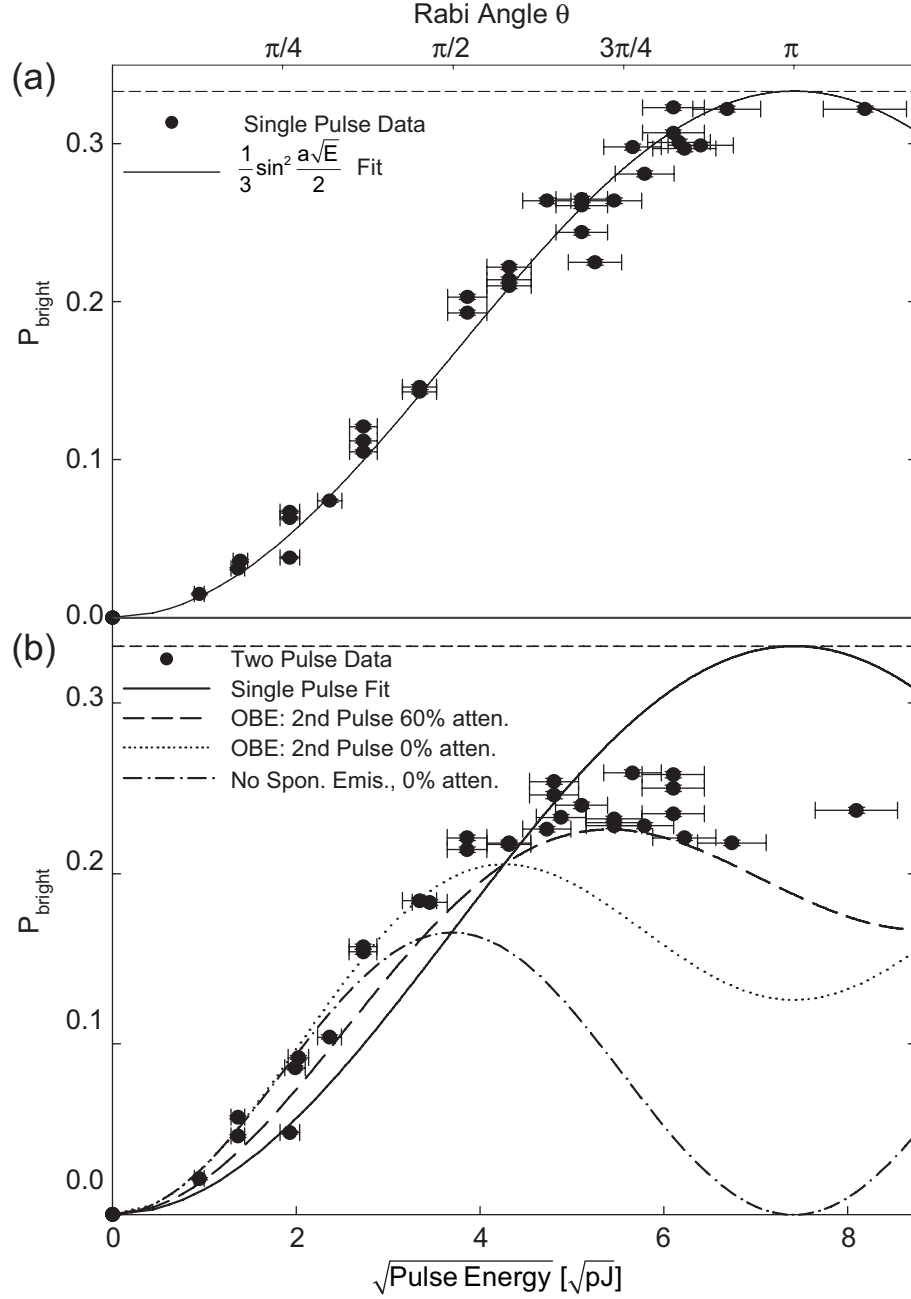


Figure 8.2: The ion bright state population as a function of pulse energy. (a) Each point represents a collection of 60,000 runs where the ion was prepared in the dark state ($|\uparrow\rangle$), a single laser pulse was applied, and then the ion state was measured. The collection of runs is fit to known bright/dark state histograms [70]. As the pulsed laser drives a π -pulse from the $S_{1/2}$ to $P_{3/2}$ states, the bright state population approaches $1/3$ (horizontal dashed line), determined by the spontaneous emission branching ratio [Fig. 8.1(b)]. The data are fit to a single parameter giving a value $a = 0.42 \text{ pJ}^{-1/2}$. (b) A second laser pulse, delayed by approximately 680 ps, further drives the ion, limited by the spontaneous emission probability (23%) and attenuation between the first and second laser pulse intensities. The solutions to the Optical Bloch Equations (OBE) are shown for a second pulse with 60% attenuation and no attenuation.

fit and is shown as a function of pulse energy [Fig. 8.3(a)]. The single laser pulse drives the ion to a superposition of the $P_{3/2}$ excited state “clock” hyperfine levels $|\downarrow'\rangle + |\uparrow'\rangle$ [Fig. 8.1(b)]. Upon spontaneous emission of a π -polarized photon, the ion hyperfine and photon frequency qubits ($|\nu_r\rangle$ and $|\nu_b\rangle$, $\nu_b - \nu_r \approx 13.9$ GHz) are in the entangled state $|\uparrow\rangle|\nu_r\rangle + |\downarrow\rangle|\nu_b\rangle$ [30, 123, 124]. However, in this experiment the photon is not measured in a controlled, precisely timed fashion. This corresponds to tracing over the photon portion of the density matrix which leads to a loss of coherence in the ion superposition, leaving the ion in a mixed state of $|\uparrow\rangle$ and $|\downarrow\rangle$. Thus, a loss of coherence in the Ramsey fringes is consistent with prior entanglement between the photon frequency qubit and the ion hyperfine qubit. The loss of contrast as a function of the pulse energy is shown in Fig. 8.3(a) and is related to the ion excitation probability [Fig. 8.2(a)] through spontaneous emission.

In order to show that this ultrafast coupling is coherent and that the emitted photon is indeed entangled with the atomic qubit, a two-pulse experiment is performed [Fig. 8.1(c)]. A second pulse (delayed from the first pulse by 680 ps) is sent to the ion between the Ramsey zones. In each individual run, the second laser pulse adds coherently to the first pulse with optical phase kx_{ion} as before. However, this dependence on the optical phase can be eliminated by using an appropriate combination of counter-propagating π -pulses [71]. The recovery of contrast in the Ramsey experiment shown in Fig. 8.3(b) indicates a coherent, controlled interaction where the first pulse transfers the superposition up to the excited state and the second pulse partly returns the population back to the ground state. The Ramsey fringes accumulate a phase during the time t (≈ 680 ps) spent in the excited state that is approximately $\Delta\omega_{HF}t = 18.9\pi$, where $\Delta\omega_{HF}$ is the frequency difference between the ground state and excited state hyperfine splittings. By reducing the delay between

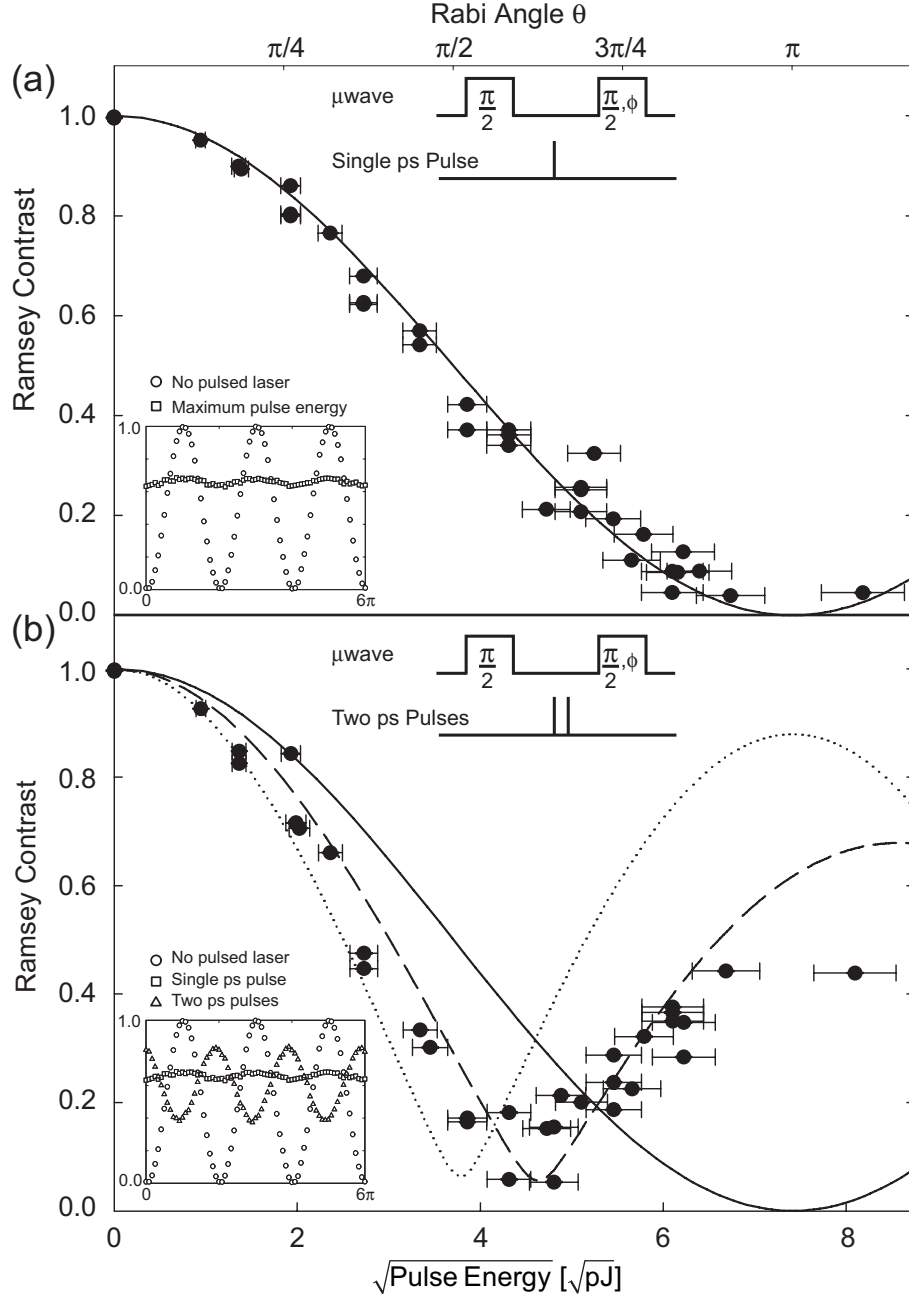


Figure 8.3: Ramsey fringe contrast. (a) The contrast of the phase curve in a Ramsey experiment with the pulsed laser interjected between the two Ramsey zones as a function of pulse energy. The contrast disappears with a π excitation because, on spontaneous emission, the photon is measured and coherence in the ion superposition is lost. The solid curve is the OBE solution for the single pulse. The inset shows the Ramsey fringes for no ultrafast pulse and for the maximum pulse energy. (b) A second laser pulse, coherently driving the population back down to the ground state, partially recovers the phase coherence of the ion with a phase shift of 18.9π . The inset shows the Ramsey fringes for no laser pulses, a single π -pulse, and two ultrafast pulses. The OBE solution for 60% attenuation of the second pulse is shown as the dashed line. The dotted line is the same model for no attenuation of the second pulse.

two π -pulses to be much less than the excited state lifetime, full Ramsey contrast can be recovered.

Numerical solution to the Optical Bloch Equations (OBE) are again used to describe the ion-pulse interaction in the Ramsey experiments including spontaneous emission. The value of the fit parameter a from Fig. 8.2(a) is used as the only free parameter in the model, giving the solid curve in Fig. 8.3(a). The two curves from the OBE in Fig. 8.3(b) use the value of a , the second pulse delay (680 ps), and are shown for two different values of attenuation of the second pulse. The OBE solution for 60% attenuation describes well the disappearance and revival of the Ramsey fringe contrast. The counter-propagating pulses also impart a momentum kick of $2\hbar k$ to the ion, but since this impulse is independent of the qubit state in this experiment, this results in a global qubit phase and the motional state factors.

8.4 Excited State Hyperfine Splitting Measurement

The phase shift of the Ramsey fringes [inset of Fig. 8.4] is also used to make a precise measurement of the frequency difference $\Delta\omega_{HF}$ between the ground state and excited state hyperfine splittings. The curved retro-reflecting mirror was replaced by a 7.5 cm lens and a movable flat mirror to control the pulse separation. The pulse energy was set to give a π -pulse on the single $S_{1/2}$ to $P_{3/2}$ transition, and the retro-reflected pulse recovers the phase coherence with a contrast of about 40%. The delay of the second pulse is then varied by translating the mirror, and the phase of each curve is extracted via a sinusoidal fit to the data. The phase as a function of pulse delay is shown in Fig. 8.4 along with the linear least-squares fit. The slope of the line gives a frequency difference of $d\phi/dt = \Delta\omega_{HF} = 2\pi \times 13.904 \pm 0.004$ GHz. Compared with the known frequency of the ground state hyperfine splitting of 14.530 GHz, this

yields the excited state hyperfine splitting of 626 ± 4 MHz. This measurement is insensitive to fluctuations in the laser pulse energy as well as small changes in the ion position, as both of these change the contrast but not the phase of the Ramsey fringes. The precision of this measurement is limited by statistics but, in principle, this technique appears to be only limited by the accuracy of the pulse delay timing as well as systematic effects common with trapped ion frequency standards [125].

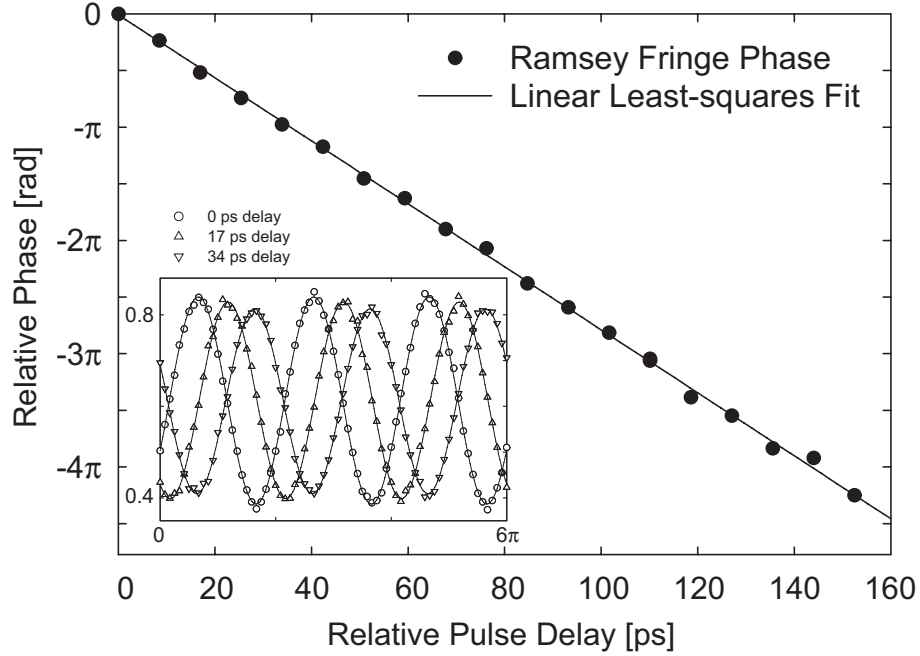


Figure 8.4: Excited state hyperfine splitting measurement. The phase of the Ramsey fringes as a function of the time delay between two picosecond laser pulses, set by the linear translation of the retro-reflecting mirror. The uncertainty in the time delay of each point is 0.1 ps and the uncertainty in the phase is 0.01 rad. The slope of the line gives the frequency difference between the ground state and excited state hyperfine splittings of $\Delta\omega_{HF} = 13.904 \pm 0.004$ GHz. The inset figure shows three Ramsey fringes for three relative delays.

In conclusion, it was shown that with a single ultrafast laser pulse, one can drive with near unit probability the optical $S_{1/2}$ to $P_{3/2}$ transition in a single trapped cadmium ion. The coherent coupling between the atomic hyperfine qubit and photon frequency qubit, shown in the disappearance and revival of Ramsey fringes, is the key component for operating probabilistic quantum logic gates that are not dependent on ion motion [30]. The resulting momentum kick is also crucial to ultrafast quantum

logic gates using Coulomb-coupled ions without stringent motional requirements [25, 26].

CHAPTER IX

Conclusion

Throughout this work we have shown key components for building a scalable trapped ion quantum computer. The techniques for ion trap modeling and desing that were described in this work have been expanded and used by many researchers in building advanced ion trap structures. The three-layer ceramic trap was used in many quantum information experiments in our research group and was a successful design. In addition, the use of three-layers made the design expandable to the first two-dimensional ion trap experiments that included ion shuttling around a corner. That advanced trap was based on the technology developed in this work.

The fabrication and successful operation of the GaAs microtrap was a key result in opening the possibility of making semiconductor-technology based ion traps. In order to scale up the number of traps in a given structure as well as to dramatically increase the trap zone density, researchers have continued to pursue similar technologies including single-layer planar traps. Research is continuing in the development of more advanced traps with better trapping characteristics for scalable quantum computing.

Although most of the work in trapped ion quantum information has been done using the quantum control of the common-mode motion of ions in tightly confined

traps, there are other possible avenues of research that are, in principle, scalable. The research described in this work involving the interaction of ultrafast laser pulses with single ions is fundamental in the implementation of these alternatives. We have shown that we can make a very precise measurement of the excited state lifetime, cool using the ultrafast laser pulses, and that we can coherently control the excitation of the electronic states of the ions. In addition, because we can excite superposition states, this allows the creation of quantum logic gates that use the ion-photon entanglement.

Future work in ion-pulsed laser interactions include the application of spin-dependent momentum kicks. It is possible to entangle Coulomb-coupled ions in thermal states of motion using these ultrafast momentum kicks. Another direction of research is to use the ultrafast excitations as a means of generating single-photon, single-ion entangled states for the generation of remotely located entangled states of ions. Both of these experiments are currently being pursued by researchers in our group.

APPENDICES

APPENDIX A

Coaxial Resonator Fields

The properties of a quarter-wave coaxial resonator can be calculated exactly. Although the helical resonator (from Section 2.7.1) has a more complicated design, the coaxial approximation is sufficient to understand the operation of the resonator. From the resonator, it is necessary to know the relationship between the input power P , the resonator Q and the maximum voltage applied to the trap V_0 . To find this relationship, the fields inside the resonator must first be found. The current on the center post of the resonator [Fig. A.1(a)] as a function of position and time is

$$I(z, t) = I_0 \sin(kz) \cos(\omega_0 t) \quad (\text{A.1})$$

where I_0 is the maximum current, $k = 2\pi/\lambda$ is the wavevector and $\omega_0 = kc$ is the natural frequency of the resonator. The magnetic field can be calculated from Ampere's Law (neglecting edge effects) and is

$$\vec{B}(\rho, z, t) = \frac{\mu_0 I_0}{2\pi\rho} \cos(kz) \cos(\omega_0 t) \hat{\phi}. \quad (\text{A.2})$$

for radial distance ρ from the center and azimuthal angle ϕ [Fig. A.1(c)]. The electric field is straightforward to calculate from the magnetic field of Eq. A.2 and is

$$\vec{E}(\rho, z, t) = \sqrt{\frac{\mu_0}{\epsilon_0}} \frac{I_0}{2\pi\rho} \sin(kz) \sin(\omega_0 t) \hat{\rho}. \quad (\text{A.3})$$

Note that the resonator is assumed to not be filled with any dielectric material. If it were, the appropriate changes must be made to accommodate the material properties in Eqs. A.2 and A.3.

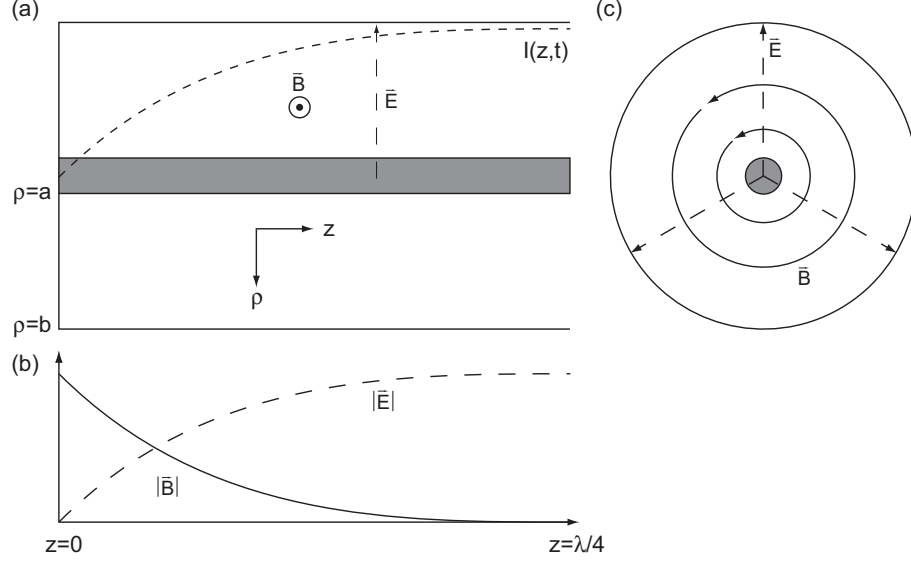


Figure A.1: Electromagnetic fields in a coaxial resonator. (a) A side view of the coaxial resonator. The current is carried on the center post and is grounded at the back. Electric and magnetic fields vectors are shown along with the current as a function of position along the z -axis. (b) The magnitude of the electric and magnetic fields as a function of position along the z -axis. (c) The direction of the electric and magnetic fields in a transverse view of the coaxial resonator. The current is carried on the center post.

The voltage drop between the center post and the outside conductor in the coaxial resonator can now be calculated from the electric field at the point $z = \lambda/4$, the length of the quarter-wave resonator:

$$\Delta V = \int_a^b \vec{E}(\rho, \lambda/4, \pi/2\omega_0) \cdot d\vec{\rho} \quad (\text{A.4})$$

where the voltage maximum at $t = \pi/2\omega_0$ was used. Because the electric field is along the $\hat{\rho}$ direction, the integral is straight-forward to carry out giving

$$\Delta V = \sqrt{\frac{\mu_0}{\epsilon_0}} \frac{I_0}{2\pi} \ln \frac{b}{a}. \quad (\text{A.5})$$

The electric field from Eq. A.3 can now be re-written in terms of the maximum

voltage drop $V_0 \equiv \Delta V$.

$$\vec{E}(\rho, z, t) = \frac{V_0}{\left(\ln \frac{b}{a}\right) \rho} \sin(kz) \sin(\omega_0 t) \hat{\rho}. \quad (\text{A.6})$$

The resonator $Q = \omega_0 U / P_{\text{loss}}$ is a function of the frequency ω_0 , the average energy stored in the resonator U and the power lost in the resonator P_{loss} . In steady-state, the power lost in the resonator is equal to the power sent to the resonator, P . The average energy stored in the resonator can be calculated from the time average of the electric field:

$$U = \left\langle \int_V \epsilon_0 |\vec{E}|^2 dV \right\rangle \quad (\text{A.7})$$

$$= \frac{\omega_0}{2\pi} \int_{-\pi/\omega_0}^{\pi/\omega_0} \int_V \epsilon_0 |\vec{E}|^2 dV dt \quad (\text{A.8})$$

$$= \epsilon_0 \left[\frac{V_0}{\ln \frac{b}{a}} \right]^2 \frac{\omega_0}{2\pi} \int_{-\pi/\omega_0}^{\pi/\omega_0} \sin^2(\omega_0 t) dt \int_0^{2\pi} d\phi \int_a^b \frac{1}{\rho^2} \rho d\rho \int_0^{\lambda/4} \sin^2(kz) dz \quad (\text{A.9})$$

$$= \epsilon_0 \left[\frac{V_0}{\ln \frac{b}{a}} \right]^2 \left(\frac{1}{2} \right) (2\pi) \left(\ln \frac{b}{a} \right) \left(\frac{\lambda}{8} \right) \quad (\text{A.10})$$

$$= \frac{\epsilon_0 \pi \lambda V_0^2}{8 \ln \frac{b}{a}} \quad (\text{A.11})$$

The relationship between the wavelength and the frequency $\lambda = 2\pi c / \omega_0$, and the speed of light $c = 1 / \sqrt{\epsilon_0 \mu_0}$ can be used to re-write Eq. A.11.

$$U = \sqrt{\frac{\epsilon_0}{\mu_0}} \frac{\pi^2 V_0^2}{4\omega_0} \ln \frac{b}{a} \quad (\text{A.12})$$

The resonator Q can now be described in terms of the maximum voltage drop at $z = \lambda/4$ and the applied power P

$$Q = \omega_0 \frac{U}{P_{\text{loss}}} \quad (\text{A.13})$$

$$PQ = \omega_0 \left[\sqrt{\frac{\epsilon_0}{\mu_0}} \frac{\pi^2 V_0^2}{4\omega_0 \ln \frac{b}{a}} \right] \quad (\text{A.14})$$

$$PQ = \sqrt{\frac{\epsilon_0}{\mu_0}} \frac{\pi^2 V_0^2}{4 \ln \frac{b}{a}} \quad (\text{A.15})$$

This last equation can be inverted, solving for the voltage V_0 giving

$$V_0 = \left[\frac{4}{\pi^2} \sqrt{\frac{\mu_0}{\epsilon_0}} \ln \frac{b}{a} \right]^{1/2} \sqrt{PQ} \quad (\text{A.16})$$

which is the same as Eq. 2.21 with

$$\zeta = \left[\frac{4}{\pi^2} \sqrt{\frac{\mu_0}{\epsilon_0}} \ln \frac{b}{a} \right]^{1/2}. \quad (\text{A.17})$$

This scale factor is geometric in nature and for a ratio of $b/a = 5$, the scale factor is $\zeta \approx 16$. This scale factor for the helical resonator is not the same, but experimental evidence shows that it is still on the order of about 10.

APPENDIX B

Analytic Solution of the Transverse Potential

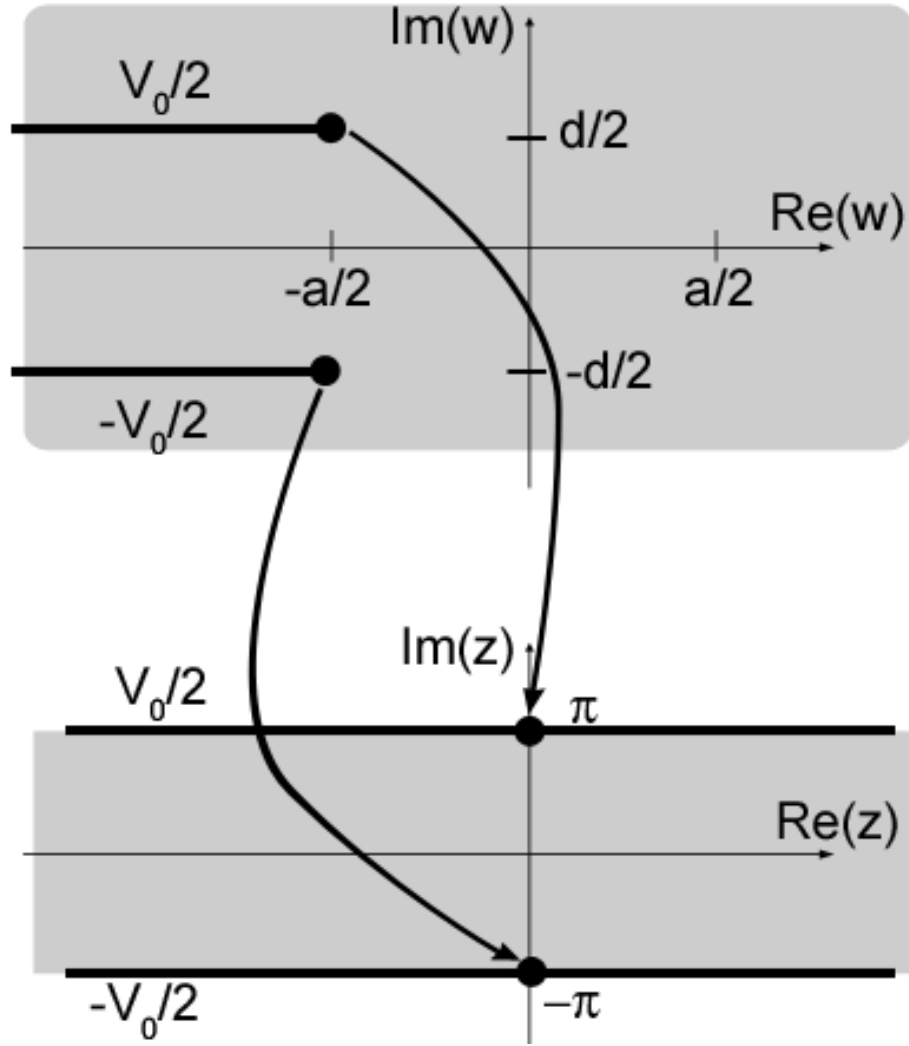


Figure B.1: A linear microtrap model in the complex plane. The linear microtrap model in the complex w plane with semi-infinite electrodes that terminate at $\pm a/2 \pm id/2$ with applied voltages $\pm V_0/2$.

The cross-section of the linear microtrap can also be modeled as semi-infinite electrodes in a complex plane. This model enables calculation of an analytic solution for the geometric factor η in the limit of infinitely thin electrodes. Following the analysis of parallel-plate capacitor fringe fields of Valluri et.al [126], the cross-section of the left cantilever electrodes are described in the complex plane as lines that go from negative infinity along the real axis and terminate at $-a/2 \pm id/2$, as shown in Fig. B.1. The right set of electrodes (not shown) are a mirror image across the $x = 0$ line and terminate at $a/2 \pm id/2$. The electrodes are then mapped to an infinite parallel plate capacitor. The function that does this mapping is

$$\pm \frac{2w\pi}{d} + \frac{a\pi}{d} - 1 = z + e^z. \quad (\text{B.1})$$

The positive value maps the parallel plate capacitor to the left set of electrodes in the w plane, and the negative corresponds to the right set. The potential in the strip between the two electrodes in the z plane is simply the potential between two parallel plates in a capacitor, written in complex notation:

$$\Phi = \frac{V_0}{2\pi} \text{Im}(z), \quad (\text{B.2})$$

where $\text{Im}(z)$ denotes the imaginary part of z .

To find the potential of the original electrode geometry, the inverse function of Eq. B.1 is needed. With that inverse map the potential in the w plane can be evaluated. The inverse map can be written in terms of the Lambert W function, $W_k(\xi)$, following [126].

$$z_{\pm} = \zeta_{\pm} - W_k(e^{\zeta_{\pm}}) \quad (\text{B.3})$$

where $\zeta_{\pm} = \pm \frac{2w\pi}{d} + \frac{a\pi}{d} - 1$ is a scaled complex variable. The Lambert W function $y = W_k(x)$ is the solution to the equation $x = y \exp y$. For complex variables, it is

important to select the proper branch of $W_k(\xi)$ when evaluating the function. The appropriate branch is found using [126]

$$k = \left\lceil \frac{\text{Im}(\zeta) - \pi}{2\pi} \right\rceil, \quad (\text{B.4})$$

where $\lceil \cdot \rceil$ denotes the ceiling function which indicates that the argument inside the ceiling function should be rounded up to the nearest integer.

If the tip-to-tip cantilever separation a is much greater than the layer separation d ($\alpha = a/d \gg 1$), the potential at the center of the trap can be approximated as the linear combination of the potential from both the left electrodes and the right electrodes

$$\Phi = \frac{V_0}{2\pi} (\text{Im}(z_+) + \text{Im}(z_-)). \quad (\text{B.5})$$

With this approximation ($\alpha \gg 1$) an asymptotic form of the Lambert W function exists that leads to a simplification of the inverse map Eq. B.3. The principal branch of the Lambert W function has an asymptotic form:

$$W_0(\xi) \approx \ln \xi - \ln(\ln \xi), \xi \gg 1. \quad (\text{B.6})$$

Inserting Eq. B.6 into Eq. B.3, the inverse map becomes: $z \approx \ln \zeta_{\pm}$. Expanding the log function about $w = 0$, Eq. B.3 can be written:

$$z_{\pm} = \ln\left(\frac{a\pi}{d} - 1\right) + \left[\pm \frac{2\pi w}{a\pi - d} - \frac{1}{2} \left[\frac{2\pi w}{a\pi - d} \right]^2 + \dots \right]. \quad (\text{B.7})$$

Since the potential is the linear combination of $\text{Im}(z_+)$ and $\text{Im}(z_-)$ (Eq. B.5) and the linear terms are opposite in sign, only the quadratic term contributes to the potential of the microtrap. Squaring the complex variable $w = u + iv$ and keeping only the second-order imaginary terms, one finds that the potential is

$$\Phi = -\frac{4\pi V_0}{(a\pi - d)^2} uv. \quad (\text{B.8})$$

By rotating the coordinate system about the origin by $\theta = \pi/4$, the potential is written in a form that allow for easy comparison with the quadrupole potential of Eq. 4.11:

$$\Phi = \frac{2\pi V_0}{(a\pi - d)^2} (u'^2 - v'^2). \quad (\text{B.9})$$

The geometric factor η can be found for a microtrap with effective distance $\ell_{\text{eff}} = \sqrt{(a/2)^2 + (d/2)^2}$.

$$\begin{aligned} \eta &= \frac{4\pi}{(a\pi - d)^2} \ell_{\text{eff}}^2 \\ &= \pi \frac{\alpha^2 + 1}{(\alpha\pi - 1)^2}. \end{aligned} \quad (\text{B.10})$$

This analytic solution of the geometric factor is valid in the limit where the trap aspect ratio is large: when the tip-to-tip cantilever separation is much larger then the layer separation. The geometric factor asymptotically approaches $\eta = 1/\pi$ in this limit. The analytic solution (Eq. B.10) is shown as the solid line in Fig. 4.5. Note that this complex model assumes infinitely thin electrodes which correspond to a large value for the ratio of the layer separation to the layer thickness $\delta = d/w \rightarrow \infty$. The values for η found via numerical simulations approach the analytic solution as δ increases and also approach the asymptotic value of $\eta = 1/\pi$ for large α .

In addition, the analytic model can be used to calculate the asymptotic values for the ponderomotive potential depth and the maximum trap size along the weak axis r_{max} . Inserting the asymptotic form of the Lambert W function (Eq. B.6) directly into the potential (Eq. B.5) and evaluating the imaginary part, the potential can be written directly as a function of u and v .

$$\begin{aligned} \Phi &= \frac{V_0}{2\pi} \left[\tan^{-1} \left(\frac{2v}{2u + a - d/\pi} \right) \right. \\ &\quad \left. + \tan^{-1} \left(\frac{-2v}{-2u + a - d/\pi} \right) \right] \end{aligned} \quad (\text{B.11})$$

The pseudopotential can then be directly evaluated, using a two-dimensional gradient, from Eq. 4.8. The maximum of the pseudopotential along the v -axis ($v = r_{\max}$) lies at

$$\begin{aligned} r_{\max} &= \frac{1}{2\pi}(a\pi - d) \\ &= \frac{a}{2}\left(1 - \frac{1}{\pi\alpha}\right). \end{aligned} \tag{B.12}$$

The location of the potential maximum asymptotically approaches $r_{\max} = a/2$ as the aspect ratio goes to infinity. The trap depth is the pseudopotential evaluated at this maximum:

$$\psi(r_{\max}) = \frac{e^2 V_0^2}{4m\Omega_T^2} \frac{1}{a^2 \pi^2 \left(1 - \frac{1}{\alpha\pi}\right)^2}. \tag{B.13}$$

The analytic solution for the scaled trap depth is shown in Fig. 4.7 and approaches the asymptotic value of 2694 [$\text{K}\cdot\mu\text{m}^2/\text{V}^2$] for large α .

APPENDIX C

Picosecond Pulse Generation and Characterization

C.1 Picosecond Generation

Generation of picosecond laser pulses in the infrared is done via the Millenia-pumped Spectra-Physics Tsunami Ti:Sapphire laser. The Ti:sapphire cavity is actively mode locked using an acousto-optic modulator (AOM) as the means of shifting cavity losses above and below the lasing threshold. In addition a Gires-Tournois Interferometer (GTI) is inserted into the cavity, fixing the pulse width of the laser in the picosecond range, nominally at 2 ps. The wavelength of the cavity is tuned with a birefringent filter (bi-fi) and can be set to sub-nanometer precision. The wavelength is measured with the Burleigh wavemeter with the Tsunami not mode-locked. The nominal wavelength is 906.28 nm (858.03 nm), four times the $S_{1/2}$ to $P_{1/2}$ ($P_{3/2}$) transition wavelength in singly ionized cadmium. With 10 W of pump power, the Tsunami produces 1.7 W (2.5 W) average power in the IR.

The pulse shape is determined by the mode-locking mechanism. Because the dominant pulse generating mechanism is the optical Kerr effect, the electric field in the time domain has the envelope of a sech function [127]:

$$E(t) = \sqrt{\frac{W}{2\tau_s}} \operatorname{sech}\left(\frac{t}{\tau_s}\right) e^{i\omega t + \varphi} \quad (\text{C.1})$$

where W is the pulse energy and τ_s is the pulse width.

C.1.1 Pulse Width Measurement. The width of the intensity envelope can be measured directly using an auto-correlator. The intensity of the pulse is

$$I(t) = I_{peak} \operatorname{sech}^2 \left(\frac{w_{\operatorname{sech}} t}{\tau_{\operatorname{FWHM}}} \right) \quad (\text{C.2})$$

with peak pulse intensity I_{peak} , full width half max (FWHM) of the peak $\tau_{\operatorname{FWHM}}$. The scale coefficient w_{sech} comes from the sech^2 by solving for the FWHM of the function $f(t) = \operatorname{sech}^2(t)$. Since the maximum of this function is $f(0) = 1$, the FWHM is twice the inverse function of $f(t) = 1/2$. This can be written as

$$w_{\operatorname{sech}} = 2 \ln(1 + \sqrt{2}) \approx 1.76. \quad (\text{C.3})$$

The functional form of the sech and sech^2 functions can be seen in Fig. C.1.

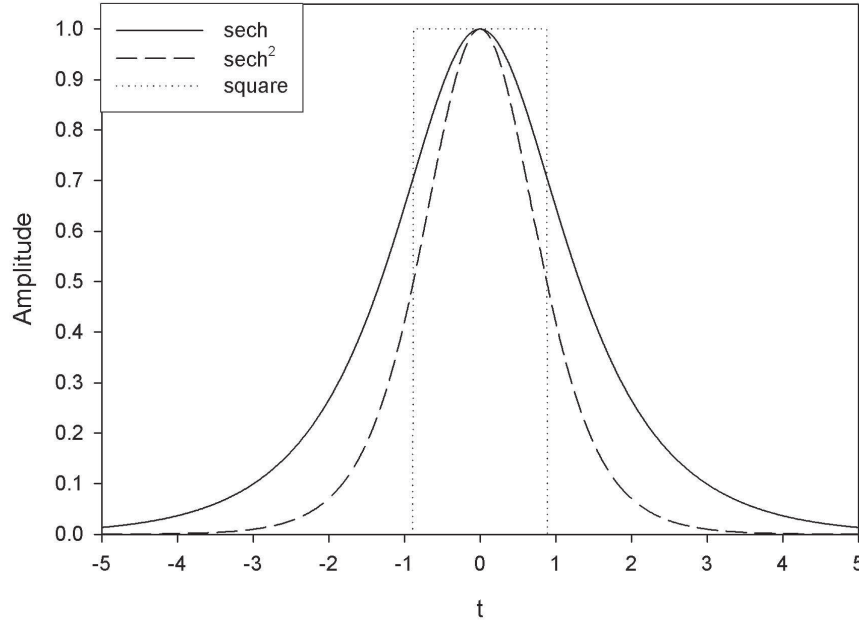


Figure C.1: Functional form of sech pulses. The functional form of $f(t) = \operatorname{sech} t$, $f(t) = \operatorname{sech}^2 t$ and a square pulse of width w_{sech} .

An optical intensity autocorrelation measurement uses second-harmonic generation (SHG) to measure the overlap of two pulses. The autocorrelation function that

is measured is

$$A^{(2)}(\tau) = \int_{-\infty}^{\infty} I(t)I(t + \tau)dt \quad (\text{C.4})$$

where the (2) indicates that this is a second-order autocorrelation. The intensity envelope must be integrated to fit to the data. The autocorrelation not only gives information about the pulse width, but it also gives information about the pulse shape. A Gaussian pulse shape has a different autocorrelation from a sech pulse. The difference in shape of the autocorrelation can be seen in Fig. C.2. The autocorrelation function of the sech^2 pulse is

$$A^{(2)}(\tau) = \frac{3(\tau \cosh \tau - \sinh \tau)}{\sinh^3 \tau} \quad (\text{C.5})$$

and the autocorrelation function of the Gaussian pulse is

$$A^{(2)}(\tau) = e^{-\tau^2/4}. \quad (\text{C.6})$$

The pulses from the Tsunami mode-locked laser were measured using the autocorrelation technique to have a pulse width of $\tau = 1.8$ ps.

C.1.2 Pulse Power There is a relationship between the peak power of the pulses and the average power. Because the average power is easier to measure experimentally, this relationship can be used to extract the peak power. Average power is defined as the time integral of the peak times the repetition rate R of the pulses

$$P_{avg} = R \int_{-\infty}^{\infty} P_{single}(t)dt. \quad (\text{C.7})$$

The single pulse power can be written as

$$P_{single} = P_{max} \text{sech}^2 w_{\text{sech}} t / \tau_{\text{FWHM}}. \quad (\text{C.8})$$

Integrating over the pulse width, the average power is

$$P_{avg} = aR\tau_{\text{FWHM}}P_{max} \quad (\text{C.9})$$

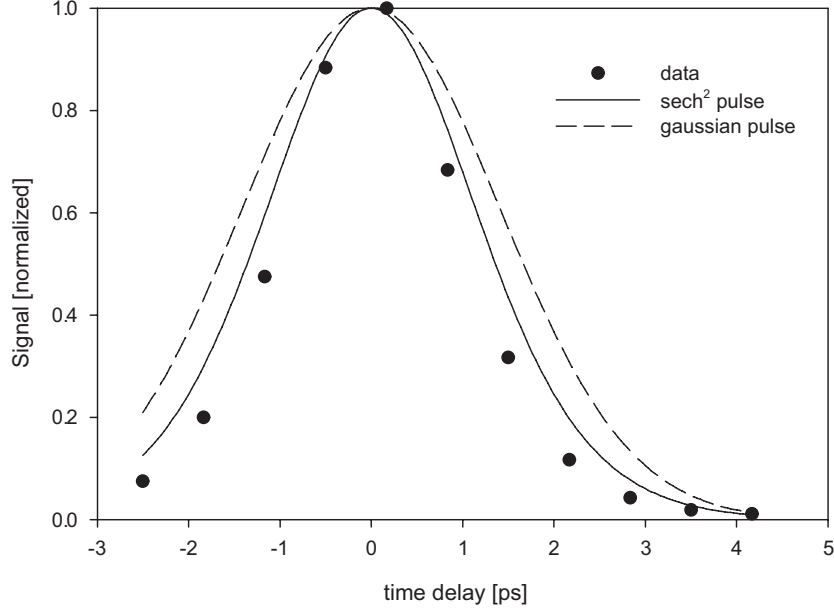


Figure C.2: Autocorrelation data and functional form of sech versus Gaussian pulses. The data are the measured autocorrelation of the Tsunami pulsed laser. The two curves are not fits, but rather sech^2 and gaussian curves. The pulse width is approximately 1.6 ps.

where $a = 2/w_{\text{sech}} \approx 1.13$ for sech^2 pulses and $a = \sqrt{\pi/4 \ln(2)} \approx 1.06$ for Gaussian pulses. The energy of a single pulse is found by inverting Eq. C.9.

$$E = \frac{P_{\text{avg}}}{R} = a\tau_{\text{FWHM}}P_{\text{max}} \quad (\text{C.10})$$

C.1.3 Second Harmonic Generation. When a pulse is frequency doubled, the electric field gets quadrupled. The change in the intensity envelope of the pulse after the electric field is thus squared. The pulse width shrinks for the doubled pulse- the new width is $w_{\text{sech}}^{(2)} = 2 \text{sech}^{-1}(1/2^{1/4})$. The ratio of the fundamental to the harmonic pulse widths is approximately 1.45. After a second SHG stage, the ratio of the initial to quadrupled pulse widths is approximately 2.11 for sech^2 pulses. This same factor is 2 for Gaussian pulses. This relationship is

$$\tau^{(4)} = 1/b\tau^{(0)} \quad (\text{C.11})$$

where $b = 2.11$ for sech^2 pulses and $b = 2$ for Gaussian. The (4) is for the fourth harmonic (UV) of the fundamental (0) or (IR).

C.2 Atomic Transitions.

The rotation of the atomic state in the Bloch sphere is dependent on the electric field pulse area. For a simple square wave, or for cw radiation this is simply $\theta = gt$, where g is the Rabi frequency $g = \mu E/\hbar$ and t is the time of the square wave. For a pulse, the rotation is also the pulse area, but the electric field must be integrated over the time duration of the single pulse. The rotation becomes

$$\theta = \frac{\mu}{\hbar} \int_{-\infty}^{\infty} E(t) dt. \quad (\text{C.12})$$

Alternatively, one could rewrite this in terms of Rabi frequencies, simplifying the connection to experiment. Let

$$g(t) = g_{max} \operatorname{sech} \frac{w_{\operatorname{sech}} t}{\tau_{\operatorname{FWHM}}^{uv}} \quad (\text{C.13})$$

where $\tau_{\operatorname{FWHM}}^{uv}$ is the width of the intensity envelope of the ultraviolet radiation, resonant with the $S_{1/2}$ to $P_{3/2}$ transition. The rotation in the Bloch sphere then becomes

$$\theta = \int_{-\infty}^{\infty} g(t) dt. \quad (\text{C.14})$$

This integral is evaluated, giving a rotation of

$$\theta = \frac{\pi g_{max} \tau_{\operatorname{FWHM}}^{uv}}{w_{\operatorname{sech}}}. \quad (\text{C.15})$$

To make the connection with experiment, the saturation parameter, which relates the Rabi frequency with the intensity of the pulse is used:

$$\frac{g_{max}^2}{\gamma^2} = \frac{I_{max} |c|^2}{2I_s} \quad (\text{C.16})$$

where I_{max} is the maximum intensity of the pulse, γ is the linewidth of the $P_{1/3}$ state, I_s is the saturation intensity for the transition, and $|c|^2$ is the relevant Clebsh-Gordon coefficient.

In addition, the maximum intensity I_{max} is written in terms of the maximum power, focused to a $1/e$ Gaussian waist of w (or beam area πw^2):

$$I_{max} = \frac{P_{max}}{\pi w^2} \quad (\text{C.17})$$

Substituting back in, the rotation angle as a function of single pulse energy (Eq. C.10) in the UV and the pulse width in the IR (Eq. C.11), which are the two parameters easily measured in the lab is

$$\theta^2 = \frac{\pi^2}{abw_{\text{sech}}^2} \frac{\gamma^2 |c|^2 \tau_{\text{FWHM}}^{IR} E}{2I_s \pi w^2}. \quad (\text{C.18})$$

The first section is the factor that the non-square pulse shape contributes to the rotation angle. For sech^2 pulses, this factor is approximately 1.33. Using the following experimental values: $\gamma = 2\pi 60.1$ MHz, $R = 80.5$ MHz, $I_s = 7955$ W/m², $|c|^2 = 2/3$ for σ^+ polarization, a beam spot area of $\pi w^2 = 1.88 \times 10^{-10}$ m², and assuming $\tau_{\text{FWHM}}^{IR} = 1.8$ ps for sech^2 pulses, the rotation, as a fraction of π is

$$\theta = (1.33)(0.057)\sqrt{E} \quad (\text{C.19})$$

where the pulse width is expressed in ps and the pulse energy E . The first factor, 1.33 comes from the sech^2 , the second contains the atomic physics including the beam area on the ion and the pulse width. Combining the two gives approximately

$$\theta = 0.28\sqrt{E}. \quad (\text{C.20})$$

For a 1.8 ps pulse width, the pulse energy required for a π pulse is 130 pJ, or an average power of 10 mW. The probability of being in the excited state, and therefore detecting a spontaneously emitted photon is shown in Fig. C.3.

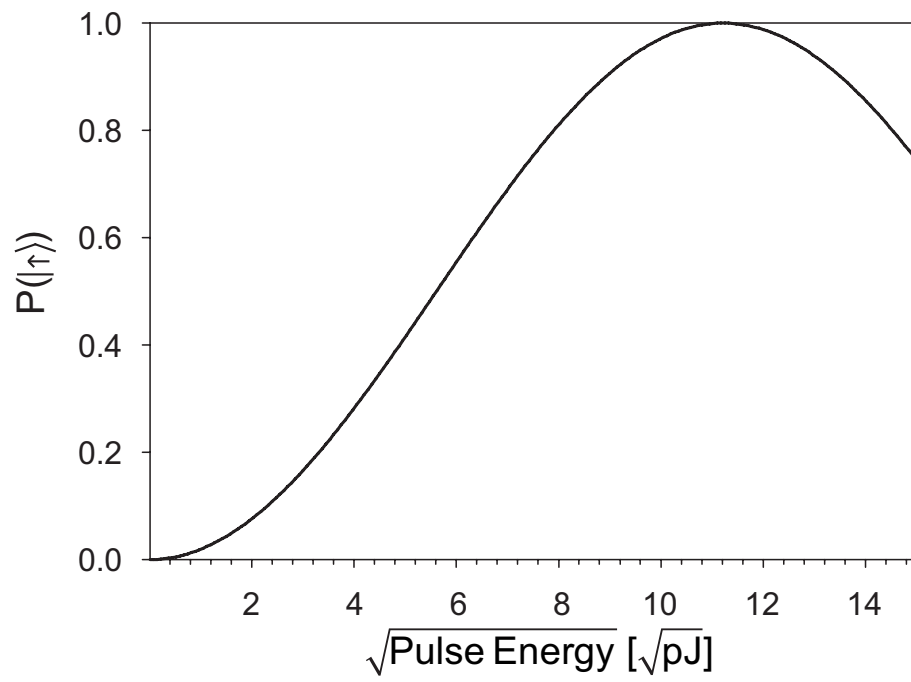


Figure C.3: Excitation Probability as a function of laser pulse energy. Probability of making the transition from the $S_{1/2}$ ground state to the $P_{3/2}$ excited state as a function of pulse width and average pulse energy. The pulse energy is in the UV.

APPENDIX D

Two-Level Ultrafast Rabi Oscillation

D.1 Introduction

The pulsed laser interaction can be described analytically because the electric field pulse envelope is approximately a hyperbolic secant function. The following will cover the basic formalism for the two-level Rabi oscillation problem with the solution for the case of the hyperbolic secant pulses.

D.2 Simple Introductory Two Level Problem

D.2.1 Two Level Setup. The $P_{3/2}$ excited state is denoted $|e\rangle$ and the $S_{1/2}$ ground state, is labeled $|g\rangle$. The frequency difference between these two states is the characteristic frequency of the atom, ω_a , and is an optical frequency of order 1500 THz. The unperturbed Hamiltonian of the two-level system has eigenstates and energies

$$H|e\rangle = \hbar\omega_a|e\rangle \quad (\text{D.1})$$

$$H|g\rangle = 0. \quad (\text{D.2})$$

The wavefunction describing these states is a general superposition of both levels $\psi(t) = c_g(t)|g\rangle + c_e(t)|e\rangle$.

The Hamiltonian is modified with the application of the laser pulse, following [128]

$$H = \frac{\vec{p}^2}{2m} - \frac{e^2}{4\pi\epsilon_0} - \vec{\mu} \cdot \vec{E} = H_0 - \vec{\mu} \cdot \vec{E} \quad (\text{D.3})$$

where the electric field is

$$\vec{E} = \vec{E}_0(t) \cos \omega_l t \quad (\text{D.4})$$

where $E_0(t) = E_0 \text{sech} t / \tau_s$ is a slowly (compared to the optical frequency) varying envelope for the electric field with pulse width τ_s . The dynamics of the problem are found in the solution to the Hamiltonian for the interaction term $-\vec{\mu} \cdot \vec{E}$.

D.2.2 Schrödinger Equation. The time evolution of the wavefunction is described by the Schrödinger equation using the unperturbed Hamiltonian of an atomic system from Eq. D.3.

$$i\hbar \frac{\partial \psi}{\partial t} = H_0 \psi - \vec{\mu} \cdot \vec{E} \psi \quad (\text{D.5})$$

Writing out this equation in terms of the wavefunction amplitudes and then taking the product with $\langle g|$ and $\langle e|$, one finds

$$\begin{aligned} i\hbar \frac{\partial}{\partial t} (c_g(t)|g\rangle + c_e(t)|e\rangle) &= H_0 (c_g(t)|g\rangle + c_e(t)|e\rangle) \\ &\quad - \vec{\mu} \cdot \vec{E} (c_g(t)|g\rangle + c_e(t)|e\rangle) \end{aligned} \quad (\text{D.6})$$

$$\begin{aligned} i\hbar (\dot{c}_g(t)|g\rangle + \dot{c}_e(t)|e\rangle) &= c_e(t)\hbar\omega_a|e\rangle \\ &\quad - \vec{\mu} \cdot \vec{E} (c_g(t)|g\rangle + c_e(t)|e\rangle) \end{aligned} \quad (\text{D.7})$$

Now, taking the product with $\langle g|$ and $\langle e|$ to get the amplitudes by themselves:

$$\begin{aligned} \langle g| [i\hbar (\dot{c}_g(t)|g\rangle + \dot{c}_e(t)|e\rangle) &= c_e(t)\hbar\omega_a|e\rangle \\ &\quad - \vec{\mu} \cdot \vec{E} (c_g(t)|g\rangle + c_e(t)|e\rangle)] \end{aligned} \quad (\text{D.8})$$

$$\begin{aligned} \langle e| [i\hbar (\dot{c}_g(t)|g\rangle + \dot{c}_e(t)|e\rangle) &= c_e(t)\hbar\omega_a|e\rangle \\ &\quad - \vec{\mu} \cdot \vec{E} (c_g(t)|g\rangle + c_e(t)|e\rangle)] \end{aligned} \quad (\text{D.9})$$

The end result gives a set of coupled differential equations for $c_g(t)$ and $c_e(t)$.

$$\imath\hbar\dot{c}_g(t) = -\langle g|\vec{\mu} \cdot \vec{E}|e\rangle c_e(t) \quad (\text{D.10})$$

$$\imath\hbar\dot{c}_e(t) = \hbar\omega_a - \langle e|\vec{\mu} \cdot \vec{E}|g\rangle c_g(t)$$

A substitution is then made in this problem and the Rabi frequency is defined using the amplitude of the electric field, but not the hyperbolic secant envelope.

$$\Omega = \frac{\langle e|\vec{\mu} \cdot \vec{E}_0|g\rangle}{\hbar}. \quad (\text{D.11})$$

Using this in equation D.10, moving the constants to the right side of the equations, and recalling the form of the electric field [Eq. D.4], one finds

$$\dot{c}_g(t) = \imath\Omega \text{sech}(t/\tau_s) \cos(\omega_l t) c_e(t) \quad (\text{D.12})$$

$$\dot{c}_e(t) = -\imath\omega_a + \imath\Omega \text{sech}(t/\tau_s) \cos(\omega_l t) c_g(t).$$

The energy of the eigenstates are shifted to the atomic reference frame to make the RWA.

$$c_e(t) = \tilde{c}_e(t) e^{-\imath\omega_a t}. \quad (\text{D.13})$$

This is substituted in equation D.12 and the time derivative is taken. To match notation, the substitution $c_g(t) = \tilde{c}_g(t)$ is also made, which corresponds to a zero energy shift. The equation for the excited state is simplified, giving

$$\dot{c}_e(t) = \dot{\tilde{c}}_e(t) e^{-\imath\omega_a t} - \imath\omega_a \tilde{c}_e(t) e^{-\imath\omega_a t} \quad (\text{D.14})$$

and the right side becomes

$$\dot{c}_e(t) = -\imath\omega_a \tilde{c}_e(t) e^{-\imath\omega_a t} + \imath\Omega \text{sech}(t/\tau_s) \cos(\omega_l t) \tilde{c}_g(t). \quad (\text{D.15})$$

Equating these gives the amplitudes

$$\begin{aligned}\dot{\tilde{c}}_e(t)e^{-i\omega_a t} &= i\omega_a \tilde{c}_e(t)e^{-i\omega_a t} - i\omega_a \tilde{c}_g(t)e^{-i\omega_a t} \\ &\quad + i\Omega \operatorname{sech}(t/\tau_s) \cos(\omega_l t) \tilde{c}_g(t)\end{aligned}\tag{D.16}$$

and, examining both amplitudes,

$$\begin{aligned}\dot{\tilde{c}}_e(t) &= i\Omega \operatorname{sech}(t/\tau_s) \cos(\omega_l t) \tilde{c}_g(t)e^{i\omega_a t} \\ \dot{\tilde{c}}_g(t) &= i\Omega \operatorname{sech}(t/\tau_s) \cos(\omega_l t) \tilde{c}_e(t)e^{-i\omega_a t}\end{aligned}\tag{D.17}$$

D.2.3 Rotating Wave Approximation. At this point in the solution of the problem, the Rotating Wave Approximation (RWA) is made by re-writing the $\cos(\omega_l t)$ optical frequency term using the exponential expansion. It is then assumed that the $\omega_l + \omega_a$ terms are negligible because they rotate at essentially twice the optical frequency. On the time scale of the laser pulse, these terms are average out to approximately zero. The coupled equations for the amplitudes, where the laser frequency is equal to the atomic frequency, are

$$\dot{\tilde{c}}_e(t) = \frac{i\Omega}{2} \operatorname{sech}(t/\tau_s) \tilde{c}_g(t)\tag{D.18}$$

$$\dot{\tilde{c}}_g(t) = \frac{i\Omega}{2} \operatorname{sech}(t/\tau_s) \tilde{c}_e(t)$$

These coupled differential equations are solved exactly for the hyperbolic secant pulse envelope. The solutions for the initial conditions $c_e(-\infty) = 0$ and $c_g(-\infty) = 1$ are

$$\tilde{c}_e(t) = \cos[\tau_s \Omega \tan^{-1} \tanh(t/\tau_s)]\tag{D.19}$$

$$\tilde{c}_g(t) = i \sin[\tau_s \Omega \tan^{-1} \tanh(t/\tau_s)]$$

The probability of being in the excited state is

$$|c_e|^2 = \sin^2 [\tau_s \Omega \tan^{-1} \tanh(t/\tau_s)] \quad (\text{D.20})$$

Note that, as explained in the text, the Rabi frequency Ω is the electric field, or which is proportional to the square root of the laser power \sqrt{P} . The rotation angle after the pulse has interacted with the ion is the integral of the argument to the sine function. For times much longer then the pulse width τ_s , the function $\tan^{-1} \tanh(t/\tau_s)$ is equal to $\pi/4$. The rotation angle is thus $\theta = \pi\tau_s\Omega$ and the excited state probability is

$$|c_e|^2 = \sin^2 \frac{\theta}{2} \quad (\text{D.21})$$

The wavefunction, as a function of time, is thus

$$\psi(t) = \cos \frac{\theta}{2} |g\rangle - ie^{-i\omega_a t} \sin \frac{\theta}{2} |e\rangle \quad (\text{D.22})$$

where the wavefunction starts in the ground state at time $t = -\infty$.

D.3 Two Pulse Approximation

If a second pulse is sent to the ion after the first pulse has rotated the state by an angle θ , the wavefunction will rotate again on the Bloch sphere. However, the optical frequency component of the wavefunction must also be accounted for. After the first pulse, the atom is in a superposition of the ground and excited states [Eq. D.22]. The second pulse has a phase shift with respect to the first based on the time delay between the first and second pulses. The probability of being in the excited state after the secon pulse is

$$|c_e|^2 = \sin^2 \frac{\theta}{2} \cos^2 \left(\frac{\omega_a \delta t}{2} \right). \quad (\text{D.23})$$

Although the ion is not in the Lamb-Dicke limit, the two pulses interact with the ion on a time scale much faster the the ion motion, so the phase $\omega_a \delta t$ is well de-

finer. However, averaging over an ensemble of experiments, each one with a slightly different delay, the second term becomes $1/2$, reducing the excited state population.

APPENDIX E

Ultrafast Optical Bloch Equations

E.1 Density Matrix Setup

The density matrix and the solutions to the optical Bloch equations (OBE) can be used to get a better understanding of the dynamics of the two pulse experiment. The energy levels of cadmium are described in an approximate fashion by only looking at the $m_F = 0$ excited states. The pulsed laser, with a bandwidth much larger than the hyperfine splitting, is assumed to couple all the ground states equally. However, to use the rotating wave approximation (RWA), the pulsed laser is initially approximated as a bichromatic field coupling both hyperfine levels equally. In addition, there is a microwave field that couples the $F = 0, m_F = 0$ ground state to the $F = 1, m_F = 0$ ground state. The pulsed laser field is

$$\vec{E}_1(\vec{x}, t) = |E_1^0(t)| \hat{e}_1 \cos(\omega_{l1}t - \vec{k}_1 \cdot \vec{x} - \phi_1) \quad (\text{E.1})$$

$$\vec{E}_2(\vec{x}, t) = |E_2^0(t)| \hat{e}_2 \cos(\omega_{l2}t - \vec{k}_2 \cdot \vec{x} - \phi_2) \quad (\text{E.2})$$

where

$$E_1^0(t) \sim E_2^0(t) \sim \text{sech}(t/\tau_s) \quad (\text{E.3})$$

is the slowly (compared to the optical frequency) varying envelope of the laser pulse. The field E_1 couples the $F = 0$ ground state with the $F = 1'$ excited state manifold.

The other field, E_2 couples the $F = 1$ ground state with the $F = 2'$ excited state. The microwave field couples the two ground state levels and is insensitive to the ion position and motion:

$$\vec{M}(t) = |M_0| \hat{e}_{\mu W} \cos(\omega_{\mu W} t - \phi_{\mu W}). \quad (\text{E.4})$$

The OBE is the density matrix version of the Schrödinger equation $\dot{\rho} = [H, \rho]$ and can be written in matrix component form:

$$\dot{\rho}_{ij} = -\frac{i}{\hbar} \sum_k (H_{ik} \rho_{kj} - \rho_{ik} H_{kj}). \quad (\text{E.5})$$

There are five relevant energy levels in our approximate system shown in Fig. E.1. The $F = 0, m_F = 0$ ground state population is represented by ρ_{00} . The $F = 1, m_F = 0$ ground state population is ρ_{11} . There is another, auxiliary, ground state population that represents any population in either the $F = 1, m_F = \pm 1$ states (ρ_{aa}), which are equally bright and, in this approximation, will not interact further with the laser. This will lead to a solution that is slightly brighter than the actual physical situation, but only by a small percentage.

The two excited hyperfine states are $F' = 1, m'_F = 0$, which has a population $\rho_{1'1'}$, and $F' = 2, m'_F = 0$ with population $\rho_{2'2'}$. There are coherences coupling the two hyperfine ground states to each other and to the two excited states.

The final set of coupled differential equations for the density matrix elements are,

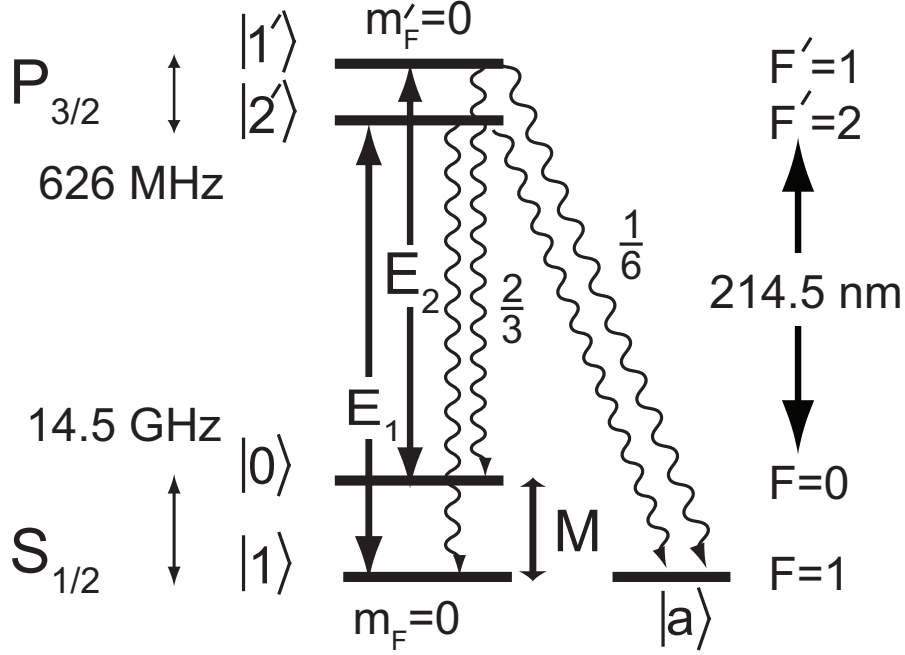


Figure E.1: The energy levels for the OBE model. Shown are the transitions between $|0\rangle$ and $|1'\rangle$ via E_1 , between $|1\rangle$ and $|2'\rangle$ via E_2 , and $|0\rangle$ and $|1\rangle$ via M . The fluorescence branching ratios are also shown to the initial states as well as the auxiliary state $|a\rangle$.

in the RWA and without spontaneous emission

$$\dot{\rho}_{2'2'} = \frac{i}{2} (\Omega_2(t) \bar{\rho}_{2'1}^* - \Omega_2^*(t) \bar{\rho}_{2'1}) \quad (\text{E.6})$$

$$\dot{\rho}_{1'1'} = \frac{i}{2} (\Omega_1(t) \bar{\rho}_{1'0}^* - \Omega_1^*(t) \bar{\rho}_{1'0}) \quad (\text{E.7})$$

$$\dot{\rho}_{11} = -\frac{i}{2} (\Omega_M \bar{\rho}_{01}^* - \Omega_M^* \bar{\rho}_{01}) - \frac{i}{2} (\Omega_2(t) \bar{\rho}_{2'1}^* - \Omega_2^*(t) \bar{\rho}_{2'1}) \quad (\text{E.8})$$

$$\dot{\rho}_{00} = \frac{i}{2} (\Omega_M \bar{\rho}_{01}^* - \Omega_M^* \bar{\rho}_{01}) - \frac{i}{2} (\Omega_1(t) \bar{\rho}_{1'0}^* - \Omega_1^*(t) \bar{\rho}_{1'0}) \quad (\text{E.9})$$

$$\dot{\rho}_{2'1} = \frac{i\Omega_2(t)}{2} (\rho_{11} - \rho_{2'2'}) - \frac{i\Omega_M}{2} \bar{\rho}_{2'0} \quad (\text{E.10})$$

$$\dot{\rho}_{1'0} = \frac{i\Omega_1(t)}{2} (\rho_{00} - \rho_{1'1'}) - \frac{i\Omega_M^*}{2} \bar{\rho}_{1'1} \quad (\text{E.11})$$

$$\dot{\rho}_{1'1} = -\frac{i\Omega_2(t)}{2} \bar{\rho}_{1'2'} e^{-i\Delta\omega t} + \frac{i\Omega_1(t)}{2} \bar{\rho}_{01} - \frac{i\Omega_M}{2} \bar{\rho}_{1'0} \quad (\text{E.12})$$

$$\dot{\rho}_{2'0} = -\frac{i\Omega_1(t)}{2} \bar{\rho}_{1'2'}^* e^{i\Delta\omega t} + \frac{i\Omega_2(t)}{2} \bar{\rho}_{01}^* - \frac{i\Omega_M^*}{2} \bar{\rho}_{2'1} \quad (\text{E.13})$$

$$\dot{\rho}_{01} = \frac{i\Omega_M}{2} (\rho_{11} - \rho_{00}) - \frac{i\Omega_2(t)}{2} \bar{\rho}_{2'0}^* - \frac{i\Omega_1^*(t)}{2} \bar{\rho}_{1'1} \quad (\text{E.14})$$

$$\dot{\rho}_{1'2'} = i\Delta\omega \bar{\rho}_{1'2'} + \left(\frac{i\Omega_1(t)}{2} \bar{\rho}_{2'0}^* - \frac{i\Omega_2^*(t)}{2} \bar{\rho}_{1'1} \right) e^{i\Delta\omega t} \quad (\text{E.15})$$

There are three Rabi frequencies listed in these coupled differential equations, each one represents an electromagnetic field (Eqs. E.1, E.2, E.4). The two laser frequencies contain the slowly varying time envelope from Eq. E.3.

$$\Omega_1(t) = \frac{E_1^0}{\hbar} \langle 0 | \mu_1 \cdot \hat{\epsilon}_1 e^{i\vec{k}_1 \cdot \vec{x}} | 1' \rangle \text{sech}(t/\tau_s) \equiv \Omega_{01} \text{sech}(t/\tau_s) \quad (\text{E.16})$$

$$\Omega_2(t) = \frac{E_2^0}{\hbar} \langle 1 | \mu_2 \cdot \hat{\epsilon}_2 e^{i\vec{k}_2 \cdot \vec{x}} | 2' \rangle \text{sech}(t/\tau_s) \equiv \Omega_{02} \text{sech}(t/\tau_s) \quad (\text{E.17})$$

$$\Omega_M(t) = \frac{M_0}{\hbar} \langle 0 | \mu_1 \cdot \hat{\epsilon}_{\mu W} | 1 \rangle \quad (\text{E.18})$$

$$(\text{E.19})$$

The optical coherences are each rotating in the frame of the atomic frequency difference, and the hyperfine coherences are rotating in the frame of the ground state hyperfine splitting.

$$\rho_{2'1} = \bar{\rho}_{2'1} e^{-i\omega_{l1}t} \quad (\text{E.20})$$

$$\rho_{1'0} = \bar{\rho}_{1'0} e^{-i\omega_{l2}t} \quad (\text{E.21})$$

$$\rho_{1'1} = \bar{\rho}_{1'1} e^{-i(\omega_{l1} + \omega_{HF})t} \quad (\text{E.22})$$

$$\rho_{2'0} = \bar{\rho}_{2'0} e^{-i(\omega_{l2} - \omega_{HF})t} \quad (\text{E.23})$$

$$\rho_{01} = \bar{\rho}_{01} e^{-i\omega_{HF}t} \quad (\text{E.24})$$

$$\rho_{1'2'} = \bar{\rho}_{1'2'} e^{-i\omega_{l2}t} \quad (\text{E.25})$$

The frequency relationships that are characteristic to this system are the atomic frequency difference between the $F = 2'$ excited state manifold and the $F = 0$ ground state, ω_a , the ground state hyperfine splitting ω_{HF} and the excited state hyperfine splitting $\omega_{HF'}$. It follows from the structure of $^{111}\text{Cd}^+$ that

$$\omega_a = \omega_{l1} - \omega_{HF'} \quad (\text{E.26})$$

$$\omega_a = \omega_{l2} - \omega_{HF} \quad (\text{E.27})$$

$$\Delta\omega = \omega_{HF} - \omega_{HF'} \quad (\text{E.28})$$

E.2 Microwave Rotations

When microwaves are sent to the ion, the density matrix evolves with a non-zero element Ω_M , but the other two Rabi frequencies are zero. The coupled differential equations that describe the time evolution of the system are as follows. The time evolution is assumed to be the a rotating frame of frequency ω_{HF} .

$$\dot{\rho}_{11} = -\frac{i}{2} (\Omega_M \bar{\rho}_{01}^* - \Omega_M^* \bar{\rho}_{01}) \quad (\text{E.29})$$

$$\dot{\rho}_{00} = \frac{i}{2} (\Omega_M \bar{\rho}_{01}^* - \Omega_M^* \bar{\rho}_{01}) \quad (\text{E.30})$$

$$\dot{\bar{\rho}}_{2'1} = -\frac{i\Omega_M}{2} \bar{\rho}_{2'0} \quad (\text{E.31})$$

$$\dot{\bar{\rho}}_{1'0} = -\frac{i\Omega_M^*}{2} \bar{\rho}_{1'1} \quad (\text{E.32})$$

$$\dot{\bar{\rho}}_{1'1} = -\frac{i\Omega_M}{2} \bar{\rho}_{1'0} \quad (\text{E.33})$$

$$\dot{\bar{\rho}}_{2'0} = -\frac{i\Omega_M^*}{2} \bar{\rho}_{2'1} \quad (\text{E.34})$$

$$\dot{\rho}_{01} = \frac{i\Omega_M}{2} (\rho_{11} - \rho_{00}) \quad (\text{E.35})$$

$$\dot{\bar{\rho}}_{1'2'} = i\Delta\omega \bar{\rho}_{1'2'} \quad (\text{E.36})$$

For an initial population of only the dark state ρ_{00} , the microwaves couple to the other hyperfine ground state ρ_{11} as well as establish a coherence ρ_{01} . The other entries in the density matrix remain zero. A second microwave pulse could be applied at some time t after the first with a phase ϕ with respect to the first. Because the microwave radiation is resonant with the atom, this second pulse would shift the

population of the first, changing Ω_M to $\Omega_M e^{i\phi}$ (noting that the complex conjugate must be taken where appropriate).

E.3 Ultrafast Laser Rotations

The interaction between the ultrafast laser pulses and the atom using the OBE and this description of the density matrix can be approximated by assuming that the two transitions between the ground and excited states couple with equal strength and are both real amplitudes:

$$\Omega_{01} = \Omega_{01}^* \approx \Omega_{02} = \Omega_{02}^* \equiv \Omega_0 \quad (\text{E.37})$$

With this approximation, the time evolution of the density matrix over the time during which a laser pulse arrives is described by the following coupled differential equations.

$$\dot{\rho}_{2'2'} = \frac{i\Omega_0 \text{sech}(t/\tau_s)}{2} (\bar{\rho}_{2'1}^* - \bar{\rho}_{2'1}) \quad (\text{E.38})$$

$$\dot{\rho}_{1'1'} = \frac{i\Omega_0 \text{sech}(t/\tau_s)}{2} (\bar{\rho}_{1'0}^* - \bar{\rho}_{1'0}) \quad (\text{E.39})$$

$$\dot{\rho}_{11} = -\frac{i\Omega_0 \text{sech}(t/\tau_s)}{2} (\bar{\rho}_{2'1}^* - \bar{\rho}_{2'1}) \quad (\text{E.40})$$

$$\dot{\rho}_{00} = -\frac{i\Omega_0 \text{sech}(t/\tau_s)}{2} (\bar{\rho}_{1'0}^* - \bar{\rho}_{1'0}) \quad (\text{E.41})$$

$$\dot{\rho}_{2'1} = \frac{i\Omega_0 \text{sech}(t/\tau_s)}{2} (\rho_{11} - \rho_{2'2'}) \quad (\text{E.42})$$

$$\dot{\rho}_{1'0} = \frac{i\Omega_0 \text{sech}(t/\tau_s)}{2} (\rho_{00} - \rho_{1'1'}) \quad (\text{E.43})$$

$$\dot{\rho}_{1'1} = -\frac{i\Omega_0 \text{sech}(t/\tau_s)}{2} (\bar{\rho}_{1'2'} e^{-i\Delta\omega t} + \bar{\rho}_{01}) \quad (\text{E.44})$$

$$\dot{\rho}_{2'0} = -\frac{i\Omega_0 \text{sech}(t/\tau_s)}{2} (\bar{\rho}_{1'2'}^* e^{i\Delta\omega t} + \bar{\rho}_{01}^*) \quad (\text{E.45})$$

$$\dot{\rho}_{01} = -\frac{i\Omega_0 \text{sech}(t/\tau_s)}{2} (\bar{\rho}_{2'0}^* - \bar{\rho}_{1'1}) \quad (\text{E.46})$$

$$\dot{\rho}_{1'2'} = i\Delta\omega \bar{\rho}_{1'2'} + \frac{i\Omega_0 \text{sech}(t/\tau_s)}{2} (\bar{\rho}_{2'0}^* - \bar{\rho}_{1'1}) e^{i\Delta\omega t} \quad (\text{E.47})$$

The time scale of the ultrafast pulses is much shorter than spontaneous emission (with excited state lifetime γ) for a single pulse. However, if there is some time between two or more ultrafast pulses, then spontaneous emission must be accounted for. In that case, the period during which spontaneous emission may occur is described by the following coupled equations.

$$\dot{\rho}_{2'2'} = -\gamma\rho_{2'2'} \quad (\text{E.48})$$

$$\dot{\rho}_{1'1'} = -\gamma\rho_{1'1'} \quad (\text{E.49})$$

$$\dot{\rho}_{11} = \frac{2}{3}\gamma\rho_{2'2'} \quad (\text{E.50})$$

$$\dot{\rho}_{00} = \frac{2}{3}\gamma\rho_{1'1'} \quad (\text{E.51})$$

$$\dot{\bar{\rho}}_{2'1} = -\frac{\gamma}{2}\bar{\rho}_{2'1} \quad (\text{E.52})$$

$$\dot{\bar{\rho}}_{1'0} = -\frac{\gamma}{2}\bar{\rho}_{1'0} \quad (\text{E.53})$$

$$\dot{\bar{\rho}}_{1'1} = -\frac{\gamma}{2}\bar{\rho}_{1'1} \quad (\text{E.54})$$

$$\dot{\bar{\rho}}_{2'0} = -\frac{\gamma}{2}\bar{\rho}_{2'0} \quad (\text{E.55})$$

$$\dot{\bar{\rho}}_{01} = 0 \quad (\text{E.56})$$

$$\dot{\bar{\rho}}_{1'2'} = 0 \dot{\rho}_{aa} = \frac{\gamma}{3}(\rho_{2'2'} + \rho_{1'1'}) \quad (\text{E.57})$$

One other consideration is made when using multiple ultrafast laser pulses in the OBE. If the optical phase is not stable between the pulses, or if on average the phase is random, this can be accounted for by resetting the values of the optical coherences to zero before applying the next ultrafast pulse. However, if the phase is maintained and controlled, the optical coherences will carry over from one pulse to the next.

BIBLIOGRAPHY

BIBLIOGRAPHY

- [1] R. P. Feynman. Simulating physics with computers. *Int. J. Th. Phys.*, 21(6/7):467–488, 1982.
- [2] D. Deutsch. Quantum theory, the church-turing principle and the universal quantum computer. *Proc. R. Soc. Lon. A*, 400:97, 1985.
- [3] D. Deutsch and R. Jozsa. Rapid solution of problems by quantum computation. *Proc. R. Soc. Lon. A*, 439:553, 1992.
- [4] P. W. Shor. Algorithms for quantum computation: Discrete logarithms and factoring. In *Proceedings of the 35th Annual Symposium on the Foundations of Computer Science*, page 124, New York, 1994. IEEE Computer Society, IEEE Computer Society Press.
- [5] P. W. Shor. Scheme for reducing decoherence in quantum computer memory. *Phys. Rev. A*, 52(4):R2493–R2496, October 1995.
- [6] P. W. Shor. Algorithm for fast factoring. *SIAM J. Comp.*, 26:1484, 1997.
- [7] L. K. Grover. Quantum mechanics helps in searching for a needle in a haystack. *Phys. Rev. Lett.*, 79(2):325–328, Jul 1997.
- [8] D. P. DiVincenzo. Quantum computation. *Science*, 270:255, 1995.
- [9] J. I. Cirac and P. Zoller. Quantum computation with cold, trapped ions. *Phys. Rev. Lett.*, 74(20):4091, 1995.
- [10] K. Mølmer and A. Sørensen. Multiparticle entanglement of hot trapped ions. *Phys. Rev. Lett.*, 82:1835, 1999.
- [11] c. Monroe, D. M. Meekhof, B. E. King, W. M. Itano, and D. J. Wineland. Demonstration of a fundamental quantum logic gate. *Phys. Rev. Lett. (USA)*, 75(25):4714 – 17, 1995/12/18.
- [12] B. E. King, C. S. Wood, C. J. Myan, Q. A. Turchette, D. Leibfried, W. M. Itano, C. Monroe, and D. J. Wineland. Cooling the collective motion of trapped ions to initialize a quantum register. *Phys. Rev. Lett. (USA)*, 81(7):1525 – 8, 1998/08/17.
- [13] C. A. Sackett, D. Kielpinski, B. E. King, C. Langer, V. Meyer, C. J. Myatt, M. A. Rowe, Q. A. Turchette, W. M. Itano, D. J. Wineland, and C. Monroe. Experimental entanglement of four particles. *Nature*, 404:256, 2000.
- [14] D. Leibfried, B. DeMarco, V. Meyer, D. Lucas, M. Barrett, J. Britton, W. M. Itano, B. Jelenkovic, C. Langer, T. Rosenband, and D. J. Wineland. Experimental demonstration of a robust, high-fidelity geometric two ion-qubit phase gate. *NATURE*, 422(6930):412–415, Mar 2003.
- [15] F. Schmidt-Kaler, H. Häffner, M. Riebe, S. Gulde, G. P. T. Lancaster, T. Deuschle, C. Becher, C. F. Roos, J. Eschner, and R. Blatt. Realization of the cirac-zoller controlled-not quantum gate. *NATURE*, 422(6930):408–411, Mar 2003.

- [16] M. D. Barrett, J. Chiaverini, T. Schaetz, J. Britton, W. M. Itano, J. D. Jost, E. Knill, C. Langer, D. Leibfried, R. Ozeri, and D. J. Wineland. Deterministic quantum teleportation of atomic qubits. *NATURE*, 429(6993):737–739, Jun 2004.
- [17] M. Riebe, H. Häffner, C. F. Roos, W. Hänsel, J. Benhelm, G. P. T. Lancaster, T. W. Körber, C. Becher, F. Schmidt-Kaler, D. F. V. James, and R. Blatt. Deterministic quantum teleportation with atoms. *NATURE*, 429(6993):734–737, Jun 2004.
- [18] D. Leibfried, E. Knill, S. Seidelin, J. Britton, R. B. Blakestad, J. Chiaverini, D. B. Hume, W. M. Itano, J. D. Jost, C. Langer, R. Ozer, R. Reichle, and D. J. Wineland. Creation of a six-atom ‘schrodinger cat’ state. *Nature*, 438:639, 2005.
- [19] J. Chiaverini, J. Britton, D. Leibfried, E. Krill, M. D. Barrett, R. B. Blakestad, W. M. Itano, J. D. Jost, C. Langer, R. Ozeri, T. Schaetz, and D. J. Wineland. Implementation of the semiclassical quantum fourier transform in a scalable system. *SCIENCE*, 308(5724):997–1000, May 2005.
- [20] H. Häffner, W. Hänsel, C. F. Roos, J. Benhelm, D. Chek al kar, M. Chwalla, T. Körber, U. D. Rapol, M. Riebe, P. O. Schmidt, C. Becher, O. Gühne, W. Dür, and R. Blatt. Scalable multiparticle entanglement of trapped ions. *Nature*, 438:643, 2005.
- [21] K.-A. Brickman, P. C. Haljan, P. J. Lee, M. Acton, L. Deslauriers, and C. Monroe. Implementation of grover’s quantum search algorithm in a scalable system. *Phys. Rev. A*, 72:050306, 2005.
- [22] A. Steane. *quant-ph/0603273*, 2006.
- [23] D. Kielpinski, C. Monroe, and D.J. Wineland. Architecture for a large-scale ion-trap quantum computer. *Nature*, 417:709–711, 2002.
- [24] J. F. Poyatos, J. I. Cirac, R. Blatt, and P. Zoller. Trapped ions in the strong-excitation regime: ion interferometry and nonclassical states. *Phys. Rev. A*, 54(2):1532 – 40, 8 1996.
- [25] J. J. Garcia-Ripoll, P. Zoller, and J. I. Cirac. Speed optimized two-qubit gates with laser coherent control techniques for ion trap quantum computing. *Phys. Rev. Lett.*, 91:157901, 2003.
- [26] S.-L. Zhu, C. Monroe, and L-M Duan. Arbitrary-speed quantum gates within large ion crystals through minium control of laser beams. *Europhys. Lett.*, 73(4):485–491, 2006.
- [27] C. Simon and W. T. M. Irvine. Robust long-distance entanglement and loophole-free bell test with ions and photons. *Phys. Rev. Lett.*, 91(110):405, 2003.
- [28] L.-M. Duan, B. B. Blinov, D. L. Moehring, and C. Monroe. Scalable trapped ion quantum computation with a probabilistic ion-photon mapping. *Quantum Inf. Comput.*, 4:165–173, 2004.
- [29] L.-M. Duan and R. Raussendorf. Efficient quantum computation with probabilistic quantum gates. *arXiv:quant-ph/0502120*, 2005.
- [30] L.-M. Duan, M. J. Madsen, D. L. Moehring, P. Maunz, Jr. R. N. Kohn, and C. Monroe. Probabilistic quantum gates between remote atoms through interference of optical frequency qubits. *quant-ph/0603285*, 2006.
- [31] M. A. Rowe, A. Ben Kish, B. L. DeMarco, D. Leibfried, V. Meyer, J. Britton, J. Huhners, W. M. Itano, B. M. Jelenkovic, C. Langer, T. Rosenband, and D. J. Wineland. Transport of quantum states and separation of ions in a dual rf ion trap. *Quantum Inf. Comput.*, 2:257–271, 2002.

- [32] M.J. Madsen, W.K. Hensinger, D. Stick, J.A. Rabchuk, and C. Monroe. Planar ion trap geometry for microfabrication. *Applied Physics B: Lasers and Optics*, 78(5):639 – 651, 2004.
- [33] D. Stick, W. K. Hensinger, S. Olmschenk, M. J. Madsen, K. Schwab, and C. Monroe. Ion trap in a semiconductor chip. *Nature Physics*, 2:36, 2006.
- [34] H.G. Dehmelt. Radiofrequency spectroscopy of stored ions i: Storage. *Adv. At. Mol. Phys.*, 3:53, 1967.
- [35] D. J. Wineland, C. Monroe, W. M. Itano, D. Leibfried, B. E. King, and D. M. Meekhof. Experimental issues in coherent quantum-state manipulation of trapped atomic ions. *Journal of Research of the National Institute of Standards and Technology*, 103:259–328, 1998.
- [36] D. Leibfried, R. Blatt, C. Monroe, and D. J. Wineland. Quantum dynamics of single trapped ions. *Rev. Mod. Phys.*, 75:281–324, 2003.
- [37] J. Metcalf and P. van der Straten. *Laser Cooling and Trapping*. Springer, Stony Brook, NY, 1999.
- [38] D. J. Wineland and H. Dehmelt. Proposed $10^{14}\delta\nu/\nu$ laser fluorescence spectroscopy on tl^+ mono-ion oscillator. *Bull. Am. Phys. Soc.*, 20:657, 1975.
- [39] D. J. Wineland and W. M. Itano. Radiation-pressure cooling of bound resonant absorbers. *Phys. Rev. A*, 20:1521–1540, 1979.
- [40] W. M. Itano and D. J. Wineland. Laser cooling of ions stored in harmonic and penning traps. *Phys. Rev. A*, 25:35, 1982.
- [41] D.J. Berkeland, J.D. Miller, J.C. Bergquist, W.M. Itano, and D.J. Wineland. Minimization of ion micromotion in a paul trap. *J. Appl. Phys.*, 83(10):5025 – 5033, 1998.
- [42] K. Odaka and S. Ueda. Dependence of outgassing rate on surface oxide layer thickness in type 304 stainless steel before and after surface oxidation in air. *Vacuum*, 47:689, 1996.
- [43] Ligo vacuum compatible materials list. <http://www.ligo.caltech.edu/>, 1996.
- [44] W. W. Macalpine and R. O. Schildknecht. Coaxial resonators with helical inner conductor. *Proc. of the IRE*, 959:2099, 1959.
- [45] A. I. Zverev and H. J. Blinchikoff. Realization of a filter with helical components. *IRE Trans. on Comp. Parts*, 1961:99, 1961.
- [46] S. J. Fiedziuszko and R. S. Kwok. Novel helical resonator filter structures. *IEEE MTT-S*, 1998:1323, 1998.
- [47] The Mathworks, Inc., Natick, MA. *Partial Differential Equation Toolbox User's Guide*, 1996.
- [48] John David Jackson. *Classical Electrodynamics*. John Wiley & Sons, Inc., New York, NY, 3rd edition, 1999.
- [49] W. Paul. Electromagnetic traps for charged and neutral particles. *Rev. Mod. Phys.*, 62:531–540, 1990.
- [50] P. T. H. Fisk. Trapped-ion and trapped-atom microwave frequency standards. *Reports on Progress in Physics*, 60:761–817, 1997.
- [51] R.S. Van Dyck Jr., P.B. Pschwinberg, and H.G. Dehmelt. New high-precision comparison of electron and positron g factors. *Phys. Rev. Lett.*, 59:26–29, 1987.
- [52] A. Steane. The ion trap quantum information processor. *Appl. Phys. B*, 64:623–642, 1997.

- [53] J. Ye, D. W. Vernooy, and H. J. Kimble. Trapping of Single Atoms in Cavity QED. *Phys. Rev. Lett.*, 83:4987–4990, 1999.
- [54] P. W. H. Pinkse, T. Fischer, P. Maunz, and G. Rempe. Trapping an atom with single photons. *Nature*, 404:365–368, 2000.
- [55] G. R. Guthöhrlein, M. Keller, K. Hayasaka, W. Lange, and H. Walther. A single ion as a nanoscopic probe of an optical field. *Nature*, 414:49, 2001.
- [56] A.B. Mundt, A. Kreuter, C. Becher, D. Leibfried, J. Eschner, F. Schmidt-Kaler, and R. Blatt. Coupling a single atomic quantum bit to a high finesse optical cavity. *Phys. Rev. Lett.*, 89:103001, 2002.
- [57] S. Taylor, R. F. Tidnall, and R. R. A. Syms. Silicon based quadrupole mass spectrometry using microelectromechanical systems. *J. Vac. Sci. Tech.*, 19:557, 2001.
- [58] R. Folman, P. Krüger, J. Schmiedmayer, J. Denschlag, and C. Henkel. Microscopic atom optics: From wires to an atom chip. *Advances in Atomic, Molecular and Optical Physics*, 48:263–356, 2002.
- [59] C. Henkel, S. Pötting, and M. Wilkens. Loss and heating of particles in small and noisy traps. *Appl. Phys. B*, 69:379–387, 1999.
- [60] Q. A. Turchette, D. Kielpinski, B. E. King, D. Leibfried, D. M. Meekhof, C. J. Myatt, M. A. Rowe, C. A. Sackett, C. S. Wood, W. M. Itano, C. Monroe, and D. J. Wineland. Heating of trapped ions from the quantum ground state. *Phys. Rev. A*, 61:063418, 2000.
- [61] F. C. Witteborn and W. M. Fairbank. Apparatus for measuring the force of gravity on freely falling electrons. *Rev. Sci. Instr.*, 48:1–11, 1977.
- [62] M. G. Raizen, J. M. Gilligan, J. C. Bergquist, W. M. Itano, and D. J. Wineland. Ionic crystals in a linear paul trap. *Phys. Rev. A*, 45:6493, 1992.
- [63] J. P. Cleveland, S. Manne, D. Bocek, and P. K. Hansma. A nondestructive method for determining the spring constant of cantilevers for scanning force microscopy. *Rev. Sci. Instr.*, 64:403, 1993.
- [64] R. Lifshitz and M. L. Roukes. Thermoelastic damping in micro- and nanomechanical systems. *Phys. Rev. B*, 61:5600–5609, 2000.
- [65] J.P.R. David and G.E. Stillman. *Carrier Ionisation Coefficients of GaAs*, chapter 4.9, pages 190–197. INSPEC, The Institution of Electrical Engineers., 1996.
- [66] C. M. S. Rauthan and J. K. Srivastava. Electrical breakdown voltage characteristics of buried silicon nitride layers and their correlation to defects in the nitride layer. *Materials Letters*, 9:252, 1990.
- [67] R. R. A. Syms, T. J. Tate, M. M. Ahmad, and S. Taylor. Design of a Microengineered Electrostatic Quadupole Lens. *IEEE Transactions on Electron Devices*, 45:2304, 1998.
- [68] P. Berman, editor. *Cavity QED*. Adv. At. Molec. Opt. Phys. Supplement 2. Academic Press, 1994.
- [69] L. Deslauriers, P. C. Haljan, P. J. Lee, K-A. Brickman, B. B. Blinov, M. J. Madsen, and C. Monroe. Zero-point cooling and low heating of trapped $^{111}\text{Cd}^{+}$ ions. *Physical Review A (Atomic, Molecular, and Optical Physics)*, 70(4):043408, 2004.
- [70] M. Acton, K-A Brickman, P. C. Haljan, P. J. Lee, L. Deslauriers, and C. Monroe. Near-perfect simultaneous measurement of a qubit register. *quant-ph/0511257*, 2005.

- [71] P J Lee, K-A Brickman, L Deslauriers, P C Haljan, L-M Duan, and C Monroe. Phase control of trapped ion quantum gates. *Journal of Optics B: Quantum and Semiclassical Optics*, 7(10):S371–S383, 2005.
- [72] P. C. Haljan, P. J. Lee, K-A. Brickman, M. Acton, L. Deslauriers, and C. Monroe. Entanglement of trapped-ion clock states. *Physical Review A (Atomic, Molecular, and Optical Physics)*, 72(6):062316, 2005.
- [73] P. C. Haljan, K.-A. Brickman, L. Deslauriers, P. J. Lee, and C. Monroe. Spin-dependent forces on trapped ions for phase-stable quantum gates and entangled states of spin and motion. *Physical Review Letters*, 94(15):153602, 2005.
- [74] W. K. Hensinger, S. Olmschenk, D. Stick, D. Hucul, M. Yeo, M. Acton, L. Deslauriers, C. Monroe, and J. Rabchuk. T-junction ion trap array for two-dimensional ion shuttling, storage, and manipulation. *Applied Physics Letters*, 88(3):034101, 2006.
- [75] M. A. Rowe, D. Kielpinski, V. Meyer, C. A. Sackett, W. M. Itano, C. Monroe, and D. J. Wineland. Experimental violation of a bell’s inequality with efficient detection. *Nature*, 409:791, 2001.
- [76] D. L. Moehring, B. B. Blinov, D. W. Gidley, Jr. R. N. Kohn, M. J. Madsen, T. D. Sanderson, R. S. Vallery, and C. Monroe. Precision lifetime measurement of a single trapped ion with fast laser pulses. *Phys. Rev. A*, 76:023413, 2006.
- [77] C. S. Wood, S. C. Bennett, D. Cho, B. P. Masterson, J. L. Roberts, C. E. Tanner, and C. E. Wieman. Measurement of Parity Nonconservation and an Anapole Moment in Cesium. *Science*, 275(5307):1759–1763, 1997.
- [78] L.J. Curtis. *Atomic Structure and Lifetimes*. Cambridge Univ. Press, 2003.
- [79] Z.S. Li, H. Lundberg, G.M. Wahlgren, and C.M. Sikstrom. Lifetime measurements in ce i, ce ii, and ce iii using time-resolved laser spectroscopy with application to stellar abundance determinations of cerium. *Phys. Rev. A*, 62(3):032505 – 1, 2000.
- [80] L. Young, III Hill, W.T., S.J. Sibener, S.D. Price, C.E. Tanner, C.E. Wieman, and S.R. Leone. Precision lifetime measurements of cs $6p^2p_{1/2}$ and $6p^2p_{3/2}$ levels by single-photon counting. *Phys. Rev. A*, 50(3):2174 – 81, 1994.
- [81] R.G. DeVoe and R.G. Brewer. Precision measurements of the lifetime of a single trapped ion with a nonlinear electro-optic switch. *Opt. Lett.*, 19(22):1891 – 3, 1994.
- [82] R.G. DeVoe and R.G. Brewer. Observation of superradiant and subradiant spontaneous emission of two trapped ions. *Phys. Rev. Lett.*, 76(12):2049 – 52, 1996.
- [83] E.H. Pinnington, J.J.V. van Hunen, R.N. Gosselin, B. Guo, and R.W. Berends. Beam-laser and cascade-corrected beam-foil measurements of the lifetimes of the 5p levels in singly-ionized cadmium. *Phys. Scr.*, 49(3):331 – 4, 1994.
- [84] S. Aubin, E. Gomez, L.A. Orozco, and G.D. Sprouse. Lifetime measurement of the 9s level of atomic francium. *Opt. Lett.*, 28(21):2055 – 7, 2003.
- [85] H.L. Xu, A. Persson, S. Svanberg, K. Blagoev, G. Malcheva, V. Pentchev, E. Biemont, J. Campos, M. Ortiz, and R. Mayo. Radiative lifetime and transition probabilities in cd i and cd ii. *Phys. Rev. A, At. Mol. Opt. Phys.*, 70(4):42508 – 1, 2004.
- [86] A. Gaupp, P. Kuske, and H.J. Andra. Accurate lifetime measurements of the lowest $^2p_{1/2}$ states in neutral lithium and sodium. *Phys. Rev. A, Gen. Phys.*, 26(6):3351 – 9, 1982.

- [87] R.J. Rafac, C.E. Tanner, A.E. Livingston, and H.G. Berry. Fast-beam laser lifetime measurements of the cesium $6p^2p_{1/2,3/2}$ states. *Phys. Rev. A, At. Mol. Opt. Phys.*, 60(5):3648 – 62, 1999.
- [88] R.E. Imhof and F.H. Read. Measured lifetimes of the $c\ ^3\pi_u$ state of n_2 and the $a\ ^3\sigma_g^+$ state of h_2 . *J. Phys. B, At. Mol. Phys.*, 4(8):1063 – 9, 1971.
- [89] D.A. Shaw, A. Adams, and G.C. King. Lifetime measurements in cadmium ii using the electron-photon delayed coincidence technique. *J. Phys. B, At. Mol. Phys.*, 8(15):2456 – 60, 1975.
- [90] J. Lefers, N. Miller, D. Rupke, D. Tong, and M. Walhout. Direct measurement of the metastable 3p_2 decay rate in krypton. *Phys. Rev. A, At. Mol. Opt. Phys.*, 66(1):012507 – 1, 2002.
- [91] M. Zinner, P. Spoden, T. Kraemer, G. Birkel, and W. Ertmer. Precision measurement of the metastable 3p_2 lifetime of neon. *Phys. Rev. A, At. Mol. Opt. Phys.*, 67(1):10501 – 1, 2003.
- [92] C.W. Oates, K.R. Vogel, and J.L. Hall. High precision linewidth measurement of laser-cooled atoms: resolution of the na $3p^2p_{3/2}$ lifetime discrepancy. *Phys. Rev. Lett.*, 76(16):2866 – 9, 1996.
- [93] W.I. McAlexander, E.R.I. Abraham, N.W.M. Ritchie, C.J. Williams, H.T.C. Stoof, and R.G. Hulet. Precise atomic radiative lifetime via photoassociative spectroscopy of ultracold lithium. *Phys. Rev. A, At. Mol. Opt. Phys.*, 51(2):871 – 4, 1995.
- [94] E. Peik, G. Hollemann, and H. Walther. Laser cooling and quantum jumps of a single indium ion. *Phys. Rev. A, At. Mol. Opt. Phys.*, 49(1):402 – 8, 1994.
- [95] S.R. Jefferts, C. Monroe, E.W. Bell, and D.J. Wineland. Coaxial-resonator-driven rf (paul) trap for strong confinement. *Phys. Rev. A, At. Mol. Opt. Phys.*, 51(4):3112 – 16, 1995.
- [96] M.P. Silverman, S. Haroche, and M. Gross. General theory of laser-induced quantum beats. i. saturation effects of single laser excitation. *Phys. Rev. A, Gen. Phys.*, 18(4):1507 – 16, 1978.
- [97] R.S. Vallery, P.W. Zitzewitz, and D.W. Gidley. Resolution of the orthopositronium-lifetime puzzle. *Phys. Rev. Lett.*, 90(20):203402 – 1, 2003.
- [98] J. Hamel and J.-P. Barrat. Lifetime and depolarisation by collisions of $5^2p_{3/2}$ and $5^2p_{1/2}$ levels of the cd^+ ion with helium. *Opt. Commun.*, 10(4):331 – 6, 1974.
- [99] M.D. Kunisz, J. Migdalek, and J. Rutkowski. Influence of relativistic effects on oscillator strengths of certain one-electron transitions in the cd ii spectrum. *Acta Phys. Pol. A*, A47(2):227 – 30, 1975.
- [100] Hsiang-Shun Chou and W.R. Johnson. Relativistic many-body perturbation-theory calculations of transition rates for copperlike, silverlike, and goldlike ions. *Phys. Rev. A, At. Mol. Opt. Phys.*, 56(3):2424 – 7, 1997.
- [101] S.R. Baumann and W.H. Smith. Atomic transition probabilities: Ultraviolet multiplets of zn i, ii and cd i, ii. *J. Opt. Soc. Am.*, 60(3):345 – 7, 1970.
- [102] T. Andersen and Sørensen G. *J. Quant. Spectrosc. Radiat. Transf.*, 13:369, 1973.
- [103] F.H.K. Rambow and L.D. Scheerer. Radiative lifetimes of some group ii ions by the hanle effect in a fast-flowing helium afterglow. *Phys. Rev. A, Gen. Phys.*, 14(5):1735 – 8, 1976.
- [104] T. Andersen, O. Poulse, and P.S. Ramanujam. *J. Quant. Spectrosc. Radiat. Transf.*, 16:521, 1976.

- [105] Ya.F. Verolainen and V.I. Privalov. Radiation lifetimes of 2p and 2d states in cd ii. *Opt. Spectrosc.*, 48(3):245 – 7, 1980.
- [106] T. Hansch and A. Schawlow. Cooling of gases by laser radiation. *Opt. Comm.*, 13:68–71, 1975.
- [107] J. Hoffnalge. Proposal for continuous white-light cooling of an atomic beam. *Opt. Lett.*, 13:102–104, 1998.
- [108] M. Zhu, C. W. Oates, and J. L. Hall. Continuous high-flux monovelocity atomic beam based on a broadband laser-cooling technique. *Phys. Rev. Lett.*, 67:46–49, 1991.
- [109] I. C. M. Littler, H. M. Keller, U. Gaubatz, and K. Bergmann. Velocity control and cooling of an atomic beam using a modeless laser. *Z. Phys. D.*, 18:307–308, 1991.
- [110] W. Ketterle, A. Martin, M. A. Joffe, and D. E. Pritchard. Slowing and cooling atoms in isotropic laser light. *Phys. Rev. Lett.*, 69:2483, 1992.
- [111] R. Calabrese, V. Guidi, P. Lenisa, E. Mariotti, and L. Moi. Transverse laser cooling of ions in a storage ring. *Opt. Commun.*, 123:530–534, 1996.
- [112] S. N. Atutov, R. Calabrese, R. Grimm, V. Guidi, I. Lauer, P. Lenisa, V. Luger, E. Mariotti, L. Moi, A. Peters, U. Schramm, and M. S. el. “white-light” laser cooling of a fast stored ion beam. *Phys. Rev. Lett.*, 80:2129–2132, 1998.
- [113] P. Strohmaier, A. Horn, T. Kersebom, and J. Schmand. Na-beam cooling by a mode-locked laser. *Z. Phys. D*, 21:215, 1991.
- [114] M. Watanabe, R. Omukai, U. Tanaka, K. Hayasaka, H. Imajo, and S. Urabe. Velocity control of an yb beam by a frequency-doubled mode-locked laser. *J. Opt. Soc. Am. B*, 13:2377, 1996.
- [115] A. Goepfert, I. Bloch, D. Haubrich, F. Lison, R. Schtze, R. Wynands, and D. Meschede. Stimulated focusing and deflection of an atomic beam using picosecond laser pulses. *Phys. Rev. A*, 56:R3354–R3357, 1997.
- [116] B B Blinov, R N Kohn Jr, M J Madsen, P Maunz, D L Moehring, and C Monroe. Broadband laser cooling of trapped atoms with ultrafast pulses. *quant-ph/0507074*, 2005.
- [117] R. Blümel, C. Kappler, W. Quint, and H. Walther. Chaos and order of laser-cooled ions in a paul trap. *Phys. Rev. A*, 40:808–823, 1989.
- [118] N. Rosen and C. Zener. Double stern-gerlach experiment and related collision phenomena. *Phys. Rev.*, 40:502, 1932.
- [119] D. Kielpinski. Laser cooling with ultrafast pulse trains. *arXiv:quant-ph/0306099*, 2003.
- [120] M. J. Madsen, D. L. Moehring, P. Maunz, Jr. R. N. Kohn, L.-M. Duan, and C. Monroe. Ultrafast coherent coupling of atomic hyperfine and photon frequency qubits. *quant-ph/0603258*, 2006.
- [121] P. J. Lee, B. B. Blinov, K. Brickman, L. Deslauriers, M. J. Madsen, R. Miller, D. L. Moehring, D. Stick, and C. Monroe. Atomic qubit manipulations with an electro-optic modulator. *Optics Lett.*, 28(17):1582, 2003.
- [122] R. Blatt and P. Zoller. Quantum jumps in atomic systems. *Eur. J. Phys.*, 9(4):250 – 6, 1988.
- [123] B. B. Blinov, D. L. Moehring, L.-M. Duan, and C. Monroe. Observation of entanglement between a single trapped atom and a single photon. *Nature*, 428:153, 2004.
- [124] D. L. Moehring, M. J. Madsen, B. B. Blinov, and C. Monroe. Experimental bell inequality violation with an atom and a photon. *Phys. Rev. Lett.*, 93:090410, 2004.

- [125] D. J. Berkeland, J. D. Miller, J. C. Bergquist, W. M. Itano, and D. J. Wineland. Laser-cooled mercury ion frequency standard. *Phys. Rev. Lett.*, 80:2089, 1998.
- [126] S. R. Valluri, D. J. Jeffery, and R. M. Corless. Some Applications of the Lambert W Function to Physics. *Can. J. Phys.*, 78:823–831, 2000.
- [127] F. Krausz, M. E. Fermann, T. Brabec, P. F. Curley, M. Hofer, M. H. Ober, C. Spielmann, E. Wintner, and A. J. Schmidt. Femtosecond solid-state lasers. *IEEE Journal of Quantum Optics*, 28:2097, 1992.
- [128] M. Sargent III, M. O. Scully, and W. E. Lamb Jr. *Laser Physics*. Perseus Books, Cambridge, MA, 3rd edition, 1977.